PT-SYMMETRIC HAMILTONIAN $\mathcal{H} = p^2 - (ix)^N$

Welcome to the Complex World

by

Cheng Tang

B.Sc. (Hons., Physics), University of Manitoba, 2013

A Thesis Submitted in Partial Fulfillment of the

Requirements for the Degree of

Master of Science

in the

Department of Physics

Faculty of Science

SIMON FRASER UNIVERSITY

Spring 2017

Approval

Name: **Cheng Tang**

Degree: **Master of Science (Physics)**

Title: PT**-symmetric Hamiltonian** $\mathcal{H} = p^2 - (ix)^N$
Welcome to the Complex World

Examining Committee: **Chair**: Malcolm Kennett
Associate Professor

Andrei Frolov
Senior Supervisor
Associate Professor

Andrew DeBenedictis
Supervisor
Senior lecturer

Stephanie Simmons
Supervisor
Assistant Professor

Leslie Ballentine
Internal Examiner
Professor Emeritus

Date Defended/Approved: March 21, 2017

Abstract

The Hermiticity from conventional quantum mechanics guarantees that the energy spectrum is real. However, if replace this mathematical condition by the physically transparent condition of parity-time reflection symmetry (PT-symmetry), the non-Hermitian Hamiltonian still guarantees that its entire energy spectrum is real if the Hamiltonian has unbroken PT-symmetry. If its PT-symmetry is broken, then two cases can happen - its entire energy spectrum is complex for the first case, or a finite number of real energy levels can still be obtained for the second case. This was "officially" discovered since 1998. After that, the developments in PT-symmetric quantum theory rapidly grew in the last 15 years - with more than 20 international conferences and symposia, and over 2000 research papers about PT-symmetry already published. Furthermore, at least 50 experiments to observe PT-symmetric system were published during the last 10 years. Those experiments told us that it was possible to experimentally measure complex eigenvalue and observe broken and unbroken PT-symmetry.

Admittedly, PT-symmetric quantum theory is a young and new field - currently, still not many professors and researchers familiar with this subject. That is why this thesis comes in, and tries to serve a role to introduce this subject to wide audience from students to professors. In this thesis, the energy spectrum from the PT-symmetric Hamiltonian $\mathcal{H} = p^2 - (ix)^N$ with $x \in \mathbb{C}$, $N \in \mathbb{R}$ and $N \geq 1$ was studied in detail by using numerical and WKB approximation. What the corresponding eigenfunctions look like were also examined in numerical way. Lastly, a few interesting and weird phenomena from PT-symmetric non-relativistic classical mechanics were explored in brief. We hope that this study could not only demystify but also help people appreciate many aspects of PT-symmetry.

"Truth is stranger than fiction, but it is because Fiction is obliged to stick to possibilities; Truth isn't."

MARK TWAIN
Following the Equator
1897

Acknowledgment

When look up and see the night sky, most people concentrate on and are fascinated by those shining stars. However, barely do any people ever pay attention to, let alone appreciate the beauty of the gigantic and void space which encloses all stars.

When you have space, you have potential. Dr. Frolov, my senior supervisor, is not an "ordinary" professor I have seen in schools both in China and Canada. Instead of using those "ordinary" and rigid ways of supervising - which often involve criticism, hard deadlines, forcing student to work forward, rigid and periodic meetings to force discussion about research progress, and so on - he gave me a lot of freedom, without which my journey in physics would have been ended years ago. He forgave my laziness and procrastination - based on his action, he understood the power of forgiveness (An important principle from psychology). Most importantly, rather than required me to strictly follow his footprints in Cosmology, he let me decide my research topic. Such free choice was crucial to keep my motivation going in the research. I feel so lucky and glad to work with him!

I also thank you for Dr. DeBenedictis and Dr. Simmons, who enthusiastically and patiently explained many physics to me! Without their helps, it could take forever to finish this thesis!

Thank you so much for all the people who supported me, especially, for my classmates, officemates and dorm-mates!

Lastly, for my parents who gave me vast space to overcome difficulty in my life, I love them, forever!

Cheng Tang

26 Nov. 2016

Contents

Approval ii

Abstract iii

Quote iv

Acknowledgment v

1 Background 1
- 1.1 PT-symmetry and real energy . . . 1
- 1.2 The hidden charge operator $\hat{C}$ . . . 5
- 1.3 Observable . . . 9
- 1.4 Experiment realizing PT-symmetric system . . . 10

2 The Eigenvalue Problem for the Potential $V = -(ix)^N$ 17
- 2.1 Introduction of the current chapter . . . 17
- 2.2 Local asymptotic analysis . . . 18
  - 2.2.1 For $N \geq 2$ . . . 18
  - 2.2.2 For $0 < N < 2$ . . . 23
- 2.3 Numerical approximation . . . 25
  - 2.3.1 Levenberg-Marquardt algorithm . . . 25
  - 2.3.2 Parametrization, eigenvalue and eigenfunction . . . 27
    - 2.3.2.1 Parametrization . . . 27
    - 2.3.2.2 When $N = 2$ . . . 30
    - 2.3.2.3 When $N = 3$ and $N = 2.9$ . . . 43
    - 2.3.2.4 Summarize what we know so far . . . 48
  - 2.3.3 Comparison between two pairs of PT-symmetric wedges . . . 49
  - 2.3.4 Eigenvalue E versus N . . . 51
    - 2.3.4.1 Conclusion . . . 58

3 WKB Approximation 59
- 3.1 Introduction of the current chapter . . . 59
- 3.2 The leading order conventional WKB approximation . . . 59
- 3.3 The subtlety of analytic continuation . . . 63
- 3.4 Phase Integral Method . . . 67
  - 3.4.1 Stokes diagram . . . 67
  - 3.4.2 Connection formula . . . 69
  - 3.4.3 When $N = 1$ . . . 71

3.4.4 When $N = 2$ . . . 72
3.4.5 When $N = 3$ . . . 74
3.4.6 When $N = 5$ . . . 77
3.4.7 Question, observation and future work . . . 78
3.4.7.1 Question 1: apply PIM on the pair of the green wedges for $N = 5$ . . . 78
3.4.7.2 Question 2: mathematical validity for our assumption . . . 79
3.4.7.3 Question 3: degenerate Stokes lines . . . 79
3.4.7.4 Question 4: Stokes diagram of the higher order . . . 82
3.4.7.5 Fractional N and broken PT-symmetry . . . 82
3.4.7.6 Virtual turning point . . . 84
3.5 Conclusion of the current chapter . . . 89

4 A Brief Survey of PT-symmetric Classical Mechanics **90**
4.1 Introduction of the current chapter . . . 90
4.2 Classical complex oscillator . . . 90
4.2.1 For $N \geq 2$ and N is an integer . . . 90
4.2.2 For $N \geq 2$ and N is fractional . . . 98
4.2.3 For $N < 2$ . . . 101
4.2.4 Summarize what we found in this section . . . 104
4.3 Simple complex pendulum . . . 105
4.3.1 Classical tunneling . . . 105
4.3.2 A deterministic model to explain why large object can not tunnel . . . 112

5 Conclusion **113**

References **114**

Appendix **119**

List of Figures

1.1 [54]Electronic implementation of a PT-symmetric circuit. (The following figure(link to DOI) is reprinted with permission from Joseph Schindler, Ang Li, Mei C. Zheng, F. M. Ellis, and Tsampikos Kottos, Phys. Rev. A 84, 040101(R), October 2011, Copyright 2011 by the American Physical Society.) 11

1.2 [54]Eigenfrequencies ω_l versus the normalized gain/loss parameter γ/γ_{PT}. (The following figure(link to DOI) is reprinted with permission from Joseph Schindler, Ang Li, Mei C. Zheng, F. M. Ellis, and Tsampikos Kottos, Phys. Rev. A 84, 040101(R), October 2011, Copyright 2011 by the American Physical Society.) 14

1.3 [54]The phase difference $\theta_l = \phi_2^{(l)} - \phi_1^{(l)}$ versus the normalized gain/loss parameter γ/γ_{PT}. (The following figure(link to DOI) is reprinted with permission from Joseph Schindler, Ang Li, Mei C. Zheng, F. M. Ellis, and Tsampikos Kottos, Phys. Rev. A 84, 040101(R), October 2011, Copyright 2011 by the American Physical Society.) 15

1.4 [54]Measured total energy $E_C^{tot}(\tau)$ of capacitors of the whole system versus τ. (The following figure(link to DOI) is reprinted with permission from Joseph Schindler, Ang Li, Mei C. Zheng, F. M. Ellis, and Tsampikos Kottos, Phys. Rev. A 84, 040101(R), October 2011, Copyright 2011 by the American Physical Society.) 16

2.1 All Stokes wedges for non-negative integer N and all corresponding turning points (yellow point with black edge) 22

2.2 The chosen Stokes wedges for non-negative integer N and all corresponding turning points (yellow point with black edge) 23

2.3 The eigenfunction of the ground state for $N = 4$ along the Stokes lines (non-differentiable at origin) with $r_0 = 4$. The vertical-blue dotlines represent two numerical infinities $\pm \mathrm{Re}(x_0) = \pm r_0 \cos 30°$. Along the Stokes lines, the numerical result for the eigenvalue E does not change even though the shape of the eigenfunction is not smooth, in comparison with the smooth eigenfunctions associated with the hyperbolic paths. 28

2.4 The eigenfunctions of the ground state for $N = 4$ along the differentiable (hyperbolic) paths with three different values of a defined by the hyperbolic equation $Y_- = -a\sqrt{1 + \frac{X^2}{b^2}}$. All three paths have the same eigenvalue. The vertical-blue dotlines represent two numerical infinities $\pm \mathrm{Re}\,(x_0) = \pm r_0 \cos 30°$ with $r_0 = 4$. 29
2.5 The differentiable path for $N < 2$ by choosing $c = \frac{1}{10}$ and $t = 8$. . . 30
2.6 Four distinct contour paths we follow for $N = 2$. 31
2.7 Parametric curve crosses itself. 32
2.8 $\mathrm{Re}\,(x)$ versus the eigenfunction of the ground level along the real and sinusoidal path for $N = 2$ (Before using (2.72) to normalize). 34
2.9 $\mathrm{Re}\,(x)$ versus the eigenfunction of the ground level along the real and sinusoidal path for $N = 2$ (after using (2.72) to normalize). . 34
2.10 $\mathrm{Re}\,(x)$ or p versus the eigenfunction of the ground level along three paths (real, sin. and sym. path) for $N = 2$ 37
2.11 $\mathrm{Im}\,(x)$ versus the eigenfunction of the ground level along three paths (real, sin. and sym. path) for $N = 2$ 37
2.12 $\mathrm{Re}\,(x)$ or p versus the eigenfunction of the ground level along three paths (real, sin. and non-sym. path) for $N = 2$ (See magnification on Fig.(2.13)) 38
2.13 $\mathrm{Re}\,(x)$ versus the eigenfunction of the ground level along three paths (real, sin. and non-sym. path) for $N = 2$ (after magnifying) 38
2.14 $\mathrm{Im}\,(x)$ versus the eigenfunction of the ground level along three paths (real, sin. and non-sym. path) for $N = 2$ 39
2.15 $\mathrm{Re}\,(x)$ or p versus the eigenfunction of the 4th level along three paths (real, sin. and non-sym. path) for $N = 2$ (See magnification on Fig.(2.16)) 40
2.16 $\mathrm{Re}\,(x)$ versus the eigenfunction of the 4th level along three paths (real, sin. and non-sym. path) for $N = 2$ (after magnifying) 40
2.17 $\mathrm{Im}\,(x)$ versus the eigenfunction of the 4th level along three paths (real, sin. and non-sym. path) for $N = 2$ (See magnification on Fig.(2.18)) 41
2.18 $\mathrm{Im}\,(x)$ versus the eigenfunction of the 4th level along three paths (real, sin. and non-sym. path) for $N = 2$ (after magnifying) 41
2.19 $\mathrm{Re}\,(x)$ or p versus the eigenfunction of the ground level along the pink path for $N = 2$ 42
2.20 $\mathrm{Im}\,(x)$ versus the eigenfunction of the ground level along the pink path for $N = 2$ 43
2.21 Six distinct contour paths we follow for $N = 3$ 43
2.22 $\mathrm{Re}\,(x)$ versus the eigenfunction of the ground level along two paths (poly. CD and sin. CD) for $N = 3$. The number of crossing events is equal to the number of intersection points between the two paths. 45
2.23 $\mathrm{Re}\,(x)$ versus the eigenfunction of the ground level along two paths (poly. AB and sin. CD) for $N = 3$. No crossing event happens. 45
2.24 $\mathrm{Re}\,(x)$ versus the eigenfunction of the ground level along two paths (sin. CD and real C'D') for $N = 3$. No crossing event happens. 46

2.25 Six distinct contour paths we follow for $N = 2.9$ 47
2.26 Two distinct contour paths we follow for $N = 5$ 49
2.27 Energy spectrum of the 1st family from the pair of the orange wedges (The grey curves are WKB approximation) 51
2.28 Energy spectrum of the 2nd family from the pair of the green wedges (The grey curves are WKB approximation) 54
2.29 A single eigenvalue curve from the pair of the green wedges . . . 55
2.30 Energy spectrum of the 3rd family from the pair of the pink wedges (The grey curves are WKB approximation) 56
2.31 Four energy spectra of the first four families from four pairs of PT-symmetric (orange, green, pink, yellow) wedges 57

3.1 [30]The asymptotic behaviors of $\psi_{\pm}(z)$ as $|z| \to \infty$ 65
3.2 [30]The orange Stokes wedges rotate clockwisely when α rotates counter-clockwisely 66
3.3 Stokes diagram for $N = 1$ and $E = 1$, where the yellow points are the turning points, the green dot-lines are Stokes lines and the orange dot-lines are anti-Stokes lines 71
3.4 Stokes diagram for $N = 2$ and $E = 1$, where the yellow points are the turning points, the green dot-lines are Stokes lines and the orange dot-lines are anti-Stokes lines 72
3.5 Stokes diagram for $N = 3$ and $E = 1$, where the yellow points are the turning points, the green dot-lines are Stokes lines and the orange dot-lines are anti-Stokes lines 74
3.6 Stokes diagram for $N = 5$ and $E = 1$, where the yellow points are the turning points, the green dot-lines are Stokes lines and the orange dot-lines are anti-Stokes lines 77
3.7 Stokes diagram for $N = 5$ and $E = 1$, where the yellow points are the turning points, the green dot-lines are Stokes lines and the orange dot-lines are anti-Stokes lines 78
3.8 Stokes diagram for $N = 4$ and $E = 1$, where the green dot-lines are Stokes lines and the orange dot-lines are anti-Stokes lines . . 80
3.9 Stokes diagram for $N = 3.9$ and $N = 4.1$ when $E = 1$, where the yellow points are the principal turning points, the green dot-lines are Stokes lines and the orange dot-lines are anti-Stokes lines . . 80
3.10 Stokes diagram for $N = 6$ and $E = 1$, where the yellow points are the turning points, the green dot-lines are Stokes lines and the orange dot-lines are anti-Stokes lines 81
3.11 Stokes diagram for $N = 1.5$ and $N = 3.5$ when $E = 1$, where the yellow points are the principal turning points, two Stokes lines cross at point C, the green dot-lines are Stokes lines and the orange dot-lines are anti-Stokes lines. Also, note that the anti-Stokes flows suddenly change direction after crossing the positive imaginary axis. 82
3.12 Stokes diagram for $N = 2.5$ and $N = 3$ when $E = 1$, where the yellow points are the principal turning points, the green dot-lines are Stokes lines and the orange dot-lines are anti-Stokes lines . . 84

3.13 [41, p.26]Solid lines are Stokes lines for the BNR equation and they cross at points C_1 and C_2. The red thick-dash lines are branch cuts. 86
3.14 [41, p.32]Bicharacteristic curve (the blue curve on this figure) for BNR equation. The two singular points from B-curve projected on the x-plane are the turning points $x = \pm 1$; Whereas the x-component of the self-intersection point, which is $x = 0$, is the virtual turning point. (Only $\mathrm{Im}\,(y)$ is plotted here, since $\mathrm{Re}\,(y) = 0$ by (3.84). So is $\mathrm{Im}\,(x)$.) 87
3.15 [41, p.32]Complete Stokes lines for BNR equation. Solid lines are active Stokes lines, the blue dash line segment are inert Stokes lines, and red thick-dash lines are branch cuts. 87

4.1 Classical trajectories when $N = 2$ and $E_0 = 1$, where by (4.10) all orbits have the same period $T = 4.4428829381$. Particles move clockwisely in all orbits. 93
4.2 Energy E versus time t for $N = 2$ with period $T = 4.4428829381$. The vertical blue dot lines indicate the time when the particle crosses the imaginary axis. 93
4.3 Classical trajectories when $N = 5$ and $E_0 = 1$ 94
4.4 Energy E versus time t for $N = 5$ with period $T = 2.0843368815$. The vertical blue dot lines indicate the time when the particle crosses the imaginary axis. 95
4.5 Classical trajectories when $N = 3$ and $E_0 = 1$. The green curve shows the half of the orbit 2. 97
4.6 Energy E versus time t for $N = 3$. The vertical blue dot line indicates the time of the half period of the orbit 2 from Fig.(4.5). . 97
4.7 Classical trajectories when $N = 2.5$ and $E_0 = 1$. We did not find any orbit which only encloses non-principal turning points. 98
4.8 Energy E versus time t for $N = 2.5$ with period $T = 3.9586963635$. The vertical blue dot lines indicate the time when the particle crosses the imaginary axis. 99
4.9 A classical trajectory when $N = 2.5$, $E_0 = 1$ and $x_0 = i$ 100
4.10 Energy E versus time t for $N = 2.5$ with initial period $T_0 = 3.792$. The vertical blue dot lines indicate the time when the particle crosses the imaginary axis. 100
4.11 Energy E versus longer time t for $N = 2.5$ with initial period $T_0 = 3.792$ 101
4.12 Classical trajectories when $N = 1.8$ and $N = 1.6$ and $E_0 = 1$ . . . 102
4.13 Energy E versus time t for $N = 1.6$ the blue trajectory on Fig.(4.12) 102
4.14 Classical trajectories when $N = 1.3$ and $E_0 = 1$ 103
4.15 Energy E versus time t for $N = 1.3$ 104
4.16 A simple pendulum 105
4.17 Classical trajectories for complex pendulum with $E_0 = 0$ and period $T = 7.4162987092$. All particles in closed orbits move in clockwise direction. 106

4.18 Energy E versus time t with $E_0 = 0$ for particle to escape to the complex infinity, starting from $x_0 = \pi$ shown on Fig.(4.17). The corresponding setup is shown on Fig.(4.19). Note that when $x_0 = \pi$, the pendulum still tries to form an elliptic orbit, but the radius of this orbit becomes infinite long. To maintain the constant period T, the speed of the pendulum becomes infinite as well. This causes unstable numerical result for infinite speed, and therefore the numerical energy blows up when speed becomes huge. 107
4.19 The initial position of the pendulum with $E_0 = 0$ is chosen to be $x_0 = \theta_0 = \pi$, which is inside the dynamically inaccessible region because $V > 0$ and $E_0 < V$ in this region. In this setup, the pendulum is in an unstable equilibrium position. Intuitively, the pendulum should stay at this position forever if $E_0 = 0$. However, this is not true in this case, because (4.21) implies that for the chosen E_0 and x_0, the velocity of the pendulum is non-zero, but equal to an purely imaginary number $\sqrt{2}i$, and that is why the pendulum starts to move along the vertical direction in the complex plane of x. 108
4.20 Energy E versus time t with $E_0 = 0$ for one of orbits shown on Fig.(4.17). The vertical blue dot lines indicate the time when the particle crosses the imaginary axis. 109
4.21 Classical trajectories for complex pendulum with $E_0 = \frac{1}{2}$ and period $T = 8.6260625694$. All particles in closed orbits move in counter-clockwise direction. 110
4.22 A classical trajectory for complex pendulum with $E_0 = \frac{1}{2}i$ and $x_0 = 0$ 110
4.23 A classical trajectory for complex pendulum with $E_0 = 0.5 + 0.1i$ and $x_0 = 0$ 111
4.24 Well-behaved energy E versus time t with $E_0 = 0.5 + 0.1i$ and $x_0 = 0$ 112

List of Tables

2.1 Eigenvalues E from four distinct paths for $N = 2$ 33
2.2 Eigenvalues of the 0th and 2nd level from six distinct paths for $N = 3$ 44
2.3 Eigenvalues of the 0th and 2nd level from six distinct paths for $N = 2.9$ 47
2.4 Eigenvalues E from the two distinct paths for $N = 5$ 50
2.5 Ratios of eigenvalues ($\mathrm{Im}\,(E)$ ignored) from the two distinct paths for $N = 5$ 50
2.6 Locations of the green data points (two nearest to the degenerated eigenvalues) 53

3.1 Eigenvalues E for $N = 3$ obtained by the three methods 76
3.2 Eigenvalues E for $N = 5$ obtained by the three methods 77
3.3 Locations of a few crossing points C for various N, with error less than 10^{-12} 83

4.1 When $N = 5$ and $E_0 = 1$, the period T is obtained by analytical and numerical method (with numerical integration step $dt = 0.001$) 94
4.2 When $N = 2.5$ and $E_0 = 1$, the period T is obtained by analytical and numerical method (with numerical integration step $dt = 0.001$) 99

Chapter 1

Background

Sec.(1.1), Sec.(1.2) and Sec.(1.3) contain the primary work by Bender[8]. In those sections, we introduce the concept of parity and time reversal symmetry along with the charge operator. In Sec.(1.4), we introduce an experiment by Schindler *et al.*[54] to realize the PT-symmetric system.

1.1 PT-symmetry and real energy

The operator $\hat{P}$ is the parity reflection operator such that[8, p.3]

$$\hat{P}x\hat{P} = -x \qquad \hat{P}p\hat{P} = -p \qquad \hat{P}i\hat{P} = i \tag{1.1}$$

where x and p represent particle's position and momentum in quantum mechanics. The time reversal operator is $\hat{T}$ such that

$$\hat{T}x\hat{T} = x \qquad \hat{T}p\hat{T} = -p \qquad \hat{T}i\hat{T} = -i \tag{1.2}$$

where in quantum mechanics with real x and p, the canonical commutation relation $[\hat{x}, \hat{p}] = i$ is invariant under both parity reflection and time reversal operations. Consequently, we have

$$\left(\hat{P}\right)^2 x \left(\hat{P}\right)^2 = x \qquad \left(\hat{P}\right)^2 p \left(\hat{P}\right)^2 = p \tag{1.3}$$

$$\left(\hat{T}\right)^2 x \left(\hat{T}\right)^2 = x \qquad \left(\hat{T}\right)^2 p \left(\hat{T}\right)^2 = p \qquad \left(\hat{T}\right)^2 i \left(\hat{T}\right)^2 = i \tag{1.4}$$

and therefore

$$\left(\hat{P}\right)^2 = \left(\hat{T}\right)^2 = \left(\hat{P}\hat{T}\right)^2 = \mathbf{I} \tag{1.5}$$

where $\mathbf{I}$ is an identity matrix. And the following commutation relation holds:

$$\left[\hat{P}, \hat{T}\right] = 0 \tag{1.6}$$

The commutation relation $[\hat{x}, \hat{p}] = i$ still holds even if x and p are complex. In such case, by (1.1) and (1.2) we have

$$\hat{P}\mathrm{Re}\,(x)\,\hat{P} = -\mathrm{Re}\,(x) \qquad \hat{P}\mathrm{Im}\,(x)\,\hat{P} = -\mathrm{Im}\,(x) \tag{1.7}$$

$$\hat{P}\mathbf{Re}\,(p)\,\hat{P} = -\mathbf{Re}\,(p) \qquad \hat{P}\mathbf{Im}\,(p)\,\hat{P} = -\mathbf{Im}\,(p) \tag{1.8}$$

and

$$\hat{T}\mathbf{Re}\,(x)\,\hat{T} = \mathbf{Re}\,(x) \qquad \hat{T}\mathbf{Im}\,(x)\,\hat{T} = -\mathbf{Im}\,(x) \tag{1.9}$$

$$\hat{T}\mathbf{Re}\,(p)\,\hat{T} = -\mathbf{Re}\,(p) \qquad \hat{T}\mathbf{Im}\,(p)\,\hat{T} = \mathbf{Im}\,(p) \tag{1.10}$$

$$\hat{T}i\hat{T} = -i \tag{1.11}$$

By (1.5) and (1.11), we have

$$\hat{T}i\left(\hat{T}\right)^2 = -i\hat{T} \Longrightarrow \hat{T}i = -i\hat{T} \tag{1.12}$$

Let ψ be an eigenfunction of the operations $\hat{P}\hat{T}$ with eigenvalue λ such that

$$\hat{P}\hat{T}\psi = \lambda\psi \tag{1.13}$$

then by (1.12)

$$\begin{aligned} &\hat{P}\hat{T}\hat{P}\hat{T}\psi = \hat{P}\hat{T}\lambda\psi \\ \Longrightarrow &\left(\hat{P}\hat{T}\right)^2\psi = \hat{P}\lambda^*\hat{T}\psi \\ \Longrightarrow &\left(\hat{P}\hat{T}\right)^2\psi = \lambda^*\hat{P}\hat{T}\psi \\ \Longrightarrow &\left(\hat{P}\hat{T}\right)^2\psi = \lambda^*\lambda\psi \end{aligned}$$

By (1.5) the eigenvalue for the operator $\hat{P}\hat{T}$ must be (with $\theta \in \mathbb{R}$)

$$\begin{aligned} &\lambda^*\lambda = 1 \\ \Longrightarrow &\lambda = e^{i\theta} \end{aligned} \tag{1.14}$$

We say a Hamiltonian $\mathcal{H}$ is PT**-symmetric** if the operator $\hat{P}\hat{T}$ commutes with $\mathcal{H}$ such that

$$\left[\hat{P}\hat{T}, \mathcal{H}\right] = \mathcal{H}\left(\hat{P}\hat{T}\right) - \left(\hat{P}\hat{T}\right)\mathcal{H} = 0 \tag{1.15}$$

where $\mathcal{H}$ does not have to be Hermitian. By (1.5), (1.15) can be rewritten as

$$\begin{aligned} \left(\hat{P}\hat{T}\right)\mathcal{H}\left(\hat{P}\hat{T}\right) - \left(\hat{P}\hat{T}\right)^2\mathcal{H} &= 0 \\ \mathcal{H} &= \left(\hat{P}\hat{T}\right)\mathcal{H}\left(\hat{P}\hat{T}\right) \\ \mathcal{H} &= \mathcal{H}^{PT} \end{aligned} \tag{1.16}$$

where the notation[8, p.3] $\mathcal{H}^{PT}$ is an analogue of the notation for the Hermiticity $\mathcal{H}^\dagger$.

There are infinitely many PT-symmetric Hamiltonians. What do they look like? We list a few of their forms without explaining details of them in here (See the corresponding references for details):

- $$\mathcal{H} = \begin{bmatrix} a - ib & 0 \\ 0 & a + ib \end{bmatrix} \qquad a, b \in \mathbb{R} \tag{1.17}$$

- From quantum mechanical brachistochrone system[38]

$$\mathcal{H} = E_0 \begin{bmatrix} 1 & 0 \\ 0 & 1 \end{bmatrix} + s \begin{bmatrix} i\sin\alpha & 1 \\ 1 & -i\sin\alpha \end{bmatrix} \qquad E_0, s, \alpha \in \mathbb{R} \tag{1.18}$$

- From quantum computing[16, 63]

$$\mathcal{H} = \begin{bmatrix} x + (z+iy) & \frac{z}{\tan\gamma} - iy\tan\gamma \\ \frac{z}{\tan\gamma} - iy\tan\gamma & x - (z+iy) \end{bmatrix} \qquad x, y, z, \gamma \in \mathbb{R} \tag{1.19}$$

- From Lee model[45, 43, 13]

$$\mathcal{H} = \mathcal{H}_0 + g\mathcal{H}_1 \tag{1.20}$$

where

$$\mathcal{H}_0 = m_{v_0} V^\dagger V + m_N N^\dagger N + m_\theta a^\dagger a \tag{1.21}$$

$$\mathcal{H}_1 = V^\dagger N a + a^\dagger N^\dagger V \tag{1.22}$$

- From time-like Liouville conformal logarithmic quantum field theory[25]

$$\mathcal{H} = p^2 - igx\left(e^{iax}\right) \tag{1.23}$$

- From Painlevé transcendents problem[20, 27]

$$\mathcal{H} = \frac{1}{2}p^2 + 2ix^3 \qquad \text{(Painlevé I)} \tag{1.24}$$

$$\mathcal{H} = \frac{1}{2}p^2 - \frac{1}{2}x^4 \qquad \text{(Painlevé II)} \tag{1.25}$$

$$\mathcal{H} = \frac{1}{2}p^2 + \frac{1}{8}x^6 \qquad \text{(Painlevé IV)} \tag{1.26}$$

- From supergravity[33, 2, 3, 26]

$$\mathcal{H} = p^2 - x^4\ln(ix) \tag{1.27}$$

- From Higgs vacuum[57, 26]

$$\mathcal{H} = p^2 - x^4\ln\left(x^2\right) \tag{1.28}$$

As an example, let's see why the non-Hermitian Hamiltonian $\mathcal{H} = p^2 + ix^3$ is PT-symmetric.

$$\begin{aligned}
\mathcal{H} - \left(\hat{P}\hat{T}\right)\mathcal{H}\left(\hat{P}\hat{T}\right) &= p^2 + ix^3 - \left(\hat{P}\hat{T}\right)\left(p^2 + ix^3\right)\left(\hat{P}\hat{T}\right) \\
&= p^2 + ix^3 - \left(\hat{P}\hat{T}\right)p^2\left(\hat{P}\hat{T}\right) - \left(\hat{P}\hat{T}\right)ix^3\left(\hat{P}\hat{T}\right) \\
&= p^2 + ix^3 - \left(\hat{P}\hat{T}\right)p^2\left(\hat{T}\hat{P}\right) - \left(\hat{P}\hat{T}\right)ix^3\left(\hat{T}\hat{P}\right) \\
&= p^2 + ix^3 - \left(\hat{P}\right)(-p)^2\left(\hat{P}\right) - \left(\hat{P}\right)(-i)\,x^3\left(\hat{P}\right) \\
&= p^2 + ix^3 - (p)^2 - (-i)\,(-x)^3 \\
&= 0
\end{aligned}$$

By (1.16), $\mathcal{H} = p^2 + ix^3$ is PT-symmetric. How about $\mathcal{H} = p^2 - (ix)^N$ for $N \in \mathbb{R}$?

$$\begin{aligned}
\mathcal{H} - \left(\hat{P}\hat{T}\right)\mathcal{H}\left(\hat{P}\hat{T}\right) &= p^2 - (ix)^N - \left(\hat{P}\hat{T}\right)\left(p^2 - (ix)^N\right)\left(\hat{P}\hat{T}\right) \\
&= p^2 - (i\hat{x})^N - \left(\hat{P}\hat{T}\right)p^2\left(\hat{T}\hat{P}\right) + \left(\hat{P}\hat{T}\right)(ix)^N\left(\hat{T}\hat{P}\right) \\
&= p^2 - (i\hat{x})^N - \left(\hat{P}\right)(-p)^2\left(\hat{P}\right) + \left(\hat{P}\right)(-i)^N x^N\left(\hat{P}\right) \\
&= p^2 - (i\hat{x})^N - (p)^2 + (-i)^N(-x)^N \\
&= -(ix)^N + (-1)^{2N}(ix)^N \\
&= -(ix)^N + (1)^N(ix)^N \\
&= 0
\end{aligned}$$

Therefore

$$\mathcal{H} = p^2 - (ix)^N \tag{1.29}$$

is PT-symmetric for any real N.

Let ψ be an eigenfunction of $\mathcal{H}$ such that

$$\mathcal{H}\psi = E\psi \tag{1.30}$$

We know that if two linear operators commute, they can be simultaneously diagonalized. If a linear operator commutes with Hamiltonian $\mathcal{H}$, then the eigenfunction ψ of $\mathcal{H}$ is simultaneously the eigenfunction of that linear operator. However, from (1.11), the operation of complex conjugation by time reversal operator $\hat{T}$ causes the operator $\hat{P}\hat{T}$ to be a nonlinear operator. To continue the story, we assume that the eigenfunction ψ of $\mathcal{H}$ is simultaneously the eigenfunction of the operator $\hat{P}\hat{T}$ with eigenvalue $\lambda = e^{i\theta}$. By (1.5),

$$\hat{P}\hat{T}\mathcal{H}\psi = \hat{P}\hat{T}E\left[\left(\hat{P}\hat{T}\right)^2\right]\psi \tag{1.31}$$

By (1.15), (1.13) and (1.12)

$$\begin{aligned}
&\Longrightarrow \mathcal{H}\hat{P}\hat{T}\psi = \hat{P}\hat{T}E\hat{P}\hat{T}\lambda\psi \\
&\Longrightarrow \mathcal{H}\lambda\psi = \hat{P}\hat{T}E\left(\hat{P}\hat{T}\right)\lambda\psi \\
&\Longrightarrow \lambda\mathcal{H}\psi = \hat{P}E^*\hat{T}\hat{P}\hat{T}\lambda\psi \\
&\Longrightarrow \lambda E\psi = E^*\hat{P}\hat{T}\hat{P}\hat{T}\lambda\psi \\
&\Longrightarrow \lambda E\psi = E^*\left(\hat{P}\hat{T}\right)^2\lambda\psi \\
&\Longrightarrow E\lambda\psi = E^*\lambda\psi
\end{aligned}$$

By (1.14), $\lambda \neq 0$, and consequently energy E is real.

$$E = E^* \tag{1.32}$$

In general, this conclusion about the reality of the energy is not true because the eigenfunction ψ of $\mathcal{H}$ may not be simultaneously the eigenfunction of the operator $\hat{P}\hat{T}$.

If every eigenfunction of a PT-symmetric Hamiltonian is also an eigenfunction of the operator $\hat{P}\hat{T}$, we say that the PT-symmetry of $\mathcal{H}$ is unbroken. Conversely, if some of the eigenfunctions of a PT-symmetric Hamiltonian are not simultaneously eigenfunctions of the operator $\hat{P}\hat{T}$, we say that the PT-symmetry of $\mathcal{H}$ is broken. For example, the PT-symmetry of the Hamiltonian $\mathcal{H} = p^2 - (ix)^N$ from (1.29) is broken when $N < 2$ and unbroken[1] when $N \geq 2$. In general, for a given Hamiltonian, it is difficult to prove whether the PT-symmetry is broken or unbroken, so we omit[2] this rigorous proof here, but accept this as a fact. To correctly interpret (1.32), we say that all eigenvalues associated with the Hamiltonian are real if that Hamiltonian has an unbroken PT-symmetry.

1.2 The hidden charge operator $\hat{C}$

In Hermitian quantum mechanics

$$\langle\psi|\,\mathcal{H}\,|\psi\rangle = E\,\langle\psi\,|\psi\rangle \tag{1.33}$$

with $\mathcal{H}^\dagger = \mathcal{H}$, we have

$$(E^* - E)\,\langle\psi\,|\psi\rangle = 0 \tag{1.34}$$

In continuous basis,

$$(E^* - E)\int \psi^*(x)\,\psi(x)\,dx = 0 \tag{1.35}$$

Since $\int \psi^*\psi dx$ is positive definite, so $(E^* - E)$ should vanish and consequently, E is real.

For PT-symmetric potential, where

$$\begin{aligned} V(x)^{PT} &= V(x) \\ \Longrightarrow \left(\hat{P}\hat{T}\right) V(x) \left(\hat{P}\hat{T}\right) &= V(x) \\ \Longrightarrow \hat{P}V^*(x)\,\hat{P} &= V(x) \\ \Longrightarrow V^*(-x) &= V(x) \end{aligned} \tag{1.36}$$

we still have

$$(E^* - E)\,\langle\psi\,|\psi\rangle = 0 \tag{1.37}$$

However, we can not simply conclude that E is real, since we don't know what the norm $\langle\psi\,|\psi\rangle$ is. In fact, $\langle\psi\,|\psi\rangle = 0$ may be true if PT-symmetry is broken. So in cases of broken PT-symmetry $\langle\psi\,|\psi\rangle$ is not positive-definite. This rises an urgent problem - for PT-symmetric quantum mechanics, we need to find the inner product otherwise we may have trouble with the probabilistic interpretation.

[1] "Unbroken when $N \geq 2$" is actually not true if different pair of Stokes wedges is involved. We will dig into the details in the next chapter.

[2] See [36] for rigorous proof, where techniques, such as monodromy group, Bethe ansatz, Baxter T-Q relation, are used.

To solve this problem, let's look at PT-normalization first. By the definition of unbroken PT-symmetry, if the PT-symmetry is not broken, then every eigenfunction $\psi_n(x)$ of a PT-symmetric Hamiltonian is also an eigenfunction of the operator $\hat{P}\hat{T}$ with eigenvalue $\lambda_n = e^{i\theta_n}$ from (1.14). If we define

$$\phi_n(x) \equiv \exp\left(i\theta_n/2\right)\psi_n(x) \tag{1.38}$$

then what happens? We know that $\exp\left(i\theta_n/2\right)$ is just a phase factor so that $\phi_n(x)$ is still an eigenfunction of the PT-symmetric Hamiltonian and also an eigenfunction of the operator $\hat{P}\hat{T}$. With this property and using (1.13), (1.38), (1.5), (1.12) and (1.14), we obtain

$$\begin{aligned}
\hat{P}\hat{T}\phi &= \rho\phi \\
\hat{P}\hat{T}\exp\left(i\theta/2\right)\psi &= \rho\exp\left(i\theta/2\right)\psi \\
\left(\hat{P}\hat{T}\right)^2\exp\left(i\theta/2\right)\psi &= \hat{P}\rho^*\exp\left(-i\theta/2\right)\hat{T}\psi \\
\exp\left(i\theta/2\right)\psi &= \rho^*\exp\left(-i\theta/2\right)\lambda\psi \\
\exp\left(i\theta/2\right)\psi &= \rho^*\exp\left(-i\theta/2\right)\exp\left(i\theta\right)\psi \\
\psi &= \rho^*\psi
\end{aligned}$$

So the eigenvalue of the eigenfunction $\phi(x)$ for the operator $\hat{P}\hat{T}$ is

$$\rho = 1 \tag{1.39}$$

Therefore, $\phi_n(x)$ from (1.38) is called "PT**-normalized eigenfunction**", which satisfies[15]

$$\hat{P}\hat{T}\phi_n(x) = \phi_n^*(-x) = \phi_n(x) \tag{1.40}$$

Notice that for un-normalized eigenfunction $\psi_n(x)$, by (1.13) we still have

$$\hat{P}\hat{T}\psi_n(x) = e^{i\theta_n}\psi_n(x) \tag{1.41}$$

where the phase angle θ_n is a function of energy level n.

Now we have to guess what the inner product is, before examining the orthogonality of eigenstates. The natural guess for the inner product of the PT-normalized eigenfunction must be

$$\begin{aligned}
\left\langle \phi_m(x), \phi_n(x)\right\rangle_{PT} &= \int_c \hat{P}\hat{T}\phi_m(x)\,\phi_n(x)\,dx \\
&= \int_c \phi_m^*(-x)\,\phi_n(x)\,dx \\
&= \int_c \phi_m(x)\,\phi_n(x)\,dx \\
&= 0 \qquad \text{for } m \neq n
\end{aligned}$$

This looks promising, however, the critical issue is that in general the norm

$$\left\langle \phi_n(x), \phi_n(x)\right\rangle_{PT} = \int_c \hat{P}\hat{T}\phi_n(x)\,\phi_n(x)\,dx \neq 1 \tag{1.42}$$

It's difficult but possible[8, 12] to use either numerical or analytical approximation to show that the contour integral $\int_c \hat{P}\hat{T}\phi_n(x)\,\phi_n(x)\,dx$ approximately behaves like $(-1)^n$ in great accuracy[3] for $N \geq 2$ from (1.29). Therefore, heuristically, the PT**-norm** is defined exactly to be $(-1)^n$.

$$\langle \phi_n(x), \phi_n(x)\rangle_{PT} = \int_c \hat{P}\hat{T}\phi_n(x)\,\phi_n(x)\,dx = \int_c \phi_n(x)\,\phi_n(x)\,dx \equiv (-1)^n \tag{1.43}$$

Hence we obtain the following completeness relation[12]

$$\sum_{n=0}^{\infty} (-1)^n \phi_n(x)\,\phi_n(y) = \delta(x-y) \tag{1.44}$$

Note that so far we only know the PT-norm for $\mathcal{H} = p^2 - (ix)^N$ is $(-1)^n$ and we are not sure whether the value of the PT-norm is going to change for different PT-symmetric Hamiltonian or not. Furthermore, the boundary condition associated with $\phi_n(x)$ is assumed to be $\phi_n(x) \to 0$ and $\phi_n'(x) \to 0$ as $|x| \to \infty$, and the contour path $\int_c$ can be any path which satisfies the boundary condition. Whether the value of the PT-norm is independent from the boundary condition and the shape of contour path or not is unknown. More researches are needed.

Since the PT-norm is not positive-definite, inspired by Dirac, we define[8, p.39] a linear operator $\hat{C}$ represented in coordinate space as a sum over the PT-normalized eigenfunctions

$$\hat{C}(x,y) \equiv \sum_{n=0}^{\infty} \phi_n(x)\,\phi_n(y) \tag{1.45}$$

whose form is similar to (1.44) except of $(-1)^n$. Therefore, $\hat{C}(x,y)$ satisfies the following translation relation

$$\hat{C}\phi_n(x) = \int_c \hat{C}(x,y)\,\phi_n(y)\,dy \tag{1.46}$$

which is similar to the translation relation $\phi_n(x) = \int \delta(x-y)\,\phi_n(y)\,dy$ from Dirac delta function. With (1.46), we can define the CPT **inner product** as

$$\langle \phi_m(x), \phi_n(x)\rangle_{CPT} = \int_c \hat{C}\hat{P}\hat{T}\phi_m(x)\,\phi_n(x)\,dx = \int_c\int_{c'} \hat{C}(x,y)\,\phi_m^*(-y)\,\phi_n(x)\,dxdy \tag{1.47}$$

The operator $\hat{C}$ has eigenvalues ± 1, since from (1.46) and (1.43)

$$\begin{aligned}\hat{C}\phi_n(x) &= \int_c \hat{C}(x,y)\,\phi_n(y)\,dy \\ &= \sum_{m=0}^{\infty} \phi_m(x) \int_c \phi_m(y)\,\phi_n(y)\,dy \\ &= (-1)^n \phi_n(x)\end{aligned} \tag{1.48}$$

[3] Assume accurate at least 20 decimal places.

So the operator $\hat{C}$ measures the sign of the PT-norm and behaves like a charge conjugation operator who changes the sign of all quantum charges. Thus, we also call $\hat{C}$ as a **charge operator**. Following from (1.47) and using (1.48), we have

$$\begin{aligned}
\left\langle \phi_m(x), \phi_n(x) \right\rangle_{CPT} &= \int_c \int_{c'} \hat{C}(x,y)\, \phi_m^*(-y)\, dy \phi_n(x)\, dx \\
&= \int_c \int_{c'} \hat{C}(x,y)\, \phi_m(y)\, dy \phi_n(x)\, dx \\
&= \int_c (-1)^m \phi_m(x)\, \phi_n(x)\, dx \\
&= (-1)^m \int_c \phi_m(x)\, \phi_n(x)\, dx \\
&= 0
\end{aligned}$$

So the CPT**-norm** is positive-definite since

$$\begin{aligned}
\left\langle \phi_n(x), \phi_n(x) \right\rangle_{CPT} &= \int_c \int_{c'} \hat{C}(x,y)\, \phi_n^*(-y)\, \phi_n(x)\, dxdy \\
&= (-1)^n \int_c \phi_n(x)\, \phi_n(x)\, dx \\
&= 1
\end{aligned} \tag{1.49}$$

Notice that it would be wrong[11, p.4] to use $(-1)^n \int_c \phi_n^*(x)\, \phi_n(x)\, dx$ for non-Hermitian PT-symmetric Hamiltonian. It is $\phi_n^2(x)$, not $|\phi_n(x)|^2$ so that the complex conjugation is not involved.

Consequently, using (1.46), (1.48) and (1.44), the CPT-completeness relation must be

$$\begin{aligned}
\sum_{n=0}^{\infty} \phi_n(x) \left[\hat{C}\hat{P}\hat{T}\phi_n(y) \right] &= \sum_{n=0}^{\infty} \phi_n(x) \left[\int_c \hat{C}(x,y)\, \phi_n(x)\, dx \right] \\
&= \sum_{n=0}^{\infty} \phi_n(x) (-1)^n \phi_n(y) \\
&= \delta(x-y)
\end{aligned}$$

The operator $\hat{C}$ also has following properties, which are stated below without proof. For more information about this, see references [7, 8].

- The operator $\hat{C}^2$ gives identity 1

$$\begin{aligned}\hat{C}^2\phi_n(x) &= \hat{C}(x,y)\int_c \hat{C}(x,y)\,\phi_n(y)\,dy \\ &= \hat{C}(x,y)\sum_{m=0}^{\infty}\phi_m(x)\int_c \phi_m(y)\,\phi_n(y)\,dy \\ &= \hat{C}(x,y)(-1)^n\phi_n(x) \\ &= (-1)^n\int_c \hat{C}(x,y)\,\phi_n(y)\,dy \\ &= (-1)^n(-1)^n\phi_n(x) \\ &= \phi_n(x)\end{aligned}$$

- The operator $\hat{C}$ commutes with Hamiltonian.

$$\left[\hat{C},\mathcal{H}\right] = 0 \tag{1.50}$$

  where in coordinate space representation

$$\mathcal{H}(x,y) \equiv \sum_{n=0}^{\infty}(-1)^n\,\phi(x)\,\phi(y)\,E_n \tag{1.51}$$

- It also commutes with the operator $\hat{P}\hat{T}$

$$\left[\hat{C},\hat{P}\hat{T}\right] = 0 \tag{1.52}$$

- However, the operator $\hat{C}$ does not commute $\hat{P}$ or $\hat{T}$.
- In general, the operator $\hat{C}$ is not the same as the parity operator $\hat{P}$, only in special case when $N = 2$ from (1.29)

$$\hat{C} = \hat{P} \qquad \text{only if } N = 2 \tag{1.53}$$

where the parity operator $\hat{P}$ in coordinate space is defined as

$$\hat{P}(x,y) \equiv \sum_{n=0}^{\infty}(-1)^n\,\phi_n(x)\,\phi_n(-y) = \delta(x+y) \tag{1.54}$$

where we have used the completeness relation from (1.44). Since $\hat{C}^2 = 1$ and $\hat{P}^2 = 1$, $\hat{C}$ and $\hat{P}$ are distinct square roots of the unity $\delta(x-y)$. For $N \neq 2$, $\hat{C}$ is complex but $\hat{P}$ is still real.

1.3 Observable

In PT-symmetric quantum mechanics, the position operator $\hat{x}$ and momentum operator $\hat{p}$ are not observables. In fact, by solving Hamilton's equations, the

classical trajectories show that the expectation value in the ground state for position operator is a purely imaginary number (See Fig.(4.3)). However, the charge C and the energy E are observables. Hence, for a given particle, we can measure its charge and energy, but not its position and momentum. These are quite similar to the fermion quantum field, which is complex and has no classical limit.

1.4 Experiment realizing PT-symmetric system

This section is the primary work by Schindler *et al.* based on the papers[54, 50]. All experimental data and graphs shown in the current section are extracted from the paper[54].

Since 1998 when Bender *et al.* introduced[10] the PT-symmetric Hamiltonian $\mathcal{H} = p^2 - (ix)^N$, the scientific research activity and interest of this new type of Hamiltonian grew rapidly. The number of conferences about PT-symmetry grew exponentially. During the years of 2000s, more and more experimental evidences appeared in the science community, so that nowadays this subject originated from purely mathematical physics has been expanded into the realm of experimental physics. In the last ten years, there are numerous and interesting experiments[1, 21, 32, 35, 37, 39, 44, 46, 47, 48, 49, 51, 52, 53, 59, 62, 63, 64] of studying PT-symmetry. In this section, we briefly introduce one experiment[54] designed by Schindler *et al.* in 2011, and we are trying to answer three questions:

1. Is it possible to build a physical system which is PT-symmetric?
2. Within the regime of broken PT-symmetry, part of the eigenvalue spectrum or the whole spectrum becomes complex. Is it possible to measure complex eigenvalues?
3. Is it possible in the experiment to find a critical point or region which determines the broken and unbroken PT-symmetry? In other words, is it possible to observe PT-phase transition?

The experimental setup is shown on Fig.(1.1), which includes two LRC circuits with mutual coupling $\mu = \frac{M}{L} = 0.2$ and an amplifier on the left side of the system to increase the power of the left LRC circuit (the Gain side). This amplifier acts like an air-pumper, which boosts the total energy of the Gain side by a factor of 2. However, this boost is balanced or compensated by the loss of energy due to two reasons. One is that the Gain side has internal resistance so that the energy is lost due to its dissipation in the form of heat; The other one is that through the mutual inductance, part of the energy from the Gain side is transferred to the right LRC circuit (the Loss side), where an external resistor is connected so that much more energy on the Loss side is dissipated. This whole system is a physical realization of parity and time-reversal symmetry.

Figure 1.1: *[54]Electronic implementation of a PT-symmetric circuit. (The following figure(link to DOI) is reprinted with permission from Joseph Schindler, Ang Li, Mei C. Zheng, F. M. Ellis, and Tsampikos Kottos, Phys. Rev. A 84, 040101(R), October 2011, Copyright 2011 by the American Physical Society.)*

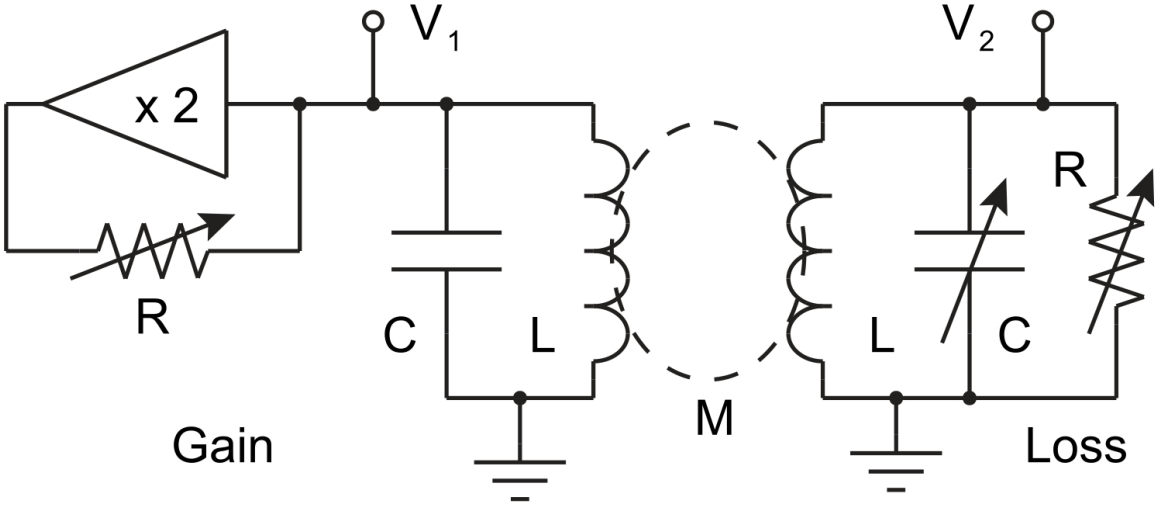

By Kirchhoff's law and some algebra, a system of two equations, which are invariant under the combined $\hat{P}$ (i.e. $n = 1 \longleftrightarrow n = 2$) and $\hat{T}$ (i.e. $\tau \longleftrightarrow -\tau$) operations, are obtained:

$$\begin{cases} \frac{d^2Q_1^c}{d\tau^2} &= -\alpha Q_1^c + \mu\alpha Q_2^c + \gamma\frac{dQ_1^c}{d\tau} \\ \frac{d^2Q_2^c}{d\tau^2} &= \mu\alpha Q_1^c - \alpha Q_2^c - \gamma\frac{dQ_2^c}{d\tau} \end{cases} \tag{1.55}$$

where Q_1^c is the charge of the capacitor on the Gain side, Q_2^c is the charge of the capacitor on the Loss side and

$$\gamma = R^{-1}\sqrt{\frac{L}{C}} \tag{1.56}$$

$$Q_n^c = CV_n \qquad \text{for } n = 1, 2 \tag{1.57}$$

$$\alpha \equiv \frac{1}{1-\mu^2} \geq 1 \tag{1.58}$$

$$\tau \equiv \omega_0 t \tag{1.59}$$

in which ω_0 is the natural (or damped) frequency for the isolated LC circuit. Due to the use of τ, rather than the time t, all frequencies are measured in units of ω_0. The value γ is called gain/loss parameter which can be adjusted by changing the external resistance on the Loss side and determines whether the whole system is in the broken or unbroken PT-symmetry. When the resistance on the Loss side is adjusted to be large, then γ becomes the loss parameter since more energy is dissipated on the Loss side. When the resistance on the Loss side is adjusted to be small, then γ becomes the gain parameter since less energy is dissipated on the Loss side and meanwhile the amplifier is kept to

constantly boost the total energy of the Gain side by a factor of 2. By adjusting γ, they are able to balance the gain and loss for the whole circuit.

By Liouvillian formalism, (1.55) can be transformed into a new form

$$\frac{d\Psi}{d\tau} = \mathcal{L}\Psi \qquad \mathcal{L} = \begin{bmatrix} 0 & 0 & 1 & 0 \\ 0 & 0 & 0 & 1 \\ -\alpha & \mu\alpha & \gamma & 0 \\ \mu\alpha & -\alpha & 0 & -\gamma \end{bmatrix} \tag{1.60}$$

where $\Psi \equiv \left(Q_1^c, Q_2^c, \dot{Q}_1^c, \dot{Q}_2^c\right)^T$. This new form (1.60) can be interpreted[4][50, p.2] as a Schrodinger equation with non-Hermitian effective Hamiltonian $\mathcal{H}_{eff} = i\mathcal{L}$. This Hamiltonian is symmetric with respect to generalized $\hat{P}_0\hat{T}_0$ operations so that $\left[\hat{P}_0\hat{T}_0, \mathcal{H}\right] = 0$ where

$$\hat{P}_0 = \begin{bmatrix} \sigma_x & 0 \\ 0 & \sigma_x \end{bmatrix} \qquad \hat{T}_0 = \begin{bmatrix} \mathbb{I} & \\ & -\mathbb{I} \end{bmatrix} \hat{\kappa} \tag{1.61}$$

where σ_x is a Pauli matrix, $\mathbb{I}$ is a 2×2 identity matrix and $\hat{\kappa}$ is the operation of complex conjugation. By a similarity transformation $\mathcal{R}$, where

$$\mathcal{R} = \begin{bmatrix} b+c & b+c & i & -i \\ b-c & -(b-c) & i & i \\ -(b-c) & b-c & i & i \\ b+c & b+c & -i & i \end{bmatrix} \tag{1.62}$$

with $b \equiv \sqrt{\left(\alpha+\alpha^{1/2}\right)/2}$ and $c \equiv -\sqrt{\left(\alpha-\alpha^{1/2}\right)/2}$, $\mathcal{H}_{eff}$ can be related to a transposition-symmetric, PT-symmetric and non-Hermitian Hamiltonian $\mathcal{H}$. Specifically,

$$\mathcal{H} = \mathcal{H}^T = \mathcal{R}\mathcal{H}_{eff}\mathcal{R}^{-1} \qquad \left[\hat{P}\hat{T}, \mathcal{H}\right] = 0 \tag{1.63}$$

where

$$\hat{T} = \hat{\kappa} = \mathcal{R}\hat{T}_0\mathcal{R}^{-1} \qquad \hat{P} = \begin{bmatrix} 0 & 0 & 0 & 1 \\ 0 & 0 & 1 & 0 \\ 0 & 1 & 0 & 0 \\ 1 & 0 & 0 & 0 \end{bmatrix} = \mathcal{R}\hat{P}_0\mathcal{R}^{-1} \tag{1.64}$$

$$\mathcal{H} = \begin{bmatrix} 0 & b+i\frac{\gamma}{2} & c+i\frac{\gamma}{2} & 0 \\ b+i\frac{\gamma}{2} & 0 & 0 & c-i\frac{\gamma}{2} \\ c+i\frac{\gamma}{2} & 0 & 0 & b-i\frac{\gamma}{2} \\ 0 & c-i\frac{\gamma}{2} & b-i\frac{\gamma}{2} & 0 \end{bmatrix} \tag{1.65}$$

Similarity transformation preserves all eigenvalues so that $\mathcal{H}_{eff}$ and $\mathcal{H}$ have the same spectrum. If there exists a Hermitian Hamiltonian which also describes the same system shown on Fig. (1.1), then this Hermitian Hamiltonian must have the exactly same spectrum of the non-Hermitian Hamiltonian $\mathcal{H}_{eff}$ or $\mathcal{H}$. Is this mathematically allowed? We don't know yet.

[4]Since they used the effective Hamiltonian $\mathcal{H}_{eff}$ to interpret the system, so it seems that $\mathcal{H}_{eff}$ is not a "natural" Hamiltonian of the system.

The system of two equations from (1.55) can be solved by using the substitution

$$Q_n^c = A_n e^{i\omega t} \tag{1.66}$$

where ω is the driving (or undamped) frequency for the voltage V_n (or Q_n^c by (1.57)), and wait to be measured. By the substitution, (1.55) has four solutions ($l = 1, 2, 3, 4$) for the eigenfrequencies ω_l:

$$\omega_{1,4} = \pm\sqrt{-\frac{2+\gamma^2\left(\mu^2-1\right)+\sqrt{4\left(\mu^2-1\right)+\left[2+\gamma^2\left(\mu^2-1\right)\right]^2}}{2\left(\mu^2-1\right)}} \tag{1.67}$$

$$\omega_{2,3} = \pm\sqrt{\frac{-2+\gamma^2\left(\mu^2-1\right)+\sqrt{4\left(\mu^2-1\right)+\left[2+\gamma^2\left(\mu^2-1\right)\right]^2}}{2\left(\mu^2-1\right)}} \tag{1.68}$$

These solutions can also be obtained by a direction diagonalization of the matrix $\mathcal{L}$ from (1.60).

When $\gamma < \gamma_{PT}$, where

$$\gamma_{PT} \equiv \frac{1}{\sqrt{1-\mu}} - \frac{1}{\sqrt{1+\mu}} \tag{1.69}$$

all four eigenfrequencies ω_l are real, since the PT-symmetry is unbroken. When in the broken PT-symmetry $\gamma > \gamma_{PT}$, $\mathrm{Im}\left(\omega_l\right) \neq 0$. So γ_{PT} is the critical point which distinguishes the broken and unbroken PT-symmetry. When $\gamma > \gamma_2$, where

$$\gamma_2 \equiv \frac{1}{\sqrt{1-\mu}} + \frac{1}{\sqrt{1+\mu}} > \gamma_{PT} \tag{1.70}$$

all four eigenfrequencies ω_l become purely imaginary.

Figure 1.2: *[54]Eigenfrequencies ω_l versus the normalized gain/loss parameter γ/γ_{PT}. (The following figure(link to DOI) is reprinted with permission from Joseph Schindler, Ang Li, Mei C. Zheng, F. M. Ellis, and Tsampikos Kottos, Phys. Rev. A 84, 040101(R), October 2011, Copyright 2011 by the American Physical Society.)*

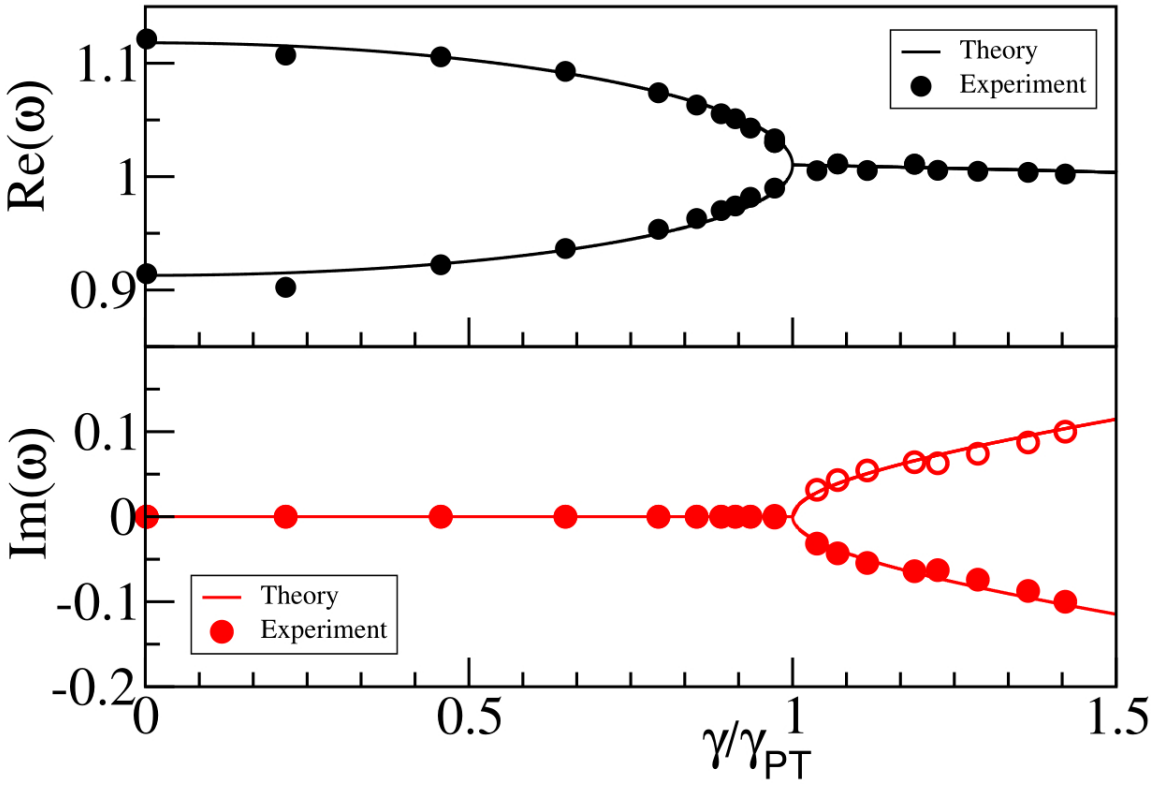

Now we come to the second question which is how to measure the complex eigenfrequency ω_l. All thanks should give to our old and lovely friend the exponential - when ω_l becomes complex, by (1.66) the exponential $e^{i\omega t}$ becomes real so that the charge within either one of the capacitors grows up or vanishes as time t goes. When ω_l is real, $e^{i\omega t}$ is oscillatory so that the average charge within either one of the capacitors keeps constant with respect to time. The oscillatory frequency of charge (or voltage) versus γ is measured and shown on Fig.(1.2). When $\gamma < \gamma_{PT}$, the purely oscillatory behavior with constant amplitude keeps the eigenfrequency purely real. When $\gamma > \gamma_{PT}$, the amplitude of the oscillation starts to grow exponentially and meanwhile $\mathrm{Im}\,(\omega_l)$ is no longer zero. The open circles in the lower graph are reflections of the experimental data (lower curve) with respect to the axis $\mathrm{Im}\,(\omega) = 0$, because only the exponentially growing mode with $\mathrm{Im}\,(\omega) < 0$ is dominant and can be observed. The experimental data matches the theoretical prediction pretty well.

Figure 1.3: *[54]The phase difference $\theta_l = \phi_2^{(l)} - \phi_1^{(l)}$ versus the normalized gain/loss parameter γ/γ_{PT}. (The following figure(link to DOI) is reprinted with permission from Joseph Schindler, Ang Li, Mei C. Zheng, F. M. Ellis, and Tsampikos Kottos, Phys. Rev. A 84, 040101(R), October 2011, Copyright 2011 by the American Physical Society.)*

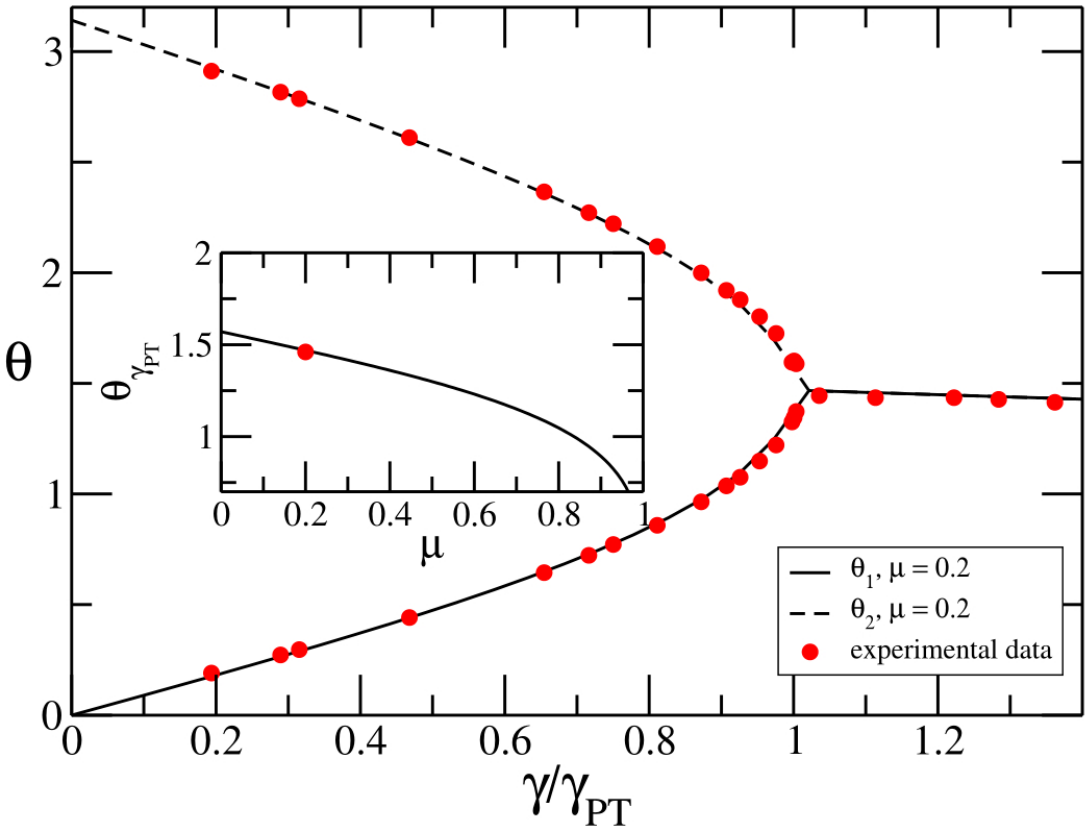

The voltage for either one of the capacitors must have the form similar to

$$V_n^c = \frac{A_n}{C} e^{i\omega t} = \left|\frac{A_n}{C}\right| e^{i(\omega t + \phi_n)} \tag{1.71}$$

where ϕ_n is the phase angle. Studying the relative phase difference $\theta_l = \phi_2^{(l)} - \phi_1^{(l)}$ within the voltages from the two capacitors is an excellent way to explore related PT-symmetric feature, because this phase difference not only can be measured but also has a critical point $\theta_{PT}(\mu)$ when $\gamma = \gamma_{PT}$ and can be calculated analytically.

$$\theta_{PT}(\mu) = \arccos\left(\sqrt{1-\sqrt{1-\mu^2}}/\sqrt{1+\sqrt{1+\mu^2}}\right) \tag{1.72}$$

When the mutual coupling $\mu \to 0$, $\theta_{PT} \to \frac{\pi}{2}$. When $\mu \to 1$, $\theta_{PT} \to 0$. This feature along with the phase difference versus normalized gain/loss parameter γ/γ_{PT} is plotted on Fig.(1.3). The experimental data agrees with the theoretical prediction.

Fig.(1.3) also shows that when $\gamma = 0$, the initial phase difference is π. Nonetheless, as γ increases, their subsequent phases can be anywhere since their

eigenmodes are not orthogonal. The non-orthogonality causes the power to oscillate (even if $\gamma < \gamma_{PT}$), so that the whole system is open - the total energy E_{tot} for the whole system is not conserved, even if $\gamma < \gamma_{PT}$. As shown on Fig.(1.4), when $\gamma < \gamma_{PT}$, the total energy $E_C^{tot}(\tau)$ of these capacitors is not conserved and still oscillates with respect to time; When $\gamma > \gamma_{PT}$, unstable dynamics are observed in that $E_C^{tot}(\tau)$ not only oscillates but also grows exponentially with a rate given by the maximum imaginary part of the eigenvalue $\max[\mathrm{Im}(\omega_l)]$.

Figure 1.4: *[54]Measured total energy $E_C^{tot}(\tau)$ of capacitors of the whole system versus τ. (The following figure(link to DOI) is reprinted with permission from Joseph Schindler, Ang Li, Mei C. Zheng, F. M. Ellis, and Tsampikos Kottos, Phys. Rev. A 84, 040101(R), October 2011, Copyright 2011 by the American Physical Society.)*

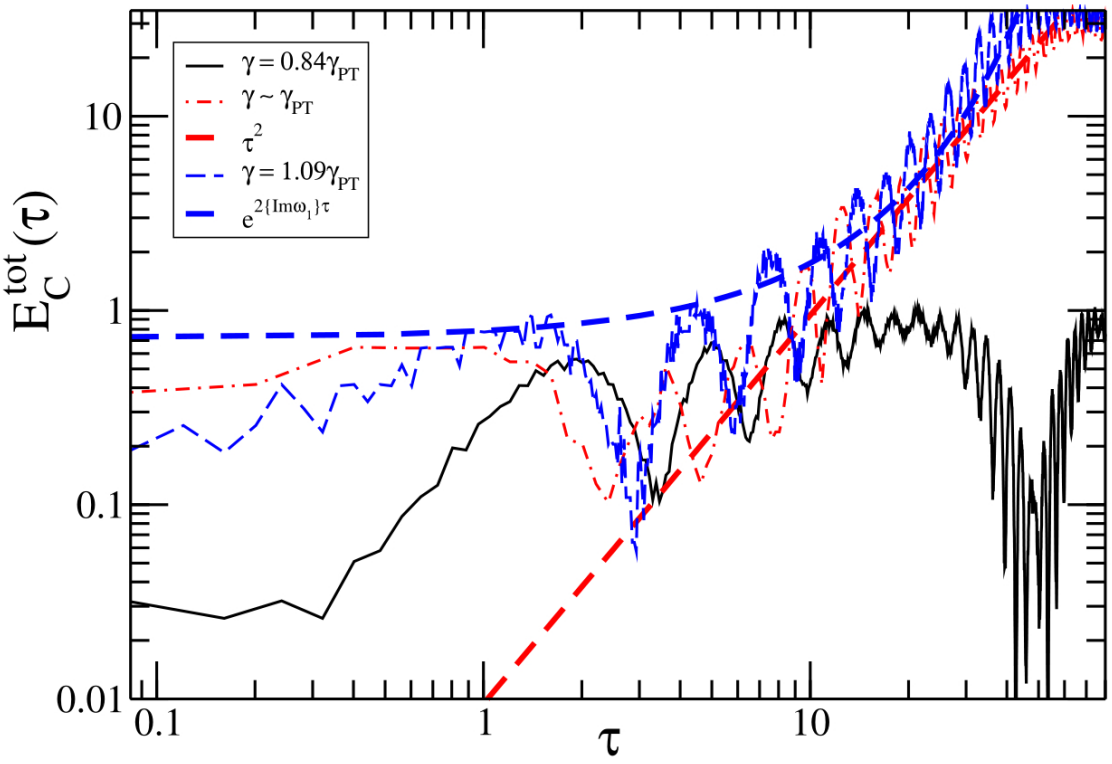

Chapter 2

The Eigenvalue Problem for the Potential $V = -(ix)^N$

2.1 Introduction of the current chapter

In this chapter, we will study the energy spectra of the PT-symmetric Hamiltonian $\mathcal{H} = p^2 - (ix)^N$. There are two reasons why we study this Hamiltonian:

- Historically, this is the first PT-symmetric Hamiltonian scientists[10] had studied since 1998.
- When $N = 2$, the PT-symmetric Hamiltonian describes the harmonic oscillator, which is familiar to most students. So this Hamiltonian provides a good introduction to understand PT-symmetry.

Based this Hamiltonian, we have 1D Schrodinger equation in the complex plane with $N \in \mathbb{R}$ and $x \in \mathbb{C}$,

$$-\psi''(x) - (ix)^N \psi(x) = E\psi(x) \tag{2.1}$$

and we try to numerically calculate the eigenvalue E in the current chapter. The boundary condition $\psi(x) \to 0$ and $\psi'(x) \to 0$ as $|x| \to \infty$ causes a great difficulty for numerical or analytical method, because there are infinite number of contour paths which go from a complex infinity to another complex infinity. However, do all paths yield positive and discrete eigenvalue or just some of paths? We'll see.

The current chapter contains original work and is organized in the following way. In Sec.(2.2), we introduce the concepts of Stokes lines, anti-Stokes lines and Stokes wedges. In Sec.(2.3), through parametrization we numerically calculate the eigenvalue E by integrating along various paths to see if the eigenvalues and eigenfunctions are independent from paths or not. Since the Hamiltonian contains multiple families of energy spectrum, in Subsec.(2.3.4), we plot the first four families and discuss the relation among them.

2.2 Local asymptotic analysis

In our local asymptotic analysis, the definition of "**asymptotic to**" is straightforward. Let $f(x)$ and $g(x)$ be two complex functions with the independent variable x, we say $f(x)$ is asymptotic to $g(x)$

$$f(x) \sim g(x) \qquad \text{as } x \to x_0 \tag{2.2}$$

to mean that $f(x)$ is arbitrarily close to $g(x)$ without actually being equal to $g(x)$. A more rigorous definition about "asymptotic to" is

$$\lim_{x \to x_0} \frac{f(x)}{g(x)} = 1 \tag{2.3}$$

from which $g(x) \neq 0$. Therefore, we can never say in any case that function $f(x)$ is asymptotic to zero!

$$f(x) \nsim 0 \qquad \text{as } x \to x_0 \tag{2.4}$$

2.2.1 For $N \geq 2$

To find an ansatz to the solution of (2.1), we can easily solve the following differential equation by just observation

$$\psi'(x) - 5x^2 \psi(x) = 0 \tag{2.5}$$

whose solution is

$$\psi(x) = Ce^{\frac{5}{3}x^3} \tag{2.6}$$

which suggests that we can try the solution

$$\psi(x) = e^{S(x)} \tag{2.7}$$

where with $a \in \mathbb{C}$, $a \neq 0$ and $b > 0$, the phase $S(x)$ is of the form

$$S(x) = ax^b \tag{2.8}$$

So

$$\psi'(x) = S'(x) e^{S(x)} \tag{2.9}$$

$$\psi''(x) = \left\{ [S'(x)]^2 + S''(x) \right\} e^{S(x)} \tag{2.10}$$

Plugging (2.7) and (2.10) into (2.1) yield

$$S''(x) + [S'(x)]^2 + E + (ix)^N = 0 \tag{2.11}$$

From (2.8)

$$S''(x) = ab(b-1)x^{b-2} \tag{2.12}$$

$$[S'(x)]^2 = a^2 b^2 x^{2b-2} \tag{2.13}$$

For $b > 0$, as $|x| \to \infty$,

$$\begin{aligned} b - 2 &< 2b - 2 \\ \implies |x|^{b-2} &< |x|^{2b-2} \\ \implies |S''(|x|)| &< \left|[S'(|x|)]^2\right| \end{aligned}$$

which implies that as $|x| \to \infty$ and when $N > 0$, $\left|(ix)^N\right| \gg |E|$, and $\left|[S'(x)]^2\right| \gg |S''(x)|$. Hence

$$\begin{aligned} [S'(x)]^2 &\sim -(ix)^N \\ \implies S'(x) &\sim \pm\sqrt{-(ix)^N} \\ \implies S(x) &\sim \pm\int^x \sqrt{-(i\alpha)^N}\, d\alpha \\ \implies S(x) &\sim \pm\frac{i^{\frac{N}{2}+1}}{\frac{N}{2}+1} x^{\frac{N}{2}+1} \end{aligned}$$

We have assumed that the solution must have the form from (2.7), so is it true if $S(x) \sim \pm\frac{i^{\frac{N}{2}+1}}{\frac{N}{2}+1} x^{\frac{N}{2}+1}$, then $\exp[S(x)] \sim \exp\left[\pm\frac{i^{\frac{N}{2}+1}}{\frac{N}{2}+1} x^{\frac{N}{2}+1}\right]$ as $|x| \to \infty$? The answer is "not true in general". Let two functions have the asymptotic relation $f(x) \sim g(x)$, then $\exp[f(x)] \sim \exp[g(x)]$ as $x \to x_0$ is true only if $f(x) - g(x) \ll 1$ as $x \to x_0$, due to the definition from (2.3)

$$e^{f(x)} \sim e^{g(x)} \Leftrightarrow \lim_{x\to x_0} \frac{e^{f(x)}}{e^{g(x)}} = 1 = \lim_{x\to x_0} e^{f(x)-g(x)} \Leftrightarrow f(x) - g(x) \ll 1 \tag{2.14}$$

As we'll see that as $|x| \to \infty$, the difference of $S(x) - x^{\frac{N}{2}+1}$ is not negligible in comparing with 1, so $\psi(x) \nsim \exp\left[\pm\frac{i^{\frac{N}{2}+1}}{\frac{N}{2}+1} x^{\frac{N}{2}+1}\right]$, but instead, $\psi(x) \sim \exp\left[\pm\frac{i^{\frac{N}{2}+1}}{\frac{N}{2}+1} x^{\frac{N}{2}+1} + \text{some function of } x\right]$. We can improve $S(x) \sim \pm\frac{i^{\frac{N}{2}+1}}{\frac{N}{2}+1} x^{\frac{N}{2}+1}$ by assuming that $S(x)$ has the following form

$$S(x) = \pm\frac{i^{\frac{N}{2}+1}}{\frac{N}{2}+1} x^{\frac{N}{2}+1} + A(x) \tag{2.15}$$

such that

$$S'(x) = \pm i^{\frac{N}{2}+1} x^{\frac{N}{2}} + A'(x) \tag{2.16}$$

$$S''(x) = \pm i^{\frac{N}{2}+1} \left(\frac{N}{2}\right) x^{\frac{N}{2}-1} + A''(x) \tag{2.17}$$

where as $|x| \to \infty$,

$$\left|\pm\frac{i^{\frac{N}{2}+1}}{\frac{N}{2}+1} x^{\frac{N}{2}+1}\right| \gg |A(x)| \tag{2.18}$$

$$\left|\pm i^{\frac{N}{2}+1} x^{\frac{N}{2}}\right| \gg |A'(x)| \tag{2.19}$$

$$\left|\pm i^{\frac{N}{2}+1}\left(\frac{N}{2}\right)x^{\frac{N}{2}-1}\right| \gg |A''(x)| \tag{2.20}$$

Substituting (2.15), (2.16) and (2.17) into (2.11) yields

$$\pm i^{\frac{N}{2}+1}\left(\frac{N}{2}\right)x^{\frac{N}{2}-1}+A''(x)+i^{2\left(\frac{N}{2}+1\right)}x^{N}\pm 2i^{\frac{N}{2}+1}x^{\frac{N}{2}}A'(x)+[A'(x)]^{2}+E+(ix)^{N}=0 \tag{2.21}$$

By cancellation, (2.18), (2.19) and (2.20), we obtain following asymptotic equation as $|x|\to\infty$

$$\begin{aligned}
\pm 2i^{\frac{N}{2}+1}x^{\frac{N}{2}}A'(x) &\sim -E\mp i^{\frac{N}{2}+1}\left(\frac{N}{2}\right)x^{\frac{N}{2}-1}\\
\Longrightarrow A'(x) &\sim \frac{\mp E}{2i^{\frac{N}{2}+1}x^{\frac{N}{2}}}-\frac{N}{4x}\\
\Longrightarrow A(x) &\sim -\frac{N}{4}\ln|x|\mp\frac{Ex^{-\frac{N}{2}+1}}{(-N+2)\,i^{\frac{N}{2}+1}}+C_1
\end{aligned} \tag{2.22}$$

where we have included a constant C_1 here, because if $N>2$, then $x^{-\frac{N}{2}+1}\to 0\ll C_1$ as $|x|\to\infty$. For $N>2$, the condition (2.14) allows us to obtain the leading order asymptotic behavior of $\psi(x)$.

By (2.7), (2.15) and (2.22), the leading order behavior of $\psi(x)$ is

$$\psi(x)\sim C|x|^{-\frac{N}{4}}\exp\left[\pm\frac{i^{\frac{N}{2}+1}}{\frac{N}{2}+1}x^{\frac{N}{2}+1}\right] \qquad \text{when } N\geq 2 \text{ and } |x|\to\infty \tag{2.23}$$

where C is a constant. Note that the asymptotic relation (2.23) for $N\geq 2$ is independent from the eigenvalue E. The dominant contribution in the leading order behavior is the exponential factor $\exp\left[\pm\frac{i^{\frac{N}{2}+1}}{\frac{N}{2}+1}x^{\frac{N}{2}+1}\right]$. To satisfy the boundary condition $\psi(x)\to 0$ as $|x|\to\infty$, we expect that

$$\exp[S_{1,2}(x)]\equiv\exp\left[\pm\frac{i^{\frac{N}{2}+1}}{\frac{N}{2}+1}x^{\frac{N}{2}+1}\right]\to 0 \qquad \text{as } |x|\to\infty \tag{2.24}$$

which means that the oscillatory behavior of the exponential should eventually vanish as $|x|\to\infty$. If the oscillatory part of the exponential is equal to zero for any value of $|x|$, then $\exp[S_{1,2}(x)]$ approaches zero in the fastest speed. For example, for two real functions $a(x), b(x)\in\mathbb{R}$, as $|x|\to\infty$

$$\exp[a(x)+ib(x)]=\exp[a(x)]\overset{\text{fastest}}{\longrightarrow}0 \qquad \text{when } b(x)=0,\ a(x)<0 \tag{2.25}$$

Therefore, to satisfy the boundary condition in the fastest manner, we require the following condition is true

$$\mathrm{Im}[S_1(x)-S_2(x)]=0 \tag{2.26}$$

The solution of (2.26) is the definition of so-called "**Stokes lines**". Then we have

$$\begin{aligned}\mathrm{Im}\left[\frac{i^{\frac{N}{2}+1}}{\frac{N}{2}+1}x^{\frac{N}{2}+1}-\left(-\frac{i^{\frac{N}{2}+1}}{\frac{N}{2}+1}x^{\frac{N}{2}+1}\right)\right]&=0\\ \Longrightarrow \mathrm{Im}\left[i^{\frac{N}{2}+1}x^{\frac{N}{2}+1}\right]&=0\end{aligned}$$

Let's assume that

$$x=re^{i\theta} \tag{2.27}$$

then

$$\begin{aligned}\Longrightarrow \mathrm{Im}\left[e^{i\frac{\pi}{2}\left(\frac{N}{2}+1\right)}e^{i\theta\left(\frac{N}{2}+1\right)}\right]&=0\\ \Longrightarrow \frac{\pi}{2}\left(\frac{N}{2}+1\right)+\theta\left(\frac{N}{2}+1\right)&=\pm\pi\end{aligned}$$

So we obtain

$$\begin{cases}\theta_{left}=-\pi+\frac{N-2}{N+2}\frac{\pi}{2}\\ \theta_{right}=-\frac{N-2}{N+2}\frac{\pi}{2}\end{cases} \tag{2.28}$$

which define the locations of Stokes lines for the problem (2.1). Note that

$$\theta_{left}=-\pi-\theta_{right} \tag{2.29}$$

These Stokes lines are plotted on Fig.(2.2).

In fact, there are many Stokes lines, since

$$\begin{aligned}\mathrm{Im}\left[e^{i\frac{\pi}{2}\left(\frac{N}{2}+1\right)}e^{i\theta\left(\frac{N}{2}+1\right)}\right]&=0\\ \Longrightarrow \frac{\pi}{2}\left(\frac{N}{2}+1\right)+\theta\left(\frac{N}{2}+1\right)&=\pm k\pi \qquad \text{for } k=0,1,2,3,\cdots\end{aligned}$$

which gives

$$\begin{cases}\theta_{left}=-\pi+\frac{N-4k+2}{N+2}\frac{\pi}{2}\\ \theta_{right}=-\frac{N-4k+2}{N+2}\frac{\pi}{2}\end{cases} \qquad \text{when } k=0,1,2,3,\cdots \tag{2.30}$$

We plot all those Stokes lines on Fig.(2.1).

If the exponential is purely oscillatory, then based on the example from (2.25), as $|x|\to\infty$,

$$\exp\left[a\left(x\right)+ib\left(x\right)\right]=\exp\left[ib\left(x\right)\right]\to \text{maximally oscillatory} \qquad \text{when } a\left(x\right)=0 \tag{2.31}$$

So the locations of "**anti-Stokes lines**" are defined as the solution of the following equation

$$\mathrm{Re}\left[S_1\left(x\right)-S_2\left(x\right)\right]=0 \tag{2.32}$$

then

$$\begin{aligned}\mathrm{Re}\left[\frac{i^{\frac{N}{2}+1}}{\frac{N}{2}+1}x^{\frac{N}{2}+1}-\left(-\frac{i^{\frac{N}{2}+1}}{\frac{N}{2}+1}x^{\frac{N}{2}+1}\right)\right]&=0\\ \Longrightarrow \frac{\pi}{2}\left(\frac{N}{2}+1\right)+\theta\left(\frac{N}{2}+1\right)&=\frac{\pi}{2}\text{ or }\frac{3\pi}{2}\end{aligned}$$

gives

$$\theta_1 = \frac{\pi}{N+2} - \frac{\pi}{2} \qquad \theta_2 = \frac{3\pi}{N+2} - \frac{\pi}{2} \tag{2.33}$$

which define the width of the "**Stokes sector**" or "**Stokes wedge**"

$$\triangle = |\theta_1 - \theta_2| = \frac{2\pi}{N+2} \tag{2.34}$$

The shape of a Stokes wedge is not really like a wedge or a slice of pie. They are asymptotic concepts. The angular opening $\triangle$ from (2.34) of the wedge only refers to the opening for $|x|$ at certain range of complex infinity.

Figure 2.1: *All Stokes wedges for non-negative integer N and all corresponding turning points (yellow point with black edge)*

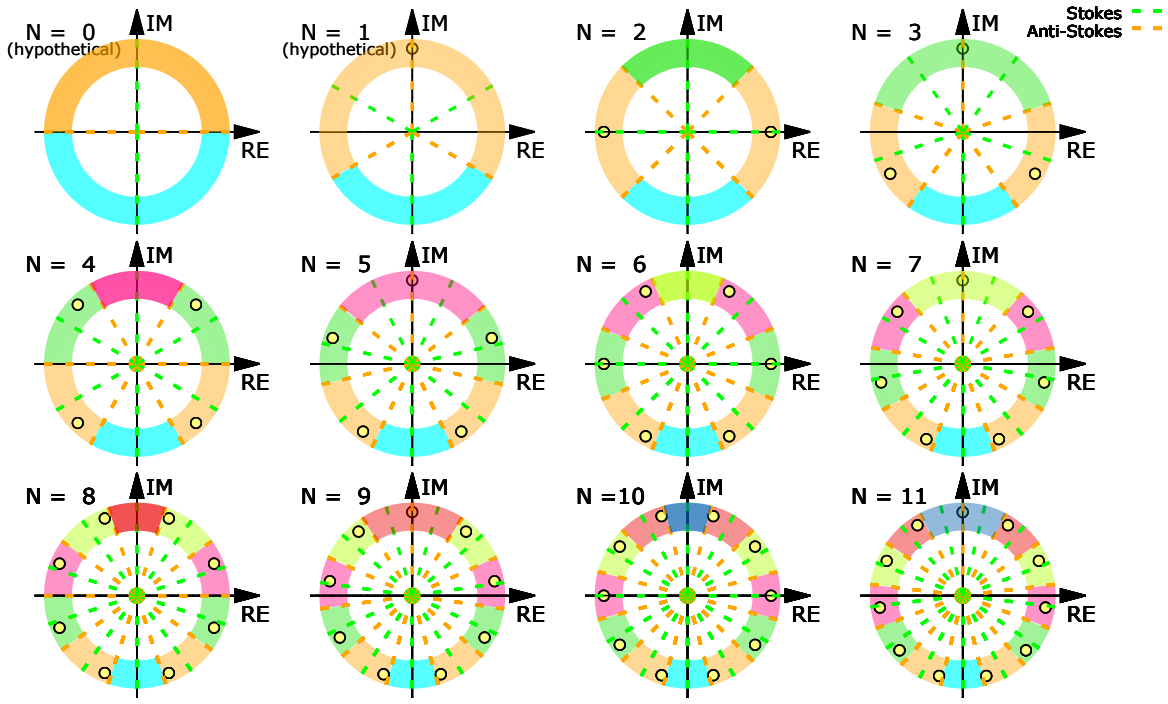

Except the top and bottom wedges which contain the imaginary axis, Fig.(2.1) shows that the rest of all wedges form pairs symmetric with respect to the imaginary axis. Each pair are labeled with a color - orange, green, pink, yellow, red, etc. We may sometimes call those pairs as "PT-symmetric Stokes wedges". Each pair contains a pair of turning points[1] which are also symmetric with respect to the imaginary axis. The larger the N is, the more pairs of wedges and of turning points are. Any wedge whose anti-Stokes line coincides with the imaginary axis only shares one singular turning point with its pair, and that singular turning point must be located on the imaginary axis. On Fig.(2.1), when $N = 0$ and $N = 1$, we label the wedges as "hypothetical wedges", because

[1]Turning points are defined by the solutions from the equation $E = V$. (See (3.1) for more detail.) Based on this definition, the locations of turning points are eigenvalue E-dependent. Here, for the purpose of visualization we set E as an appropriate constant. The phase angle for each turning point are calculated and shown on (3.1).

the locations of these wedges on the figure are actually not true[2] for $N < 2$ according to (2.51) and (2.52) on Sec.2.2.2, where these wedges are eigenvalue E-dependent.

Since different pair of wedges will pose different eigenvalue problem, to proceed, we now only focus on one pair of wedges by choosing the orange pair with the Stokes lines defined from (2.28) shown on Fig.(2.2) to calculate the eigenvalue.

Figure 2.2: *The chosen Stokes wedges for non-negative integer N and all corresponding turning points (yellow point with black edge)*

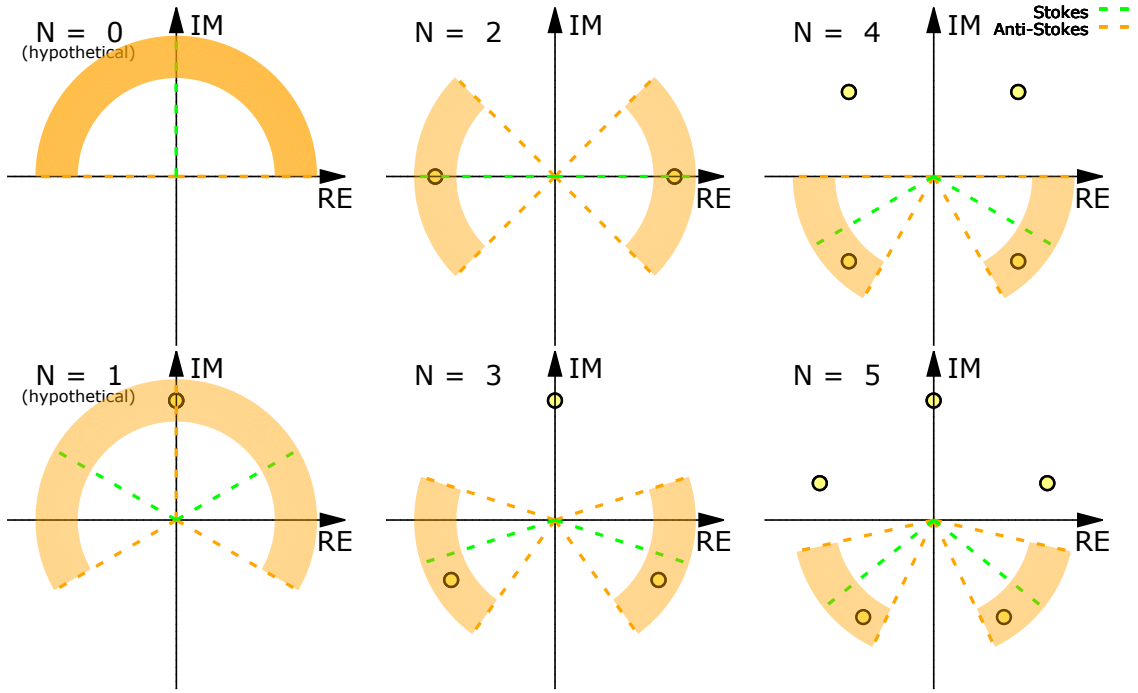

2.2.2 For $0 < N < 2$

We see that if $N < 2$, then $x^{-\frac{N}{2}+1} \nrightarrow 0$ and $x^{-\frac{N}{2}+1} \gg C_1$ as $|x| \to \infty$. So for $0 < N < 2$, (2.22) becomes

$$A(x) \sim -\frac{N}{4} \ln|x| \mp \frac{E x^{-\frac{N}{2}+1}}{(-N+2)\, i^{\frac{N}{2}+1}} \tag{2.35}$$

by the condition (2.14), As $|x| \to \infty$, we can conclude the leading order behavior of $\psi(x)$ is

$$\psi(x) \sim k\,|x|^{-\frac{N}{4}} \exp\left[\pm \frac{i^{\frac{N}{2}+1}}{\frac{N}{2}+1} x^{\frac{N}{2}+1} \mp \frac{E\left(x^{-\frac{N}{2}+1}\right)}{(-N+2)\, i^{\frac{N}{2}+1}}\right] \qquad \text{when unknown} < N < 2 \tag{2.36}$$

[2]Even if the locations of these wedges for $N < 2$ on Fig.(2.1) is not true, we still plot them since they can help us understand the origin of all those wedges for $N > 2$.

where the lower bound of N is a positive and unknown number which can be found by continuing our local asymptotic analysis.

Based on (2.15) and (2.35), we assume that $S(x)$ has the following form

$$S(x)=\pm\frac{i^{\frac{N}{2}+1}}{\frac{N}{2}+1}x^{\frac{N}{2}+1}-\frac{N}{4}\ln|x|\mp\frac{Ex^{-\frac{N}{2}+1}}{(-N+2)\,i^{\frac{N}{2}+1}}+B(x) \tag{2.37}$$

so that, by using $\frac{d}{dx}(\ln|x|)=\frac{1}{x}$,

$$S'(x)=\pm i^{\frac{N}{2}+1}x^{\frac{N}{2}}\mp\frac{E}{2i^{\frac{N}{2}+1}x^{\frac{N}{2}}}-\frac{N}{4x}+B'(x) \tag{2.38}$$

$$S''(x)=\pm i^{\frac{N}{2}+1}\left(\frac{N}{2}\right)x^{\frac{N}{2}-1}\mp\frac{E}{2i^{\frac{N}{2}+1}}\left(-\frac{N}{2}\right)x^{-\frac{N}{2}-1}-\frac{N}{4x^2}+B''(x) \tag{2.39}$$

where as $|x|\to\infty$,

$$\left|-\frac{N}{4}\ln|x|\right|\gg|B(x)| \tag{2.40}$$

$$\left|-\frac{N}{4x}\right|\gg|B'(x)| \tag{2.41}$$

$$\left|-\frac{N}{4x^2}\right|\gg|B''(x)| \tag{2.42}$$

and

$$\left|\pm\frac{i^{\frac{N}{2}+1}}{\frac{N}{2}+1}x^{\frac{N}{2}+1}\right|\gg\left|\mp\frac{Ex^{-\frac{N}{2}+1}}{(-N+2)\,i^{\frac{N}{2}+1}}\right| \tag{2.43}$$

$$\left|\pm\frac{i^{\frac{N}{2}+1}}{\frac{N}{2}+1}x^{\frac{N}{2}+1}\right|\gg\left|\frac{N}{4}\ln|x|\right| \tag{2.44}$$

$$\left|\pm i^{\frac{N}{2}+1}x^{\frac{N}{2}}\right|\gg\left|\mp\frac{E}{2i^{\frac{N}{2}+1}x^{\frac{N}{2}}}\right| \tag{2.45}$$

$$\left|\pm i^{\frac{N}{2}+1}x^{\frac{N}{2}}\right|\gg\left|-\frac{N}{4x}\right| \tag{2.46}$$

$$\left|\pm i^{\frac{N}{2}+1}\left(\frac{N}{2}\right)x^{\frac{N}{2}-1}\right|\gg\left|\mp\frac{E}{2i^{\frac{N}{2}+1}}\left(-\frac{N}{2}\right)x^{-\frac{N}{2}-1}\right| \tag{2.47}$$

$$\left|\pm i^{\frac{N}{2}+1}\left(\frac{N}{2}\right)x^{\frac{N}{2}-1}\right|\gg\left|-\frac{N}{4x^2}\right| \tag{2.48}$$

Substituting (2.37), (2.38) and (2.39) into (2.11), and after cancellation yield

$$\pm2i^{\frac{N}{2}+1}x^{\frac{N}{2}}B'\mp\frac{EB'}{i^{\frac{N}{2}+1}x^{\frac{N}{2}}}\pm\frac{EN}{2i^{\frac{N}{2}+1}x^{\frac{N}{2}+1}}-\frac{B'N}{2x}+(B')^2+\frac{N^2}{16x^2}+B''+\frac{N}{4x^2}-\frac{E^2}{4i^Nx^N}=0 \tag{2.49}$$

By (2.41) and (2.42), we conclude that $\left|-\frac{B'N}{2x}\right|\gg\left|(B')^2\right|$, $\left|\frac{N^2}{16x^2}\right|\gg|B''|$. And by (2.45), (2.46) and (2.47), we conclude that $\left|\pm2i^{\frac{N}{2}+1}x^{\frac{N}{2}}B'\right|\gg\left|\left(\mp\frac{E}{i^{\frac{N}{2}+1}x^{\frac{N}{2}}}-\frac{N}{2x}\right)B'\right|$.

So we neglect those smaller terms to have the following asymptotic relation as $|x| \to \infty$

$$\begin{aligned}
\pm 2i^{\frac{N}{2}+1}x^{\frac{N}{2}}B' &\sim \mp\frac{EN}{2i^{\frac{N}{2}+1}x^{\frac{N}{2}+1}} - \frac{N^2}{16x^2} - \frac{N}{4x^2} + \frac{E^2}{4i^N x^N} \\
B' &\sim -\frac{EN}{4i^{N+2}x^{N+1}} \mp \frac{N^2}{32i^{\frac{N}{2}+1}x^{\frac{N}{2}+2}} \mp \frac{N}{8i^{\frac{N}{2}+1}x^{\frac{N}{2}+2}} \pm \frac{E^2}{8i^{\frac{3N}{2}+1}x^{\frac{3N}{2}}} \\
B &\sim -\frac{E}{4i^N}x^{-N} \pm \left(\frac{N^2}{32i^{\frac{N}{2}+1}\left(\frac{N}{2}+1\right)} + \frac{N}{8i^{\frac{N}{2}+1}\left(\frac{N}{2}+1\right)}\right)x^{-\frac{N}{2}-1} \\
&\quad \pm \frac{E^2}{8i^{\frac{3N}{2}+1}\left(1-\frac{3N}{2}\right)}x^{-\frac{3N}{2}+1}
\end{aligned}$$

It follows from (2.37) so that

$$\begin{aligned}
S(x) = &\pm\frac{i^{\frac{N}{2}+1}}{\frac{N}{2}+1}x^{\frac{N}{2}+1} - \frac{N}{4}\ln|x| \mp \frac{Ex^{-\frac{N}{2}+1}}{(-N+2)i^{\frac{N}{2}+1}} - \frac{E}{4i^N}x^{-N} \\
&\pm\left(\frac{N^2}{32i^{\frac{N}{2}+1}\left(\frac{N}{2}+1\right)} + \frac{N}{8i^{\frac{N}{2}+1}\left(\frac{N}{2}+1\right)}\right)x^{-\frac{N}{2}-1} \pm \frac{E^2}{8i^{\frac{3N}{2}+1}\left(1-\frac{3N}{2}\right)}x^{-\frac{3N}{2}+1} + C_2
\end{aligned} \tag{2.50}$$

As $|x| \to \infty$, for $0 < N < 2$, $\left|x^{\frac{N}{2}+1}\right| \to \infty$, $|\ln|x|| \to \infty$, $\left|x^{-\frac{N}{2}+1}\right| \to \infty$, and $x^{-\frac{N}{2}-1} \to 0$. For $0 < N < \frac{2}{3}$, $x^{-\frac{3N}{2}+1} \to \infty$ as well. Therefore, by the condition (2.14), as $|x| \to \infty$, the leading order behavior of $\psi(x)$ is

$$\psi(x) \sim k|x|^{-\frac{N}{4}}\exp\left[\pm\frac{i^{\frac{N}{2}+1}}{\frac{N}{2}+1}x^{\frac{N}{2}+1} \mp \frac{E\left(x^{-\frac{N}{2}+1}\right)}{(-N+2)i^{\frac{N}{2}+1}}\right] \qquad \text{when } \frac{2}{3} < N < 2 \tag{2.51}$$

$$\psi(x) \sim k|x|^{-\frac{N}{4}}\exp\left[\pm\frac{i^{\frac{N}{2}+1}}{\frac{N}{2}+1}x^{\frac{N}{2}+1} \mp \frac{E\left(x^{-\frac{N}{2}+1}\right)}{(-N+2)i^{\frac{N}{2}+1}} \pm \frac{E^2}{8i^{\frac{3N}{2}+1}\left(1-\frac{3N}{2}\right)}x^{-\frac{3N}{2}+1}\right] \tag{2.52}$$

$$\text{when } 0 < N < \frac{2}{3}$$

In comparison with (2.23), we observe that these two asymptotic relations are eigenvalue-dependent.

2.3 Numerical approximation

2.3.1 Levenberg-Marquardt algorithm

To solve the eigenvalue problem (2.1), by Levenberg-Marquardt algorithm (LMA) we choose to minimize a square-function $F(x_\infty, E)$ of the following complex modulus with respect to the energy E,

$$F(x_\infty, E) \equiv |f(x_\infty, E) - \psi(x_\infty, E)|^2 \tag{2.53}$$

where x_∞ is the right boundary point located within a right Stokes wedge and $f(x_\infty, E)$ can be calculated by Gauss-Legendre integration method (GLI)[34], a type of implicit Runge-Kutta method. Fortran code for GLI is provided in Alg.(1) in Appendix. Due to one of boundary conditions $\lim_{|x|\to\infty} \psi(x) = 0$,

$$F(x_\infty, E) = |f(x_\infty, E)|^2 . \tag{2.54}$$

LMA is an iterative procedure, where the previous estimate E is replaced by a new estimate, $E+\delta E$, for each iterative step. We can approximate $f(x_\infty, E+\delta E)$ by

$$f(x_\infty, E+\delta E) \approx f(x_\infty, E) + J\,\delta E, \tag{2.55}$$

where J is the gradient of $f(x_\infty, E)$ with respect to E,

$$J = \frac{\partial f(x_\infty, E)}{\partial E}. \tag{2.56}$$

In our case, the range of $f(x_\infty, E)$ is complex and so is E. Let u, v, a and b be real such that

$$f(x_\infty, E) = u(a,b) + iv(a,b), \tag{2.57}$$

$$E = a + ib, \tag{2.58}$$

then we have the following Jacobian matrix **J**

$$\mathbf{J} = \begin{bmatrix} \frac{\partial u}{\partial a} & \frac{\partial u}{\partial b} \\ \frac{\partial v}{\partial a} & \frac{\partial v}{\partial b} \end{bmatrix}, \tag{2.59}$$

and (2.55) in vector notation is

$$\mathbf{f}(\mathbf{x}_\infty, \mathbf{E}+\delta\mathbf{E}) \approx \mathbf{f}(\mathbf{x}_\infty, \mathbf{E}) + \mathbf{J}\,\delta\mathbf{E}, \tag{2.60}$$

where

$$\mathbf{f}(\mathbf{x}_\infty, \mathbf{E}) = \begin{bmatrix} u \\ v \end{bmatrix} \qquad \delta\mathbf{E} = \begin{bmatrix} \delta a \\ \delta b \end{bmatrix}. \tag{2.61}$$

By (2.54) and (2.60), we obtain

$$F(\mathbf{x}_\infty, \mathbf{E}+\delta\mathbf{E}) = [\mathbf{f}(\mathbf{x}_\infty, \mathbf{E}) + \mathbf{J}\,\delta\mathbf{E}]^2 = [\mathbf{f}(\mathbf{x}_\infty, \mathbf{E}) + \mathbf{J}\,\delta\mathbf{E}]^T [\mathbf{f}(\mathbf{x}_\infty, \mathbf{E}) + \mathbf{J}\,\delta\mathbf{E}]. \tag{2.62}$$

To find the minimum, we set

$$\frac{\partial F(\mathbf{x}_\infty, \mathbf{E}+\delta\mathbf{E})}{\partial(\delta\mathbf{E})} = 0.$$

Let $\mathbf{G}\left(\mathbf{x}_{\infty}, \mathbf{E}, \delta\mathbf{E}\right) \equiv \mathbf{f}\left(\mathbf{x}_{\infty}, \mathbf{E}\right) + \mathbf{J}\,\delta\mathbf{E}$ and we have

$$\begin{aligned}
\frac{\partial\left\{\left[\mathbf{G}\left(\mathbf{x}_{\infty}, \mathbf{E}, \delta\mathbf{E}\right)\right]^{T}\mathbf{G}\left(\mathbf{x}_{\infty}, \mathbf{E}, \delta\mathbf{E}\right)\right\}}{\partial\mathbf{G}\left(\mathbf{x}_{\infty}, \mathbf{E}, \delta\mathbf{E}\right)}\frac{\partial\mathbf{G}\left(\mathbf{x}_{\infty}, \mathbf{E}, \delta\mathbf{E}\right)}{\partial\left(\delta\mathbf{E}\right)} &= 0 \\
2\left[\mathbf{G}\left(\mathbf{x}_{\infty}, \mathbf{E}, \delta\mathbf{E}\right)\right]^{T}\mathbf{J} &= 0 \\
\left[\mathbf{f}\left(\mathbf{x}_{\infty}, \mathbf{E}\right) + \mathbf{J}\,\delta\mathbf{E}\right]^{T}\mathbf{J} &= 0 \\
\left(\delta\mathbf{E}\right)^{T}\mathbf{J}^{T}\mathbf{J} &= -\mathbf{f}^{T}\left(\mathbf{x}_{\infty}, \mathbf{E}\right)\mathbf{J} \\
\left[\left(\delta\mathbf{E}\right)^{T}\mathbf{J}^{T}\mathbf{J}\right]^{T} &= \left[-\mathbf{f}^{T}\left(\mathbf{x}_{\infty}, \mathbf{E}\right)\mathbf{J}\right]^{T} \\
\delta\mathbf{E} &= -\left(\mathbf{J}^{T}\mathbf{J}\right)^{-1}\mathbf{J}^{T}\mathbf{f}\left(\mathbf{x}_{\infty}, \mathbf{E}\right).
\end{aligned}$$

Due to Levenberg's and Marquardt's modification on the last equation, we have a damped factor λ, which is a positive parameter, such that

$$\delta\mathbf{E} = -\left[\mathbf{J}^{T}\mathbf{J} + \lambda\mathrm{diag}\left(\mathbf{J}^{\mathbf{T}}\mathbf{J}\right)\right]^{-1}\mathbf{J}^{T}\mathbf{f}\left(\mathbf{x}_{\infty}, \mathbf{E}\right), \tag{2.63}$$

where $\mathrm{diag}\left(\mathbf{J}^{\mathbf{T}}\mathbf{J}\right)$ means a diagonal matrix with entries on the diagonal from the matrix $\mathbf{J}^{T}\mathbf{J}$. As $|x| \to \infty$, if the function $\sqrt{F\left(\mathbf{x}_{\infty}, \mathbf{E}_{new}\right)} \leq \sqrt{F\left(\mathbf{x}_{\infty}, \mathbf{E}_{old}\right)}$ after a single iterative step, we update $\mathbf{E}_{old}$ by

$$\mathbf{E}_{new} = \mathbf{E}_{old} + \delta\mathbf{E} = \mathbf{E}_{old} - \left[\mathbf{J}^{T}\mathbf{J} + \lambda\mathrm{diag}\left(\mathbf{J}^{\mathbf{T}}\mathbf{J}\right)\right]^{-1}\mathbf{J}^{T}\mathbf{f}\left(\mathbf{x}_{\infty}, \mathbf{E}\right), \tag{2.64}$$

and meanwhile decrease the value λ_{old} by a factor, for example, $\lambda_{new} = {}^{\lambda_{old}}/_{\sqrt{2}}$. If after a single iterative step $\sqrt{F\left(\mathbf{x}_{\infty}, \mathbf{E}_{new}\right)} > \sqrt{F\left(\mathbf{x}_{\infty}, \mathbf{E}_{old}\right)}$, this means our λ value is too small and we then increase λ_{old} by a factor, for example, $\lambda_{new} = 10\lambda_{old}$. And the eigenvalue will not be updated so that we still have

$$\mathbf{E}_{new} = \mathbf{E}_{old}. \tag{2.65}$$

How we adjust the value of λ becomes important to efficiently find the eigenvalue, yet so far there is no absolutely best way to optimize the value of λ.

2.3.2 Parametrization, eigenvalue and eigenfunction

2.3.2.1 Parametrization

We set up the following initial condition at the numerical infinity $x_0 \equiv \infty_{left}$ within the left Stokes wedge on Fig.(2.2):

$$x_0 = r_0\exp\left(i\theta_{left}\right) \qquad \psi\left(x_0\right) = 0 \qquad \frac{d\psi\left(x_0\right)}{dx} = 10^{-7}, \tag{2.66}$$

where θ_{left} is defined by (2.28) and r_0 is the complex modulus of the numerical infinity x_0. In other words, r_0 is the distance between the origin and the point where the wave function and the derivative of the wave function almost vanish. By observation on data, we choose r_0 to be around 4. To have the fastest convergence to the eigenvalue, we're tempted to use GLI to integrate along the two Stokes lines given by (2.28). However, they are connected at the origin

where is non-differentiable for $N \neq 2$. Since this causes non-smoothness (See Fig.(2.3)) on the eigenfunction at the origin, one way to have smooth-looking eigenfunction is to integrate along some new paths, which should satisfy the following four conditions:

1. The potential $-(ix)^N$ has a numerical cut on the positive-imaginary axis. So the new path must not cross it; otherwise we must have a different eigenvalue problem.

2. The new path must go from one complex infinity within one Stokes wedge and back to the other complex infinity in the other Stokes wedge. These two complex infinities are symmetric with respect to the imaginary axis of x.

3. The new path is smooth everywhere and can be parametrized by a differentiable function.

4. Since GLI converges fastest if integrate along the two Stokes lines, it would be more efficient if the path or the differentiable function has two asymptotic lines coincident with the locations of the two Stokes lines.

Figure 2.3: *The eigenfunction of the ground state for $N = 4$ along the Stokes lines (non-differentiable at origin) with $r_0 = 4$. The vertical-blue dot-lines represent two numerical infinities $\pm \mathrm{Re}\,(x_0) = \pm r_0 \cos 30°$. Along the Stokes lines, the numerical result for the eigenvalue E does not change even though the shape of the eigenfunction is not smooth, in comparison with the smooth eigenfunctions associated with the hyperbolic paths.*

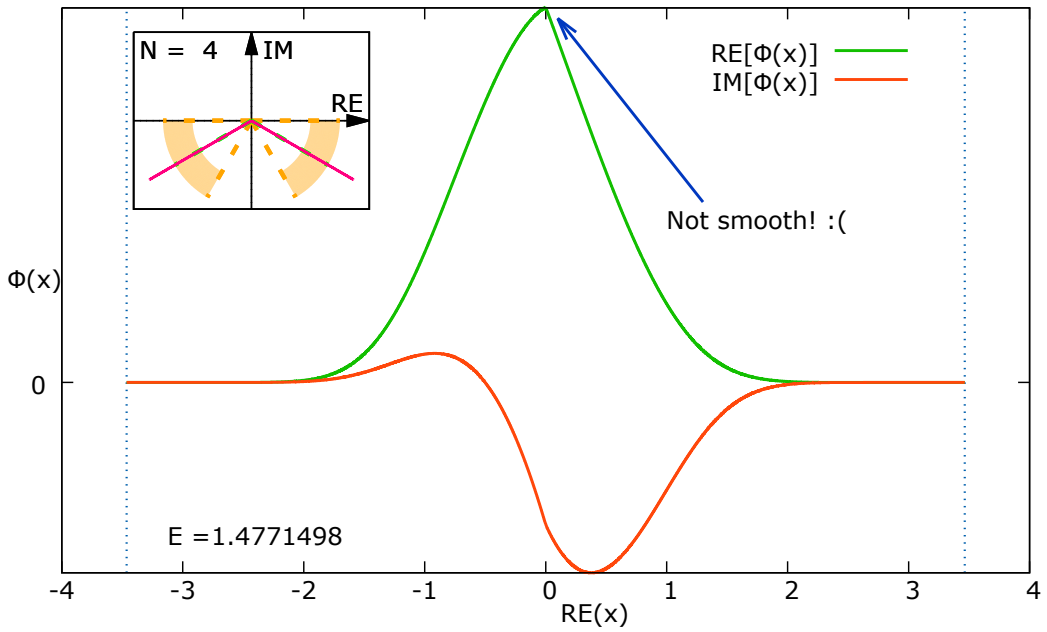

Figure 2.4: *The eigenfunctions of the ground state for $N = 4$ along the differentiable (hyperbolic) paths with three different values of a defined by the hyperbolic equation $Y_- = -a\sqrt{1+\frac{X^2}{b^2}}$. All three paths have the same eigenvalue. The vertical-blue dotlines represent two numerical infinities $\pm \mathrm{Re}\,(x_0) = \pm r_0 \cos 30°$ with $r_0 = 4$.*

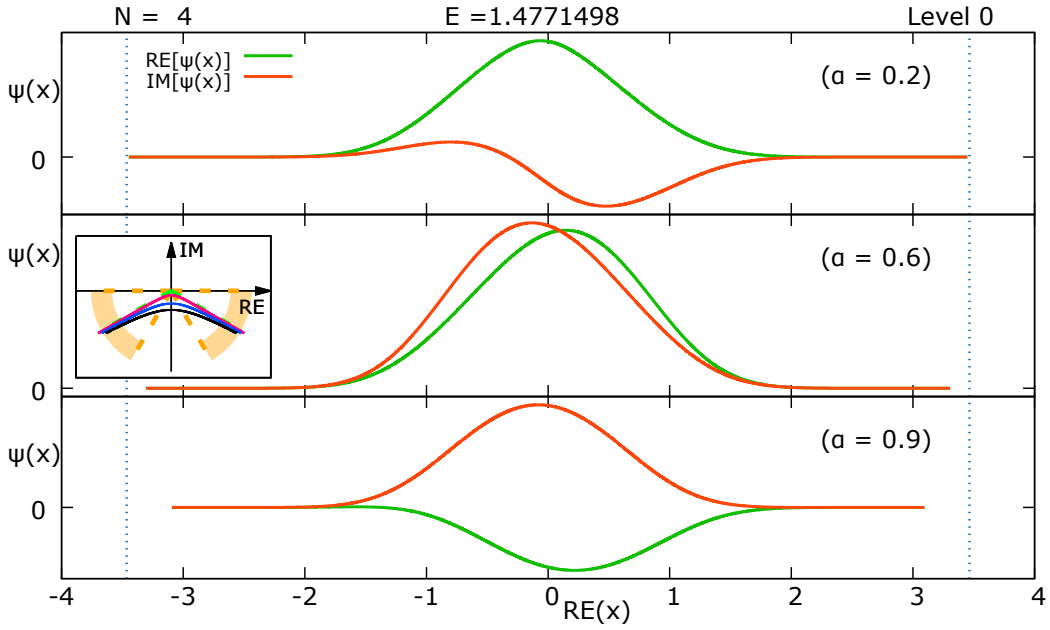

To satisfy all four conditions and since Fig.(2.2) shows that the two Stokes lines move below the real axis when $N > 2$, the best differentiable function used for the parametrization when $N > 2$ must be hyperbola shown on the miniplot on Fig.(2.4). In this hyperbolic parametrization, we treat $\mathrm{Re}\,(x)$ as the parameter so that

$$x = \mathrm{Re}\,(x) + i\,\mathrm{Im}\,(x) = \mathrm{Re}\,(x) - i\sqrt{a^2 + [\mathrm{Re}\,(x)]^2\,(\tan\theta)^2}, \tag{2.67}$$

where the angle θ between one of the asymptotic lines and the horizontal axis is $\theta = \arctan\left(\frac{a}{b}\right)$. Also, $\theta = \theta_{right}$ from (2.28). Fig.(2.4) shows that the shapes of the corresponding eigenfunctions are smooth and different-looking since the values of a defined by the hyperbolic equation $Y_- = -a\sqrt{1+\frac{X^2}{b^2}}$ is different. For the upcoming work, we choose $a = 0.2$ since this hyperbola is quite close to the location of the two Stokes lines and meanwhile keeps the shape of eigenfunction smooth.

For $0 < N < 2$, Fig.(2.2) shows that the two Stokes lines move above the real axis. Does the function satisfy the four conditions exist? Yes. As $X \to \pm\infty$ the following function with $k > 0$, real parameters c and t

$$f\,(X) = \frac{X^2 - c}{\sqrt{kX^2 + t}} \tag{2.68}$$

has two asymptotic lines:

$$Y = \frac{1}{\sqrt{k}}X \quad \text{as } X \to +\infty, \qquad Y = -\frac{1}{\sqrt{k}}X \quad \text{as } X \to -\infty. \tag{2.69}$$

The angle θ between the asymptotic line associated with $X \to +\infty$ and the horizontal axis satisfies

$$k = \left(\frac{1}{\tan\theta}\right)^2. \tag{2.70}$$

Fig.(2.5) shows a good news that the function satisfies all four conditions.

Figure 2.5: *The differentiable path for* $N < 2$ *by choosing* $c = \frac{1}{10}$ *and* $t = 8$.

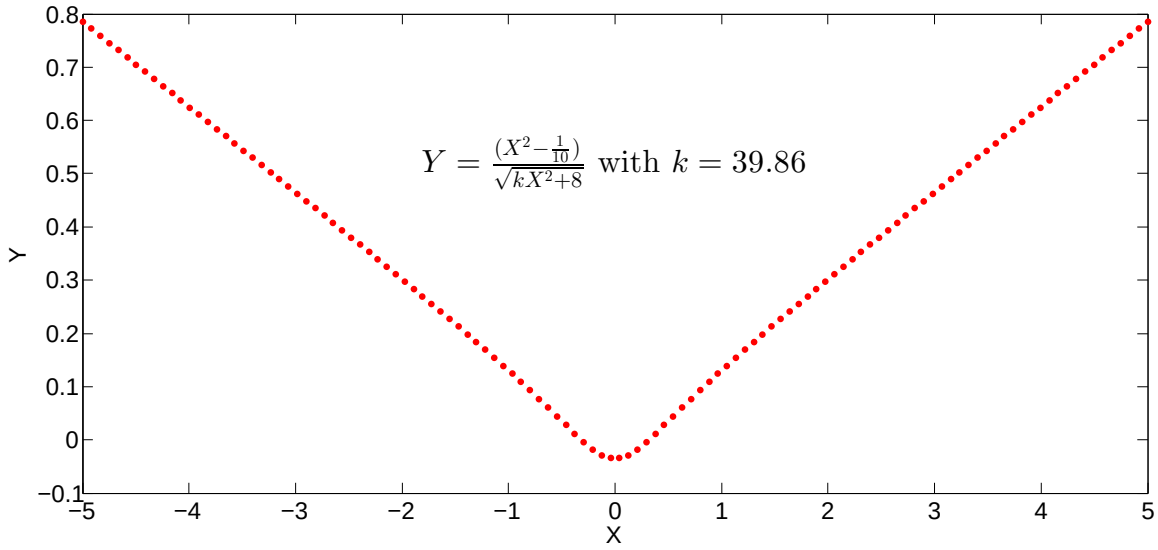

With these parametrizations (2.67), (2.68) and along the real axis of x, we are able to use LMA and GLI to find all eigenvalues and eigenfunctions associated with all pairs of wedges defined by Fig.(2.1). The final result of eigenvalues is shown on Fig.(2.31), and we will explain it later.

2.3.2.2 When $N = 2$

The concept of Stokes wedge implies that the same eigenvalue is obtained if we integrate along different paths, as along as the conditions 1 and 2 are satisfied. However, can we justify this by numerical analysis? How about their eigenfunctions? Are they independent from the shape of path or not?

Figure 2.6: *Four distinct contour paths we follow for* $N = 2$.

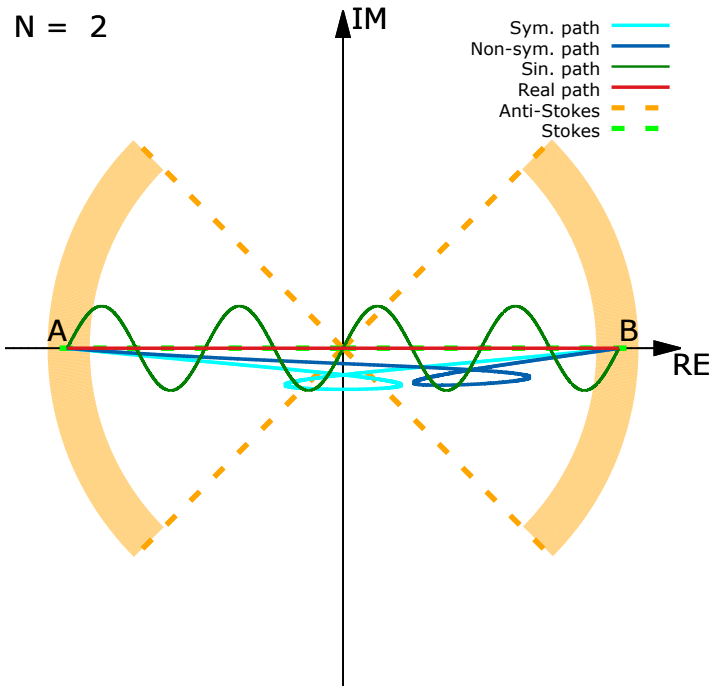

The first step to answer these questions is to parametrize various paths and calculate the corresponding eigenvalues to see if they agree each other or not. We start with the case when $N = 2$ as a harmonic oscillator, and use LMA and GLI to search for the eigenvalue by integrating along the four different paths shown on Fig.(2.6), where two symmetric points A and B are located on the real axis and treated as two numerical infinities. These four different paths start from the same boundary point A and end to the same boundary point B. One of the four paths is along the real axis, two complex paths (sym. path and non-sym. path) are defined by (2.71), and we add another complex path (sin. path) defined by a sinusoidal function.

It's a bit of a challenge to parametrize the non-sym. path on Fig.(2.6). We start with the following parametric curve with real parameter p shown on Fig.(2.7)

$$\begin{cases} X = p - 2\sin p \\ Y = p^2 \end{cases} \tag{2.71}$$

which crosses itself once and is symmetric with respect to the Y-axis. So this curve can be used to define the sym. path on Fig.(2.6). To get the non-symmetric version, we can just rotate the curve by an given angle.

Figure 2.7: *Parametric curve crosses itself.*

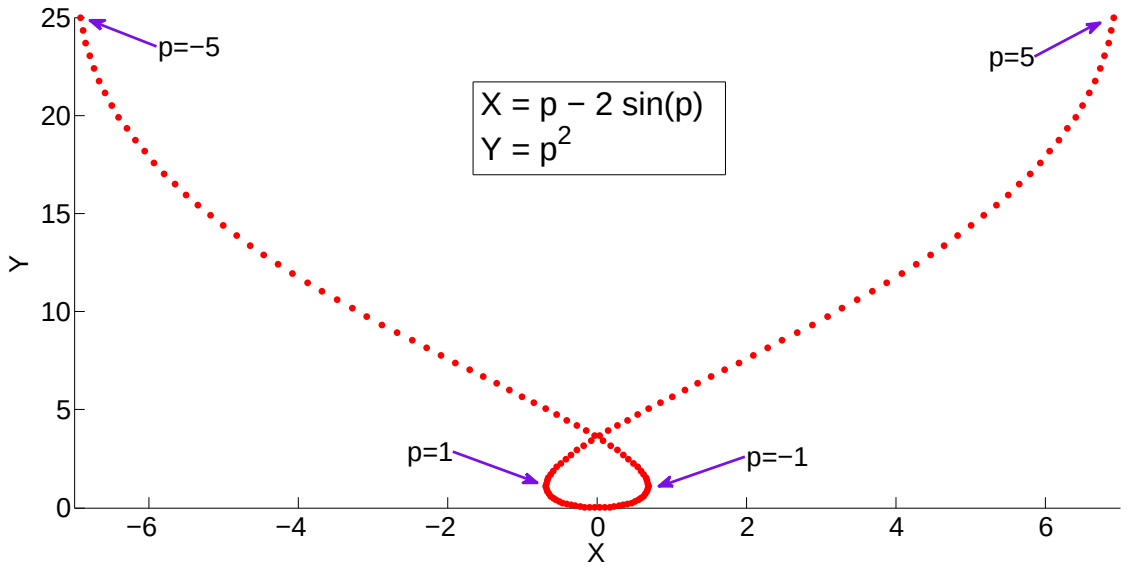

The eigenvalues we found by following all four paths defined by Fig.(2.6) are shown on the following Tab.(2.1), where the corresponding residues are obtained by calculating the complex modulus of the numerical eigenfunctions at the right boundary point B. Ideally, these values should be zero, so we set our tolerance of residue to be 10^{-13}. Through observation, the real parts of eigenvalues are almost the same for all four paths, whereas the imaginary parts are so small that they can be ignored. When the energy level increases, both real and imaginary parts of eigenvalues E start to shift from the analytic results, which are $E_i \in \{1, 3, 5, 7 \cdots\}$. The higher energy level, the larger the shift. This is typical, since we fix the locations of boundary points A and B, and define them as numerical infinities. When energy level becomes higher, the pattern of corresponding eigenfunctions becomes more complicated - they wiggle more before vanishing at the infinity so that the length of non-vanishing parts becomes longer. Ideally, to minimize the shift, we need to separate A and B even farther to accommodate longer eigenfunction for higher energy level. For those, who are meticulous, you may observe from Tab.(2.1) that following the real path has relatively smaller imaginary parts of eigenvalues than following complex paths. The reason is the same as what we have just said. The non-vanishing parts of corresponding eigenfunctions by following the complex paths are longer than by following the real path, because the shapes of these complex paths are more complicated than of the real path. In example from the next Sec.2.3.2.3, we will numerically demonstrate that within the same pair of Stokes wedges and independent from the shape of path, imaginary parts of eigenvalues become smaller by separating A and B farther.

Table 2.1: *Eigenvalues E from four distinct paths for $N = 2$*

	Re(E)	Im(E)	Residue
Sym. path	1.000000000000000	-0.1003620374557331E-17	0.6933467498458673E-14
Non-sym. path	1.000000000000000	-0.9129470301709489E-16	0.6621862749722552E-15
Sin path	1.000000000000000	-0.1480602937730059E-19	0.6507080581691370E-13
Real path	1.000000000000000	-0.6115913653696003E-24	0.4344033594013260E-13
Sym. path	3.000000000000000	-0.3812557322801343E-17	0.7481390208835876E-14
Non-sym. path	3.000000000000002	-0.1004110601426235E-14	0.6295535561555787E-13
Sin path	3.000000000000000	-0.3128964148841211E-16	0.2291971606424135E-13
Real path	3.000000000000000	-0.9155685463116496E-25	0.4493053239887049E-16
Sym. path	5.000000000000013	0.2518834186125261E-15	0.2558806183336114E-13
Non-sym. path	5.000000000000021	-0.5549557037887328E-14	0.7809314498766232E-15
Sin path	5.000000000000013	-0.1256496099524602E-14	0.2522954352155260E-13
Real Path	5.000000000000013	-0.3282017032228570E-21	0.4056238283715534E-14
Sym. path	7.000000000000336	0.7951061118291276E-14	0.8926074464266579E-14
Non-sym. path	7.000000000000333	-0.2055555160518695E-13	0.9050089495233448E-14
Sin path	7.000000000000346	-0.3247942276399777E-13	0.5055081369636703E-13
Real Path	7.000000000000349	-0.1069414905172819E-21	0.5135175134438069E-16
Sym. path	9.000000000006479	0.1538114392730817E-12	0.9039626517473521E-13
Non-sym. path	9.000000000005852	-0.5231255443223443E-13	0.6176568383960844E-15
Sin path	9.000000000007047	-0.4597603658801041E-13	0.3218450841772004E-14
Real path	9.000000000006735	-0.5114475804683816E-18	0.1308960170235510E-13
Sym. path	11.00000000009739	0.2259281344709882E-11	0.6716526118006623E-13
Non-sym. path	11.00000000008690	-0.9751759350366208E-14	0.1637934803002069E-13
Sin path	11.00000000010035	-0.8913171072104399E-11	0.2633758435143849E-13
Real path	11.00000000010117	-0.2465880422978931E-18	0.4331758624064671E-15
Sym. path	13.00000000118508	0.2671384985266084E-10	0.6520143632534298E-13
Non-sym. path	13.00000000105809	0.1377279869903961E-11	0.1290710233287906E-13
Sin path	13.00000000122042	-0.1050745001235918E-09	0.3099083730781987E-13
Real path	13.00000000122972	-0.1303098653403670E-18	0.1945701205719875E-16

Figure 2.8: $\mathrm{Re}\,(x)$ *versus the eigenfunction of the ground level along the real and sinusoidal path for* $N = 2$ *(Before using* (2.72) *to normalize).*

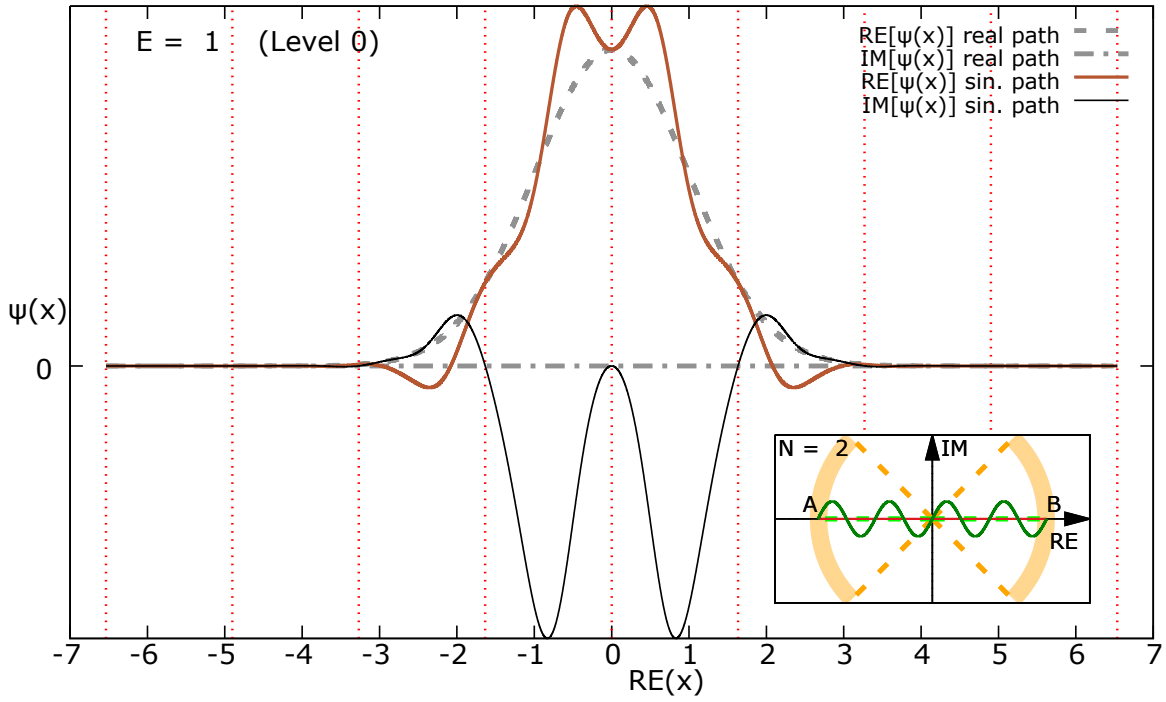

Figure 2.9: $\mathrm{Re}\,(x)$ *versus the eigenfunction of the ground level along the real and sinusoidal path for* $N = 2$ *(after using* (2.72) *to normalize).*

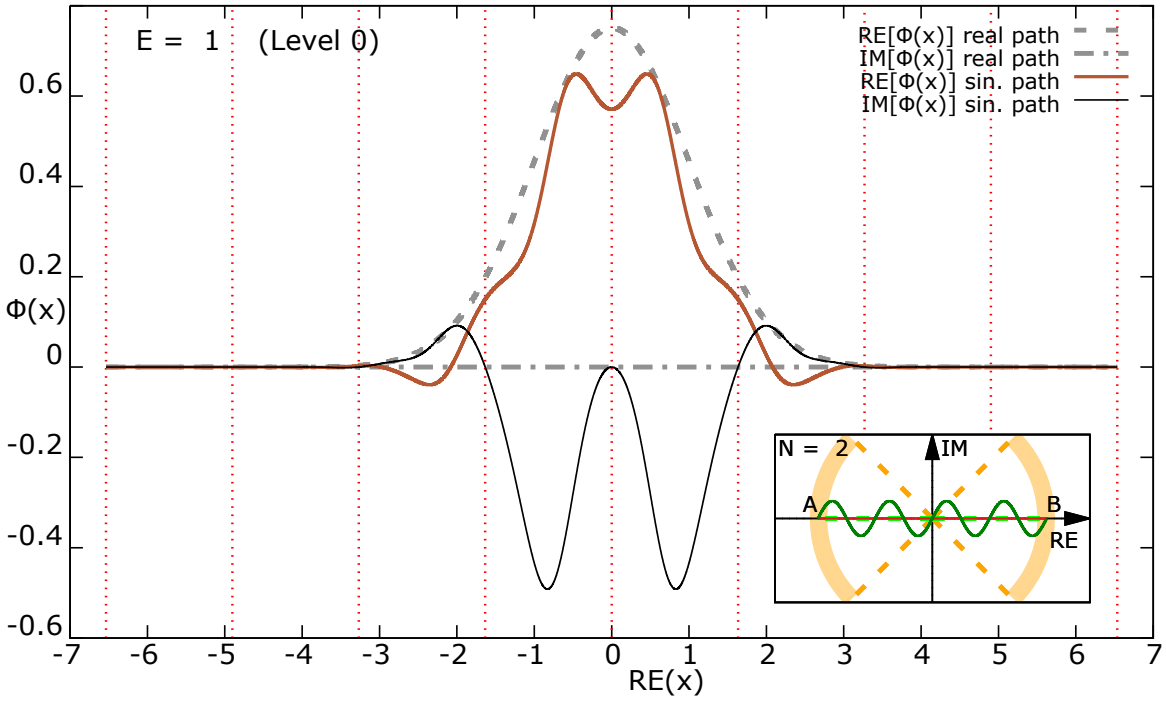

Now we plot the eigenfunctions associated with different paths. Fig.(2.10) shows two mini-plots. One mini-plot is to show the shape of paths, while the

other shows the parameter p defined by (2.71) versus the corresponding eigenfunction $\psi(p)$ by following the sym. path. For $N=2$, since all imaginary parts of eigenfunctions associated with the real path are zero, that is why we only see a vertical segment (the grey dash line) contributed by $\mathrm{Re}[\psi(x)]$ along the real path on Fig.(2.11), Fig.(2.14) and Fig.(2.17).

It seems that the different path has different eigenfunction even though the eigenvalues are the same. This is an illusion! All corresponding eigenfunctions are independent from the shape of paths as well. To demonstrate this, we draw the vertical-red dotlines on all those figures to indicate where two different paths intersect each other. At all those intersection points, the corresponding two eigenfunctions cross each other as well. We call these behaviors as "**crossing events**". Suppose that two different paths intersect at one point x_*, then a **single crossing event** is that the eigenfunction $\psi(x_*)$ from the one path and $\psi(x_*)$ from the other path are crossed at x_*. For example, on Fig.(2.8), $\mathrm{Re}[\psi(x)]$ from the real path and $\mathrm{Re}[\psi(x)]$ from the sinusoidal path are crossed at 9 locations, and meanwhile $\mathrm{Im}[\psi(x)]$ from the real path and $\mathrm{Im}[\psi(x)]$ from the sinusoidal path are crossed at another 9 locations. These two sets of 9 locations can be connected pair by pair by 9 vertical-red dotlines, whose horizontal coordinates are the real coordinates of the 9 intersection points between the two paths. On Fig.(2.11), however, the horizontal coordinates are changed to be the imaginary coordinates of the corresponding intersection points. By observation on all figures from Fig.(2.10) to Fig.(2.18), we conclude that the number of crossing events is equal to the number of vertical-red dotlines, and further conclude that the eigenfunctions are independent from the shape of paths so long as those paths all start from the same boundary point A and end at the same boundary point B. In the later case (See Fig.(2.21)), we will numerically demonstrate that the eigenfunction is not independent from path if that path starts and ends on different boundary point.

The amplitude of eigenfunction depends on the shape of path. If a path contains some points whose distances are far away from the origin, then the amplitude of the corresponding eigenfunction must be large. That is why the amplitude along the real axis is the smallest; whereas the amplitude along the sym. path (on Fig.(2.10) and Fig.(2.11)) is the largest.

How about normalization? We're tempted to use standard normalization from conventional quantum mechanics. In numerical approximation, the normalized wavefunction $\phi_n(x)$ would be

$$\phi_n(x)=\frac{\psi_n(x)}{\sqrt{\int_c \psi_n^*(x)\,\psi_n(x)\,dx}}\approx\frac{\psi_n(p)}{\sqrt{\int_{p_1}^{p_2}\psi_n^*(p)\,\psi_n(p)\,dp}}\approx\frac{\psi_n(p)}{\sqrt{\sum_p \psi_n^*(p)\cdot\psi_n(p)\cdot dp}}. \tag{2.72}$$

where p is the real parameter which parametrizes the path. By this way, we find that $\phi_n(x)$ satisfies

$$\int_c \phi_n^*(x)\,\phi_n(x)\,dx\approx\int_{p_1}^{p_2}\phi_n^*(p)\,\phi_n(p)\,dp\approx\sum_p \phi_n^*(p)\cdot\phi_n(p)\cdot dp=1\,. \tag{2.73}$$

for all wave functions from different energy level and different path. Hence, it is possible to "normalize"[3] all wave functions we have encountered so far! However, except of the case by following the real path when $N = 2$, the condition of orthogonality $\int_c \phi_m^* (x) \phi_n (x) dx = 0$ may not hold to be true in all other paths. For example, following the sinusoidal path on Fig.(2.9), we find that, numerically,

$$\int_c \phi_0^* (x) \phi_1 (x) dx \approx 0 \qquad \int_c \phi_6^* (x) \phi_3 (x) dx \approx 0 \qquad \int_c \phi_0^* (x) \phi_5 (x) dx \approx 0, \tag{2.74}$$

but

$$\int_c \phi_0^* (x) \phi_2 (x) dx = -0.92145 + 1.56493i \neq 0. \tag{2.75}$$

The "official" way of normalization introduced by Bender[8] is to use the recipe, which at first requires to find the PT-normalized eigenfunction through

$$\phi_n (x) = \exp\left(i\theta_n/2\right) \psi_n (x), \tag{2.76}$$

which satisfies $\phi_n^* (-x) = \phi_n (x)$. Then we can verify

$$\int_c \phi_n (x) \phi_n (x) dx = (-1)^n. \tag{2.77}$$

After that, we can use CPT-normalization defined by

$$\langle \phi_m (x), \phi_n (x) \rangle_{CPT} = \int_c \int_{c'} \hat{C} (x, y) \phi_m (y) dy \phi_n (x) dx = \delta_{mn}, \tag{2.78}$$

which in some case may require to find the charge operator $\hat{C}$ first. For the potential $-(ix)^N$, the most difficult part is to find the phase angle θ_n from (2.76). In this paper, we made no attempt to find θ_n, and therefore no attempt to normalize any eigenfunction we have encountered.

Since (2.72) is only a numerical approximation of the normalization from conventional quantum mechanics, Fig.(2.9) indicates that due to numerical error or using the conventional/wrong method to normalize, the two eigenfunctions no longer cross each other precisely at those intersection points between the two paths. This means that the crossing events no longer happen. We suspect that such conundrum will still exist even if we undertake the procedure of the PT-normalization initiated at (2.76), because eventually (2.76) and (2.78) may require us to use numerical approximation again. This adds another reason why we don't normalize eigenfunctions.

[3] However, we are not able to use $\mathrm{Re}(x)$ to "normalize" $\psi(x)$ if $\mathrm{Re}(x)$ is not used to parametrize the contour path (For example, see (2.71)).

Figure 2.10: *$\mathrm{Re}\,(x)$ or p versus the eigenfunction of the ground level along three paths (real, sin. and sym. path) for $N = 2$*

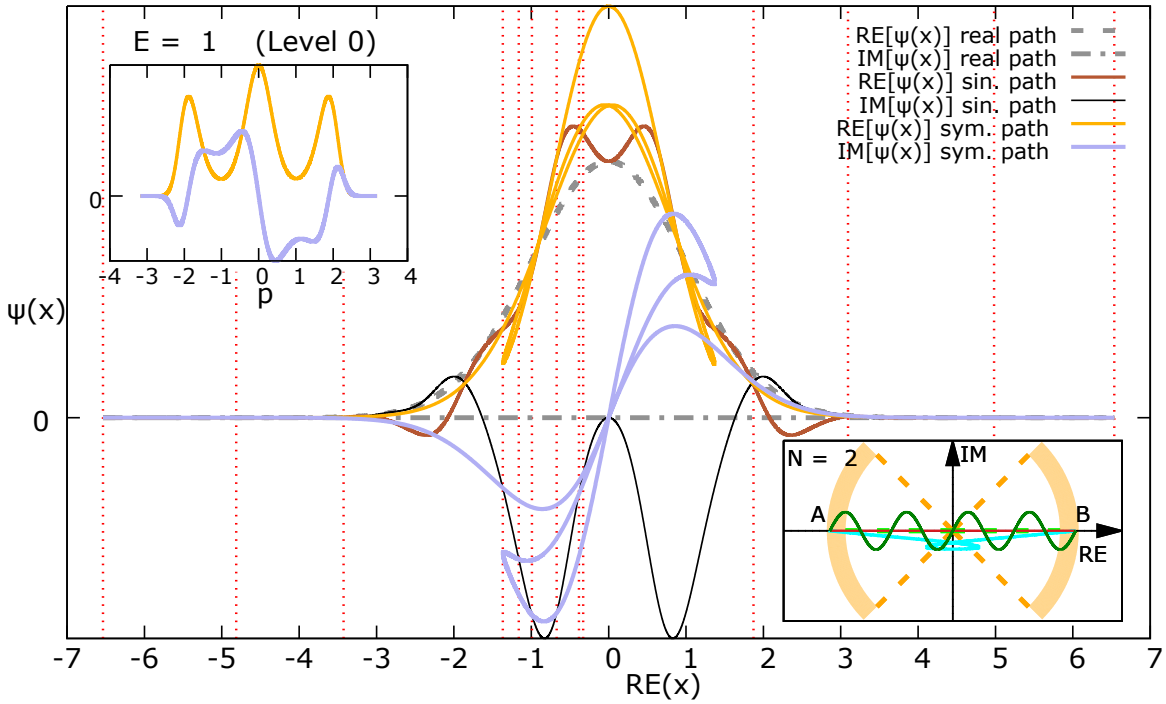

Figure 2.11: *$\mathrm{Im}\,(x)$ versus the eigenfunction of the ground level along three paths (real, sin. and sym. path) for $N = 2$*

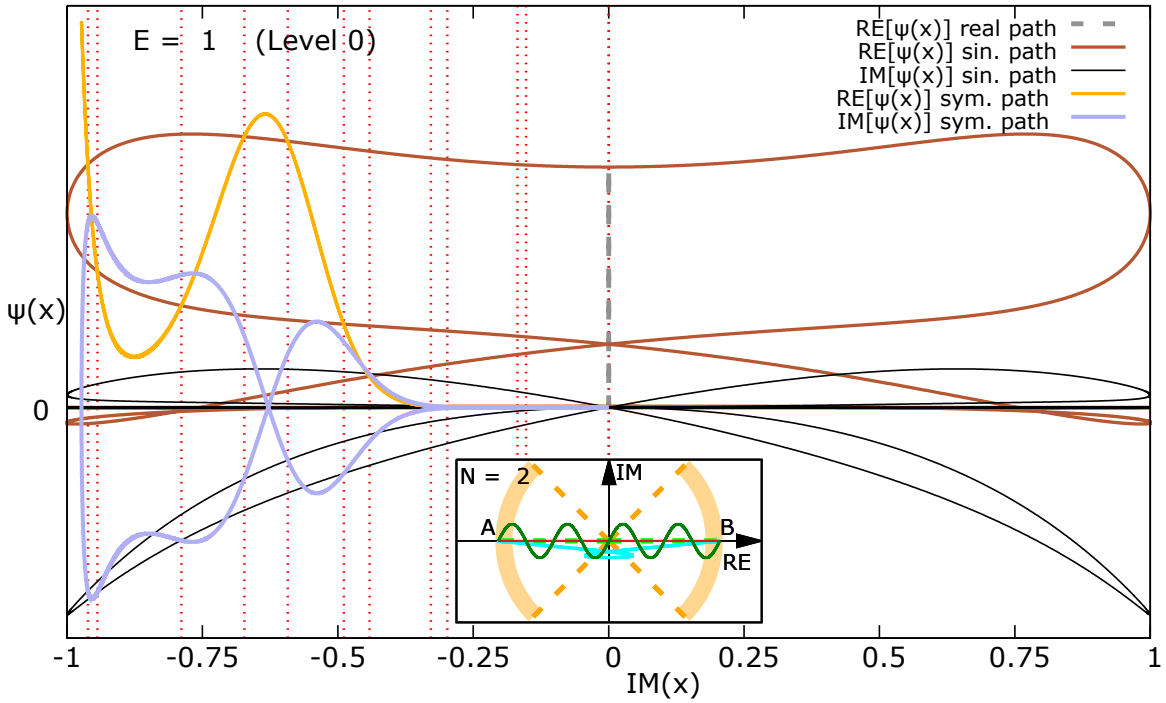

Figure 2.12: $\mathrm{Re}\,(x)$ *or* p *versus the eigenfunction of the ground level along three paths (real, sin. and non-sym. path) for* $N = 2$ *(See magnification on Fig.(2.13))*

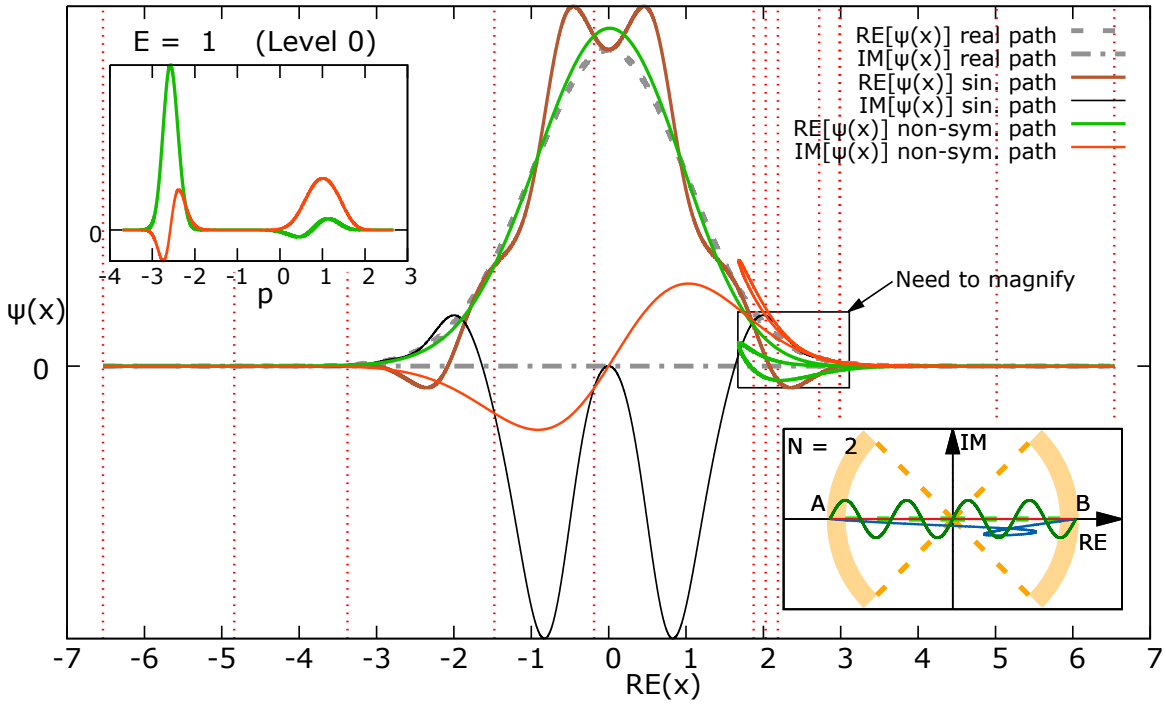

Figure 2.13: $\mathrm{Re}\,(x)$ *versus the eigenfunction of the ground level along three paths (real, sin. and non-sym. path) for* $N = 2$ *(after magnifying)*

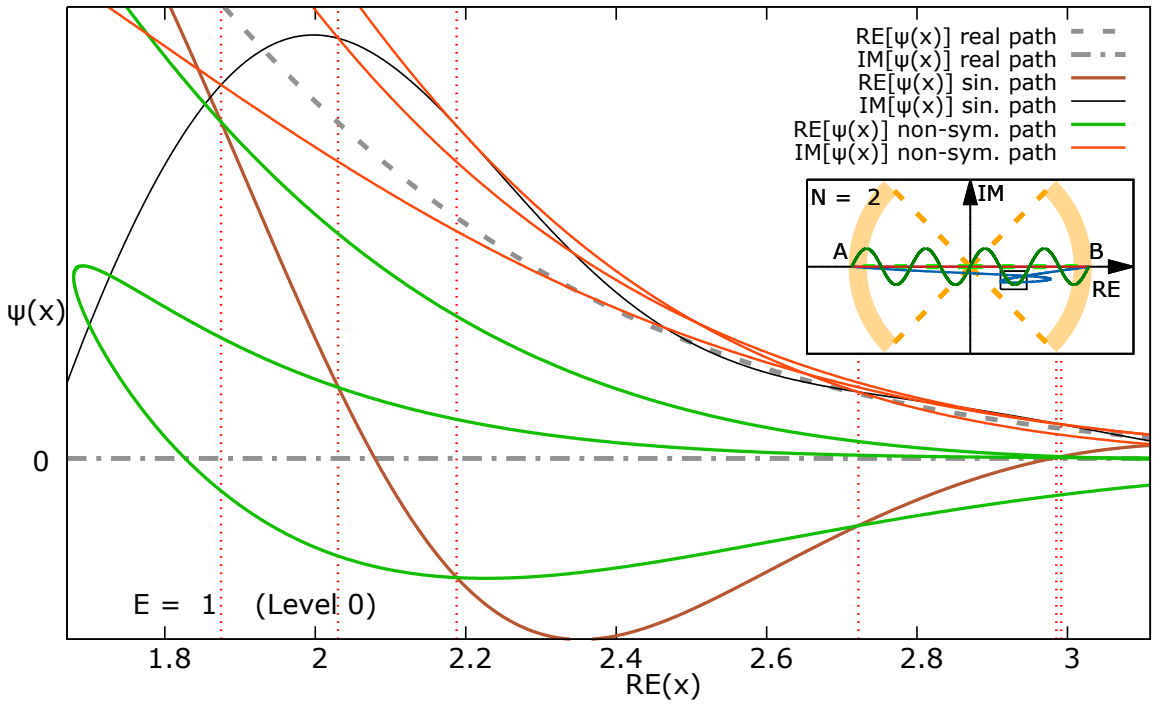

Figure 2.14: *$\mathrm{Im}\,(x)$ versus the eigenfunction of the ground level along three paths (real, sin. and non-sym. path) for $N = 2$*

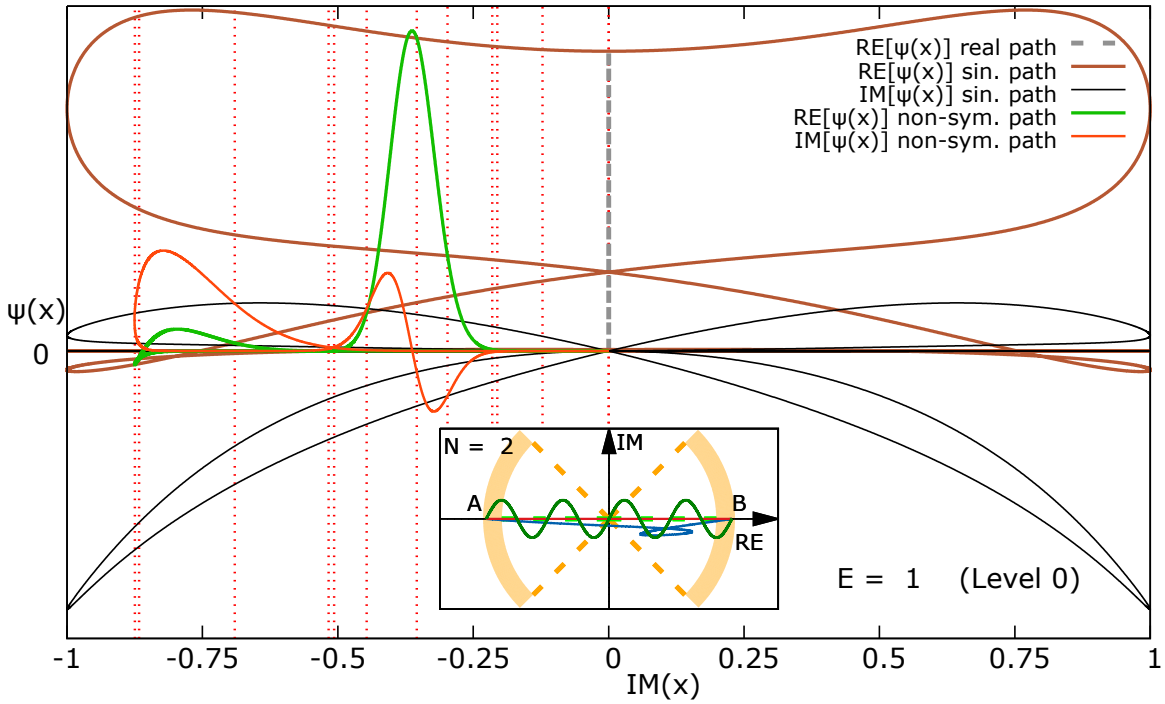

For higher energy state, we plot the 4th level on the following figures where we observe that the number of crossing events is equal to the number of intersection points between two different paths as well.

Figure 2.15: $\mathrm{Re}\,(x)$ *or* p *versus the eigenfunction of the* 4*th level along three paths (real, sin. and non-sym. path) for* $N = 2$ *(See magnification on Fig.*(2.16)*)*

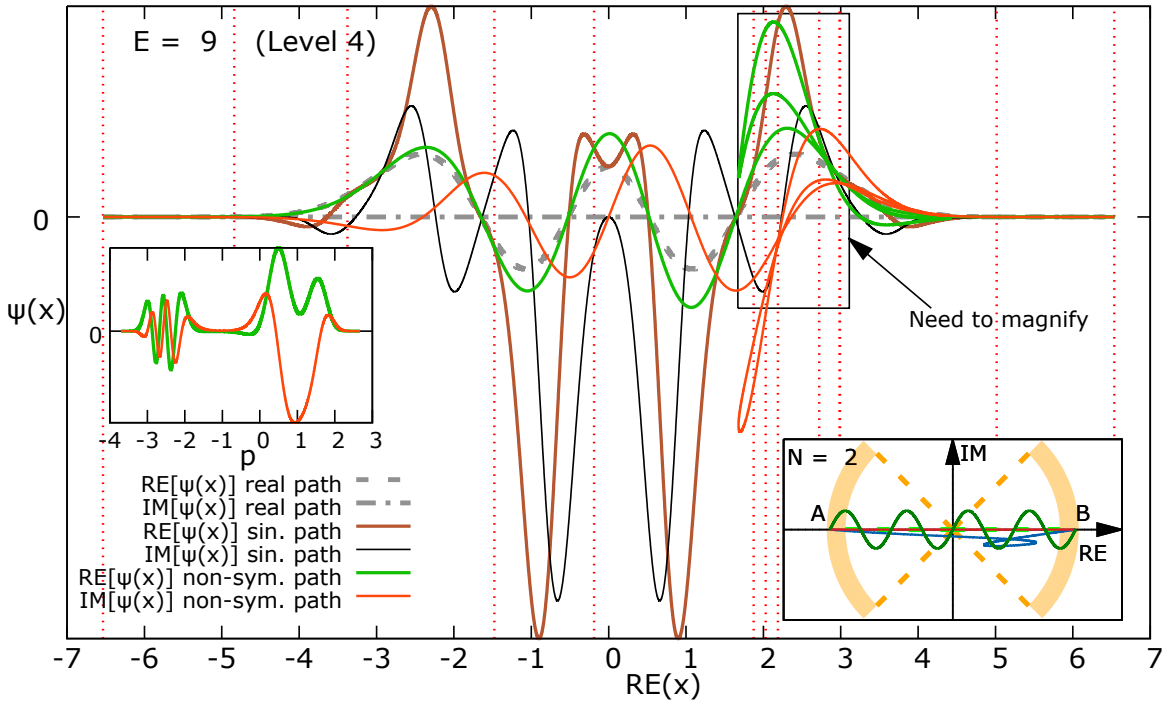

Figure 2.16: $\mathrm{Re}\,(x)$ *versus the eigenfunction of the* 4*th level along three paths (real, sin. and non-sym. path) for* $N = 2$ *(after magnifying)*

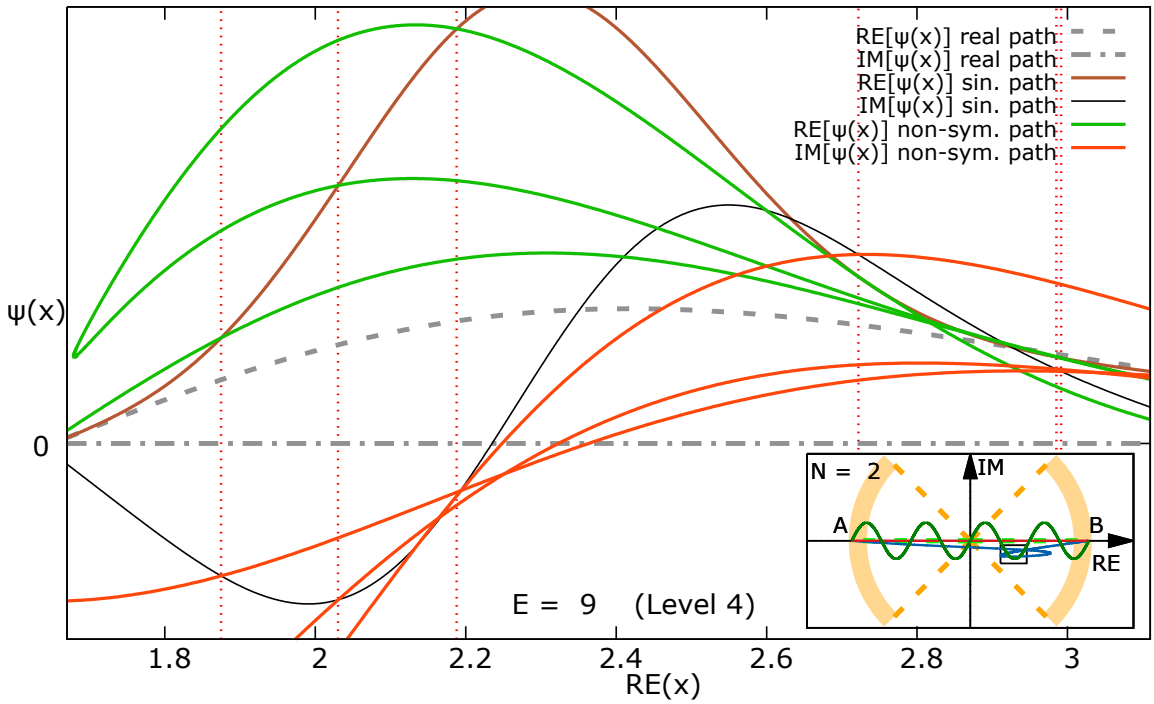

Figure 2.17: $\mathrm{Im}\,(x)$ *versus the eigenfunction of the* 4*th level along three paths (real, sin. and non-sym. path) for* $N = 2$ *(See magnification on Fig.*(2.18)*)*

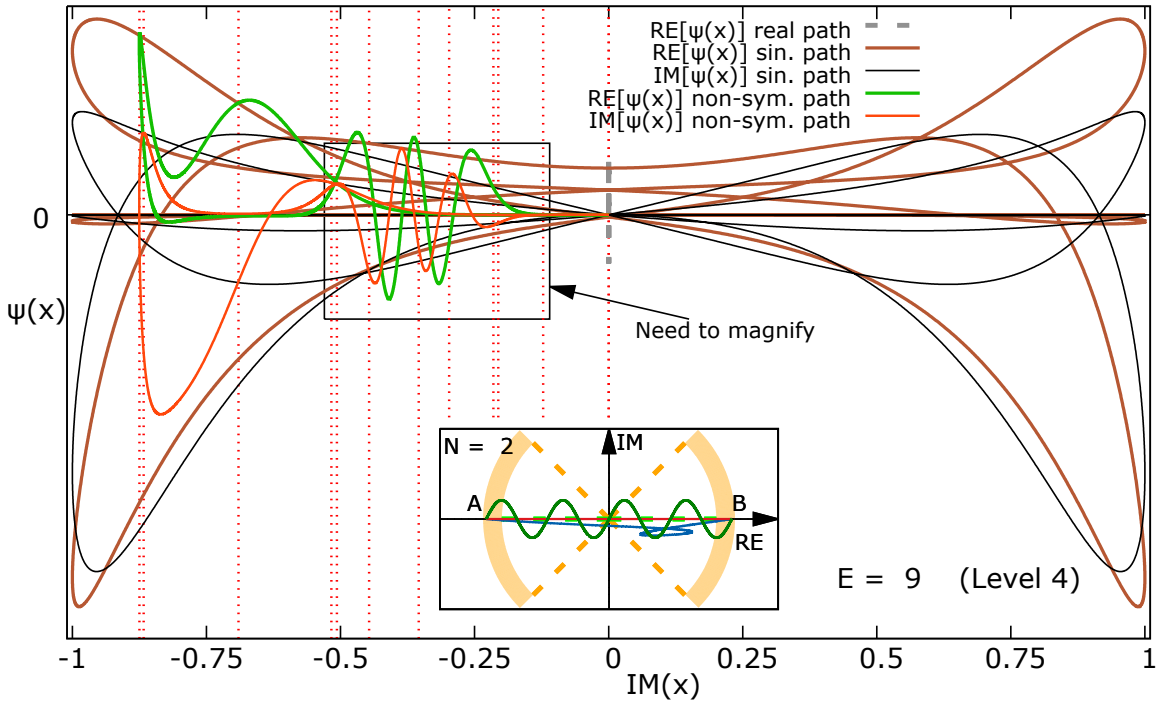

Figure 2.18: $\mathrm{Im}\,(x)$ *versus the eigenfunction of the* 4*th level along three paths (real, sin. and non-sym. path) for* $N = 2$ *(after magnifying)*

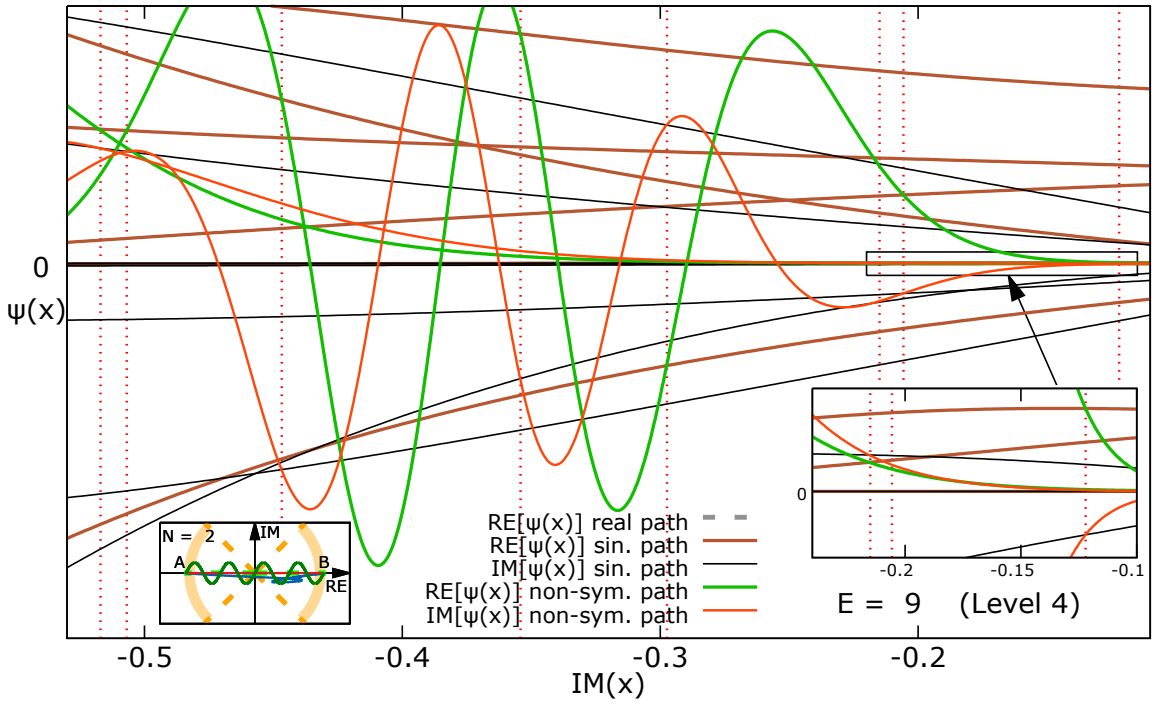

By the way, it is not really that clear by looking at Fig.(2.10) and Fig.(2.11) to figure out how the eigenfunction of the ground state associated with the

sym. path behaves. To make more visualized, we shift the path from the grey to the pink shown on Fig.(2.19) but still from A to B, and plot the eigenfunction associated with the pink path (not with the grey path). Since the parametric curve crosses itself, the corresponding eigenfunction also crosses itself but the times of cross are more than once, as the figures clearly show!

Figure 2.19: *Re*(x) *or* p *versus the eigenfunction of the ground level along the pink path for* $N = 2$

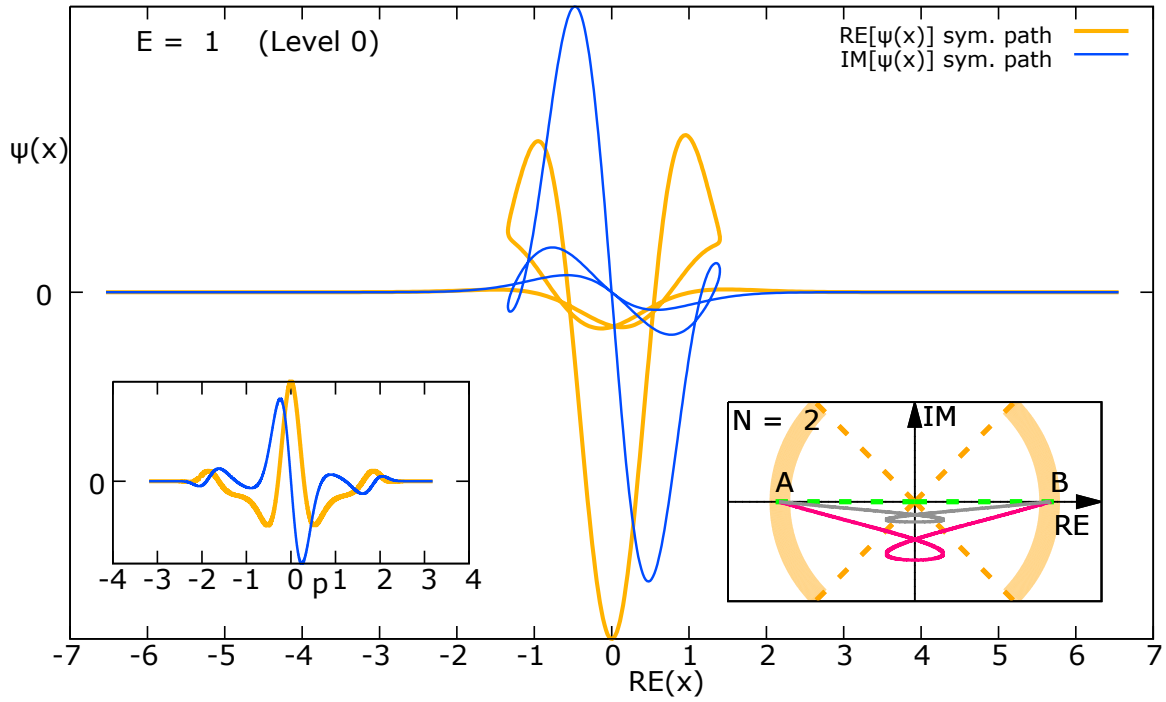

Figure 2.20: *Im(x) versus the eigenfunction of the ground level along the pink path for $N = 2$*

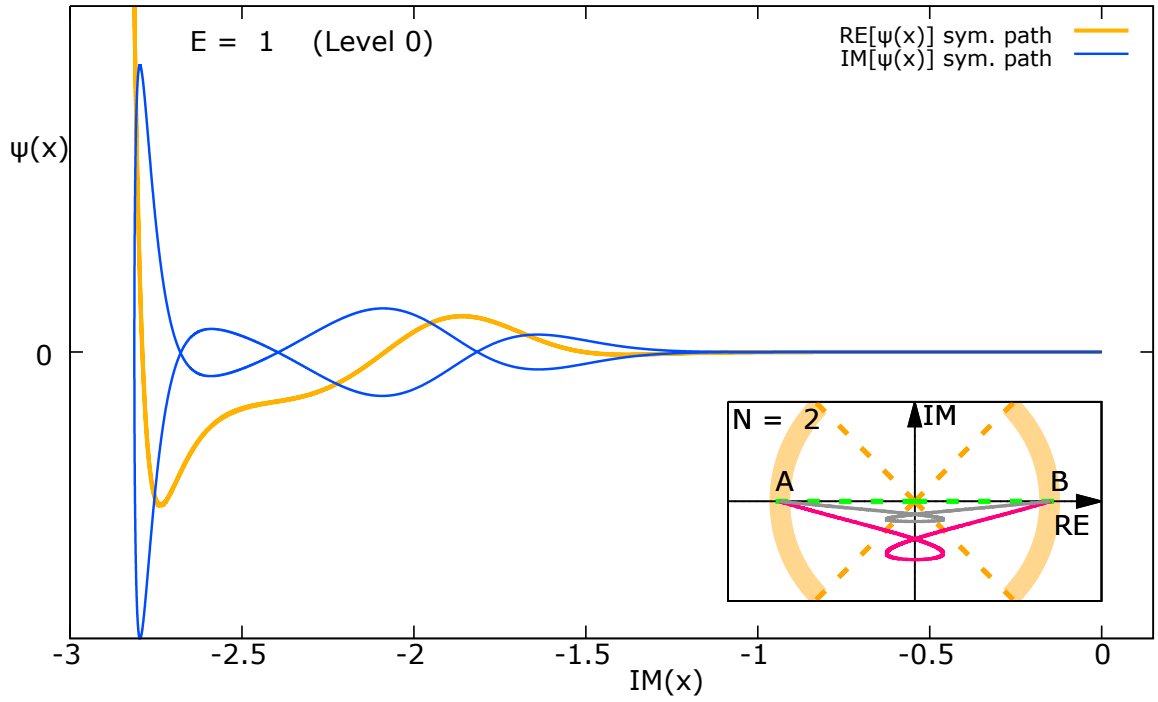

2.3.2.3 When $N = 3$ and $N = 2.9$

Figure 2.21: *Six distinct contour paths we follow for $N = 3$*

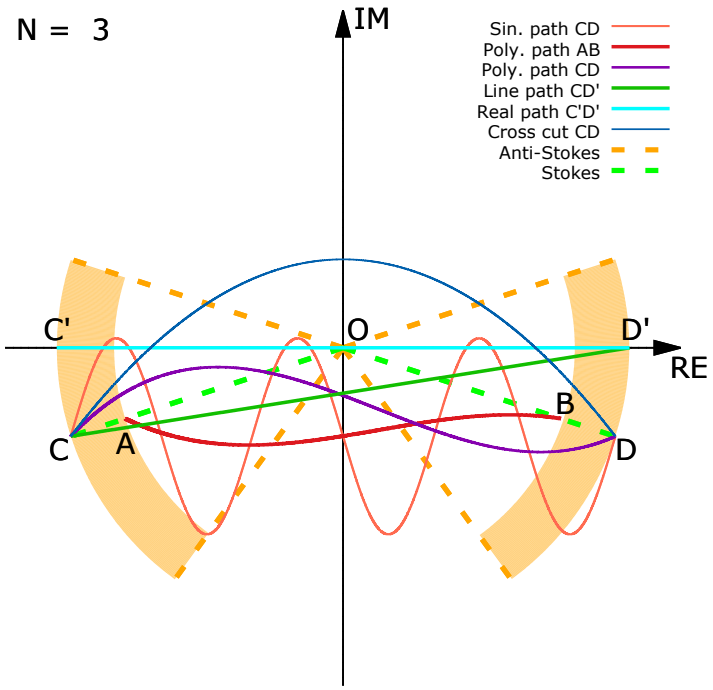

First, we draw three pairs of boundary points on Fig.(2.21). All these pairs AB, CD, and $C'D'$ are symmetric with respect to the imaginary axis of x. If label the origin as O, then $OA = OB$ and $OC = OD = OC' = OD'$. For further test, we set six different paths for the case of $N = 3$. Poly. path AB and poly. path CD are parametrized by two different polynomials, and both of paths are non-symmetric with respect to the imaginary axis, and start on the left Stokes line and end on the right Stokes line. In comparison, we add another four different paths on Fig.(2.21), one of which is our old friend the sinusoidal path CD, the other one from C to D crosses the positive-imaginary axis, and the rest two are straight lines. One straight line path (real path $C'D'$) is along the real axis from C' to D'. The other straight line path (line path CD') is slant, non-symmetric and connects C to D'.

Table 2.2: *Eigenvalues of the* 0*th and* 2*nd level from six distinct paths for* $N = 3$

	Re(E)	Im(E)	Residue
Ploy. AB	1.156267071989019	0.8699974233760738E-14	0.5837413712624328E-15
Poly. CD	1.156267071988113	0.2052808885668437E-23	0.3977525289004519E-13
Sin CD	1.156267071988113	-0.1490592751548809E-18	0.1223996206474492E-13
Real path	1.156267071988114	-0.8801464383118945E-17	0.4067876425200419E-14
Line CD'	Unknown	Unknown	Unknown
Cross cut CD	1.156267071988113	0.1230205329821445E-22	0.1793822595065940E-13
Ploy. AB	7.562273854416516	-0.8134071897365131E-12	0.6660422421018381E-15
Ploy. CD	7.562273854978828	-0.4436873189935206E-21	0.3680421771030331E-14
Sin CD	7.562273854978828	-0.7501915540619571E-17	0.2072196034721804E-13
Real path	7.562273854979419	0.5552050139288675E-14	0.8638177790903146E-15
Line CD'	Unknown	Unknown	Unknown
Cross cut CD	7.562273854978828	-0.8294706637359862E-20	0.3759133276627254E-13

We summarize the results on Tab.(2.2), where we choose the 2nd level to represent the eigenvalue for higher energy state. As shown on Tab.(2.2), when we separate AB even farther to CD, all imaginary parts of eigenvalues E along the poly. path become smaller. These demonstrate the claim we made in the previous example.

Since the straight line path CD' does not yield any real eigenvalue, we then conclude that the two infinities ∞_{left} and ∞_{right} or two boundary points have to be symmetric with respect to the imaginary axis to have real eigenvalue.

Figure 2.22: *Re(x) versus the eigenfunction of the ground level along two paths (poly. CD and sin. CD) for $N = 3$. The number of crossing events is equal to the number of intersection points between the two paths.*

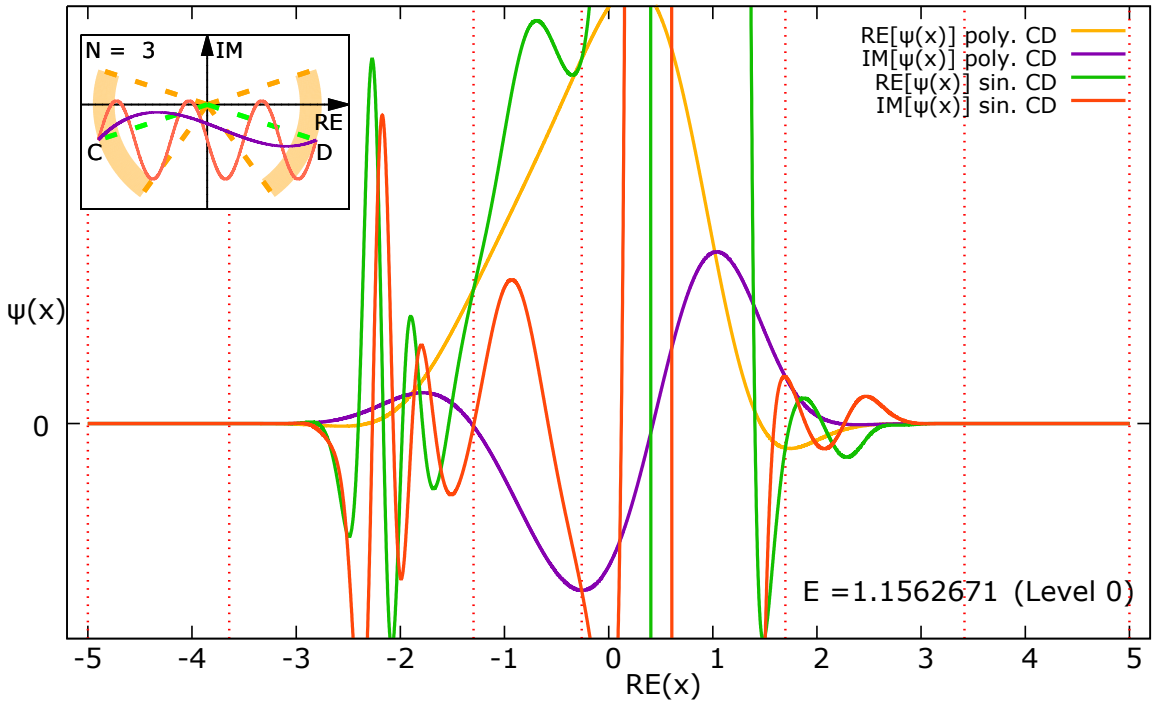

Figure 2.23: *Re(x) versus the eigenfunction of the ground level along two paths (poly. AB and sin. CD) for $N = 3$. No crossing event happens.*

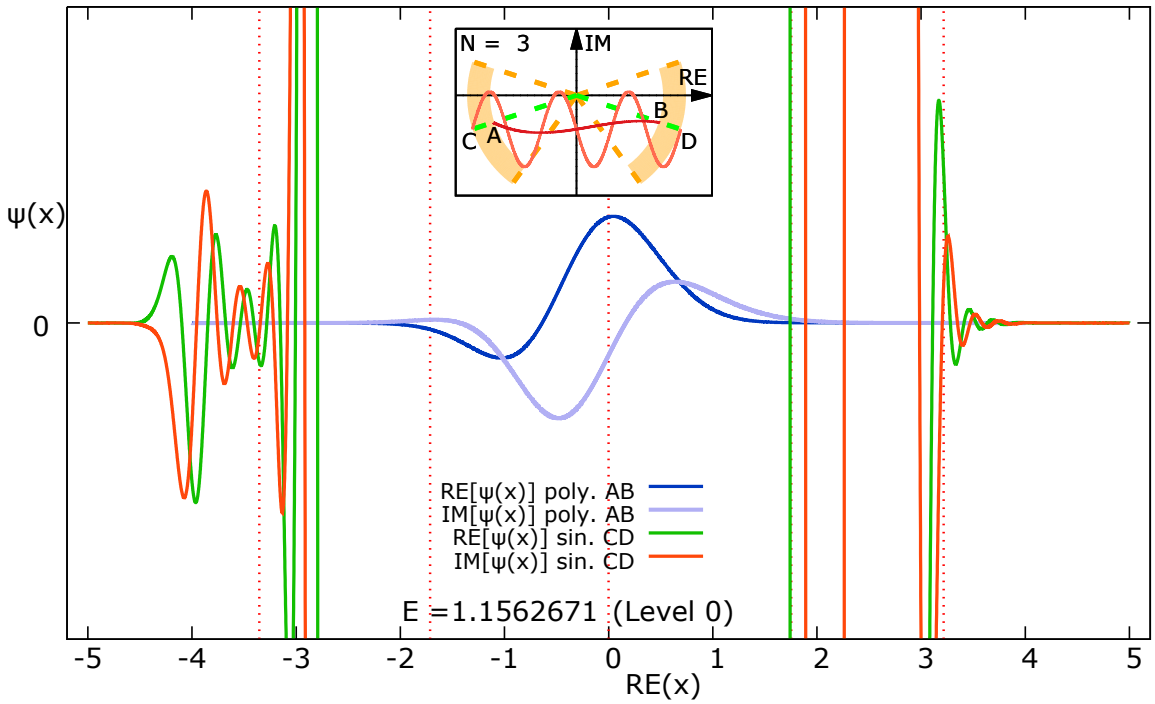

Figure 2.24: *Re(x) versus the eigenfunction of the ground level along two paths (sin. CD and real C'D') for $N = 3$. No crossing event happens.*

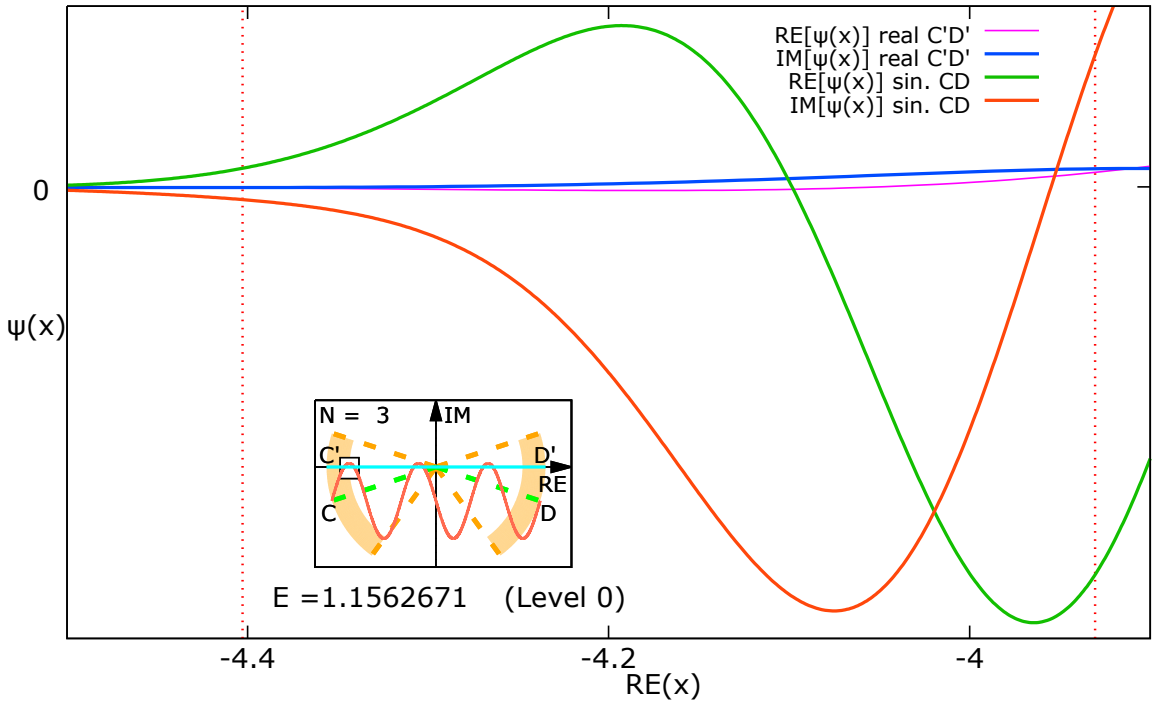

On Fig.(2.22), Fig.(2.23) and Fig.(2.24), our purpose is not to plot the entire eigenfunctions, but only to show whether the crossing events occur or not. On Fig.(2.22), we observe that the number of crossing events is equal to the number of intersection points between the two paths. This is not only true for integer N but also for fractional N (e.g. $N = 2.9$). However, if any two paths start and end at different boundary points within a pair of Stokes wedges, then the crossing event will not happen - for example, on Fig.(2.23) one path goes from C to D while the other goes from A to B. Since A and B are closer to the origin, the amplitude of the wave function is smaller so that no crossing event happens. Another example is shown on Fig.(2.24), where one path goes from C to D while the other goes from C' to D', and no crossing event happens even though $OC = OD = OC' = OD'$. Here, we want to emphasize that we do not know if the missing crossing events from these two examples can recover after applying the procedure of the CPT-normalization. More researches are needed.

On Tab.(2.2), it is a little surprise to see that the path (cross cut CD) yields the same eigenvalues as those paths without crossing the cut. The crossing events also happen in this case, where the two paths (cross cut CD and sin. CD) are involved. However, it is not "safe" to cross the cut if N is not an integer. For example, in case when $N = 2.9$, the locations of Stokes lines and anti-Stokes lines on Fig.(2.25) are slightly changed, so that we shift the boundary points A, B, C, D accordingly and calculate eigenvalues again. Tab.(2.3) shows that the eigenvalue associated with the path (cross cut CD) is drastically changed even if N is changed only by 0.1. We only find one real and negative eigenvalue. The rest eigenvalues may be complex. Tab.(2.2) and Tab.(2.3) imply that the

path which crosses the cut on the positive-imaginary axis must give the same eigenvalue as those paths without crossing it, only if N is an integer. The reason why the eigenvalue is drastically changed for fractional N along the path is discussed in Sec.(3.4.7.5).

Figure 2.25: *Six distinct contour paths we follow for* $N = 2.9$

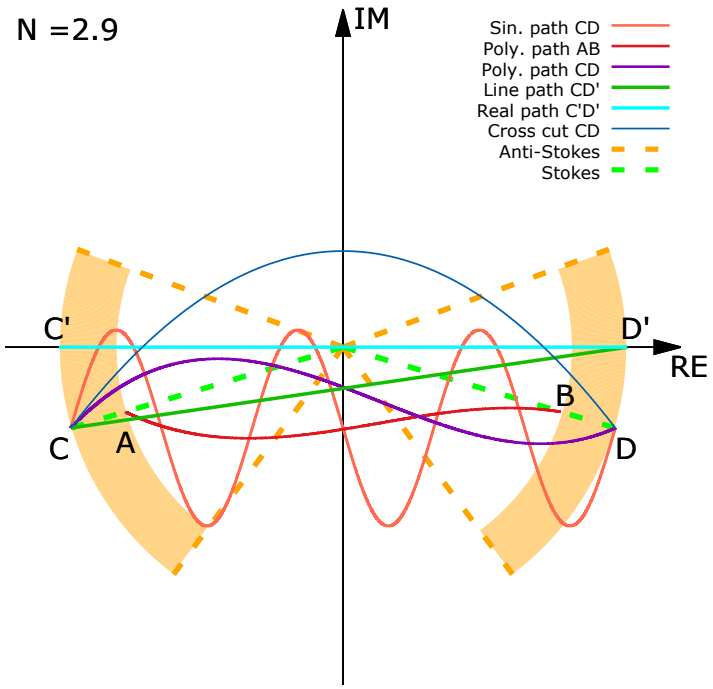

Table 2.3: *Eigenvalues of the* 0*th and* 2*nd level from six distinct paths for* $N = 2.9$

	Re(E)	Im(E)	Residue
Ploy. AB	1.131396959784506	0.5777489913638163E-13	0.8569487352765512E-14
Poly. CD	1.131396959777214	0.8957303021505091E-22	0.9308100275667645E-14
Sin CD	1.131396959777214	-0.8447986496680406E-20	0.4154156286659572E-13
Real path	1.131396959777217	-0.9406628029377684E-16	0.5091289899541294E-14
Line CD'	Unknown	Unknown	Unknown
Cross cut CD	-0.1948727126451554	-0.4623434058293826E-22	0.2252527395492111E-13
Ploy. AB	7.227036694681535	0.3149672198986876E-11	0.1429208479853561E-14
Poly. CD	7.227036699223195	0.5786131273235737E-19	0.9719366946079896E-14
Sin CD	7.227036699223195	-0.1490158943940993E-18	0.3886710658215337E-13
Real path	7.227036699222438	0.2781860593649764E-13	0.7206282171398339E-14
Line CD'	Unknown	Unknown	Unknown
Cross cut CD	Unknown	Unknown	Unknown

2.3.2.4 Summarize what we know so far

1. For the potential $-(ix)^N$ with $N > 1$, one necessary condition to have real-positive eigenvalue is that the two boundary points for any path must be symmetric with respect to the imaginary axis of x.

2. If none of paths crosses the cut, and suppose that one path has boundary points A and B symmetric with respect to the imaginary axis, whereas the other path has boundary points C and D symmetric with respect to the imaginary axis, and A, B, C, D all lie within the same pair of Stokes wedges, then eigenvalues for these two paths must be the same even if $A \neq C$ and $B \neq D$. However, their eigenfunctions may be different.

3. Suppose that two paths have the same boundary points A and B symmetric with respect to the imaginary axis, one path crosses the cut on the positive-imaginary axis and the other does not, and A, B lie within a pair of Stokes wedges, then their eigenvalues and eigenfunctions must be all independent from the shape of path if N is an integer; and dependent if N is an non-integer.

4. Suppose that two paths have the same boundary points A and B symmetric with respect to the imaginary axis, none of the paths crosses the cut on the positive-imaginary axis, and A, B lie within a pair of Stokes wedges, then their eigenvalues and eigenfunctions must be all independent from the shape of path.

2.3.3 Comparison between two pairs of PT-symmetric wedges

Figure 2.26: *Two distinct contour paths we follow for* $N = 5$

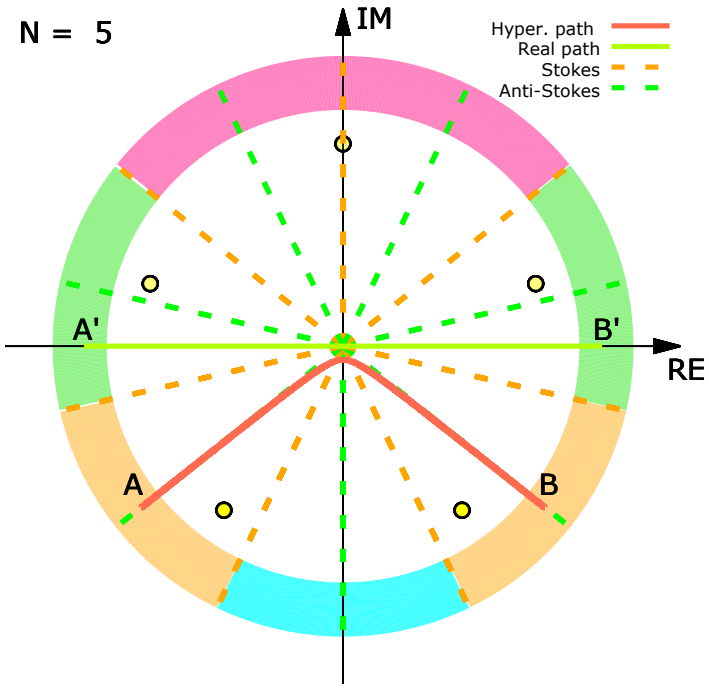

A typical question is what if we follow a path whose boundary points are outside of the chosen (orange) wedges. Can we find any real eigenvalue? The answer is yes. As shown on Tab.(2.4), we have one family of real spectrum by following the hyperbola path within the orange wedges and another family of real spectrum by the real path within the green wedges on Fig.(2.26), and the ratios between the two families approach to a constant as the energy level increases. Here, we want to emphasize that based on our numerical test, integrating along path starting from an orange wedge and ending in a green wedge will not obtain any real eigenvalue. This strengthens our claim that the two complex infinities must be symmetric with respect to imaginary axis in order to have real eigenvalue.

Table 2.4: *Eigenvalues E from the two distinct paths for $N = 5$*

	Re(E)	Im(E)	Residue
Hyper. path	1.908264578170778	-0.1280852237254063E-29	0.2539743864912583E-15
Real path	1.164770407943415	-0.8118987372709177E-21	0.4528149482897403E-14
Hyper. path	8.587220836207222	-0.1377335521357117E-29	0.7836293195505335E-15
Real path	4.363784367712109	-0.1808147123828949E-19	0.4415401140561282E-13
Hyper. path	17.71080901173115	-0.4585871458868370E-28	0.4832720245229763E-14
Real Path	8.955166998240672	-0.2144296494147817E-18	0.9918986297875471E-13
Hyper. path	28.59510331173597	0.4326400861354853E-27	0.5138431564845830E-13
Real path	14.41775483027413	-0.1782545184561158E-17	0.2579378482133023E-13
Hyper. path	40.91889089052085	-0.9188980351779116E-26	0.1003605863909237E-13
Real path	20.61013751004891	-0.1197910951175074E-16	0.4827237348929240E-14

Table 2.5: *Ratios of eigenvalues (*Im (E) *ignored) from the two distinct paths for $N = 5$*

	Re(E)	Ratio
Hyper. path	1.908264578170778	1.638318217184208
Real path	1.164770407943415	
Hyper. path	8.587220836207222	1.967838030619607
Real path	4.363784367712109	
Hyper. path	17.71080901173115	1.977719568513977
Real path	8.955166998240672	
Hyper. path	28.59510331173597	1.983325673682043
Real path	14.41775483027413	
Hyper. path	40.91889089052085	1.985376898653392
Real path	20.61013751004891	

From (3.17) in the next chapter, we used conventional WKB method and derived the following asymptotic relation[56]

$$\frac{E_n(\gamma_2)}{E_n(\gamma_1)} \sim \left[\frac{\cos(\gamma_1)}{\cos(\gamma_2)}\right]^{\frac{2N}{N+2}} \qquad \text{for } n \to \infty \tag{2.79}$$

where γ_1 and γ_2 are the phase angles associated with two turning points respectively on the green and orange wedge on the right side of the imaginary axis of x (see Fig.(2.26)). These two turning points and the other two associated with β_1 and β_2 defined by (3.2) form two symmetric pairs.

When $N = 5$, by (3.1) the right turning point on the green wedge has the phase angle γ_1

$$\gamma_1 = \left(\frac{2-N}{2N} + \frac{2j}{N}\right)\pi = \left(\frac{-3}{10} + \frac{4j}{10}\right)\pi = \frac{1}{10}\pi \tag{2.80}$$

where by observing Fig.(2.26) we set $j = 1$. The right turning point on the orange wedge has the phase angle γ_2

$$\gamma_2 = \left(\frac{2-N}{2N} + \frac{2j}{N}\right)\pi = \left(\frac{-3}{10} + \frac{4j}{10}\right)\pi = \frac{-3}{10}\pi \tag{2.81}$$

where by observing Fig.(2.26) we set $j = 0$. Hence,

$$\left[\frac{\cos(\gamma_1)}{\cos(\gamma_2)}\right]^{\frac{2N}{N+2}} = \left[\frac{\cos\left(\frac{1}{10}\pi\right)}{\cos\left(-\frac{3}{10}\pi\right)}\right]^{\frac{10}{7}} = 1.988629015490531 \tag{2.82}$$

Therefore, our numerical results from Tab.(2.5) agrees with the WKB approximation as the energy level n increases.

So the conclusion[56] is that there exists more than one family of real spectra if N is large enough, and, as energy level increases, one family of real spectrum over the other family maybe approaches to a constant ratio, which sometimes can be predicted by the WKB approximation. For integer N, how many families of real spectra there are depends on how many pairs of symmetric turning points there are or how many pairs of symmetric but non-contacting wedges there are. We will discuss more in Sec.(2.3.4) about the families of real spectra.

2.3.4 Eigenvalue E versus N

Figure 2.27: *Energy spectrum of the* 1*st family from the pair of the orange wedges (The grey curves are WKB approximation)*

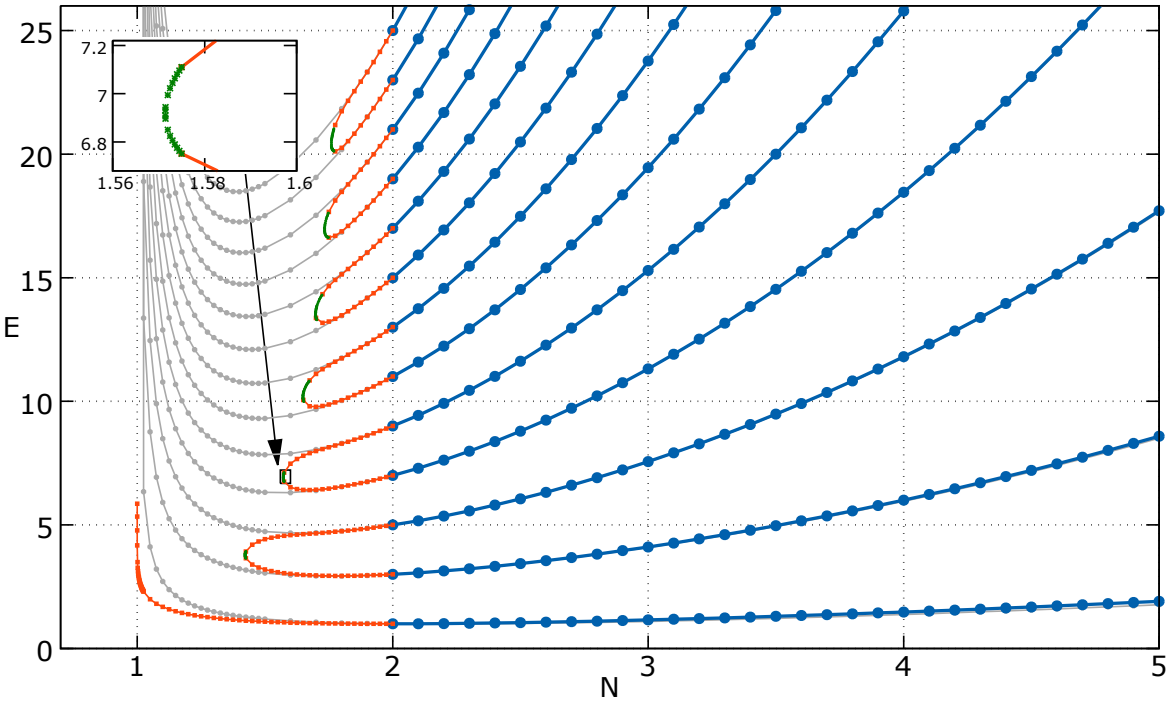

Fig.(2.27) shows the relation between E and N after applied the boundary condition within the orange wedges defined by Fig.(2.2). The grey curves are obtained by WKB approximation from (3.20). The other colored curves are numerical results, which are displayed in blue for $N \geq 2$, in orange for $N < 2$, and in green whenever N is near to a location of degeneracy.

The leading-order WKB method is a very good approximation, since on the most part of Fig.(2.27) those grey curves are covered by the blue and orange curves so that we barely see them. However, whenever N is approaching a location of degeneracy, the WKB approximation is no longer reliable. The WKB also fails when N approaches to 1, where only the ground state has real eigenvalue. When $N = 1$ exactly, we did not find any real eigenvalue, including the ground level. We will talk more about the WKB approximation later.

How do we generate those eigenvalue curves on Fig.(2.27)? When $N < 2$, the orange wedges shift above the real axis; when $N > 2$, the orange wedges shift below the real axis. Based on this fact, in our code we set when $N \leq 1.6$, we follow the parametric path defined by (2.68); when $1.6 < N < 3.0$, we follow the real axis; when $N \geq 3.0$, the hyperbolic path is followed. To obtain Fig.(2.27), we start with the harmonic oscillator ($N = 2$), increase N by 0.1 and use the previously found eigenvalue as a guess to search for he new eigenvalue. By repeating this process until $N = 5$, we obtain the blue part of Fig.(2.27). Due to the degeneracies of energy occur in the region where $N < 2$, we become more careful so as to decrease N by just 0.025 rather than by 0.1. We start with the harmonic oscillator ($N = 2$) and use the previously found eigenvalue as a guess as well. When we approach to locations of degeneracies, we decrease N by even lesser amount of value (for example, 0.0001) so that more data points (the green points) are generated. On Fig.(2.27) the magnified region where the degeneracy occurs clearly shows the locations of the green points, two of which are very close to the actual value of the degenerated eigenvalue. We summarize all green points nearest to the corresponding degenerated eigenvalues on the following Tab.(2.6).

Table 2.6: *Locations of the green data points (two nearest to the degenerated eigenvalues)*

	N	$\mathrm{Re}(E)$
Level 1	1.42210	3.798097503566341
	1.42210	3.769947569720313
Level 2	1.57145	6.931062951894809
	1.57145	6.909904226441585
Level 3	1.64860	10.19710564838468
	1.64860	10.16647647154904
Level 4	1.69810	13.56278552311201
	1.69810	13.50221738682984
Level 5	1.73330	16.98347623074032
	1.73330	16.91803839426446
Level 6	1.76000	20.46649448240978
	1.76000	20.37974449784742

By the same way, on Fig.(2.28) we obtain the 2nd family of eigenvalues from the green wedges defined by Fig.(2.1). The most interesting discovery is that when N is around 4 and E is about 20, the eigenvalue curve starts to go in vertical direction with horizontal oscillation, whose amplitude is decreasing as E increases. When this curve oscillates to the left so that $N < 4$, we use red color to plot the curve; when oscillates to the right so that $N > 4$, we use green color. When E is around 20, the curve is in red color and inbetween $3.97 < N < 4$; when E is above 90, the curve is confined within $3.99999999998 < N < 4$, which is on the top of the figure the red part of the curve, whose oscillation is too small and can be almost ignored. We guess that as E further increases, the oscillation eventually breaks the limit so that no device is able to detect such tiny oscillation, which generates an illusion that the energy spectrum at $N = 4$ is continuous for high level (similar to the classical regime), rather than quantized. However, theoretically, when N is exactly equal to 4, no matter how high the energy E is, the eigenvalues are still quantized and discrete points whose locations distinguish the red and green part of the eigenvalue curve.

Since this eigenvalue curve has infinite number of degeneracies so we name it as a "**Curve with Infinite Number of Degeneracies**" or "**CIND**". Within the pair of the green wedges, how many CINDs are there? Here is our conjecture without solid proof. Numerical result shows that when E is above 180, the eigenvalue curve for $N = 5$ becomes another CIND. However, we did not find such trend for the eigenvalue curve when $N = 6$, possibly because the entire region where $N \geq 6$ has unbroken PT-symmetry. The broken PT-symmetry

happen within the three regions where $5 < N < 6$, $4 < N < 5$ and $3 < N < 4$. We observe that because of the existence of CINDs, PT-symmetry is never broken when $N > 3$ and N is an integer. So we conclude that CIND only exists when N is an integer, and there are two CINDs associated with the pair of the green wedges.

Figure 2.28: *Energy spectrum of the 2nd family from the pair of the green wedges (The grey curves are WKB approximation)*

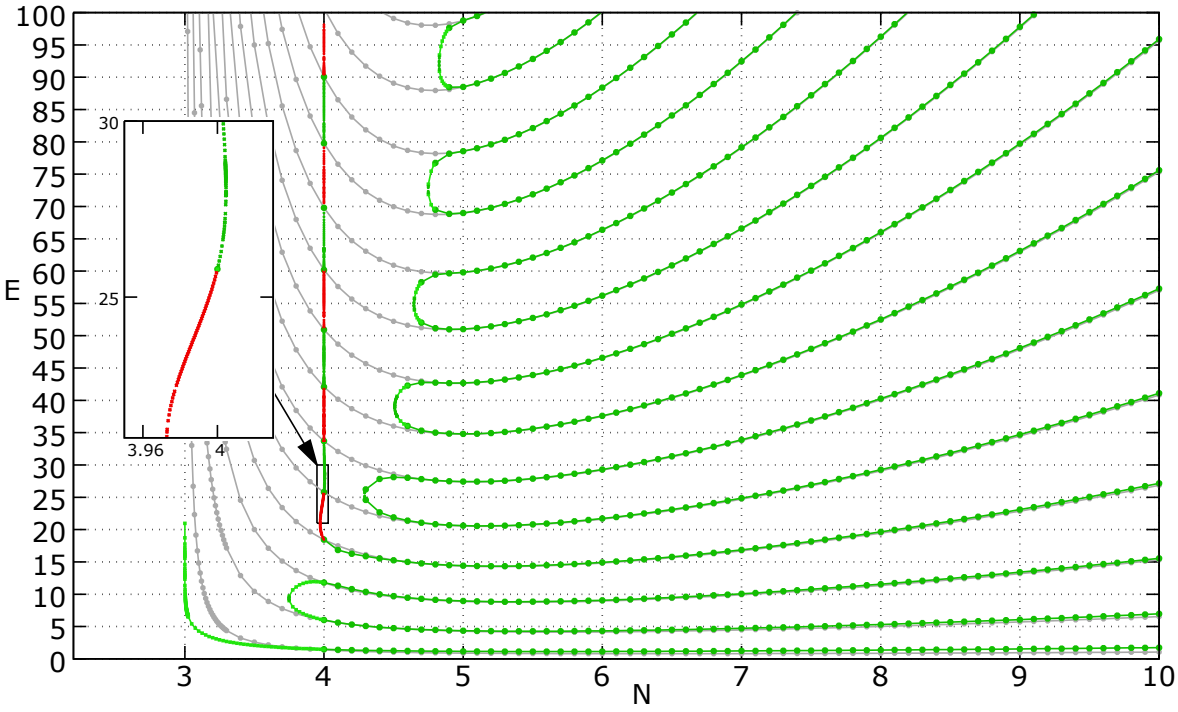

Before going further, we introduce the concept of open mouth. Most eigenvalue curves have a standard shape similar to Fig.(2.29), where we call the empty region between two adjacent and connected levels as an "open mouth". The head of an open mouth is the location of the degeneracy. As N increases, only two cases are observed: one is that the open mouth tilts upward for increasing N, and the other one is shown on Fig.(2.29) in which the open mouth initially tilts downward but eventually tilts upward if N is large enough. Particularly, for the green wedges N has to be around or larger than 6 for that part of the open mouth tilts upward. If the head of the open mouth is located far less than $N = 6$, then the tendency to initially tilt downward is more pronounced. This is especially obvious for those low-lying states as shown on Fig.(2.29) where the head of the open mouth is located at the region where $N < 4$ and far less than 6.

Why does the vertically straight line around $N = 6$ differentiate the behavior of the open mouth? This is because the location of the PT-symmetric wedges governs the behavior of the open mouth. Fig.(3.10) shows that the two turning points x_2 and x_5 within the green wedges are joined by an anti-Stokes line segment, which is right on the real axis and by its definition implies that the integral $\int_{x_2}^{x_5} dx \sqrt{E - V(x)}$ is real. When $N < 6$, Fig.(2.1) shows that the

pair of the two green wedges moves above the real axis so that the anti-Stokes line segment is no longer on the real axis but crosses the cut on the positive-imaginary axis. Except for integer N, the PT-symmetry is broken when $N < 6$ for the green wedges, and this movement may cause the open mouth to tilt downward. When $N > 6$, Fig.(2.1) shows that the pair of the green wedges moves below the real axis and towards the negative-imaginary axis. Consequently, the open mouth tilts upward for $N > 6$. In summary, whether the anti-Stokes line segment joining the two PT-symmetric wedges is above, below or on the real axis determines which direction the open mouth tilts in. This also implies that the open mouths of eigenvalue curves from the pink wedges (See Fig.(2.30)) will eventually tilt upward as $N > 10$.

Figure 2.29: *A single eigenvalue curve from the pair of the green wedges*

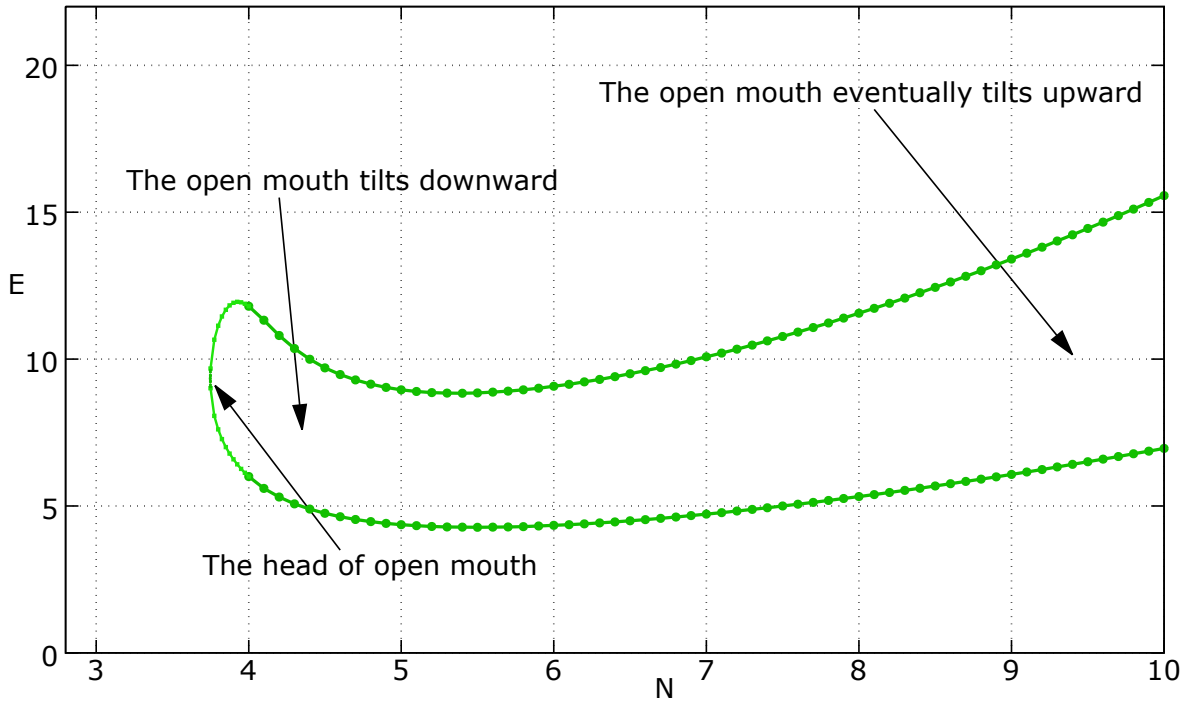

Figure 2.30: *Energy spectrum of the 3rd family from the pair of the pink wedges (The grey curves are WKB approximation)*

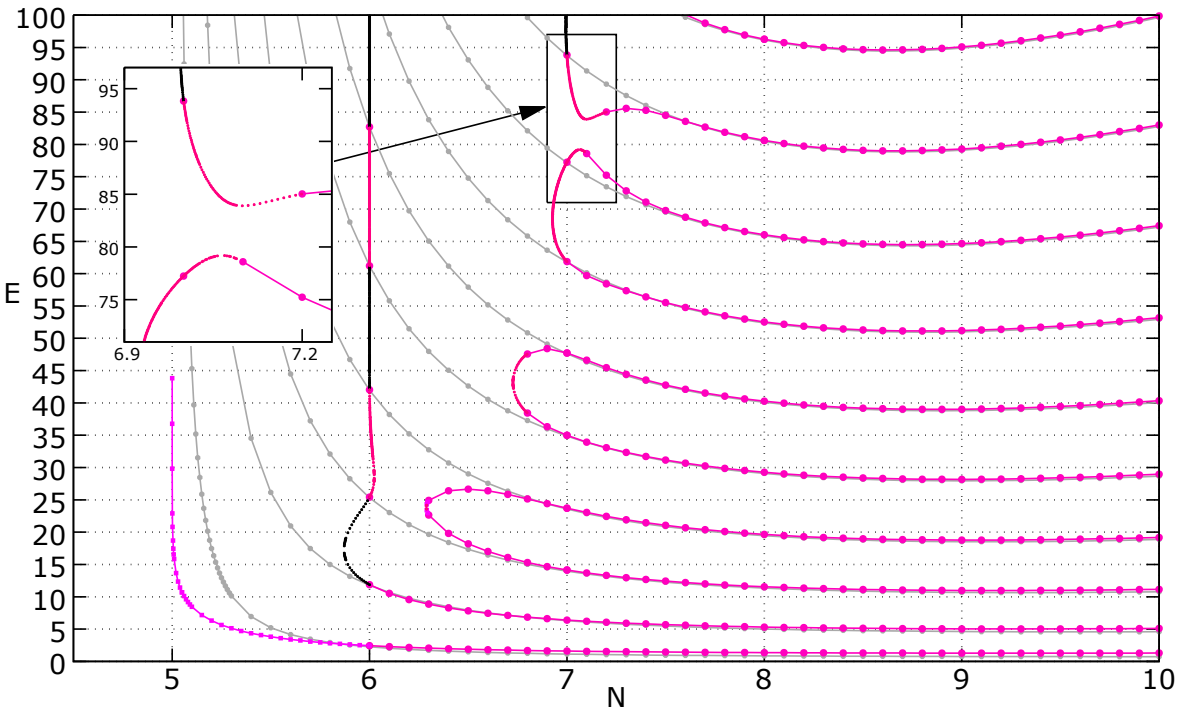

On Fig.(2.30) we plot the 3rd family of eigenvalues for the pair of the pink wedges defined by Fig.(2.1). There are four CINDs, where CINDs for $N = 8$ and $N = 9$ happen in much higher level. The region where $N \geq 10$ has unbroken PT-symmetry, whereas broken PT-symmetry happens within the region $N < 10$ except for integer N. As the previous case of the 2nd family, the amplitude of horizontal oscillation for CIND decreases as E increases. Taking the CIND for $N = 6$ as an example, the part of the CIND where $N < 6$ is plotted in black color and $N > 6$ in pink color. Within the region around $E = 15$ and $N = 6$, the black part of the CIND is confined within $5.87 < N < 6$; whereas for the region where $E > 90$, the CIND (in black color again) is within $5.9999998 < N < 6$.

On Fig.(2.30), we magnify the most interesting region, where two levels fail to connect and form a degeneracy around $E = 80$ because they are too close to the integer $N = 7$, where PT-symmetry is never broken. Consequently, the curve from the lower level merges with the curve from the even lower level; whereas the curve from the upper level form a CIND for $N = 7$. This kind of behavior is somewhat similar to the cohesion of liquid, where similar or identical particles tend to cling to one another if the distance between them is small enough. For example, two water droplets act like magnets if they are close to each other.

Figure 2.31: *Four energy spectra of the first four families from four pairs of PT-symmetric (orange, green, pink, yellow) wedges*

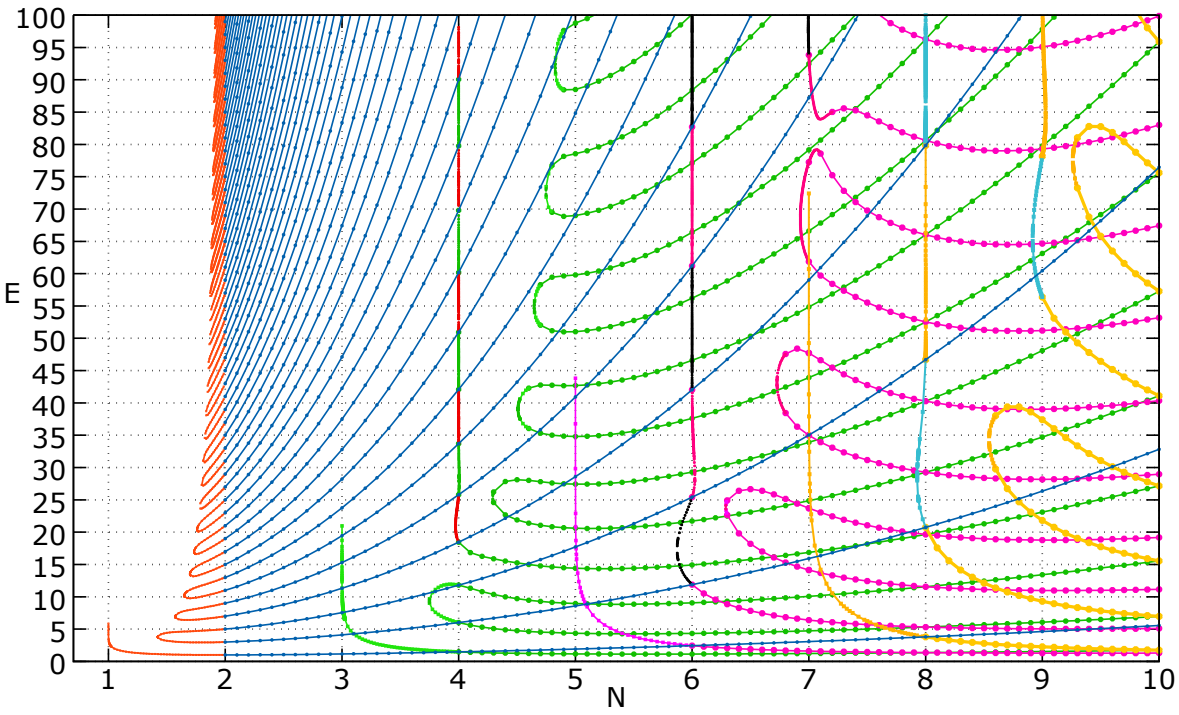

By including real eigenvalues from the four PT-symmetric wedges (the orange, green, pink and yellow wedges), we plot the first four families of energy spectra altogether shown on Fig.(2.31). An interesting feature is immediately spotted. All open mouths from the 1st family from the orange wedges tilt upward, while the open mouths from the 3rd family from the pink wedges tilt downward, and the 4th family tilts downward even more. This is because that all heads of open mouths from the 1st family including the low-lying states are quite near to the vertically straight line $N = 2$ where differentiates the regions with broken and unbroken PT-symmetry for the 1st family, while heads of open mouths from the 4th family are quite far away from $N = 14$ which differentiates the regions with broken and unbroken PT-symmetry for the 4th family.

Now let's talk about another interesting feature. At exactly $N = 4$, the eigenvalues from the 1st and 2nd family are equal, which means that rather than two families, there is only one family of eigenvalues at $N = 4$. Similarly, at exactly $N = 6$, the eigenvalues from the 1st and 3rd family are equal, which means that rather than three families, there are only two families of eigenvalues at $N = 6$. The most interesting part is at exactly $N = 8$ that not only the eigenvalues from the 1st and 4th family are equal, but the 2nd and 3rd family are also equal, which means that rather than four families, there are only two families of eigenvalues at $N = 8$. Do we expect this feature? Yes, because of symmetry. When $N = 4$, Fig.(2.1) shows that orange and green wedges are symmetric with respect to the real axis. When $N = 6$, the orange and pink wedges are symmetric with respect to the real axis while the pair of green wedges lies right on the real axis. When $N = 8$, not only the orange and yellow wedges but also the green and pink wedges are symmetric with respect to the real axis.

This symmetry reduces the number of families of eigenvalues at even N except when $N = 2$. The moment when N is an odd integer, a new PT-symmetric wedges are born from the positive-imaginary axis and consequently, a new family of spectrum is born.

2.3.4.1 Conclusion

Due to the existence of multiple PT-symmetric Stokes wedges if N is large enough, in this Subsec.(2.3.4), we have plotted and discussed the first four families of real energy spectrum associated with the Hamiltonian $\mathcal{H} = p^2 - (ix)^N$. Since this work is original and no previous study has ever shown this result before, we are eager to compare our result to any future study.

Chapter 3

WKB Approximation

3.1 Introduction of the current chapter

This chapter is organized in the following way. In Sec.(3.2), we derive the result for the leading order WKB approximation. In Sec.(3.3), some subtle aspects of analytic continuation are discussed based on the primary work by Bender and Turbiner[30]. Complex WKB method or phase integral method is introduced and discussed in Sec.(3.4).

3.2 The leading order conventional WKB approximation

This section contains some works from papers[56] and [10].

Now we find turning points by equating E and the potential from (2.1)

$$\begin{aligned} E &= -(ix)^N \\ \implies x &= (-E)^{1/N} e^{-i\left(\frac{\pi}{2}\right)} \\ \implies x &= E^{1/N} e^{i\left(\frac{\pi}{N}-\frac{\pi}{2}\right)} e^{i\frac{2j\pi}{N}} \\ \implies x &= E^{1/N} e^{i\left(\frac{2-N}{2N}+\frac{2j}{N}\right)\pi} \qquad \text{for } j = 0, \pm 1, \pm 2 \cdots \end{aligned} \tag{3.1}$$

Note that the expression from (3.1) may overestimate the total number of principal turning points, because it takes account of turning points from all branches. For example, (3.1) suggests 7 turning points for $N = 3.5$, however, only 4 turning points on the principal branch (See Fig.(3.11)).

Let's write the turning points $\{x_i\}$ from principal branch in terms of $x_\pm$ such that

$$x_- = E^{1/N} e^{i\beta} \tag{3.2}$$

$$x_+ = E^{1/N} e^{i\gamma} \tag{3.3}$$

where $\beta \neq \gamma$ due to different values from j. By the leading order WKB approx-

imation,

$$\int_{x_-}^{x_+} dx\sqrt{E-V\left(x\right)}=\left(n+\frac{1}{2}\right)\pi \tag{3.4}$$

We deform the contour path into integration with ray path from x_+ to 0 and from 0 to x_-, and obtain

$$\left(n+\frac{1}{2}\right)\pi=\int_{x_-}^{x_+} dx\sqrt{E+(ix)^N}=\int_0^{E^{1/N}e^{i\gamma}} dx\sqrt{E+(ix)^N}+\int_{E^{1/N}e^{i\beta}}^{0} dx\sqrt{E+(ix)^N} \tag{3.5}$$

By using the substitution $y=\frac{ix}{iE^{1/N}e^{i\gamma}}$ and $w=\frac{ix}{iE^{1/N}e^{i\beta}}$, the two complex contour integrations become two real integrations along real axis

$$\left(n+\frac{1}{2}\right)\pi=\int_0^1\left[E+\left(iE^{1/N}e^{i\gamma}y\right)^N\right]^{\frac{1}{2}}E^{1/N}e^{i\gamma}dy+\int_1^0\left[E+\left(iE^{1/N}e^{i\beta}w\right)^N\right]^{\frac{1}{2}}E^{1/N}e^{i\beta}dw \tag{3.6}$$

Since y and w are dummy variables, we obtain

$$\left(n+\frac{1}{2}\right)\pi=\int_0^1\left[E+\left(iE^{1/N}e^{i\gamma}y\right)^N\right]^{\frac{1}{2}}E^{1/N}e^{i\gamma}dy-\int_0^1\left[E+\left(iE^{1/N}e^{i\beta}y\right)^N\right]^{\frac{1}{2}}E^{1/N}e^{i\beta}dy \tag{3.7}$$

Note that from (3.1)

$$\begin{aligned}\left(ie^{i\gamma}\right)^N&=\left[ie^{i\left(\frac{2-N}{2N}+\frac{2j_1}{N}\right)\pi}\right]^N\\&=e^{i\frac{\pi N}{2}}e^{i\left(\frac{2-N}{2N}+\frac{2j_1}{N}\right)\pi}\\&=e^{i(\pi+2\pi j_1)}\\&=-1\\&=\left(ie^{i\beta}\right)^N\end{aligned} \tag{3.8}$$

Hence

$$\begin{aligned}\left(n+\frac{1}{2}\right)\pi&=\int_0^1 E^{\frac{1}{2}}\left(1-y^N\right)^{\frac{1}{2}}E^{1/N}e^{i\gamma}dy-\int_0^1 E^{\frac{1}{2}}\left(1-y^N\right)^{\frac{1}{2}}E^{1/N}e^{i\beta}dy\\&=E^{\frac{N+2}{2N}}\left(e^{i\gamma}-e^{i\beta}\right)\int_0^1\sqrt{1-y^N}dy\end{aligned} \tag{3.9}$$

which yields

$$E^{\frac{N+2}{2N}}=\frac{\left(n+\frac{1}{2}\right)\pi}{\left(e^{i\gamma}-e^{i\beta}\right)\int_0^1\sqrt{1-y^N}dy} \tag{3.10}$$

Since $\int_0^1 \sqrt{1-y^N}dy$ yields real value for $y \in \mathbb{C}$, $E^{\frac{N+2}{2N}}$ can be real if

$$\text{Im}\left(e^{i\gamma} - e^{i\beta}\right) = 0 \tag{3.11}$$

So

$$\begin{aligned}\text{Im}\left[\left(\cos\gamma - \cos\beta\right) + i\left(\sin\gamma - \sin\beta\right)\right] &= 0 \\ \implies \sin\gamma - \sin\beta &= 0\end{aligned}$$

which implies that

$$\beta = \pi - \gamma \tag{3.12}$$

Substituting (3.12) into (3.2) and (3.3) gives

$$x_- = E^{1/N} e^{i(\pi-\gamma)} \tag{3.13}$$

$$x_+ = E^{1/N} e^{i\gamma} \tag{3.14}$$

Therefore the turning points x_- and x_+ must be symmetrical with respect to the imaginary axis to have real eigenvalue E. By using (3.12) and

$$\int_0^1 \sqrt{1-y^N}dy = \frac{\sqrt{\pi}\Gamma\left(1+\frac{1}{N}\right)}{2\Gamma\left(\frac{3}{2}+\frac{1}{N}\right)} \qquad \text{for } \text{Re}\left(N\right) > 0 \tag{3.15}$$

we obtain the leading order approximation for the eigenvalue E_n

$$E_n \sim \left[\frac{\left(n+\frac{1}{2}\right)\sqrt{\pi}\Gamma\left(\frac{3}{2}+\frac{1}{N}\right)}{\cos\gamma\Gamma\left(1+\frac{1}{N}\right)}\right]^{\frac{2N}{N+2}} \qquad \text{for } n \to \infty \tag{3.16}$$

Suppose that we have two families of real spectra generated from different Stokes wedges, then these two families of real spectra must be associated with different pairs of turning points. Assume that one pair of turning points is associated with γ_1 and the other is associated with γ_2, then by (3.16) we have[56]

$$\frac{E_n\left(\gamma_2\right)}{E_n\left(\gamma_1\right)} \sim \left[\frac{\cos\left(\gamma_1\right)}{\cos\left(\gamma_2\right)}\right]^{\frac{2N}{N+2}} \qquad \text{for } n \to \infty \tag{3.17}$$

So if we find two families of real spectra, then their values must approximately obey the relationship (3.17). We have already numerically verified this for $N = 5$ on Tab.(2.5).

If we choose the pair of turning points within the orange wedges shown on Fig.(2.2), then

$$x_- = E^{1/N} e^{i\pi\left(\frac{3}{2}-\frac{1}{N}\right)} \qquad x_+ = E^{1/N} e^{i\pi\left(\frac{1}{N}-\frac{1}{2}\right)} \tag{3.18}$$

with $\beta = \left(\frac{3}{2}-\frac{1}{N}\right)\pi$ and $\gamma = \left(\frac{1}{N}-\frac{1}{2}\right)\pi$ such that

$$e^{i\gamma} - e^{i\beta} = 2\sin\frac{\pi}{N} \tag{3.19}$$

and therefore

$$E_n \sim \left[\frac{\left(n+\frac{1}{2}\right)\sqrt{\pi}\Gamma\left(\frac{3}{2}+\frac{1}{N}\right)}{\sin\left(\frac{\pi}{N}\right)\Gamma\left(1+\frac{1}{N}\right)}\right]^{\frac{2N}{N+2}} \qquad \text{for } n\to\infty \tag{3.20}$$

By observing Fig.(2.27), Fig.(2.28) and Fig.(2.30), the leading order WKB from (3.16) is a pretty good approximation in those regions with unbroken PT-symmetry, including integer N associated with CIND. In those regions with broken PT-symmetry, WKB is still good approximation if the eigenvalue curves are not near to the degeneracies and the ground-level-region of integer N, which does not associate with CIND but the pair of wedges is born at.

In summary, the WKB approximation may fail wherever the PT-symmetry is broken. The reason why it fails can be subtler than the reason provided by the paper[10, p.3], where it says that when $N<2$, the path along which the integral $\int_{x_-}^{x_+} dx\sqrt{E-V(x)}$ is real is in the upper-half x plane so that it crosses the cut on the positive imaginary axis and thus is not a continuous path joining the turning points. This reason is only true if the pair of the orange wedges is chosen. On Fig.(2.26), if we approximate the eigenvalue within the green wedges when $N=5$, Tab.(2.5) and Fig.(2.28) show that the WKB approximation by (3.16) is still pretty good approximation. But Fig.(3.6) shows that the two turning points x_2 and x_4 within the green wedges are joined by an anti-Stokes line segment, which crosses the positive imaginary axis and by its definition implies that the integral $\int_{x_2}^{x_4} dx\sqrt{E-V(x)}$ is real. So the argument provided by the paper[10, p.3] only works for non-integer N. For any integer N associated with a CIND, the PT-symmetry is not really broken for the chosen wedges.

So it follows that the WKB approximation is valid even if N is fractional or irrational as long as $N>2$ if the orange pair of wedges is chosen. Here, we show a paradox for fractional N. By (3.1), (3.2) and (3.3), it looks like

$$\gamma = \left(\frac{2-N}{2N}+\frac{2j_1}{N}\right)\pi \tag{3.21}$$

$$\beta = \left(\frac{2-N}{2N}+\frac{2j_2}{N}\right)\pi \tag{3.22}$$

where j_1 and j_2 are integers and $j_1\neq j_2$ so that $\gamma\neq\beta$. By the condition (3.12), we obtain

$$\beta=\pi-\gamma \Longrightarrow \left(\frac{2-N}{2N}+\frac{2j_2}{N}\right)\pi=\pi-\left(\frac{2-N}{2N}+\frac{2j_1}{N}\right)\pi \tag{3.23}$$

and solving for j_1 and j_2 yields

$$j_1+j_2=N-1 \tag{3.24}$$

When N is fractional, (3.24) no longer holds, since j_1 and j_2 are integers. Therefore, (3.24) suggests that when N is fractional, we may never find any pair of turning points which are symmetric with respect to the imaginary axis, and

consequently Im $\left(e^{i\gamma} - e^{i\beta}\right) \neq 0$, and (3.10) will not yield real eigenvalue. However, as shown Fig.(2.27), real eigenvalues for fractional N are already found. How do we solve this paradox? As we mentioned in the beginning of Sec.(3.2), only turning points from the principal branch should be considered. For fractional N, the number of principal turning points is ceiling (N), which holds to be true even if N is irrational. For example when $N = \pi$ the number of principal turning points is 4. The condition (3.24) is always satisfied if we modify it to be

$$j_1 + j_2 = \text{ceiling}\,(N) - 1 \tag{3.25}$$

The correct way to use WKB to approximate the eigenvalue for fractional N is to analytically continue the solution from integer N to non-integer N. This allows us to directly substitute fractional value of N into (3.16) to obtain approximated eigenvalues. So the analytic continuation extends the validity of the conventional WKB approximation on real axis for $N = 2$ into the complex plane for $N > 2$.

3.3 The subtlety of analytic continuation

Analytic continuation is a mathematical and subtle concept. In this section, we will illustrate some subtle aspects based on the paper[30]. All credits in this section go to Bender and Turbiner.

Consider the following eigenvalue problem[30] for $x \in \mathbb{R}$

$$-\frac{d^2\psi(x)}{dx^2} + \frac{1}{4}a^2x^2\psi(x) = E\psi(x) \tag{3.26}$$

with $a > 0$ and the usual boundary condition $\psi(x) \to 0$ as $x \to \pm\infty$. The eigenfunction associated with the ground level is known to be exactly

$$\psi_-(x) = \exp\left(-\frac{1}{4}ax^2\right) \qquad E_0 = \frac{1}{2}a \tag{3.27}$$

Now, what happens if the parameter a from (3.26) is replaced by $-a$? Well, apparently, the eigenvalue problem from (3.26) remains the same since $a^2 = (-a)^2$, however, the solution is changed - it is an entirely new eigenvalue problem!

$$-\frac{d^2\psi(x)}{dx^2} + \frac{1}{4}(-a)^2x^2\psi(x) = E\psi(x) \tag{3.28}$$

has solution for ground state

$$\psi_+(x) = \exp\left(\frac{1}{4}ax^2\right) \qquad E_0 = -\frac{1}{2}a \tag{3.29}$$

which is a surprise! Replacing a with $-a$ gives the "same" eigenvalue problem, but two different solutions! Why? The simple answer is that the boundary condition has changed.

Before we dig into the detail, let's extend this eigenvalue problem into the **complex** plane of x. In this case, we denote x by z and $z \in \mathbb{C}$. We first look at

the locations of Stokes wedges as $|z| \to \infty$. For (3.26) there are two solutions associated with the ground level.

$$\psi_+(z) = \exp\left(\frac{1}{4}az^2\right) \qquad \psi_-(z) = \exp\left(-\frac{1}{4}az^2\right) \tag{3.30}$$

We let $z = re^{i\theta}$, then by (2.26) we have Stokes lines at

$$\begin{aligned} \operatorname{Im}\left[\frac{1}{4}az^2 - \left(-\frac{1}{4}az^2\right)\right] &= 0 \\ \Longrightarrow \operatorname{Im}\left[\frac{1}{2}ar^2e^{i2\theta}\right] &= 0 \\ \Longrightarrow \sin(2\theta) &= 0 \end{aligned}$$

which gives two solutions for the locations of Stokes lines

$$\theta_+ = \frac{\pi}{2} \qquad \theta_- = 0 \tag{3.31}$$

By (2.32), we have anti-Stokes lines at

$$\begin{aligned} \operatorname{Re}\left[\frac{1}{4}az^2 - \left(-\frac{1}{4}az^2\right)\right] &= 0 \\ \Longrightarrow \operatorname{Re}\left[\frac{1}{2}ar^2e^{i2\theta}\right] &= 0 \\ \Longrightarrow \cos(2\theta) &= 0 \end{aligned}$$

which gives two solutions for the locations of anti-Stokes lines

$$\theta_s = \pm\frac{\pi}{4} \tag{3.32}$$

Thus we have the following Fig.(3.1) to illustrate the asymptotic behaviors of $\psi_\pm(z)$ as $|z| \to \infty$.

Figure 3.1: *[30]The asymptotic behaviors of* $\psi_{\pm}(z)$ *as* $|z| \to \infty$

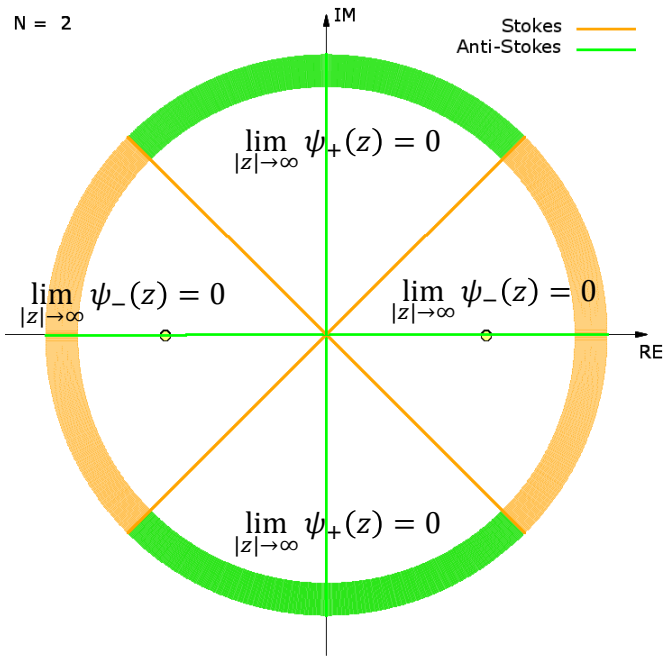

For the original eigenvalue problem from (3.26), we pick up $\psi_{-}(z) = \exp\left(-\frac{1}{4}az^2\right)$ as the solution for it satisfies the boundary condition. Now, let's observe how the analytic continuation on a affects the solution. We let

$$a = \rho e^{i\alpha} = \begin{cases} \rho & \text{when } \alpha = 0 \\ -\rho & \text{when } \alpha = \pi \end{cases} \tag{3.33}$$

When $\alpha = 0$,

$$\arg\left[\psi_{-}(z)\right] = -\frac{1}{4}az^2 = -\frac{1}{4}\rho\left(re^{i\theta}\right)^2 \tag{3.34}$$

When α rotates counter-clockwisely from 0 to π, $\arg\left[\psi_{-}(z)\right] = -\frac{1}{4}az^2$ also rotates. Specifically, when $\alpha = \pi$,

$$\arg\left[\psi_{-}(z)\right] = -\frac{1}{4}\left(\rho e^{i\pi}\right)z^2 = -\frac{1}{4}\rho\left(ze^{i\pi/2}\right)^2 = -\frac{1}{4}\rho\left(re^{i\theta}e^{i\pi/2}\right)^2 \tag{3.35}$$

When $\theta = -\frac{\pi}{2} + \theta'$, we have

$$\arg\left[\psi_{-}(z)\right] = -\frac{1}{4}\rho\left(re^{i\theta'}\right)^2 \tag{3.36}$$

The expressions from (3.34) and (3.36) are the same except that when α rotates counter-clockwisely from 0 to π, the argument of $\psi_{-}(z)$ rotates clockwisely from 0 to $-\frac{\pi}{2}$. Consequently, the orange Stokes wedges rotate clockwisely as shown on Fig.(3.2).

Figure 3.2: *[30]The orange Stokes wedges rotate clockwisely when α rotates counter-clockwisely*

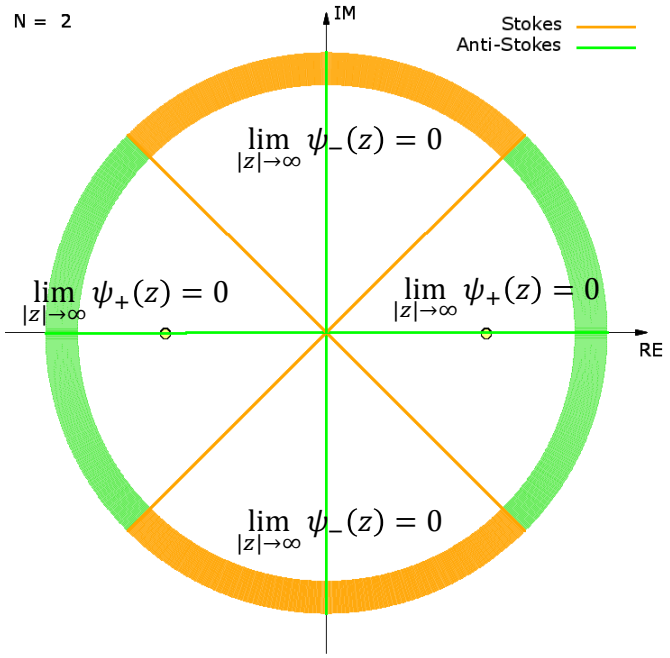

After α rotates to π, the eigenvalue problem has the same equation

$$-\frac{d^2\psi(z)}{dz^2}+\frac{1}{4}(-a)^2 z^2\psi(z)=E\psi(z) \tag{3.37}$$

but with the new boundary condition $\psi(z)\to 0$ as $z\to\pm i\infty$. We can solve this new problem by rotating this problem onto the real axis through transforming the complex value z into real value x by the following substitution

$$z=ix \tag{3.38}$$

where $x\in\mathbb{R}$ so that

$$\begin{aligned}
\implies -\frac{d}{dx}\left[\frac{d\psi(z)}{dx}\frac{dx}{dz}\right]\frac{dx}{dz}-\frac{1}{4}(-a)^2x^2\psi(x)&=E\psi(x)\\
\implies -\frac{d}{dx}\left[\frac{d\psi(x)}{dx}\frac{1}{i}\right]\frac{1}{i}-\frac{1}{4}(-a)^2x^2\psi(x)&=E\psi(x)\\
\implies \frac{d^2\psi(x)}{dx^2}-\frac{1}{4}(-a)^2x^2\psi(x)&=E\psi(x)\\
\implies -\frac{d^2\psi(x)}{dx^2}+\frac{1}{4}(-a)^2x^2\psi(x)&=-E\psi(x)
\end{aligned} \tag{3.39}$$

with boundary condition $\psi(x)\to 0$ as $x\to\pm\infty$. We observe that the eigenvalue problem from (3.39) is the same as the eigenvalue problem from (3.26) except that the sign of E is flipped. So based on the solution (3.27), the solution for this eigenvalue problem is

$$\psi_-(x)=\exp\left(-\frac{1}{4}ax^2\right)\qquad E_0=-\frac{1}{2}a \tag{3.40}$$

which is the same as the solution (3.27) but with the negative eigenvalue.

- Replacing a with $-a$ gives the eigenvalue problem $-\frac{d^2\psi(x)}{dx^2}+\frac{1}{4}\left(-a\right)^2 x^2\psi\left(x\right)=E\psi\left(x\right)$ with boundary condition $\psi\left(x\right)\to 0$ as $x\to\pm\infty$
- Analytic continuation on a from 0 to π gives the eigenvalue problem $-\frac{d^2\psi(x)}{dx^2}+\frac{1}{4}\left(-a\right)^2 x^2\psi\left(x\right)=-E\psi\left(x\right)$ with boundary condition $\psi\left(x\right)\to 0$ as $x\to\pm\infty$.

If comparing the solutions from (3.29) and (3.40), we realize that replacing a with $-a$ is not the same as the analytic continuation where we let a rotates from 0 to π. Because replacing a with $-a$ is an entirely new and independent eigenvalue problem, in which the solution suddenly changes from $\psi_{-}\left(x\right)=\exp\left(-\frac{1}{4}ax^2\right)$ to $\psi_{+}\left(x\right)=\exp\left(\frac{1}{4}ax^2\right)$, so that the only possible solution lies within the green wedges from Fig.(3.1), and Fig.(3.2) has nothing to do with this eigenvalue problem! Therefore, we can not simply replace a with $-a$ in the eigenvalue problem and expect to have the correct analytic continuation. This demonstrates a subtle point of analytic continuation.

3.4 Phase Integral Method

On a paper[9] by Bender *et al.*, a technique called complex WKB method, also known as phase integral method(PIM), is used to approximate the eigenvalue E for the following PT-symmetric Hamiltonian

$$\mathcal{H}=p^2+x^4+iAx \tag{3.41}$$

whose degeneracies of E are caused by the growing influence from two purely imaginary turning points as the real coefficient A grows larger and larger. The reason they prefer PIM to conventional WKB is because that in general, the conventional WKB approximation only consider two turning points. When more than two turning points are generated[1], PIM may give more accurate results, including degeneracies and low-lying energy levels. Here, we are very curious on what happen if we apply PIM to our potential $V=-\left(ix\right)^N$. So let's see how it works by following their way.

3.4.1 Stokes diagram

This Subsec.(3.4.1) contains the work by White[61].

For the following 1D Schrodinger equation,

$$-\frac{d^2\psi\left(x\right)}{dx^2}+V\left(x\right)\psi\left(x\right)=E\psi\left(x\right) \tag{3.42}$$

the leading order WKB approximation gives two asymptotic solutions as $|x|\to\infty$

$$\psi_{\pm}\left(x\right)\sim\frac{1}{Q\left(x\right)^{1/4}}\exp\left(\pm i\int_{x_0}^{x}\left[Q\left(t\right)\right]^{1/2}dt\right)\qquad\text{where } Q\left(x\right)=E-V\left(x\right) \tag{3.43}$$

[1]When $N\geq 3$ in our case, more than two turning points exist.

where x_0 is a turning point, and x is a complex variable. To be consistent with our previous definition, we define **Stokes line** as the solution of the following equation

$$\mathrm{Re}\left\{\int_{x_0}^{x}\left[Q\left(t\right)\right]^{1/2}dt\right\}=0 \tag{3.44}$$

and **anti-Stokes line** as the solution of the following equation

$$\mathrm{Im}\left\{\int_{x_0}^{x}\left[Q\left(t\right)\right]^{1/2}dt\right\}=0 \tag{3.45}$$

Generally, the integral $\int_{x_0}^{x}\left[Q\left(t\right)\right]^{1/2}dt$ contains imaginary part, so that the solution from (3.43) contains real exponential. If this real exponential is growing, then we say that the solution is dominant; Otherwise we say that the solution is subdominant for decaying exponential.

An **infinitesimal anti-Stokes line**[61, p.75] dx emanated from any non-turning point x_p along $\sqrt{Q\left(x\right)}dx$ which is real can be approximated[2] by solving

$$\sqrt{Q\left(x\right)}dx\approx\sqrt{Q\left(x_p\right)}dx=\pm C \tag{3.46}$$

where C is real. So

$$dx=C\left[Q\left(x_p\right)\right]^{-\frac{1}{2}}e^{i(k\pi)}=\pm C\left[Q\left(x_p\right)\right]^{-\frac{1}{2}}\qquad k=0,1 \tag{3.47}$$

where the sign $\pm$ implies two local anti-Stokes lines emanated from x_p in directions opposite to each other.

We have to be more careful if dx is emanated from any turning point x_0 where $\sqrt{Q\left(x_0\right)}$ is zero or a pole. First we introduce a notion about the order of turning point. A turning point x_0 of $Q\left(x\right)$ is said to be simple or of the first order if it satisfies[41, p.7] $Q\left(x_0\right)=0$ but $\left.\frac{dQ(x)}{dx}\right|_{x=x_0}\neq 0$. It follows that a double turning point x_0 or a turning point x_0 of the second order of $Q\left(x\right)$ satisfies $Q\left(x_0\right)=\left.\frac{dQ(x)}{dx}\right|_{x=x_0}=0$ but $\left.\frac{d^2Q(x)}{dx^2}\right|_{x=x_0}\neq 0$. By using this definition, we can generalize a turning point up to the nth order. For an infinitesimal anti-Stokes line segment $dx=(x-x_0)$ emanated from a simple turning point x_0, we write for the first order approximation $Q\left(x\right)\approx\left.\frac{dQ(x)}{dx}\right|_{x=x_0}(x-x_0)$, and require $\sqrt{Q\left(x\right)}dx$ to be real such that

$$\sqrt{Q\left(x\right)}dx\approx\sqrt{\left.\frac{dQ\left(x\right)}{dx}\right|_{x=x_0}dxdx}=\sqrt{Q'\left(x_0\right)}dx^{\frac{3}{2}}=\pm C \tag{3.48}$$

which yields

$$dx=C\left[Q'\left(x_0\right)\right]^{-\frac{1}{3}}e^{i\left(\frac{2k\pi}{3}\right)}\qquad k=0,1,2 \tag{3.49}$$

[2]Here, we assume that $\sqrt{Q\left(x_p\right)}$ is finite, non-zero and well-behaved.

which implies three anti-Stokes lines emanated from the simple turning point x_0. For an infinitesimal anti-Stokes line segment $dx = (x - x_0)^2$ emanated from a double turning point x_0, we write for the first order approximation $Q(x) \approx Q'(x_0)(x - x_0)$ such that

$$\sqrt{Q(x)}dx \approx \sqrt{Q'(x_0)\, dx^{\frac{1}{2}}}dx = \sqrt{Q'(x_0)}dx^{\frac{5}{4}} = \pm C \tag{3.50}$$

which yields

$$dx = C\left[Q'(x_0)\right]^{-\frac{2}{5}} e^{i\left(\frac{4k\pi}{5}\right)} \qquad k = 0, 1, 2, 3 \tag{3.51}$$

So four anti-Stokes lines are emanated from the double turning point x_0. Similarly, for an infinitesimal anti-Stokes line segment $dx = (x - x_0)^{-1}$ emanated from a simple pole x_0, we have

$$\sqrt{Q(x)}dx \approx \sqrt{Q'(x_0)\, dx^{-1}}dx = \sqrt{Q'(x_0)}dx^{\frac{1}{2}} = \pm C \tag{3.52}$$

which yields

$$dx = C\left[Q'(x_0)\right]^{-1} e^{i(2k\pi)} = C\left[Q'(x_0)\right]^{-1} \tag{3.53}$$

which only has one anti-Stokes line emanated from the simple pole x_0. We can set $C = 1$ for convenience.

Stokes lines can be approximated by the similar way. Armed with these tools, for

$$Q(x) = E + (ix)^N \tag{3.54}$$

Fig.(3.3), Fig.(3.4), Fig.(3.5), etc. are generated and called Stokes diagram, where the anti-Stokes lines are generated by (3.49) and the anti-Stokes flows by (3.47) so that anti-Stokes lines always go in the same direction of the anti-Stokes flows whereas Stokes lines are always perpendicular to the anti-Stokes flows.

3.4.2 Connection formula

Similar to Feynman's rules, PIM has rules[58, 61], also known as **connection formulas**:

1. By analytically continuing local WKB solutions, when cross an anti-Stokes line, the solutions exchange dominance, so that a dominant solution becomes subdominant, and vice versa.

2. When cross a Stokes line, the coefficient of the dominant term remains unchanged. However, the coefficient of the subdominant solution is changed by an amount proportional to the coefficient of the dominant term, that is,

   $$\text{new sub. coefficient} = \text{old sub. coefficient} + T \times \text{old dom. coefficient} \tag{3.55}$$

   where T is called a Stokes multiplier whose value depends on the nature of the turning point where the Stokes line originates. In the counterclockwise direction, for a Stokes line emanated from a simple turning

point the value of the Stokes multiplier $T \approx i$ for the first order approximation; For a Stokes line from a double zero, $T \approx \sqrt{2}i$ for the first order approximation; For a Stokes line from a turning point of the nth order, then[61, p.83] $T \approx 2i\cos\left(\frac{\pi}{2+n}\right)$ for the first order approximation. For clockwisely[61, p.78] crossing the Stokes line emanated from a turning point of order n, $T \approx -2i\cos\left(\frac{\pi}{2+n}\right)$ for the first order approximation,

3. The rules given in 1. and 2. refer to a WKB solution defined in terms of a particular turning point when cross a Stokes/anti-Stokes line emanated from that turning point. If it is intended to continue a solution across a line emanated from a different turning point, the WKB solution must first be rewritten in terms of this new zero. To connect solutions defined in terms of different turning points, say x_1 and x_2, use

$$\exp\left(\pm i\int_{x_1}^{x}\left[Q\left(t\right)\right]^{1/2}dt\right)=\exp\left(\pm i\int_{x_1}^{x_2}\left[Q\left(t\right)\right]^{1/2}dt\right)\exp\left(\pm i\int_{x_2}^{x}\left[Q\left(t\right)\right]^{1/2}dt\right) \tag{3.56}$$

To simplify our notation, we write (3.56) as

$$\begin{cases}\left[x_1,x\right]=\left[x_1,x_2\right]\left[x_2,x\right]\\ \left[x,x_1\right]=\left[x,x_2\right]\left[x_2,x_1\right]\end{cases}$$

where $\left[x,x_1\right]\equiv-\left[x_1,x\right]\equiv\exp\left(-i\int_{x_1}^{x}\left[Q\left(t\right)\right]^{1/2}dt\right)$.

4. When cross a cut in the counter-clockwise direction, the cut originating from a turning point of the first order, we changed the solution by

$$\begin{cases}\left[x_1,x\right]\longrightarrow-i\left[x,x_1\right]\\ \left[x,x_1\right]\longrightarrow-i\left[x_1,x\right]\end{cases} \tag{3.57}$$

If it is in the clockwise direction, we changed the solution by

$$\begin{cases}\left[x_1,x\right]\longrightarrow i\left[x,x_1\right]\\ \left[x,x_1\right]\longrightarrow i\left[x_1,x\right]\end{cases} \tag{3.58}$$

The location of branch cut can be determined by the Stokes flows, which suddenly flow in opposite direction when the branch cut is crossed.

3.4.3 When $N = 1$

Figure 3.3: *Stokes diagram for $N = 1$ and $E = 1$, where the yellow points are the turning points, the green dot-lines are Stokes lines and the orange dot-lines are anti-Stokes lines*

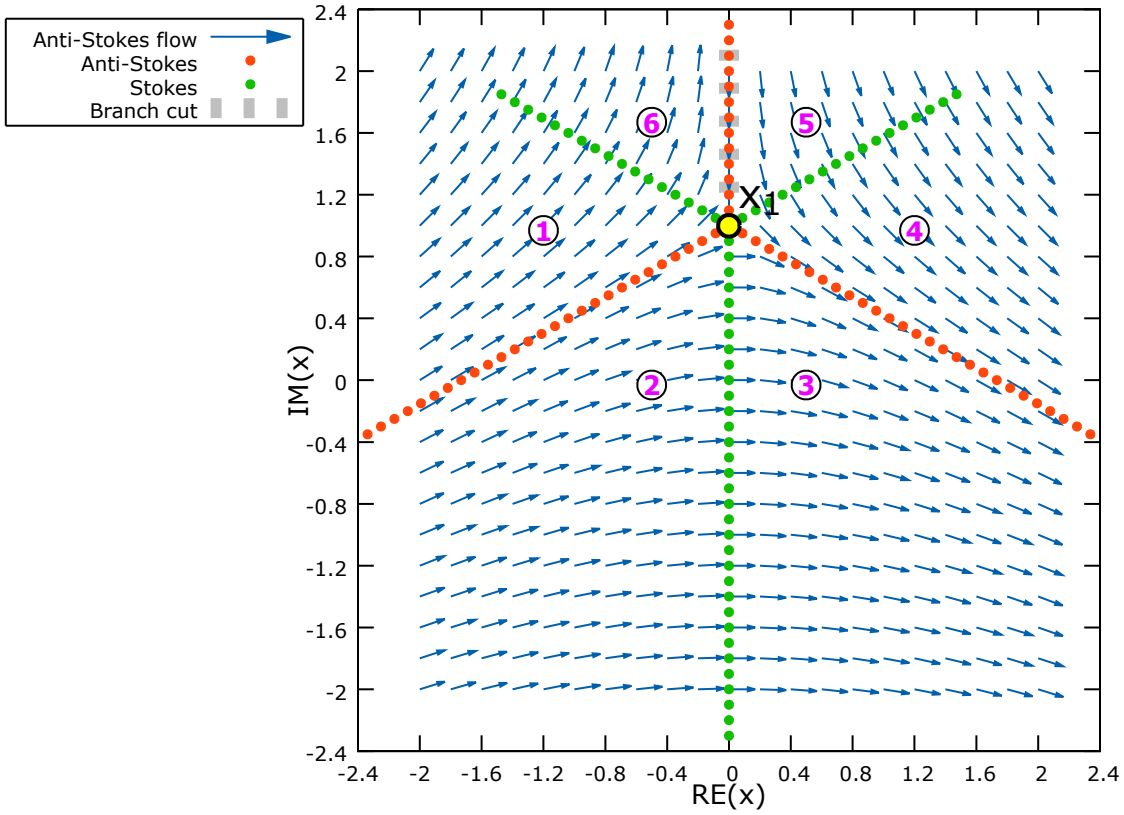

For $Q(x) = E + (ix)^N$ with $N = 1$, the turning point x_1 is of the first order, so there are three Stokes lines and three anti-Stokes lines emanated from x_1 as shown on Fig.(3.3). The boundary condition is $\psi(x) \to 0$ as $|x| \to \infty$ which suggests that we start with a subdominant WKB solution $[x, x_1]_s$ from (3.43) and counter-clockwisely continue this solution from the region 1 to the region 4. By connection formulas, we have

1. $[x, x_1]_s$
2. $[x, x_1]_d$
3. $[x, x_1]_d + i[x_1, x]_s$
4. $[x, x_1]_s + i[x_1, x]_d$

If we clockwisely continue this solution from the region 1 to the region 4, then[3]

1. $[x, x_1]_s$
6. $[x, x_1]_s$
5. $i[x_1, x]_d$
4. $[x, x_1]_s + i[x_1, x]_d$

[3]Note that when cross the region 6 into the region 5, the solution is changed due to the anti-Stokes line and the branch cut.

We see that independent from the direction of analytic continuation, we reach the same asymptotic solution in the region 4, which is as $|x| \to \infty$

$$\psi(x) \sim [x, x_1]_s + i\,[x_1, x]_d \tag{3.59}$$

where we have suppressed the factor $\frac{1}{Q(x)^{1/4}}$ within (3.43). Now, by the boundary condition, we require the coefficient of the dominant solution $[x_1, x]_d$ to be zero so that the eigenvalue quantization condition is

$$i = 0 \tag{3.60}$$

which is impossible. Therefore, this leading order approximation suggests that we do not have real eigenvalue solution. This looks consistent with our numerical result (Refer to Sec.(2.3.4)), where the real eigenvalue curve (the orange curve on Fig.(2.27)) of the ground level approaches to $N = 1$ and is arbitrarily close to it , but never actually reaches it.

3.4.4 When $N = 2$

Figure 3.4: *Stokes diagram for $N = 2$ and $E = 1$, where the yellow points are the turning points, the green dot-lines are Stokes lines and the orange dot-lines are anti-Stokes lines*

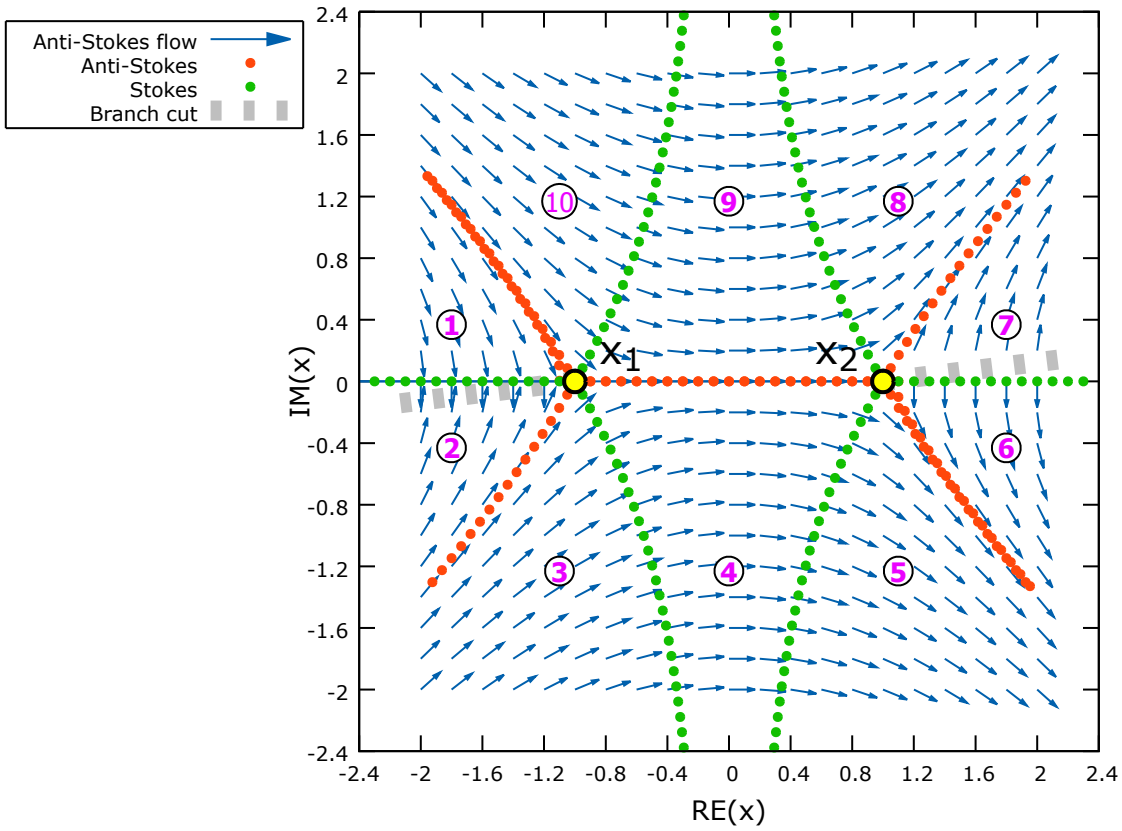

Let's set $N = 2$ and start with a subdominant WKB solution, which is $[x, x_1]_s$, and counter-clockwisely continue this solution from the region 1 to the region 7. With $B \equiv [x_1, x_2]$ and $B^{-1} \equiv [x_2, x_1]$ and by connection formulas,

1. $[x, x_1]_s$
2. $-i\,[x_1, x]_s$
3. $-i\,[x_1, x]_d$
4. $[x, x_1]_s - i\,[x_1, x]_d = B^{-1}\,[x, x_2]_s - iB\,[x_2, x]_d$
5. $(B^{-1} + B)\,[x, x_2]_s - iB\,[x_2, x]_d$
6. $(B^{-1} + B)\,[x, x_2]_d - iB\,[x_2, x]_s$
7. $-i\,(B^{-1} + B)\,[x_2, x]_d + B^{-1}\,[x, x_2]_s$

If we clockwisely continue this solution from the region 1 to the region 7, then

1. $[x, x_1]_s$
10. $[x, x_1]_d$
9. $[x, x_1]_d - i\,[x_1, x]_s = B^{-1}\,[x, x_2]_d - iB\,[x_2, x]_s$
8. $B^{-1}\,[x, x_2]_d - i\,(B + B^{-1})\,[x_2, x]_s$
7. $-i\,(B^{-1} + B)\,[x_2, x]_d + B^{-1}\,[x, x_2]_s$

Again, independent from the direction of analytic continuation, we reach the same asymptotic solution in the region 7. This is expected, since the two turning points are connected by an anti-Stokes line segment. Now, by the boundary condition, we require the coefficient of the dominant solution $[x_2, x]_d$ to be zero so that the eigenvalue quantization condition is

$$\begin{aligned} B^{-1} + B &= 0 \\ [x_2, x_1] + [x_1, x_2] &= 0 \\ \exp\left(-i\int_{x_1}^{x_2} [Q(t)]^{1/2}\,dt\right) + \exp\left(i\int_{x_1}^{x_2} [Q(t)]^{1/2}\,dt\right) &= 0 \\ \exp\left[-i\,(u + iv)\right] + \exp\left[i\,(u + iv)\right] &= 0 \\ \exp(-iu) + \exp(iu) &= 0 \\ \cos u &= 0 \\ \cos\left\{\int_{x_1}^{x_2} [Q(t)]^{1/2}\,dt\right\} &= 0 \end{aligned} \tag{3.61}$$

where $u \equiv \mathrm{Re}\left\{\int_{x_1}^{x_2} [Q(t)]^{1/2}\,dt\right\}$, $v \equiv \mathrm{Im}\left\{\int_{x_1}^{x_2} [Q(t)]^{1/2}\,dt\right\}$ and $u,\ v \in \mathbb{R}$. From Fig.(3.4), the turning points x_1 and x_2 are joined by an anti-Stokes line segment, that is why $v = 0$ and $\int_{x_1}^{x_2} [Q(t)]^{1/2}\,dt$ is purely real. Consequently we obtain the final form (3.61) of quantization which, as we expected, is the same form (3.4) obtained by the conventional WKB method.

3.4.5 When $N = 3$

Figure 3.5: *Stokes diagram for $N = 3$ and $E = 1$, where the yellow points are the turning points, the green dot-lines are Stokes lines and the orange dot-lines are anti-Stokes lines*

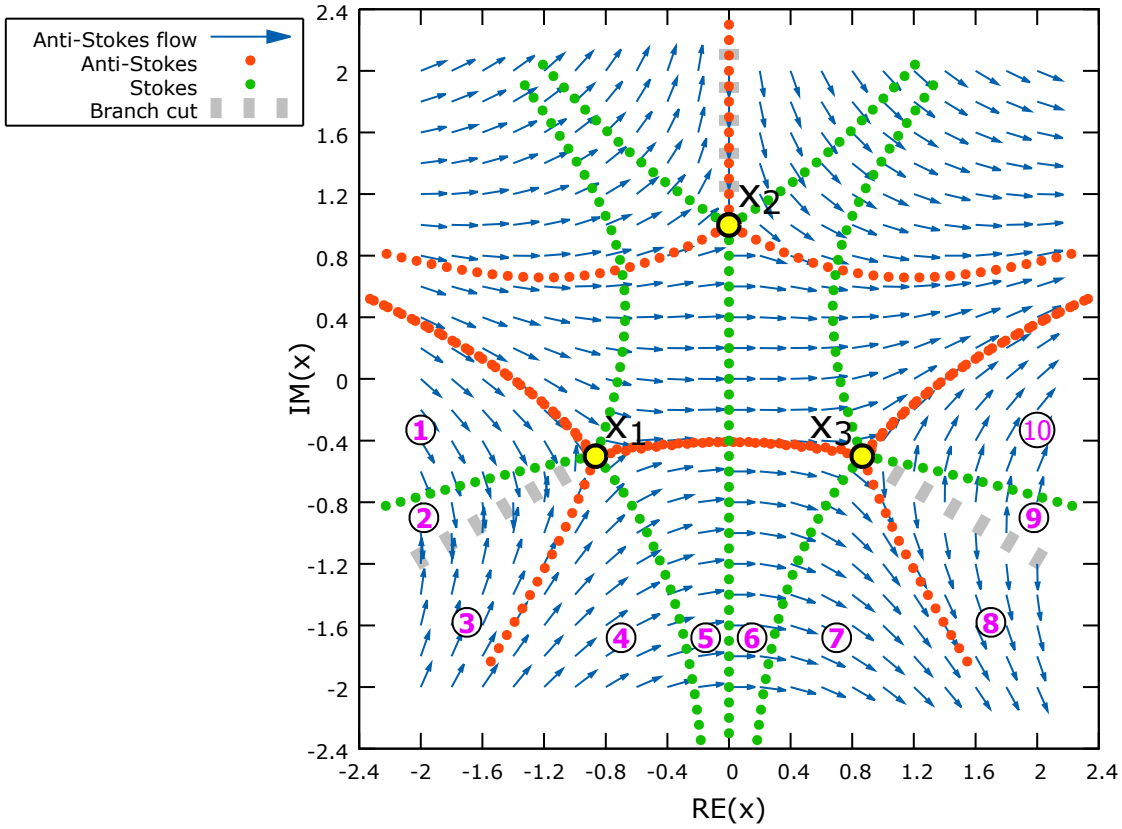

Before we try to find the eigenvalue quantization condition for $N = 3$, a common mistake we want to emphasize here. For instance, take $x = ir$ with $r \in \mathbb{R}$, then

$$\sqrt{Q} = \sqrt{E + (ix)^3} = \sqrt{E + (i \cdot ir)^3} = \sqrt{E - r^3} \tag{3.62}$$

so

$$\sqrt{Q} \sim ir^{\frac{3}{2}} \qquad \text{as } r \to +\infty \tag{3.63}$$

and

$$e^{i\int \sqrt{Q}dr} \sim e^{i\int ir^{\frac{3}{2}}dr} = e^{-\frac{2}{5}r^{\frac{5}{2}}} \Longrightarrow \text{dominant or subdominant} \tag{3.64}$$

Hence, as $x \to +i \cdot \infty$, a Stokes line should be draw above the turning point x_2 along the positive imaginary axis, rather than the anti-Stokes line shown on Fig.(3.5). However, for the turning point $x_2 = i$ when $E = 1$, let's set $r = 5$ so that $x = 5i$, then we evaluate the following integral

$$\int_i^{5i} \sqrt{Q\,(x)}dx = \int_i^{5i} \sqrt{1 + (ix)^3}dx \approx -21.3508 \tag{3.65}$$

such that

$$e^{i\int_i^{5i} \sqrt{Q(x)}dx} = e^{-21.3508i} \Longrightarrow \text{oscillatory} \tag{3.66}$$

Hence, as $x \to +i \cdot \infty$, an anti-Stokes line should be draw above the turning point x_2 along the positive imaginary axis. How do we solve this paradox? The answer is that $e^{i\int \sqrt{Q}dr}$ within (3.64) is a mistake and should be replaced by $e^{i\int \sqrt{Q}dx}$, where $dx = idr$ so that dx is complex.

For $N = 3$, unlike the previous cases for $N = 1$ and $N = 2$, if we counter-clockwisely and then clockwisely continue a solution from region 1 to 10, we will not get the same asymptotic solution. This is because[40][6, p.286] the turning point x_2 on Fig.(3.5) is not connected by any anti-Stokes line segment to the turning points x_1 and x_3. To continue our story, we assume that analytic continuation in counter-clockwise and clockwise sense will give the same asymptotic solution. The mathematical validity of this assumption is ignored here.

Let's start with a subdominant WKB solution, which is $[x, x_1]_s$, and counter-clockwisely continue this solution from the region 1 to the region 10. Let $B \equiv [x_1, x_2]$, $B^{-1} \equiv [x_2, x_1]$, $C \equiv [x_2, x_3]$ and $C^{-1} \equiv [x_3, x_2]$. Then by connection formulas,

1. $[x, x_1]_s$
2. $[x, x_1]_s$
3. $-i\,[x_1, x]_s$
4. $-i\,[x_1, x]_d$
5. $[x, x_1]_s - i\,[x_1, x]_d = B^{-1}\,[x, x_2]_s - iB\,[x_2, x]_d$
6. $(B^{-1} + B)\,[x, x_2]_s - iB\,[x_2, x]_d = (B^{-1} + B)\,C^{-1}\,[x, x_3]_s - iBC\,[x_3, x]_d$
7. $[(B^{-1} + B)\,C^{-1} + BC]\,[x, x_3]_s - iBC\,[x_3, x]_d$
8. $[(B^{-1} + B)\,C^{-1} + BC]\,[x, x_3]_d - iBC\,[x_3, x]_s$
9. $-i\,[(B^{-1} + B)\,C^{-1} + BC]\,[x_3, x]_d - BC\,[x, x_3]_s$
10. $-i\,[(B^{-1} + B)\,C^{-1} + BC]\,[x_3, x]_d + (B^{-1} + B)\,C^{-1}\,[x, x_3]_s$

Now, by the boundary condition, we require the coefficient of the dominant solution $[x_3, x]_d$ to be zero so that the eigenvalue quantization condition is

$$\begin{aligned} \left(B^{-1} + B\right) C^{-1} + BC &= 0 \\ \left[[x_2, x_1] + [x_1, x_2]\right][x_3, x_2] + [x_1, x_2]\,[x_2, x_3] &= 0 \\ \left[e^{iw(x_2,x_1)} + e^{-iw(x_2,x_1)}\right] e^{iw(x_3,x_2)} + e^{iw(x_1,x_2)} e^{iw(x_2,x_3)} &= 0 \end{aligned} \tag{3.67}$$

where $w\,(x_1, x_2) \equiv \left\{\int_{x_1}^{x_2} [Q\,(t)]^{1/2}\,dt\right\}$. Let u, $v \in \mathbb{R}$, $u \equiv \mathrm{Re}\left\{\int_{x_1}^{x_2} [Q\,(t)]^{1/2}\,dt\right\}$ and $v \equiv \mathrm{Im}\left\{\int_{x_1}^{x_2} [Q\,(t)]^{1/2}\,dt\right\}$. By PT-symmetry, we have

$$w\,(x_1, x_2) = [w\,(x_2, x_3)]^* = u + iv \tag{3.68}$$

Then (3.67) becomes

$$\begin{aligned} \left[e^{i(-u-iv)} + e^{-i(-u-iv)}\right] e^{i(-u+iv)} + e^{i(u+iv)} e^{i(u-iv)} &= 0 \\ e^{-2v} + e^{-2iu} + e^{2iu} &= 0 \\ \cos(2u) + \frac{1}{2} e^{-2v} &= 0 \end{aligned} \tag{3.69}$$

which is the final form of eigenvalue quantization condition for $N = 3$. Note that this form is exactly the same form from the paper[9].

We can evaluate the integral $I \equiv w(x_1, x_2)$ by

$$\int_{x_1}^{x_2} dx\sqrt{E+(ix)^N} = \int_{E^{1/N}e^{i\gamma}}^{E^{1/N}(\cos\gamma+i\sin\alpha)} dx\sqrt{E+(ix)^N} + \int_{E^{1/N}(\cos\gamma+i\sin\alpha)}^{E^{1/N}e^{i\alpha}} dx\sqrt{E+(ix)^N} \tag{3.70}$$

By using the substitution $y = \frac{ix}{iE^{1/N}e^{i\gamma}}$ and $w = \frac{ix}{iE^{1/N}e^{i\alpha}}$ and by (3.8)

$$I = \int_1^{\frac{\cos\gamma+i\sin\alpha}{e^{i\gamma}}} \left[E+\left(iE^{1/N}e^{i\gamma}y\right)^N\right]^{\frac{1}{2}} E^{1/N}e^{i\gamma}dy + \int_{\frac{\cos\gamma+i\sin\alpha}{e^{i\alpha}}}^{1} \left[E+\left(iE^{1/N}e^{i\alpha}w\right)^N\right]^{\frac{1}{2}} E^{1/N}e^{i\alpha}dw$$

$$= E^{\frac{N+2}{2N}}\left(e^{i\gamma}\int_1^{\frac{\cos\gamma+i\sin\alpha}{e^{i\gamma}}} \sqrt{1-y^N}dy - e^{i\alpha}\int_1^{\frac{\cos\gamma+i\sin\alpha}{e^{i\alpha}}} \sqrt{1-y^N}dy\right)$$

When $N=3$, $\gamma = \frac{7\pi}{6}$ and $\alpha = \frac{\pi}{2}$. By numerical integration,

$$I \approx (0.728598 + 1.26196i)\, E^{\frac{5}{6}} \tag{3.71}$$

Plug this into (3.69) such that

$$\cos\left(2\times 0.728598E^{\frac{5}{6}}\right) + \frac{1}{2}e^{-2\times 1.26196E^{\frac{5}{6}}} \approx 0 \tag{3.72}$$

By solving for E, we obtain the following Tab.(3.1), where the results from the WKB solution is obtained by (3.20).

Table 3.1: *Eigenvalues E for $N=3$ obtained by the three methods*

	Numerical	WKB	PIM
E_0	1.156267071988113	1.0942695005	1.1203933861
E_1	4.109228752809652	4.0894961192	4.0893475488
E_2	7.562273854978828	7.5489804375	7.5489811503
E_3	11.31442182019580	11.3042549230	11.3042549195
E_4	15.29155375039253	15.2832355296	15.2832355293

The quantization condition from (3.69) is different from (3.4) obtained by the conventional WKB method since it contains an additional exponential term $\frac{1}{2}e^{-2v}$. From Fig.(3.5), we see that this additional exponential term is caused by the influence from the turning point x_2 whose Stokes line intercepts our path of analytic continuation. In the ground level with low energy, this exponential term becomes a significant correction to the eigenvalue E_0 obtained by the WKB on Tab.(3.1). As energy increases, the exponential term vanishes so quick that the results from PIM and WKB are almost the same.

3.4.6 When $N = 5$

Figure 3.6: *Stokes diagram for $N = 5$ and $E = 1$, where the yellow points are the turning points, the green dot-lines are Stokes lines and the orange dot-lines are anti-Stokes lines*

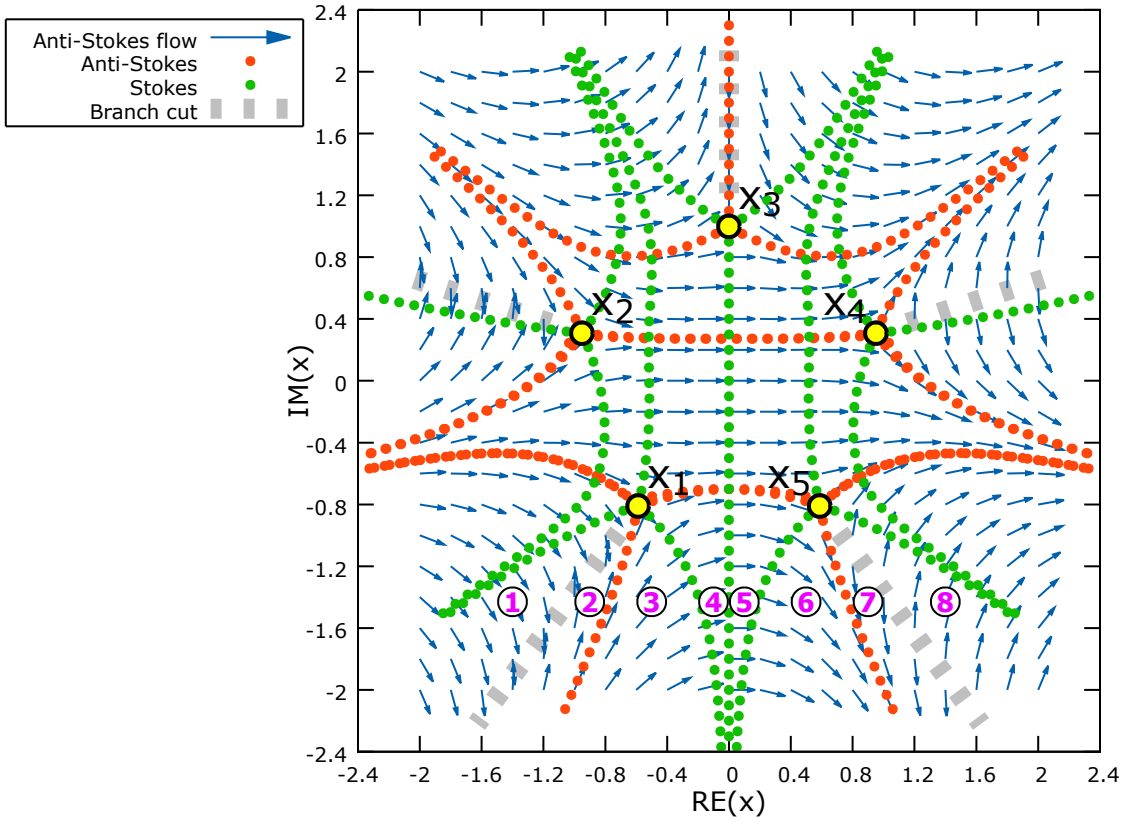

Table 3.2: *Eigenvalues E for $N = 5$ obtained by the three methods*

	Numerical	WKB	PIM
E_0	1.908264578170778	1.7712447154	1.7775754610
E_1	8.587220836207222	8.5090359785	8.5090353301
E_2	17.71080901173115	17.6525375971	17.6525375969
E_3	28.59510331173597	28.5470661784	28.5470661781
E_4	40.91889089052085	40.8772953023	40.8772953019

Based on Fig.(3.6), the final form of eigenvalue quantization condition for $N = 5$ is the same form as (3.69). Actually, for all odd N and $N > 1$, the final form of the quantization condition is unchanged, since the Stokes lines from other PT-symmetric pairs of turning points do not affect the bottom region.

$$\cos\left(2 \times 0.526374 E^{\frac{7}{10}}\right) + \frac{1}{2} e^{-2\times 1.62001 E^{\frac{7}{10}}} \approx 0 \tag{3.73}$$

By solving for E, we obtain Tab.(3.2).

Based on the result from Tab.(3.1), we expect that the correction to the ground level E_0 could be significant as well for the case $N = 5$. However, as Tab.(3.2) shows, the correction happens only on the 3rd decimal place. This implies that the additional exponential term is sensitive to the value of N as well. As N increases or energy level increases, the PT-symmetric pair of two turning points in the chosen wedges become more and more dominant, and the influence caused by other turning points are more and more subdominant.

3.4.7 Question, observation and future work

By following the PIM introduced by the paper[9], there are many unanswered questions. We present those questions here and leave them as our future work. We believe that solving any one of these questions, which are related to each other, could make breakthrough in understanding PT-symmetry.

3.4.7.1 Question 1: apply PIM on the pair of the green wedges for $N = 5$

Figure 3.7: *Stokes diagram for $N = 5$ and $E = 1$, where the yellow points are the turning points, the green dot-lines are Stokes lines and the orange dot-lines are anti-Stokes lines*

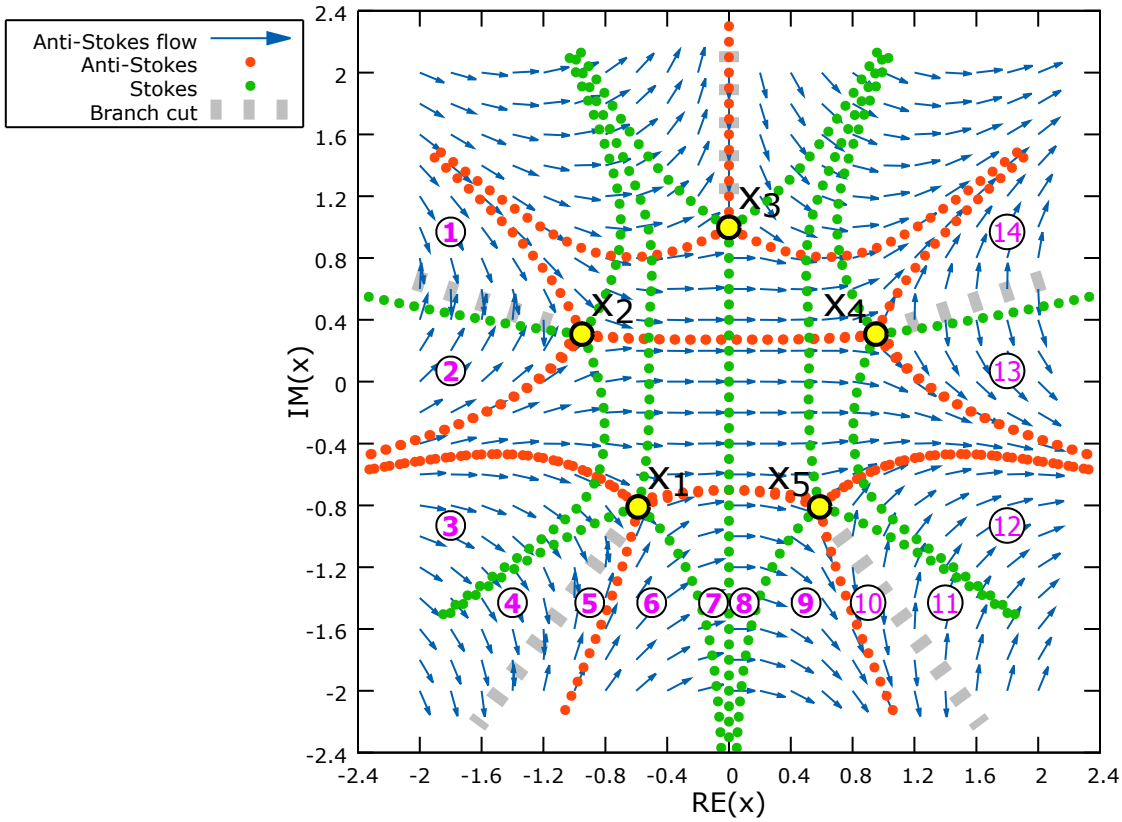

As shown on Fig.(2.26) and Fig.(2.28), for $N = 5$, within the pair of the green wedges we have another family of spectrum. Then, this naturally leads to the question how we apply PIM to estimate the eigenvalues within the pair of the green wedges. Shall we analytically continue our subdominant WKB solution along the path shown on Fig.(3.7) from region 1 to region 14? However, we have found that along this path with the given connection formulas, the quantization condition will look like

$$\left(D + D^{-1}\right) F + D^{-1}F^{-1} = 0 \tag{3.74}$$

where $D \equiv [x_1, x_3]$, $D^{-1} \equiv [x_3, x_1]$ $F \equiv [x_3, x_5]$ and $F^{-1} \equiv [x_5, x_3]$. This condition will not yield wanted eigenvalues consistent with our numerical and WKB approximation.

3.4.7.2 Question 2: mathematical validity for our assumption

In Sec.(3.4.5), for $N = 3$ we assumed that the analytic continuation in the counter-clockwise and clockwise direction would give the same asymptotic solution, even if in fact they did not. There are papers[9, 58, 6] who made the same assumption. However, we want to see how to mathematically justify this assumption.

3.4.7.3 Question 3: degenerate Stokes lines

If two turning points are connected by a Stokes line segment, then that Stokes line is degenerate. When $N > 2$ and N is even, we have degenerate Stokes lines. For example, Fig.(3.8) shows that when $N = 4$, turning points x_1 and x_2 are connected by a Stokes line, and x_3 and x_4 are connected by another Stokes line. Fig.(3.10) shows that the case for $N = 6$ contains two degenerate Stokes lines as well.

Figure 3.8: *Stokes diagram for $N = 4$ and $E = 1$, where the green dot-lines are Stokes lines and the orange dot-lines are anti-Stokes lines*

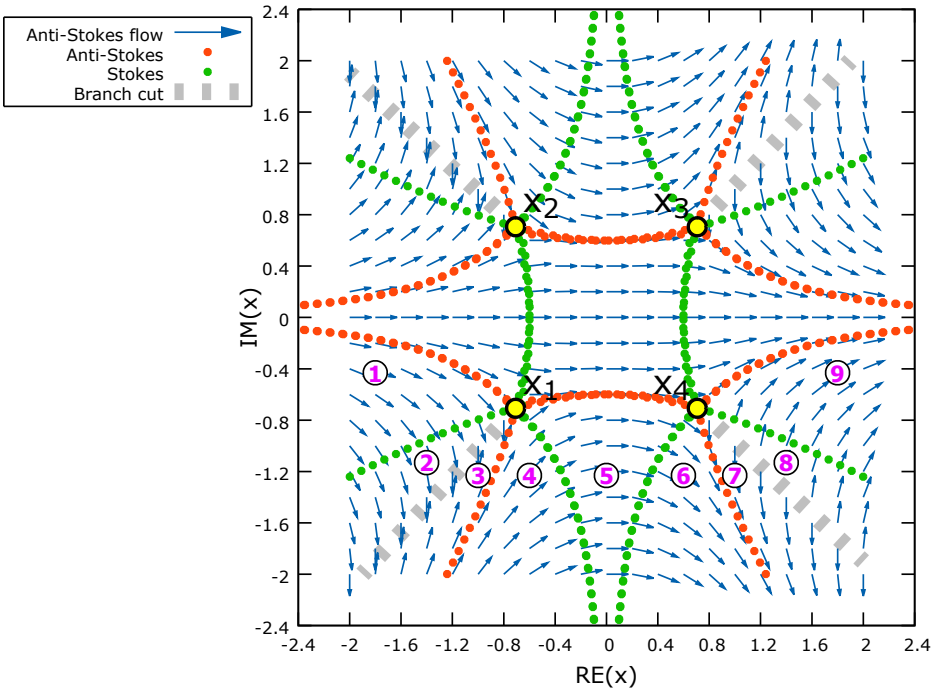

Figure 3.9: *Stokes diagram for $N = 3.9$ and $N = 4.1$ when $E = 1$, where the yellow points are the principal turning points, the green dot-lines are Stokes lines and the orange dot-lines are anti-Stokes lines*

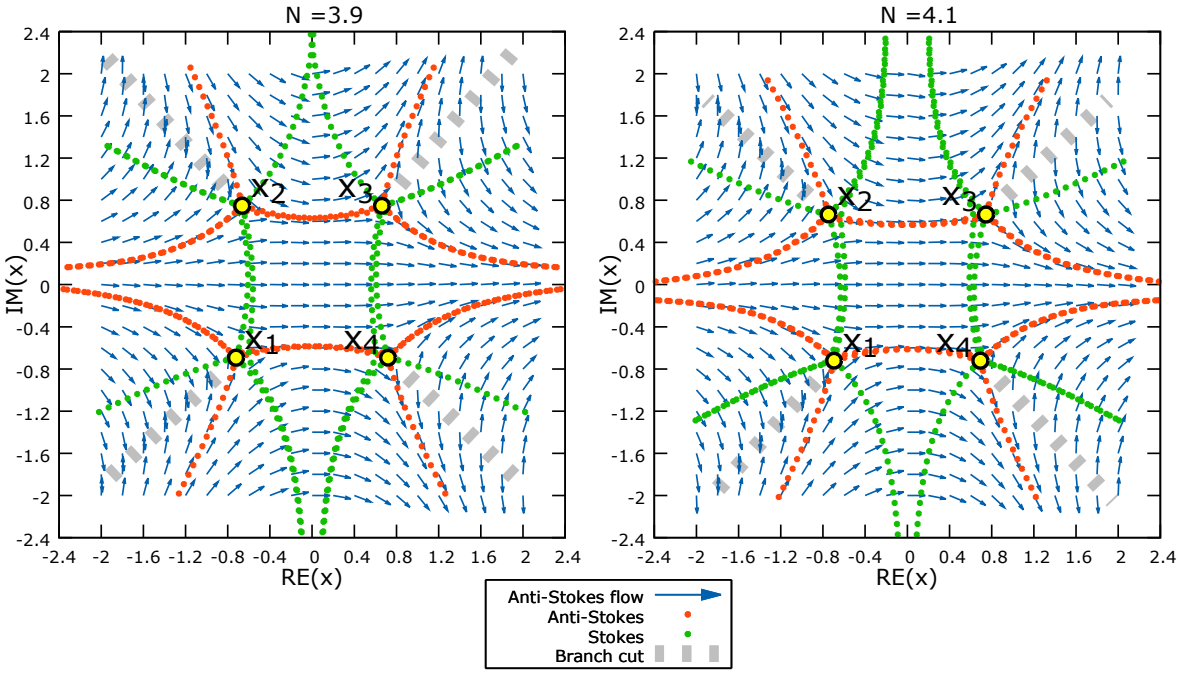

The central question is, of course, how we apply PIM if such degenerate

Stokes lines are there. If the degeneracy is ignored, then the case for any even N would be no more different than the case for $N = 2$ as we did in (3.61) where the results from PIM and conventional WKB method are the same. Taking account of the degeneracy means taking account of the influence caused by other turning points.

Fig.(3.9) shows a sudden change of the behavior of degenerate Stokes lines when N is slightly less or greater than 4. When $N = 3.9$, the two Stokes lines in the downward direction emanated from x_2 and x_3 almost coincide with the two downward Stokes lines emanated from x_1 and x_4. However, when $N = 4.1$, the two downward Stokes lines from x_2 and x_3 suddenly change their directions after crossing x_1 and x_4, and coincide with the Stokes lines on the left of x_1 and the right of x_4, respectively. This sudden change is thought to be due to the existence of branch cuts associated with x_1 and x_4. Perhaps by slightly perturbing the value of N, we may know how to apply PIM for the case of degenerate Stokes line. However, this small perturbation inevitably leads us to study cases for fractional N, which is both difficult and new as we will discuss in Sec.(3.4.7.5).

Figure 3.10: *Stokes diagram for $N = 6$ and $E = 1$, where the yellow points are the turning points, the green dot-lines are Stokes lines and the orange dot-lines are anti-Stokes lines*

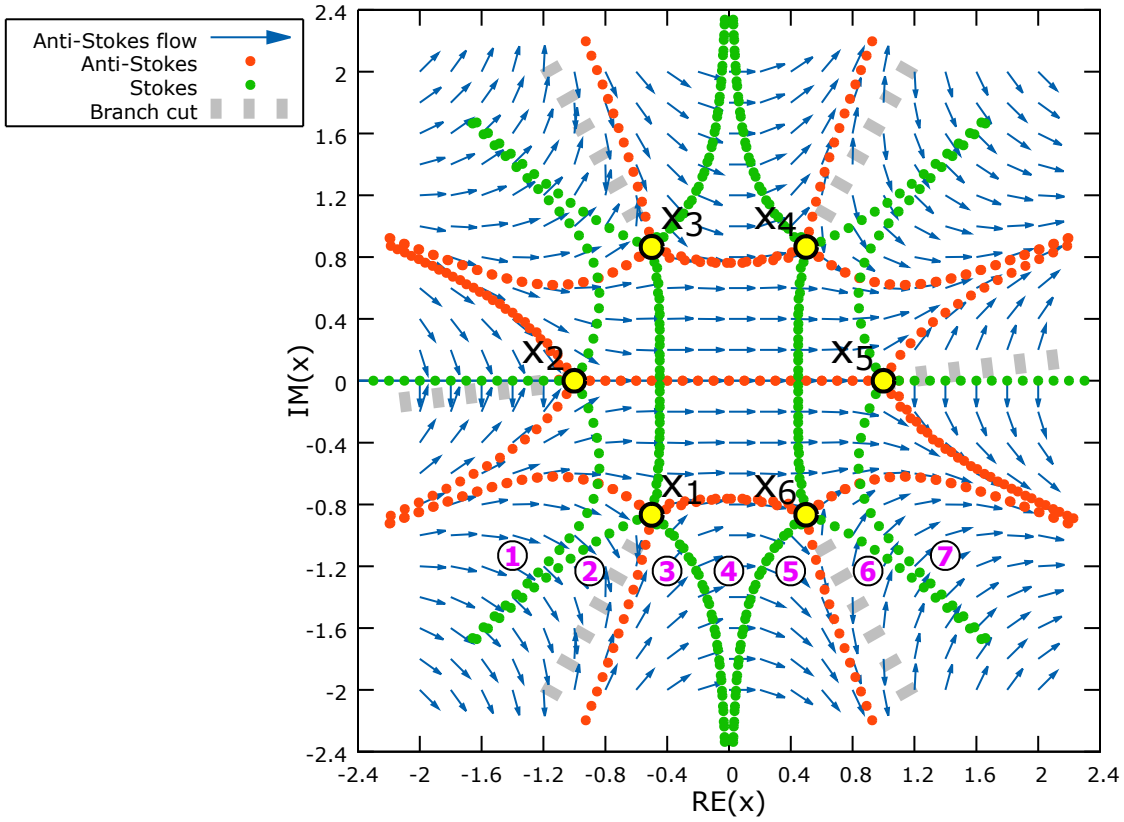

3.4.7.4 Question 4: Stokes diagram of the higher order

All our Stokes diagrams are generated based on the method from Sec.(3.4.1) so that locations of all Stokes lines and anti-Stokes lines are approximated by the leading order terms within Taylor series. However, it's possible that these locations may change if we consider the higher order terms, and consequently Stokes geometrical structure may be different from the leading order approximation.

3.4.7.5 Fractional N and broken PT-symmetry

Figure 3.11: *Stokes diagram for $N = 1.5$ and $N = 3.5$ when $E = 1$, where the yellow points are the principal turning points, two Stokes lines cross at point C, the green dot-lines are Stokes lines and the orange dot-lines are anti-Stokes lines. Also, note that the anti-Stokes flows suddenly change direction after crossing the positive imaginary axis.*

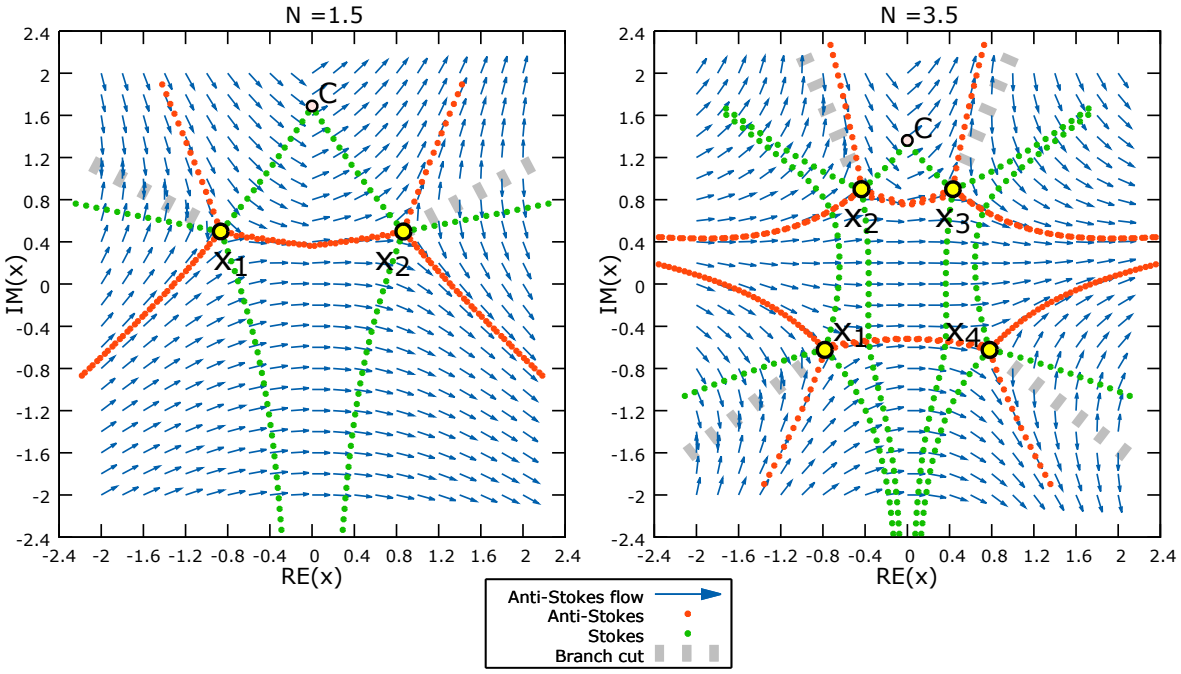

Since ${}^{dQ(x)}/_{dx} = {}^{N(ix)^N}/_x$, by the definition, any principal turning points for fractional N are simple or of the first order. As Fig.(3.11) shows, one prominent feature for fractional N and ceiling $(N) =$ even number is that two Stokes lines on the north part of diagram cross each other at the point C on the positive imaginary axis and subsequently vanish. This is a surprise! Because what mathematicians[5, p.1][41, p.26] said was:

"*In the case of second order equations such a phenomenon of vanishing of a Stokes curve never happens*".

"*It is clear that such crossing does not appear in the study of equations of the second order.*"

Well, they are wrong, at least on the principal Riemann sheet. It does happen! The exact locations for these crossing points C for various value of N are found on Tab.(3.3), where we observe that as N increases, the crossing point C moves toward the origin, and the ratio between any two adjacent crossing points is approaching to 1.

We observe that the anti-Stokes flows who cross the positive imaginary axis suddenly change their direction. Along the north direction, farther away from the anti-Stoke line segment connecting the two turning points (e.g. x_1 and x_2 for $N = 1.5$ or x_2 and x_3 for $N = 3.5$), this sudden change becomes more abrupt. However, along the south direction and below that anti-Stokes line segment, the Stokes flows behave quite smooth. The sudden change near the positive imaginary axis may be the reason for fractional N why we did not obtain the same eigenvalue along the path which crosses the cut (e.g. cross cut CD on Fig.(2.25) and Tab.(2.3)).

Here, we make a short list about what we observe for the potential $V(x) = -(ix)^N$ where $N \in \mathbb{R}$.

1. For $N > 3$, whenever N is an non-integer, there exists at least one pair of Stokes wedges where PT-symmetry is broken.

2. For $N > 1$, whenever N is an non-integer and ceiling $(N) =$ even number, there are two and only two Stokes lines crossing each other and then disappear on the principal Riemann sheet. These two Stokes lines emanate, respectively, from a pair of symmetric and principal turning points.

3. For $N > 1$, whenever N is an non-integer and ceiling $(N) =$ odd number (See Fig.(3.12)), then no Stokes lines are crossed or disappeared on the principal Riemann sheet.

Table 3.3: *Locations of a few crossing points C for various N, with error less than 10^{-12}*

N	Crossing point C
1.5	$1.6897993907261i$
3.5	$1.3638073305613i$
5.5	$1.2390039888469i$
7.5	$1.1773332445002i$
9.5	$1.1408269069328i$

Figure 3.12: *Stokes diagram for $N = 2.5$ and $N = 3$ when $E = 1$, where the yellow points are the principal turning points, the green dot-lines are Stokes lines and the orange dot-lines are anti-Stokes lines*

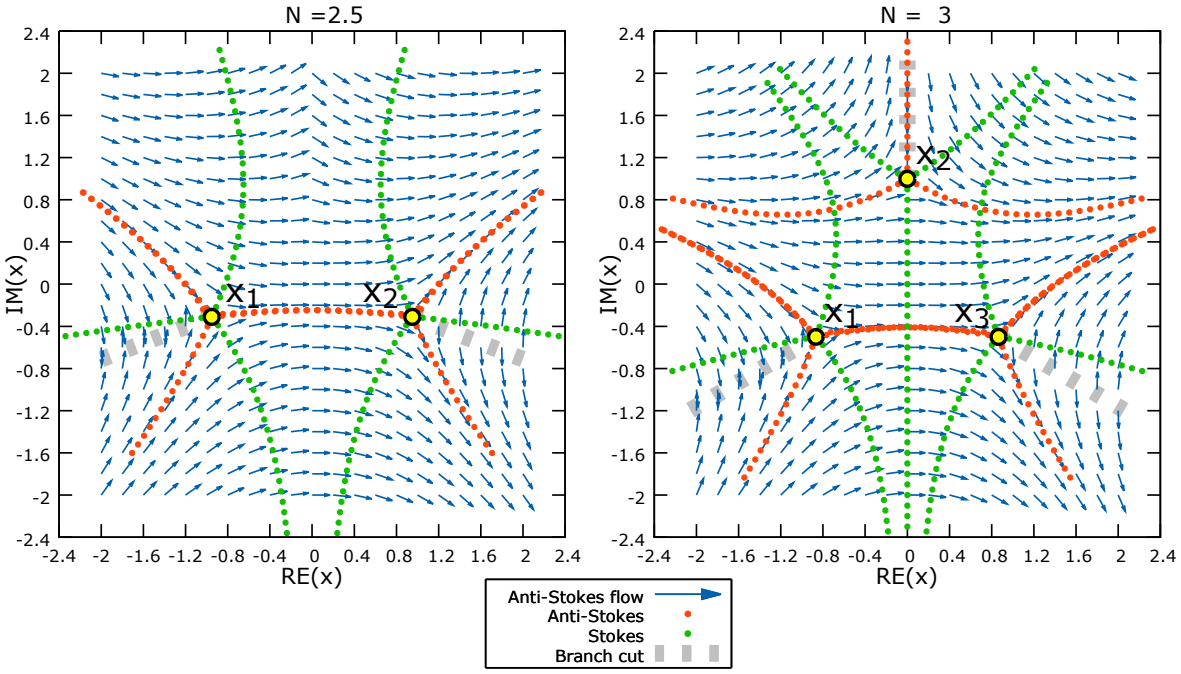

Due to the same number of Stokes and anti-Stokes lines, the quantization condition for $N = 2.5$ is no more different than the quantization condition for $N = 2$. Why does the quantization condition for $N = 2$ obtained by PIM give exact eigenvalues, but not exact eigenvalues for $N = 2.5$? Well, let's look at Fig.(3.12) and observe how the Stokes diagram for $N = 2.5$ transforms to $N = 3$ - before the new turning point is born on the positive imaginary axis, the anti-Stokes flows for $N = 2.5$ are already influenced by the birth because they suddenly change direction when cross the positive imaginary axis, and this sudden change becomes more abrupt when $x \to i \cdot \infty$. Meanwhile, the pair of Stokes line on the north of the diagram of $N = 2.5$ emanated from x_1 and x_2 becomes farther apart as if they are opening an empty space for the birth of the new turning point. All in all, this shows that the quantization condition for any non-integer N and ceiling $(N) =$ odd number is influenced by the pre-birth of the new turning point on the positive imaginary axis. Because of the pre-birth, the new turning point is invisible. This naturally arises a question: does the visible Stokes geometrical structure describe the quantization condition completely or not? Quite obvious, the answer is no. The invisible Stokes structure must be on the non-principal Riemann sheets or caused by virtural turning point.

3.4.7.6 Virtual turning point

This subsection contains primary work from their book[41, chapter 1] by Honda *et al.*.

The following equation with a large-magnitude-parameter[4] η,

$$\hat{P}\psi \equiv \left(\frac{d^3}{dx^3} + 3\eta^2 \frac{d}{dx} + 2ix\eta^3 \right) \psi = 0 \tag{3.75}$$

is called **BNR equation** after Berk, Nevins and Roberts discovered[31] it in 1982. This equation has simple turning points at $x = \pm 1$ who satisfy the following characteristic polynomial

$$\sigma \equiv \xi^3 + 3\eta^2 \xi + 2ix\eta^3 = 0 \tag{3.76}$$

or

$$\zeta^3 + 3\zeta + 2ix = 0 \tag{3.77}$$

where $\zeta \equiv \frac{\xi}{\eta}$ and $\sigma(\xi, \eta, x, y)$ is called **characteristic symbol**. Note that (3.76) does not contain the variable y, so where does this y come from? This y is obtained by Borel transformation[41, p.4]. The Borel transformed BNR operator from (3.75) is

$$\hat{P}_B \equiv \frac{\partial^3}{\partial x^3} + 3\frac{\partial}{\partial x}\frac{\partial^2}{\partial y^2} + 2ix\frac{\partial^3}{\partial y^3} \tag{3.78}$$

Since by (3.76) σ is free from y, it may be helpful to simplify some future calculation to determine bicharacteristic curve.

The definition[41, p.21] of **turning point** for higher order ODE is: If at $x = x_0$ the characteristic polynomial has multiple roots $\zeta_n(x_0)$ where integer $n \geq 2$, then the point $x = x_0$ is a turning point. Moreover, if there is any degenerate root, say

$$\zeta_j(x_0) = \zeta_k(x_0) \qquad j \neq k \tag{3.79}$$

then that turning point is said to have **type** (j, k). When $x = +1$, (3.77) becomes

$$(\zeta + i)^2 (\zeta - 2i) = 0 \tag{3.80}$$

whose roots are a simple root $\zeta_1 = 2i$ and a degenerated root $\zeta_{2,3} = -i$. When $x = -1$, (3.77) becomes

$$(\zeta - i)^2 (\zeta + 2i) = 0 \tag{3.81}$$

whose roots are a degenerated root $\zeta_{1,2} = i$ and a simple root $\zeta_3 = -2i$. Hence, we have verified that $x = +1$ is a turning points with type $(2, 3)$ and $x = -1$ is another turning points with type $(1, 2)$ for the BNR equation.

[4] η can be a complex number with large modulus.

Figure 3.13: *[41, p.26]Solid lines are Stokes lines for the BNR equation and they cross at points C_1 and C_2. The red thick-dash lines are branch cuts.*

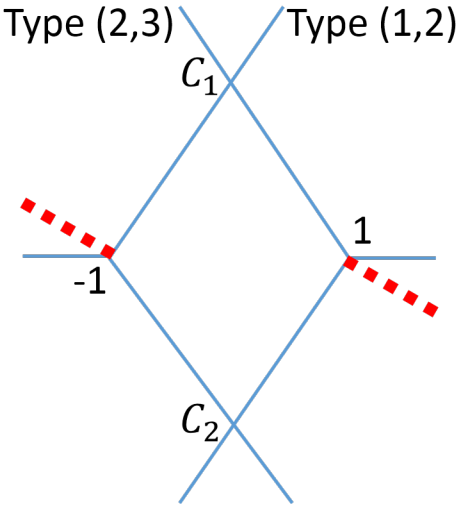

The paper[31] shows that there exists an invisible turning point called "**virtual turning point**" whose location is determined by self-intersection point[41, p.30] of a **bicharacteristic curve** (**B-curve**) which is defined as a parametric curve $\{x(t), y(t); \xi(t), \eta(t)\}$ in the cotangent bundle $T^*\mathbb{C}^2_{(x,y)}$ and satisfy the following Hamilton-Jacob equation.

$$\begin{cases} \frac{dx}{dt} = \frac{\partial \sigma}{\partial \xi} \\ \frac{dy}{dt} = \frac{\partial \sigma}{\partial \eta} \\ \frac{d\xi}{dt} = -\frac{\partial \sigma}{\partial x} \\ \frac{d\eta}{dt} = -\frac{\partial \sigma}{\partial y} \\ \sigma(x, \xi, \eta) = 0 \end{cases} \tag{3.82}$$

where $\mathbb{C}^2_{(x,y)} \equiv \{(x,y) \,|x, y \in \mathbb{C}\}$, $t \in \mathbb{R}$, $\xi \equiv \frac{\partial}{\partial x}$ and $\eta \equiv \frac{\partial}{\partial y}$.

If $\hat{P}_B$ is in some simple form, for example, say $\hat{P}'_B \equiv \frac{\partial^2}{\partial x^2} - x\frac{\partial^2}{\partial y^2}$, then $\sigma' \equiv \xi^2 - x\eta^2$ and we may easily solve the corresponding Hamilton-Jacob equation by setting $\eta = 1$ due to $-\frac{\partial \sigma}{\partial y} = 0$. So $\frac{dx}{dt} = 2\xi$, $\frac{dy}{dt} = -2x$ and its B-curve is found to be

$$\begin{cases} x(t) = t^2 \\ y(t) = -\frac{2}{3}t^3 \\ \xi(t) = t \\ \eta(t) = 1 \end{cases} \tag{3.83}$$

However, for the BNR operator $\hat{P}_B$ from (3.78), due to the difficulty of solving the Hamilton-Jacob equation, it is not easy to obtain its B-curve shown in the following form:

$$\begin{cases} x(t) = -4\left(t + \frac{1}{2}\right)\left(t^2 + t - \frac{1}{2}\right) \\ y(t) = -6i\,(t+1)^2\, t^2 \\ \xi(t) = -2it - i \\ \eta(t) = 1 \end{cases} \tag{3.84}$$

which is plotted on Fig.(3.14). When $t = -1$, we obtain a singular point[5] $x(t) = -1$ and $y(t) = 0$; When $t = 0$, we obtain another singular point $x(t) = 1$ and $y(t) = 0$. The turning points $x = \pm 1$ are the x-components of singular points from the B-curve projected on the base manifold $\mathbb{C}^2_{(x,y)}$. When $t = 0.366$ or $t = -1.366$, we have a self-intersection point $x = 0$ and $y = -\frac{3}{2}i$, which is another type of singular point. The x-component of this self-intersection point is the wanted virtual turning point.

Figure 3.14: *[41, p.32]Bicharacteristic curve (the blue curve on this figure) for BNR equation. The two singular points from B-curve projected on the x-plane are the turning points $x = \pm 1$; Whereas the x-component of the self-intersection point, which is $x = 0$, is the virtual turning point. (Only Im (y) is plotted here, since $\mathrm{Re}(y) = 0$ by (3.84). So is $\mathrm{Im}(x)$.)*

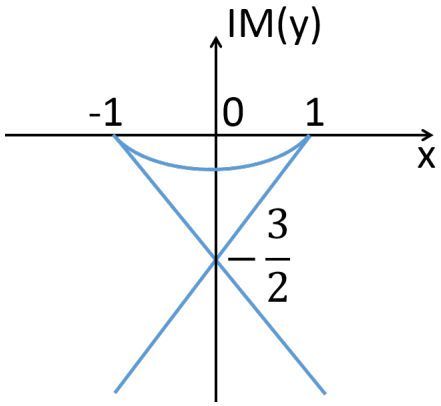

Figure 3.15: *[41, p.32]Complete Stokes lines for BNR equation. Solid lines are active Stokes lines, the blue dash line segment are inert Stokes lines, and red thick-dash lines are branch cuts.*

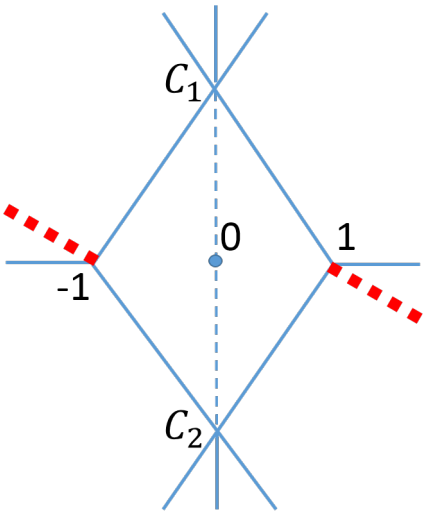

[5] A singular point of a parametric curve is the place where the curve appears to be non-smooth for the embedding parameter. Singular point may contain several different types. One common type is cusp.

There are only two new Stokes lines, both along the vertical axis, emanated from the virtual turning point $x = 0$ and shown on Fig.(3.15). The property of these new Stokes lines depends on whether the crossing points C_1 and C_2 are ordered or non-ordered. If they are ordered, then these new Stokes lines become inert or vanished before hitting the crossing points, which means that the new Stokes lines do not influence the global WKB solution by analytic continuation. After hitting or going through the crossing points, they become active and influential. We don't want to spend anymore time to further explain what it means by ordered or non-ordered crossing point, because right now we are facing a critical question: For fractional N, does the potential $V(x) = -(ix)^N$ for Schrodinger equation contain any virtual turning point or not?

The Borel transformed differential operator $\hat{P}_S$ for $1D$ Schrodinger equation

$$\left(\frac{d^2}{dx^2} - \eta Q(x)\right)\psi(x,\eta) = 0 \tag{3.85}$$

must be

$$\hat{P}_S \equiv \frac{\partial^2}{\partial x^2} - Q(x)\frac{\partial^2}{\partial y^2} \tag{3.86}$$

with the characteristic symbol σ_S

$$\sigma_S \equiv \xi^2 - Q(x)\eta^2 = \zeta^2 - Q(x) \tag{3.87}$$

and with the characteristic polynomial $\zeta^2 - Q(x) = 0$, who only has two roots[6]

$$\zeta_1(x) = \sqrt{Q(x)} \qquad \zeta_2(x) = -\sqrt{Q(x)} \tag{3.88}$$

The fact that the number of roots are less than three creates a critical problem to find any virtual point. Why? Let's first write down the definition[41, p.33] of virtual turning point.

Let x_1 be a simple turning point with type (j,k) of the following ODE

$$\hat{P}\psi = \left(\frac{d^m}{dx^m} + \eta q_1(x)\frac{d^{m-1}}{dx^{m-1}} + \cdots + \eta^m q_m(x)\right)\psi(x,\eta) = 0 \tag{3.89}$$

where $q_i(x)$ is a polynomial. Let x_2 be a simple turning point with type (k,l) of the same ODE. Suppose that one Stokes line from x_1 and another Stokes line from x_2 cross each other at a point C. For any point x_* who satisfies the following relation with distinct integers j, k, l

$$\int_{x_1}^{x_*} \zeta_j(x)\,dx = \int_{x_1}^{x_2} \zeta_k(x)\,dx + \int_{x_2}^{x_*} \zeta_l(x)\,dx \tag{3.90}$$

then we say that the point x_* is a **virtual turning point** of the ODE and the new Stokes line emanated from x_* with type (j,l) passes through the crossing point C.

[6]We know that the definition of turning point for the second order Schrodinger equation is different from the definition for higher order ODE, since we say that $x = x_0$ is a turning point whenever $Q(x_0) = 0$ for Schrodinger equation.

This definition with its subsequent claim can be mathematically proved, but we omit the proof here. The relation (3.90) requires at least three roots to work. However, we only have two roots (3.88) for the second order ODE. Therefore, this definition must have to change if there exists a virtual turning point in Schrodinger equation. Since those mathematicians had already made mistakes on the vanished Stokes lines and crossing point for the second order ODE, it is not impossible that the definition of virtual turning point extends to accommodate our case.

By (3.87), (3.82) and setting $\eta = 1$,

$$\frac{dy}{dx} = \frac{\frac{\partial \sigma}{\partial \eta}}{\frac{\partial \sigma}{\partial \xi}} = -\frac{Q(x)}{\xi} \tag{3.91}$$

Since $\sigma(x, \xi, \eta) = 0$ from (3.82), so by (3.87) $\xi = \pm\sqrt{Q(x)}$ and by (3.91) we have

$$\left(\frac{dy}{dx}\right)^2 = Q(x) \tag{3.92}$$

Therefore, the B-curve for any Schrodinger equation must satisfy

$$y = \pm \int_{x_0}^{x} \sqrt{Q(x)} dx \tag{3.93}$$

where x_0 is a turning point and $Q(x) = E - V(x)$. The expression of (3.93) is almost the same as the definition of Stoke line from (3.44). This means that the Stokes and anti-Stokes lines are parts of B-curve for Schrodinger equation.

A question arose from (3.93) is that whether the B-curve defined by (3.93) contains any singular point (e.g. self-intersection point) other than ordinary turning points. Since such hyperdimensional B-curve contains four coordinates $[\mathrm{Re}(x), \mathrm{Im}(x), \mathrm{Re}(y), \mathrm{Im}(y)]$, it is hard to visualize its complete geometry, so we leave this work for mathematician.

3.5 Conclusion of the current chapter

The conventional WKB may fail whenever the PT-symmetry is broken. From Fig.(2.28), due to the existence of CINDs for integer N, we further conclude that the conventional WKB may fail only for non-integer N if that non-integer N is located in the region with broken PT-symmetry. The reason why it fails may be due to the sudden change of directions of anti-Stokes flows around the positive imaginary axis (See Fig.(3.11) as examples). More rigorous study for the validity of conventional WKB method is needed.

By applying the phase integral method, we found that eigenvalue E, especially for the ground level, is influenced by more than two turning points if $N > 2$. It also can be influenced by invisible Stokes structure, which may be caused by non-principal turning points or virtual turning points.

Chapter 4

A Brief Survey of PT-symmetric Classical Mechanics

4.1 Introduction of the current chapter

This chapter contains the work by Bender *et al.*[8, 22, 17] and original work.

In this chapter, we will study the classical trajectories associated with the complex oscillator in Sec.(4.2) and complex pendulum in Sec.(4.3). Since positive energy is interested in quantum mechanics, we will mainly focus on the positive energy in classical mechanics. For the complex oscillator, "energy quantization" and "chaotic trajectory" are linked to the branch cut and complex energy. For the complex pendulum, the relationship between "classical tunneling" and complex energy will be explored.

4.2 Classical complex oscillator

4.2.1 For $N \geq 2$ and N is an integer

Let's set the particle's mass $m = 1$. The Hamilton's equations for

$$\mathcal{H} = \frac{1}{2}p^2 - (ix)^N \tag{4.1}$$

are

$$\dot{p} = -\frac{\partial \mathcal{H}}{\partial x} = \frac{N\,(ix)^N}{x} = iN\,(ix)^{N-1} \qquad \dot{x} = \frac{\partial \mathcal{H}}{\partial p} = p \tag{4.2}$$

so that the particle has total energy

$$E = \frac{p^2}{2} + V\,(x) = \frac{(\dot{x})^2}{2} - (ix)^N \neq \frac{(\dot{x})\,\overline{(\dot{x})}}{2} - (ix)^N \tag{4.3}$$

where $(\dot{x})^2$ can be complex but $(\dot{x})\,\overline{(\dot{x})}$ is purely real. If we set $E = \frac{(\dot{x})\overline{(\dot{x})}}{2} - (ix)^N$ instead, then E can never be real for some value of N.

By solving $\dot{x}$ from the equation $E = \frac{(\dot{x})^2}{2} - (ix)^N$, we obtain

$$\dot{x} = \frac{dx}{dt} = \sqrt{2\left[E - V\left(x\right)\right]} \tag{4.4}$$

then

$$dt = \frac{dx}{\sqrt{2\left[E - V\left(x\right)\right]}} \tag{4.5}$$

$$t_2 - t_1 = \int_{x_1}^{x_2} \frac{dx}{\sqrt{2\left[E - V\left(x\right)\right]}} \tag{4.6}$$

So the period T is

$$T = \oint_C \frac{dx}{\sqrt{2\left[E - V\left(x\right)\right]}} \tag{4.7}$$

Complex analysis allows us to deform a given orbit into a simpler orbit with exactly the same period. This simplest orbit can be the one connecting two turning points and oscillates between them rather than encircling them, so that we can deform the orbit into a pair of two rays. For the elementary case of orbits that enclose only two principal turning points, the formula for the period T of the closed orbit can be evaluated in the following way:

$$T = 2\int_{x_-}^{x_+} \frac{dx}{\sqrt{2\left[E + (ix)^N\right]}} = 2\left\{\int_0^{E^{1/N}e^{i\gamma}} \frac{dx}{\sqrt{2\left[E + (ix)^N\right]}} + \int_{E^{1/N}e^{i\beta}}^0 \frac{dx}{\sqrt{2\left[E + (ix)^N\right]}}\right\}$$

where (3.2) and (3.3) are used. By using the substitution $y = \frac{ix}{iE^{1/N}e^{i\gamma}}$ and $w = \frac{ix}{iE^{1/N}e^{i\beta}}$, the two complex contour integrations become two real integrations along real axis

$$T = 2\left\{\int_0^1 \frac{E^{1/N}e^{i\gamma}}{\sqrt{2\left[E + (iE^{1/N}e^{i\gamma}y)^N\right]}}dy + \int_1^0 \frac{E^{1/N}e^{i\beta}}{\sqrt{2\left[E + (iE^{1/N}e^{i\beta}w)^N\right]}}dw\right\} \tag{4.8}$$

Since y and w are dummy variables, we obtain

$$T = 2\left\{\int_0^1 \frac{E^{1/N}e^{i\gamma}}{\sqrt{2\left[E + (iE^{1/N}e^{i\gamma}y)^N\right]}}dy - \int_0^1 \frac{E^{1/N}e^{i\beta}}{\sqrt{2\left[E + (iE^{1/N}e^{i\beta}y)^N\right]}}dy\right\} \tag{4.9}$$

Since $\left(ie^{i\gamma}\right)^N = -1 = \left(ie^{i\beta}\right)^N$, hence

$$\begin{aligned} T &= 2\left\{\int_0^1 \frac{E^{1/N}e^{i\gamma}}{\sqrt{2\left[E-E\left(y^N\right)\right]}}dy - \int_0^1 \frac{E^{1/N}e^{i\beta}}{\sqrt{2\left[E-E\left(y^N\right)\right]}}dy\right\} \\ &= 2\left\{\int_0^1 \frac{E^{(2-N)/2N}\left(e^{i\gamma}-e^{i\beta}\right)}{\sqrt{2\left[1-\left(y^N\right)\right]}}dy\right\} \\ &= 2\left\{\frac{E^{\frac{2-N}{2N}}}{\sqrt{2}}\left(e^{i\gamma}-e^{i\beta}\right)\int_0^1 \frac{1}{\sqrt{1-\left(y^N\right)}}dy\right\} \\ &= 2\left\{\frac{E^{\frac{2-N}{2N}}}{\sqrt{2}}\left(e^{i\gamma}-e^{i\beta}\right)\sqrt{\pi}\frac{\Gamma\left(1+\frac{1}{N}\right)}{\Gamma\left(\frac{1}{2}+\frac{1}{N}\right)}\right\} \\ &= 2E^{\frac{2-N}{2N}}\left(\sqrt{2\pi}\sin\frac{\pi}{N}\right)\frac{\Gamma\left(1+\frac{1}{N}\right)}{\Gamma\left(\frac{1}{2}+\frac{1}{N}\right)} \end{aligned} \tag{4.10}$$

where we assume the 0th pair of PT-symmetric turning points within the pair of orange wedges is involved so that (3.19) is used to derive the last step. In general, for the kth pair of turning points within the kth pair of PT-symmetric Stokes wedges, we have the period

$$T = \left(2\sqrt{2\pi}E^{\frac{2-N}{2N}}\right)\cos\left[\left(\frac{2-N}{2N}+\frac{2k}{N}\right)\pi\right]\frac{\Gamma\left(1+\frac{1}{N}\right)}{\Gamma\left(\frac{1}{2}+\frac{1}{N}\right)} \qquad k=0,1,2,3\cdots \tag{4.11}$$

In order to make the total initial energy $E_0 = 1$, by (4.3) we set the initial momentum p_0 as a function of the initial position x_0

$$p_0 = \sqrt{2\left[\left(ix_0\right)^N+1\right]} \tag{4.12}$$

By using Gauss-Legendre Integrator to solve (4.2), Fig.(4.1) shows several trajectories with various initial positions x_0 with $N = 2$ and total initial energy $E_0 = 1$. All those trajectories form closed orbit with the same period $T = 4.4428829381$ which agrees with our corresponding numerical approximation. When the initial position x_0 starts right on one of the turning points, say, $x_0 = x_2$, the orbit is deformed into a straight line segment oscillating between the two turning points with the same period.

Fig.(4.2) shows the real and imaginary part of energy E versus time t for a chosen orbit with initial position $x_0 = -0.1i$. The real energy is maintained to be 1 and the imaginary energy is extremely small. The particle moves in the clockwise direction. The vertical blue dot lines on the figure indicate the exact time when the particle crosses the imaginary axis. On those regions where $\mathrm{Im}\left(E\right)$ and the vertical blue dot lines are intersected, the behavior of $\mathrm{Im}\left(E\right)$ is dramatically changed and becomes smaller. The reason to cause this behavior is unknown.

Figure 4.1: *Classical trajectories when $N = 2$ and $E_0 = 1$, where by (4.10) all orbits have the same period $T = 4.4428829381$. Particles move clockwisely in all orbits.*

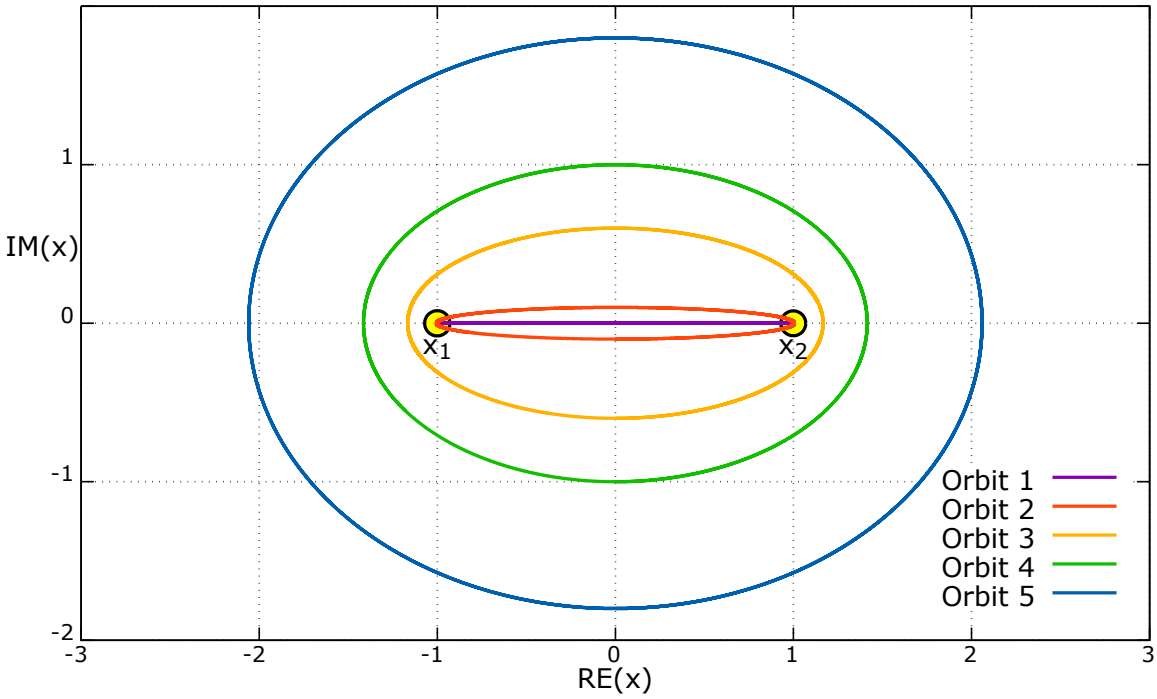

Figure 4.2: *Energy E versus time t for $N = 2$ with period $T = 4.4428829381$. The vertical blue dot lines indicate the time when the particle crosses the imaginary axis.*

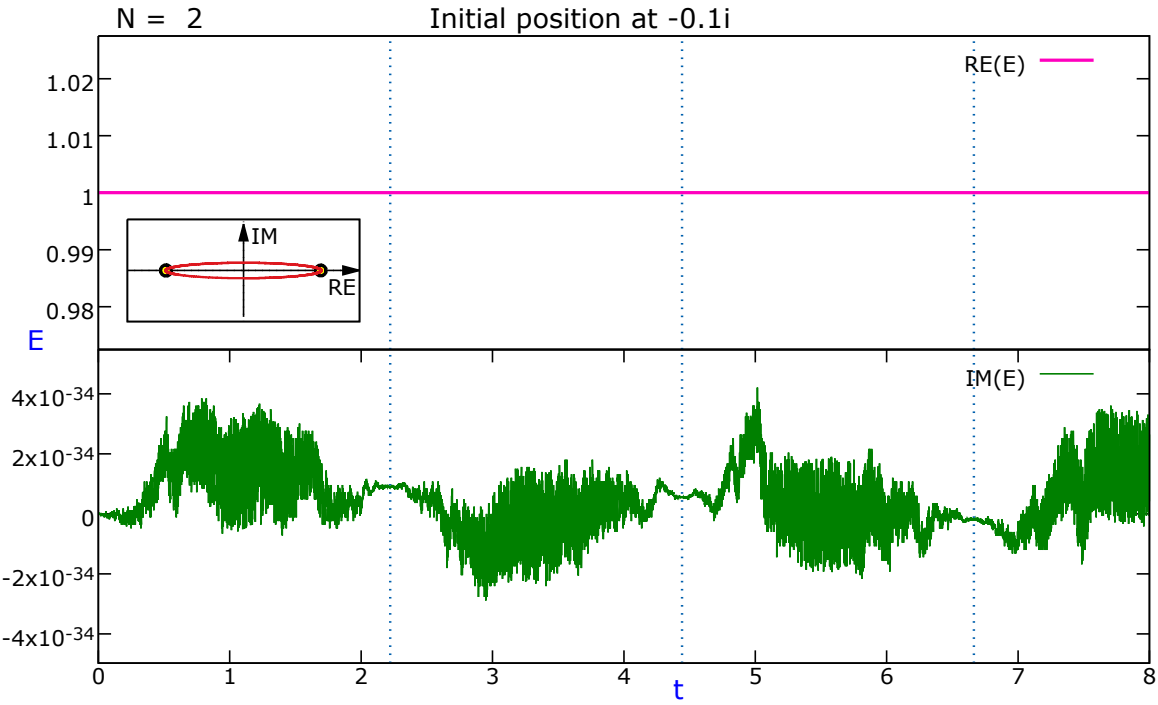

Figure 4.3: *Classical trajectories when* $N = 5$ *and* $E_0 = 1$

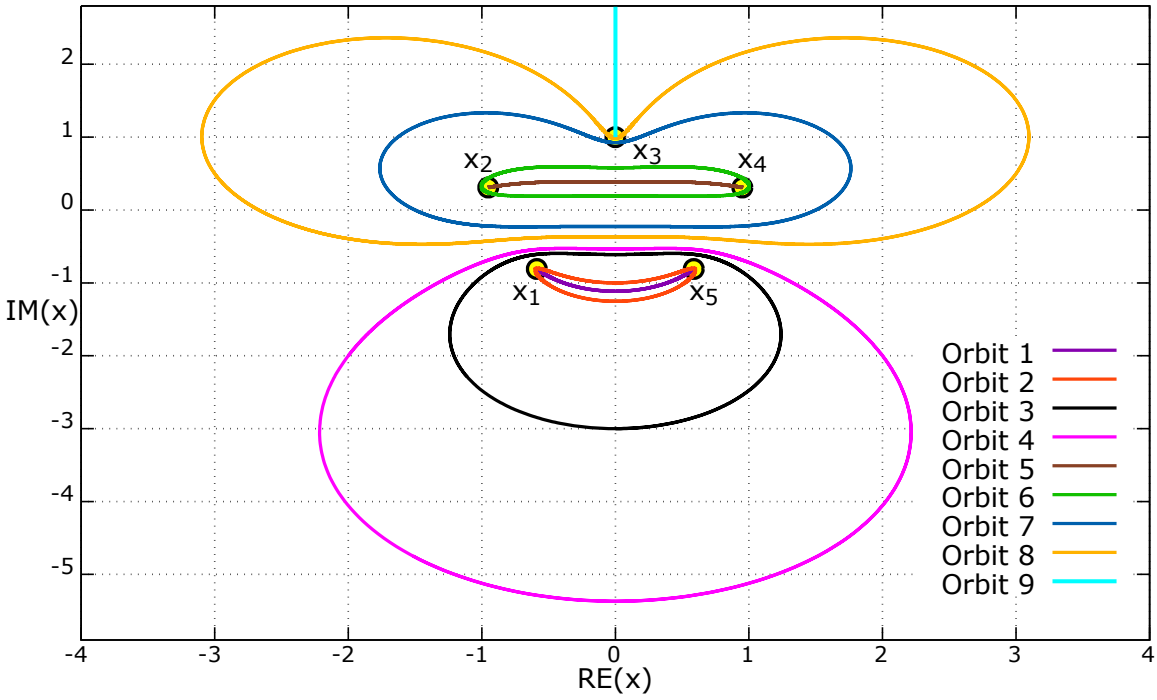

Table 4.1: *When* $N = 5$ *and* $E_0 = 1$*, the period* T *is obtained by analytical and numerical method (with numerical integration step* $dt = 0.001$*)*

	Initial position x_0	Analytical T	Numerical T
Orbit 1	On the turning point x_1		2.084
Orbit 2	$-i$	2.0843368815	2.084
Orbit 3	$-3i$		2.084
Orbit 4	$-2-2i$		2.084
Orbit 5	On the turning point x_4		3.372
Orbit 6	$1+0.3i$	3.3725279183	3.373
Orbit 7	-1.5		3.372
Orbit 8	$-3+0.5i$		3.373
Orbit 9	i	0.6440955184	0.644

Fig.(4.3) shows several orbits with various initial positions x_0 when $N = 5$. If we pick up an initial position x_0 near to the pair of turning points x_1 and x_5, then a closed orbit is formed to enclose these two turning points. If x_0 is chosen to be near to the pair of turning points x_2 and x_4, then the closed orbit encloses those two turning points instead. If x_0 is chosen to be right on the turning point, for example, $x_0 = x_4$, the orbit is deformed to be a curve segment which oscillates between the turning points x_2 and x_4. By (4.11), Tab.(4.1) shows that all orbits enclosing x_1 and x_5 have the same period $T = 2.0843368815$; All orbits

enclosing x_2 and x_4 have the same period $T = 3.3725279183$. All those analytical results are confirmed by our numerical results.

The imaginary part of the energy E for $N = 5$ for the chosen orbit shown on Fig.(4.4) does have some weird behavior[1] as time t grows, even if it is tiny. It wiggles more violently whenever cross the negative imaginary axis. However, the amplitude of the wiggle does not grow with time and still be tiny, which may be why all orbits are stable.

Figure 4.4: *Energy E versus time t for $N = 5$ with period $T = 2.0843368815$. The vertical blue dot lines indicate the time when the particle crosses the imaginary axis.*

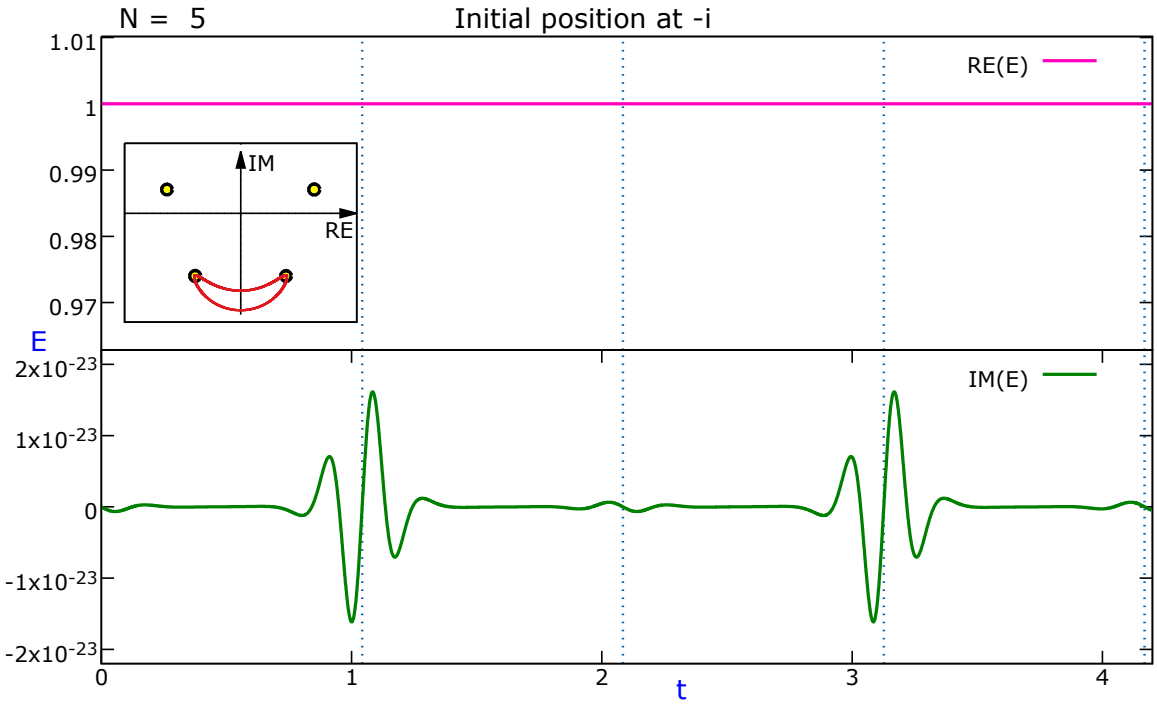

If $x_0 = x_3 = E^{1/N} e^{i\frac{\pi}{2}} = i$, then it does not form a closed orbit, instead, the particle goes from x_3 to complex infinity $i \cdot \infty$ by taking finite amount of time, which can be evaluated by

$$T = \int_i^{i\cdot\infty} \frac{dx}{\sqrt{2\left[E + (ix)^N\right]}} \tag{4.13}$$

[1] $\mathrm{Im}\,(E)$ for all other orbits for $N = 5$ have the similar behavior.

By the substitution $y = \frac{ix}{iE^{1/N}e^{i\frac{\pi}{2}}}$ and $N = 5$

$$\begin{aligned} T &= \int_1^\infty \frac{E^{1/N}e^{i\frac{\pi}{2}}}{\sqrt{2\left[E + \left(iE^{1/N}e^{i\frac{\pi}{2}}y\right)^N\right]}}dy \\ &= \int_1^\infty \frac{E^{1/5}e^{i\frac{\pi}{2}}}{E^{1/2}\sqrt{2\left[1-(y^5)\right]}}dy \\ &= i\frac{E^{(2-5)/10}}{\sqrt{2}}\int_1^\infty \frac{1}{\sqrt{1-(y^5)}}dy \\ &= 0.6440955184 \end{aligned} \tag{4.14}$$

which is also consistent with our numerical result (See Tab.(4.1)). Taking finite amount of time to reach a complex infinity means that during a short time its energy grows unbounded. However, surprisingly, this short time is extremely short - all the sudden the energy grows unbounded, which is confirmed when we look at the numerical result on its energy where both $\mathrm{Re}\,(E)$ and $\mathrm{Im}\,(E)$ suddenly grow to be huge values around $T = 0.642$.

The time $T = 0.6440955184$ for the particle to escape to the complex infinity is a "weird" value, since we so far can not find the relation between this value and other periods or orbits shown on Tab.(4.1). What do we mean by that? Consider the case for $N = 3$. If the initial position[2] starts right on the turning point x_2 (See Fig.(4.5)), by (4.13) it takes finite amount 1.7173153422 of time to escape to the complex infinity. This value is just the half of its period ($T_{N=3} = 3.434630684$), which is the time for the particle to travel in the orbit 2 starting from $-6i$ (See Fig.(4.5)) and reach the imaginary axis for its first time. Fig.(4.6) shows the energy of the particle in the orbit 1, which suddenly grows around 1.7142. The energy's behavior for $N = 5$ to escape to complex infinity is very similar to this, except that the time 0.6440955184 is not the half of any its periods shown on Tab.(4.1).

[2]For $N = 3$, if the initial position is chosen[8, p. 25] on the imaginary axis above $x = x_2$, then two cases can happen: First, the trajectory diverges to $i \cdot \infty$; Second, the particle is attracted by and comes back to the turning point x_2, then turn around and diverges to $i \cdot \infty$.

Figure 4.5: *Classical trajectories when $N = 3$ and $E_0 = 1$. The green curve shows the half of the orbit 2.*

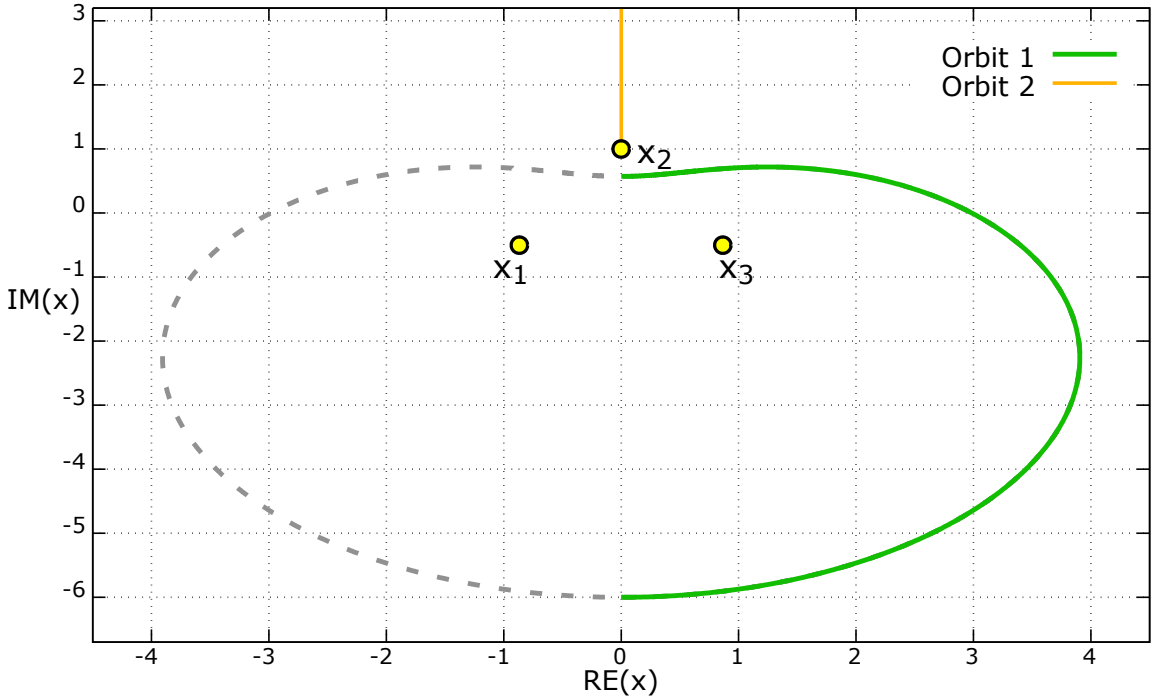

Figure 4.6: *Energy E versus time t for $N = 3$. The vertical blue dot line indicates the time of the half period of the orbit 2 from Fig.(4.5).*

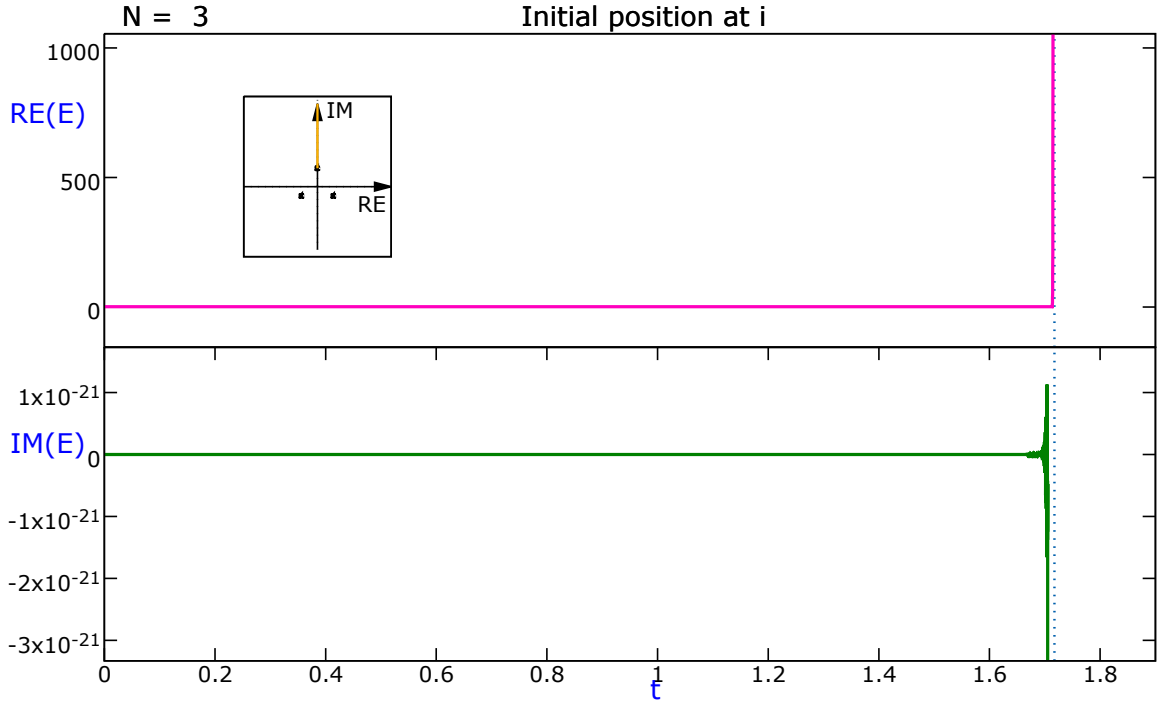

4.2.2 For $N \geq 2$ and N is fractional

How about the case when N is fractional? Fig.(4.7) shows several trajectories with $N = 2.5$ on a single Riemann sheet except the orbit[3] 7. The turning points x_2, x_3 and x_5 are not on the principal branch so that they are marked in cyan color rather than yellow. If the initial position x_0 is chosen quite near to the principal turning points, then the orbit only encloses x_1 and x_4 such that the period of the orbit can be analytically calculated by (4.10), which are consistent with our numerical approximation (See Tab.(4.2)). These orbits (orbits 1, 2, 3) are closed on all Riemann sheets. Fig.(4.8) shows the behavior of energy for this type of orbits is very similar to the case when $N = 5$ shown on Fig.(4.4).

However, when an orbit encloses any non-principal turning point, the orbit is closed only on a single Riemann sheet - when it crosses the cut on the imaginary axis, the orbit become unstable (See Fig.(4.9)). The periods of these orbits are dependent on the initial position x_0 (See Tab.(4.2)) and are harder to calculate analytically since more than two turning points are involved. Here we omit[4] how to analytically calculate these periods. If we start the initial position x_0 right on the turning point x_2, the orbit is not stable on any sheet. Its chaotic behavior is very similar to what we see on Fig.(4.9).

Figure 4.7: *Classical trajectories when $N = 2.5$ and $E_0 = 1$. We did not find any orbit which only encloses non-principal turning points.*

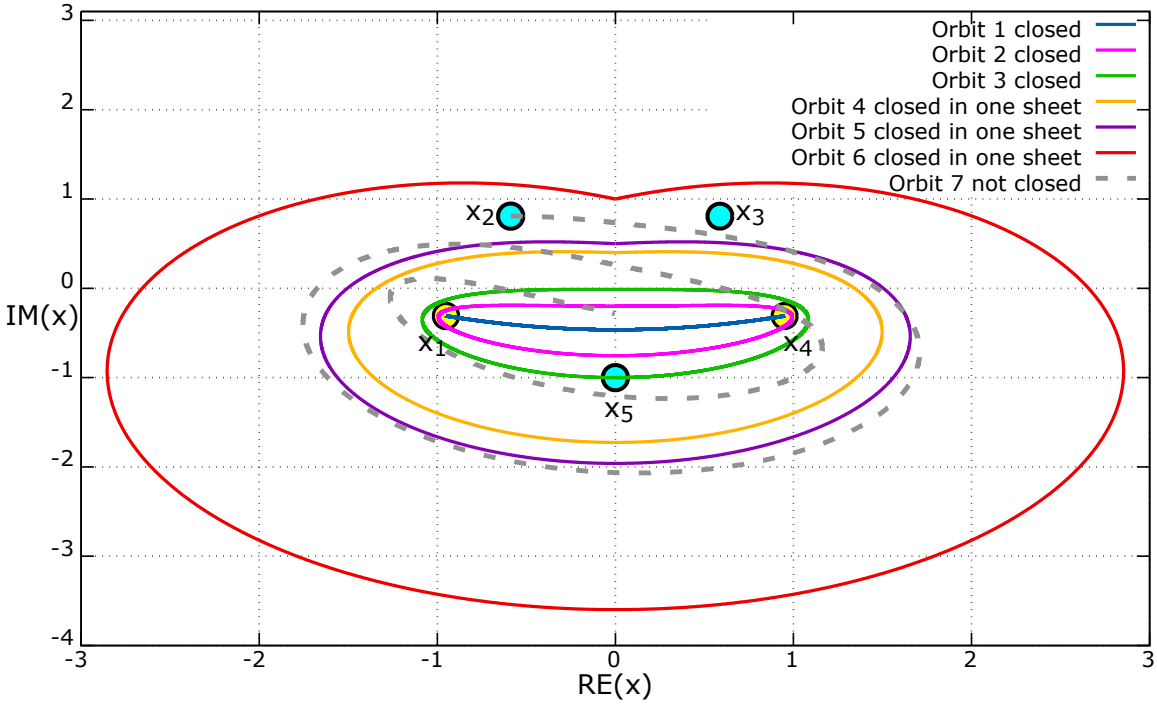

[3] On Fig.(4.7) the orbit 7 in dash-curve which starts right on the turning point x_2 is not on a single Riemann sheet since it crosses the cut on the positive imaginary axis twice.

[4] You may find some useful discussion from [8, p.30]. However, that may not work for the orbit which is closed only on a single sheet.

Figure 4.8: *Energy E versus time t for $N = 2.5$ with period $T = 3.9586963635$. The vertical blue dot lines indicate the time when the particle crosses the imaginary axis.*

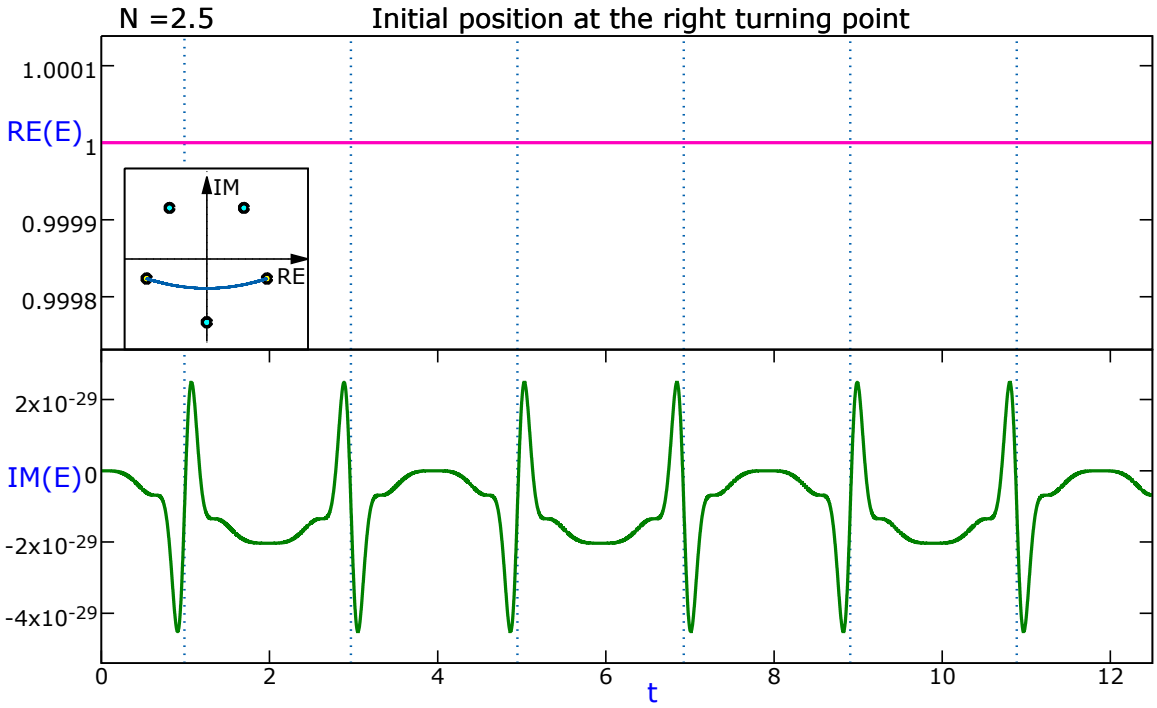

Table 4.2: *When $N = 2.5$ and $E_0 = 1$, the period T is obtained by analytical and numerical method (with numerical integration step $dt = 0.001$)*

	Initial position x_0	Analytical T	Numerical T
Orbit 1	On the turning point x_4	3.9586963635	3.959
Orbit 2	$-0.2i$		3.958
Orbit 3	On the turning point x_5		3.958
Orbit 4	$0.2 + 0.4i$	Unknown	3.813
Orbit 5	$0.5i$		3.940
Orbit 6	i		3.792
Orbit 7	On the turning point x_2	N/A	N/A

Fig.(4.9) shows what happens if we let the orbit 6 cross the cut on the positive imaginary axis. The unstable and chaotic trajectory may be caused by the influence from other non-principal turning points. Here, we want to emphasize that the trajectory never[8, p.29] intersects itself. The apparent self-intersections on Fig.(4.9) is an illusion since we put multiple Riemann sheets altogether on top to each other. Also, we have no rigorously mathematical proof to justify if the trajectory is truly chaotic or not - the claim that the trajectory is chaotic is purely based on our numerical observation.

Figure 4.9: *A classical trajectory when* $N = 2.5$, $E_0 = 1$ *and* $x_0 = i$

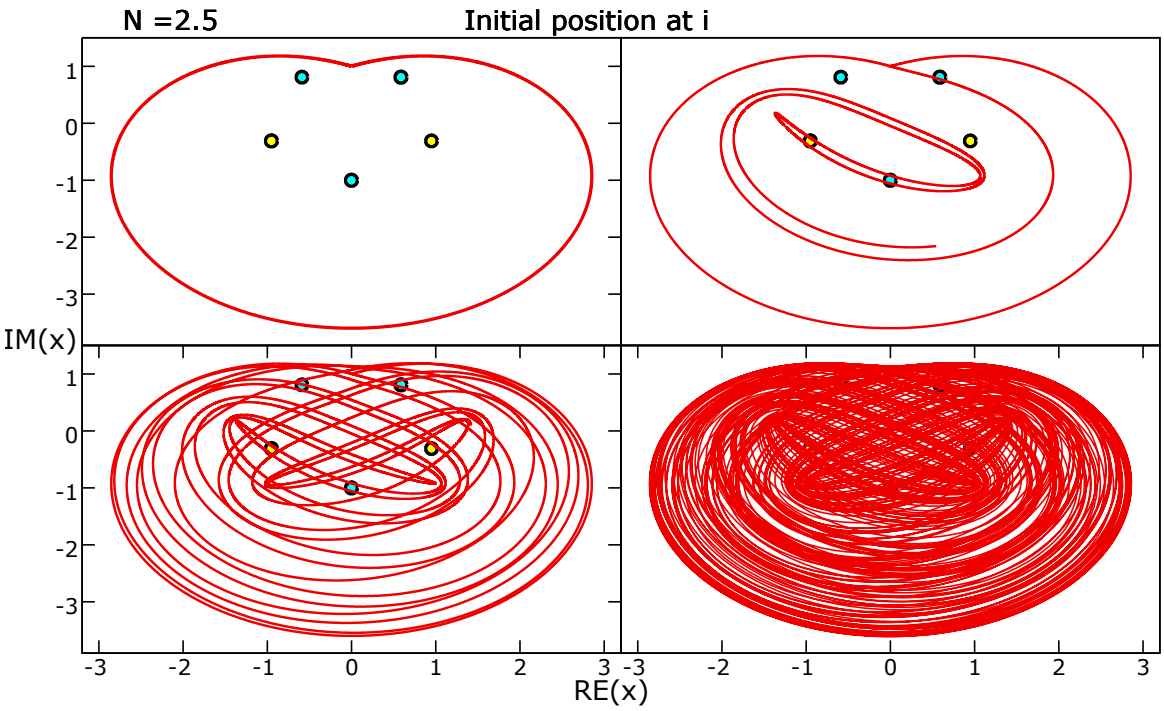

Figure 4.10: *Energy* E *versus time* t *for* $N = 2.5$ *with initial period* $T_0 = 3.792$. *The vertical blue dot lines indicate the time when the particle crosses the imaginary axis.*

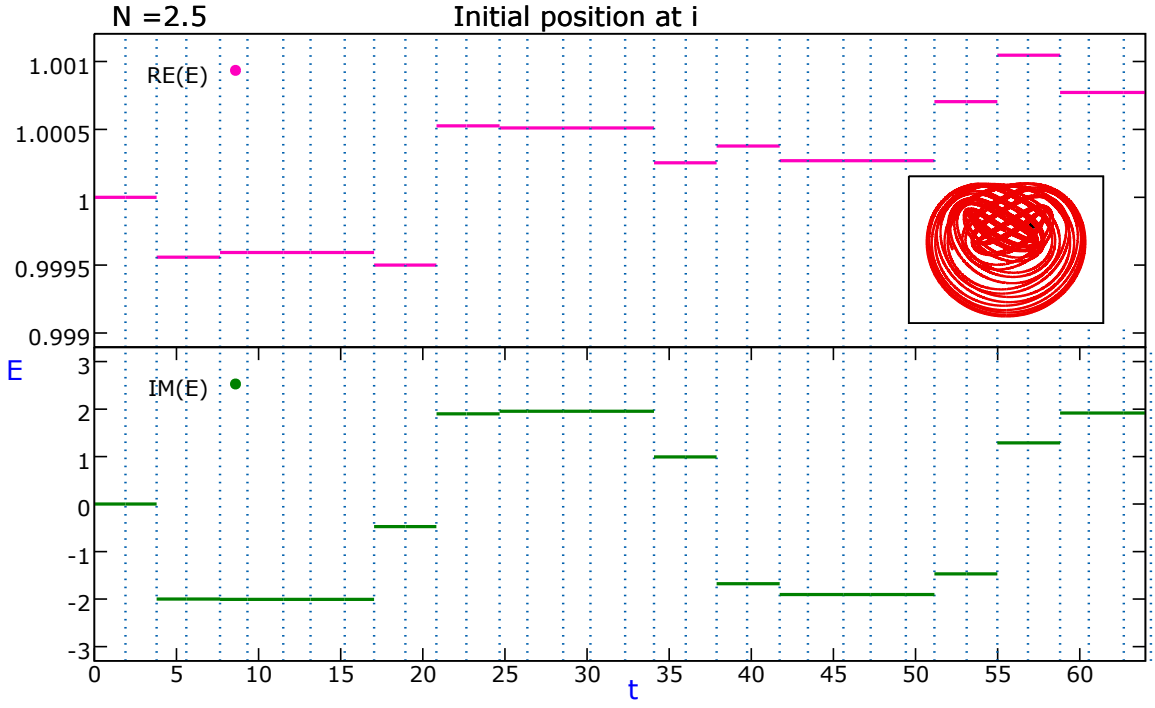

Figure 4.11: *Energy E versus longer time t for $N = 2.5$ with initial period $T_0 = 3.792$*

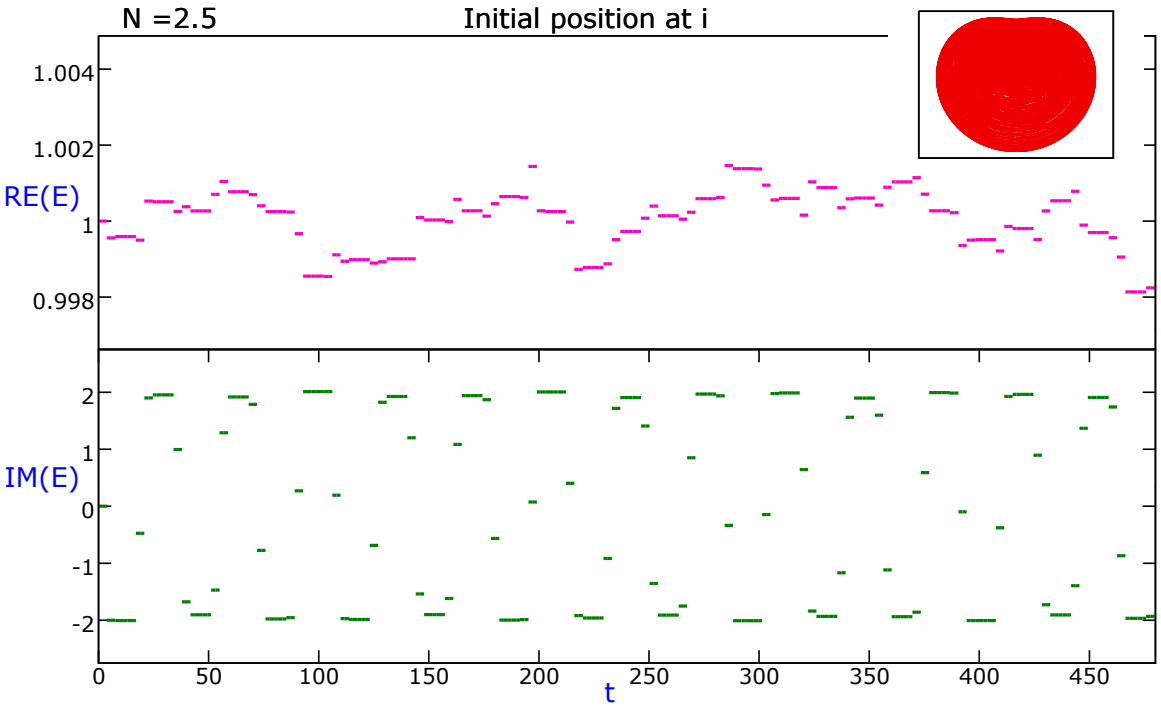

Surprisingly, these chaotic orbits all have "**quantized energy**" - energy starts to jump into a different level whenever the trajectory crosses the cut on the positive imaginary axis. After crossing the cut, the energy starts to jump again whenever crosses the imaginary axis, including the negative imaginary axis. One case the orbit 6 for $N = 2.5$ as an example is shown on Fig.(4.10), where both $\mathrm{Re}\,(E)$ and $\mathrm{Im}\,(E)$ are quantized, and the jumps from $\mathrm{Im}\,(E)$ are much more violent. Fig.(4.11) shows for longer time the pattern of the energy, whose $\mathrm{Im}\,(E)$ are bounded approximately between $+2$ and -2. Since both $\mathrm{Re}\,(E)$ and $\mathrm{Im}\,(E)$ do not grow substantially as t increases, that is why the orbit 6 does not diverge to complex infinity as t increases. We do not know why the energy jumps whenever crosses the cut. The behavior of $\mathrm{Im}\,(E)$ on Fig.(4.11) is bounded and looks like a sinusoidal pattern. If we increase the number of integration steps by decreasing dt, say $dt = 0.0001$, this sinusoidal pattern remains unchanged. However, we do not know the reason why this pattern is formed and can not predict how much the energy jumps.

4.2.3 For $N < 2$

For $N < 2$, we pick up the cases $N = 1.8$, $N = 1.6$ and $N = 1.3$ to study.

Figure 4.12: *Classical trajectories when* $N = 1.8$ *and* $N = 1.6$ *and* $E_0 = 1$

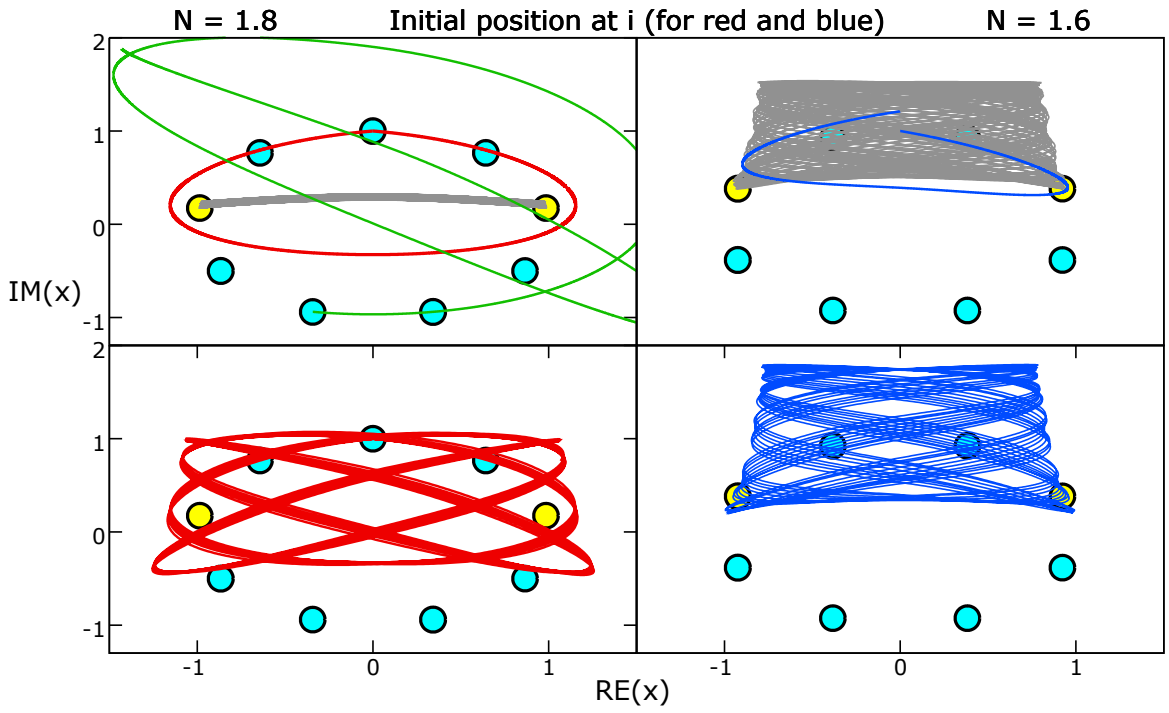

Figure 4.13: *Energy* E *versus time* t *for* $N = 1.6$ *the blue trajectory on Fig.*(4.12)

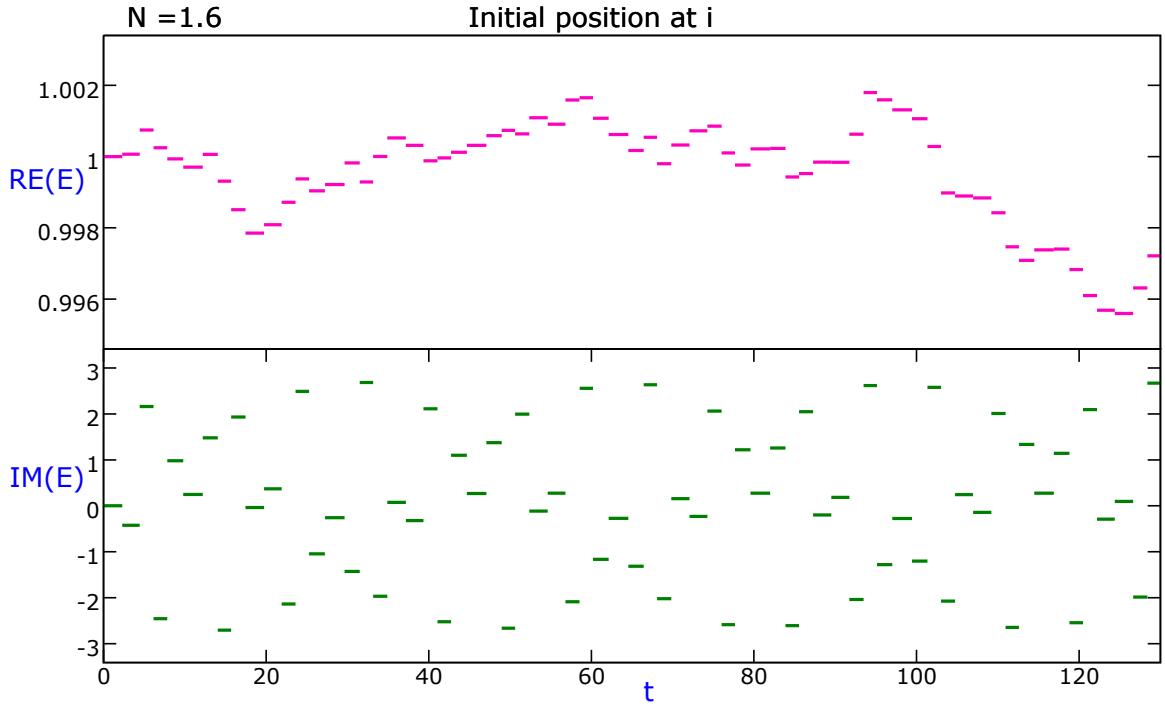

Most initial positions x_0 we tried for $N = 1.8$ do not generate closed orbits. For example, on Fig.(4.12), the green trajectory starts right on one of the non-principal turning points and is not a closed orbit. The grey trajectory starts right on one of the principal turning points and is not a closed orbit either.

It does not go to complex infinity as time increases. Instead, it behaves chaotic and forms a quite narrow band which becomes a thicker grey band (See Fig.(4.12)) in the case for $N = 1.6$.

When the initial position x_0 is chosen right on the positive imaginary axis, say, $x_0 = i$, an orbit for $N = 1.8$ can form but is closed only on a single Riemann sheet. Its period is dependent on the initial position. For $x_0 = i$, its period can only be calculated numerically to be 4.604. When it crosses the cut on the positive imaginary axis, the orbit behaves chaotic (See the red curve on Fig.(4.12)). If we further decrease $N = 1.8$ to be $N = 1.6$, with the same initial position $x_0 = i$, the trajectory is not closed on any sheet (See the blue curve on Fig.(4.12)).

Even through all those orbits are not stable, however, all orbits for $N = 1.8$ and $N = 1.6$ do not eventually diverge to complex infinity, since their energies do not grow substantially (See Fig.(4.13)). The imaginary part of energy is bounded and form a sinusoidal pattern again as time grows. Again, we do not know how this sinusoidal pattern is formed.

Figure 4.14: *Classical trajectories when* $N = 1.3$ *and* $E_0 = 1$

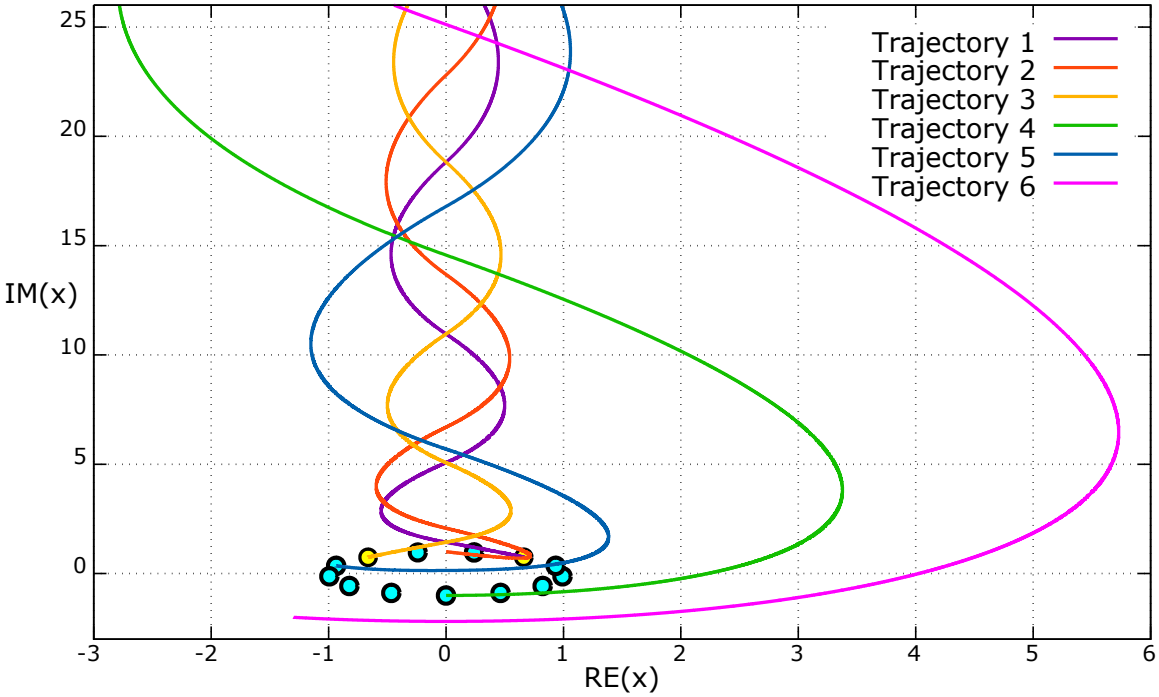

Figure 4.15: *Energy E versus time t for $N = 1.3$*

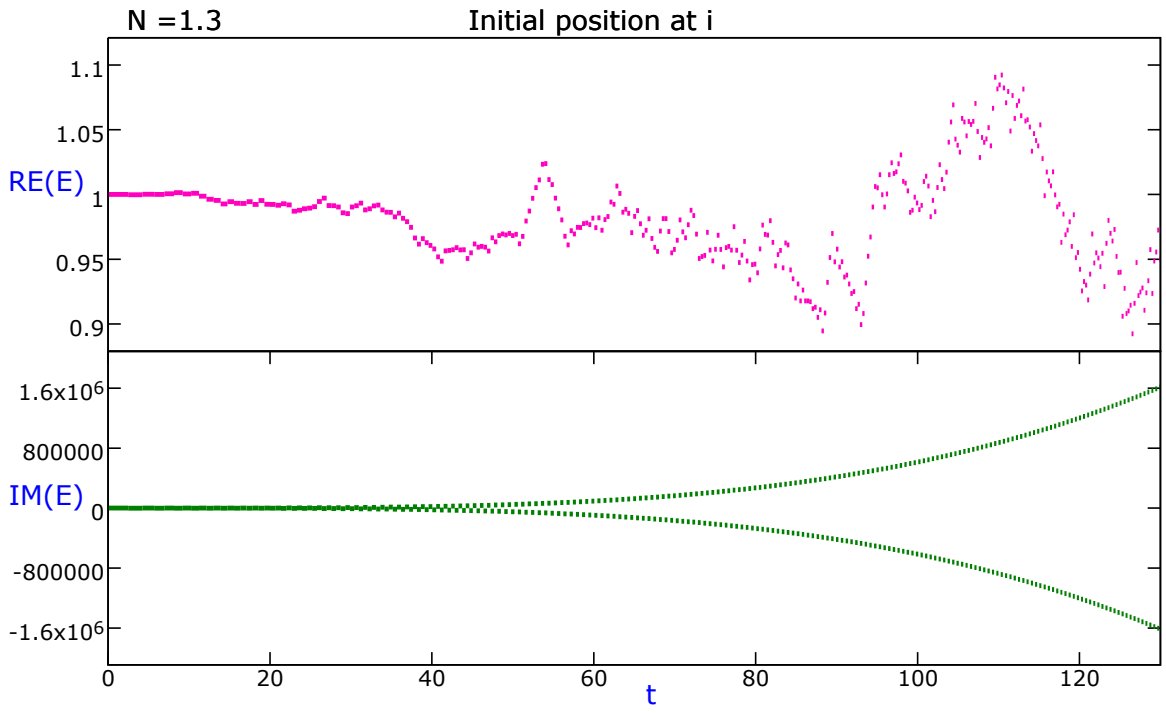

For $N = 1.3$, all trajectories with various initial positions are divergent to $i \cdot \infty$ (See Fig.(4.14)), because Fig.(4.15) shows that the imaginary part of the energy E grows exponentially. Therefore, we conclude that the increment of $\mathrm{Im}\,(E)$ determine how stable the system is.

4.2.4 Summarize what we found in this section

- When $N \geq 2$ and N is an integer, except a few trajectories go to complex infinity within finite amount of time, most trajectories form orbits closed on any Riemann sheet. The periods of these orbits can be analytically calculated and dependent on which pair of turning points its orbit encloses.

- When $N \geq 2$ and N is fractional, some trajectories form orbits closed on any Riemann sheet, whose period can be analytically calculated. Some other trajectories form orbits closed on only one Riemann sheet, and are eventually chaotic if $\mathrm{Im}\,(E)$ is bounded, or divergent to complex infinity if $\mathrm{Im}\,(E)$ is not bounded. Furthermore, the quantization process of energy with respect to time t starts whenever a trajectory crosses the cut on the positive imaginary axis.

- When $1 < N < 2$, trajectories are not stable - they are either chaotic if $\mathrm{Im}\,(E)$ is bounded or divergent to complex infinity if $\mathrm{Im}\,(E)$ is not bounded. As $N \to 1$, the trajectory becomes more unstable and more likely divergent to complex infinity. As same as the last case, energy appears to be quantized whenever a trajectory crosses the cut on the positive imaginary axis.

4.3 Simple complex pendulum

4.3.1 Classical tunneling

Figure 4.16: *A simple pendulum*

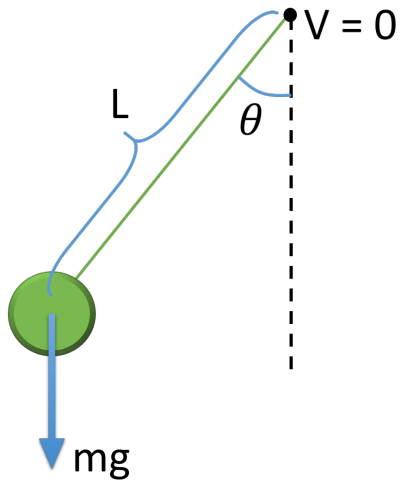

For a simple pendulum[22]

$$x = L\sin\theta \qquad y = -L\cos\theta \tag{4.15}$$

So its Hamiltonian is

$$\mathcal{H} = \frac{1}{2}mL^2\dot{\theta}^2 - mgL\cos\theta \tag{4.16}$$

Set $m = 1$, $L = 1$ and replace θ by x, we obtain

$$\mathcal{H} = \frac{1}{2}p^2 - g\cos x \neq \frac{1}{2}\left(p\overline{p}\right) - g\cos x \tag{4.17}$$

which satisfies $\mathcal{H} - \left(\hat{P}\hat{T}\right)\mathcal{H}\left(\hat{P}\hat{T}\right) = 0$. Therefore, $\mathcal{H}$ is PT-symmetric but non-Hermitian for $p \in \mathbb{C}$ and $x \in \mathbb{C}$. The Hamilton's equations are

$$\dot{p} = -\frac{\partial\mathcal{H}}{\partial x} = -g\sin x \qquad \dot{x} = \frac{\partial\mathcal{H}}{\partial p} = p \tag{4.18}$$

with total energy

$$E = \frac{p^2}{2} + V\left(x\right) = \frac{\left(\dot{x}\right)^2}{2} - g\cos x \tag{4.19}$$

The turning points for $|E| \leq 1$ are

$$\begin{aligned} E &= -g\cos x \\ \Longrightarrow x_* &= \arccos\left(-\frac{E}{g}\right) \end{aligned} \tag{4.20}$$

To make the initial energy $E_0 = 0$, we set (4.19) to be zero so that

$$\dot{x_0} = p_0 = \sqrt{2g \cos x_0} \tag{4.21}$$

For simplicity we set $g = 1$. By (4.20) the turning points for $E_0 = 0$ are

$$x_* = \frac{\pi}{2} + n\pi \qquad n \in \mathbb{Z} \tag{4.22}$$

which are displayed on Fig.(4.17) along with orbits starting in various initial positions.

Figure 4.17: *Classical trajectories for complex pendulum with $E_0 = 0$ and period $T = 7.4162987092$. All particles in closed orbits move in clockwise direction.*

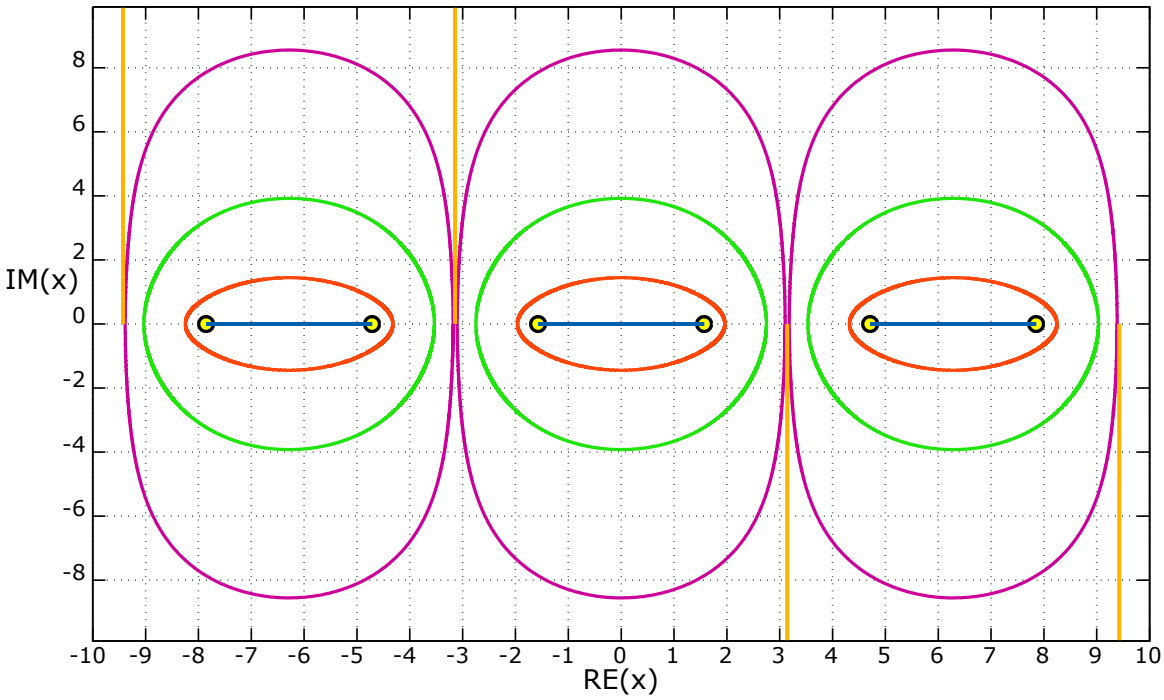

Fig.(4.17) shows that except that the particles with initial positions starting from $n\pi$ escape to complex infinity, all other trajectories are stable orbits with the same period

$$\begin{aligned} T &= \oint_c \frac{dx}{\sqrt{2\left[E - V(x)\right]}} \\ &= \oint_c \frac{dx}{\sqrt{2\left[E + \cos(x)\right]}} \\ &= 2\int_{x_-}^{x_+} \frac{dx}{\sqrt{2\left[E + \cos(x)\right]}} \\ &= 2\int_{-\frac{\pi}{2}}^{\frac{\pi}{2}} \frac{dx}{\sqrt{2\cos(x)}} \\ &= 7.4162987092 \end{aligned} \tag{4.23}$$

which is consistent with our numerical approximation $T \approx 7.416$. The horizontal line segments appeared on Fig.(4.17) correspond to the real trajectories, where particles swing between two turning points. All particles with stable orbits are well-behaved in that they stay in the same regions and swing around the same pairs of turning points forever.

Figure 4.18: *Energy E versus time t with $E_0 = 0$ for particle to escape to the complex infinity, starting from $x_0 = \pi$ shown on Fig.(4.17). The corresponding setup is shown on Fig.(4.19). Note that when $x_0 = \pi$, the pendulum still tries to form an elliptic orbit, but the radius of this orbit becomes infinite long. To maintain the constant period T, the speed of the pendulum becomes infinite as well. This causes unstable numerical result for infinite speed, and therefore the numerical energy blows up when speed becomes huge.*

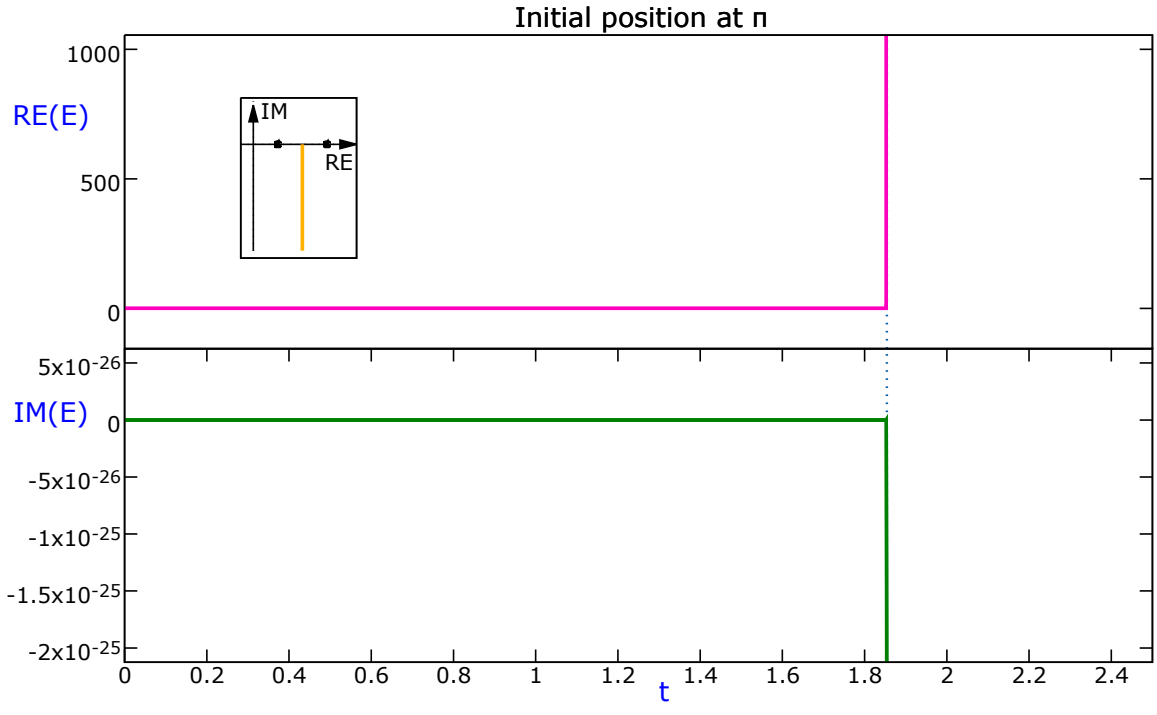

Figure 4.19: *The initial position of the pendulum with $E_0 = 0$ is chosen to be $x_0 = \theta_0 = \pi$, which is inside the dynamically inaccessible region because $V > 0$ and $E_0 < V$ in this region. In this setup, the pendulum is in an unstable equilibrium position. Intuitively, the pendulum should stay at this position forever if $E_0 = 0$. However, this is not true in this case, because (4.21) implies that for the chosen E_0 and x_0, the velocity of the pendulum is non-zero, but equal to an purely imaginary number $\sqrt{2}i$, and that is why the pendulum starts to move along the vertical direction in the complex plane of x.*

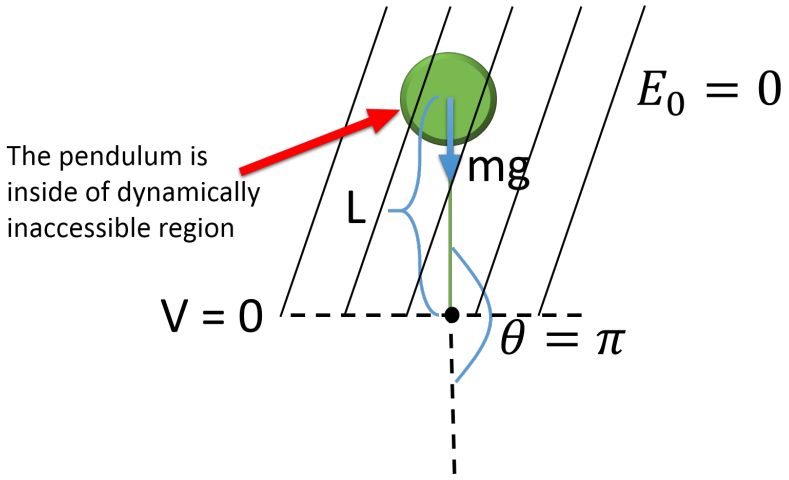

If the initial position x_0 is chosen to be right on $+\pi$ as an example shown on Fig.(4.19) (dynamically inaccessible region), then the time for the particle to escape to the complex infinity is

$$T = \int_{\pi}^{\pi - i\cdot\infty} \frac{d\,x}{\sqrt{2\cos(x)}} = 1.8540746800 \tag{4.24}$$

which is also consistent with our numerical approximation $T \approx 1.854$, when its energy suddenly increases (See Fig.(4.18)). Note that $T \approx 1.854$ is the quarter of the pendulum's period, during which the orbit from Fig.(4.20) crosses the negative imaginary axis for its first time. The energy for this ordinary orbit is very similar to Fig.(4.4), whose energy wiggles relatively more intense whenever crosses imaginary axis.

Figure 4.20: *Energy E versus time t with $E_0 = 0$ for one of orbits shown on Fig.(4.17). The vertical blue dot lines indicate the time when the particle crosses the imaginary axis.*

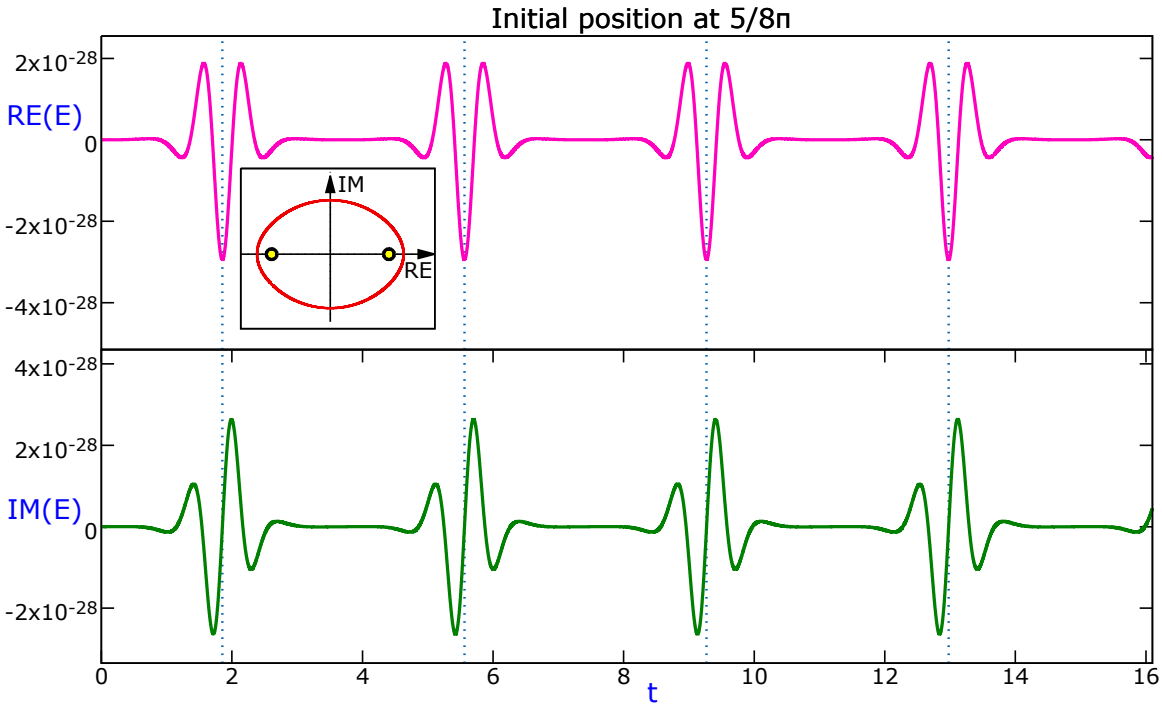

Now let's set $E_0 = \frac{1}{2}$ by using $\dot{x}_0 = p_0 = \sqrt{2\cos x_0 + 1}$. By (4.20) the turning points for $E_0 = \frac{1}{2}$ are

$$x_* = \arccos\left(-\frac{1}{2}\right) = \frac{2}{3}\pi + 2n\pi \text{ or } \frac{4}{3}\pi + 2n\pi \qquad n \in \mathbb{Z} \tag{4.25}$$

which are shown on Fig.(4.21) along with orbits starting in various initial positions. Since in the current case the initial energy E_0 is real and positive, we do not see much difference between Fig.(4.17) and Fig.(4.21), except that the position of the turning points are changed a little bit and for $\mathrm{Re}\,(x) > 0$, the direction of escaping to complex infinity is reversed.

Figure 4.21: *Classical trajectories for complex pendulum with* $E_0 = \frac{1}{2}$ *and period* $T = 8.6260625694$. *All particles in closed orbits move in counter-clockwise direction.*

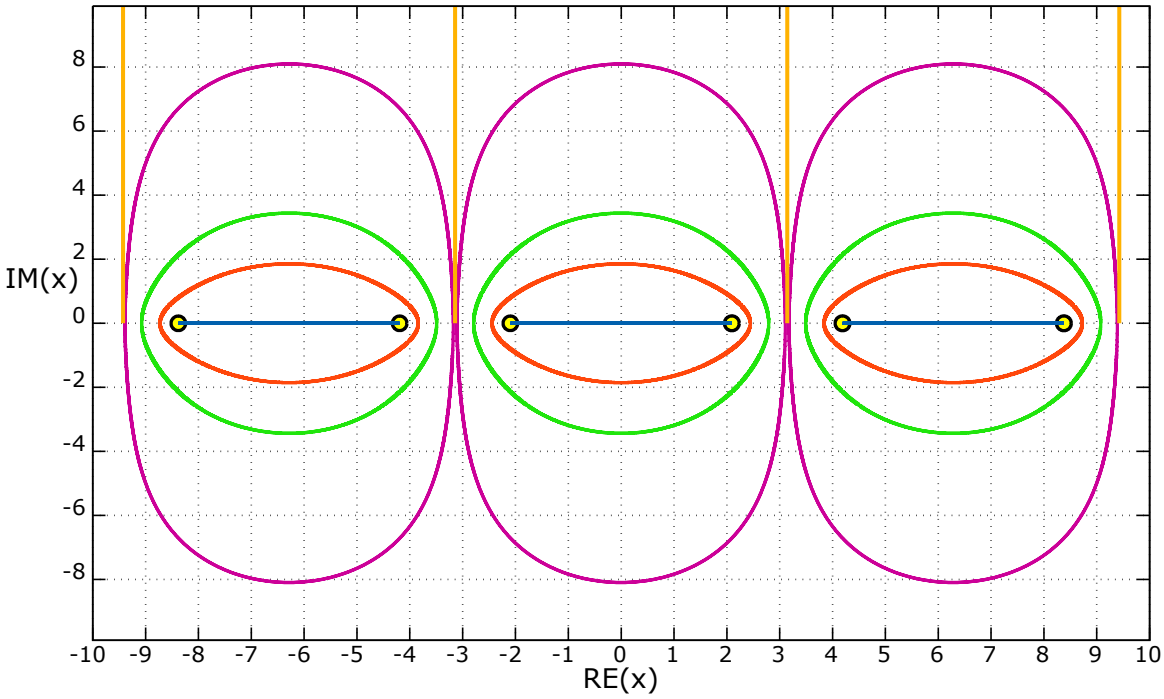

Figure 4.22: *A classical trajectory for complex pendulum with* $E_0 = \frac{1}{2}i$ *and* $x_0 = 0$

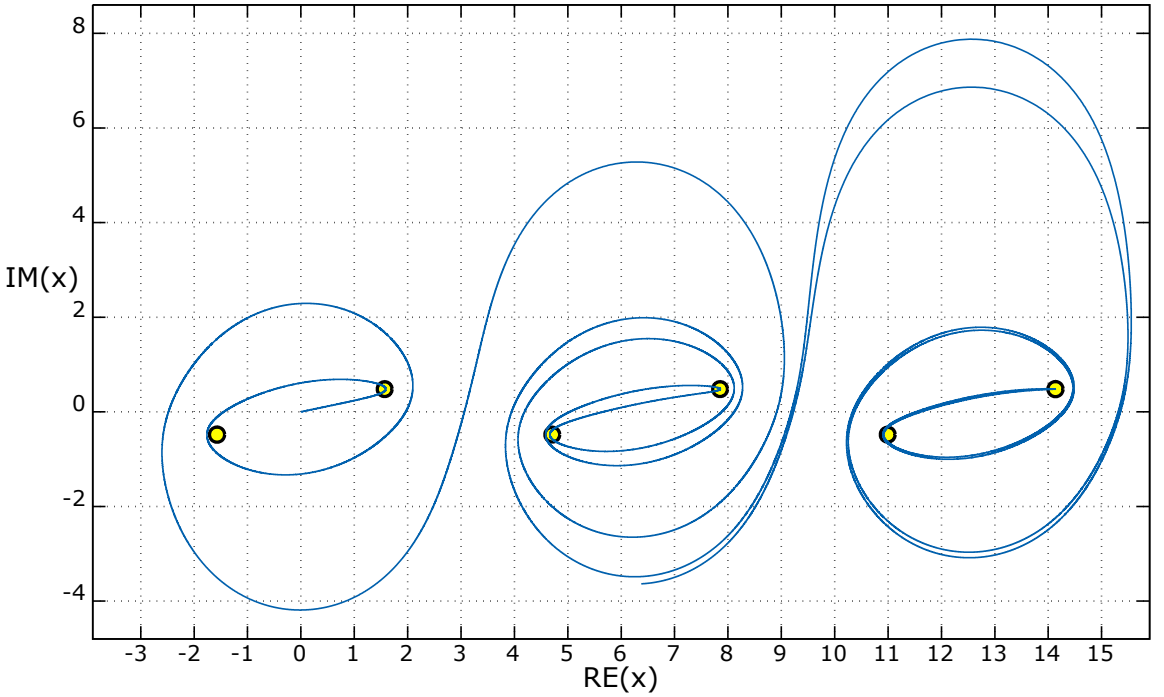

What will happen if $E_0 = \frac{1}{2}i$? By (4.20) the turning points for $E_0 = \frac{1}{2}i$ are

$$x_* = \arccos\left(-\frac{1}{2}i\right) = \frac{\pi}{2} + n\pi + i\,(-1)^n \sinh^{-1}\left(\frac{1}{2}\right) \qquad n \in \mathbb{Z} \tag{4.26}$$

where $\sinh^{-1}\left(\frac{1}{2}\right) = 0.4812118251$. If still use (4.23) to evaluate the period, then

$$T = \int_{-\frac{\pi}{2}-i\cdot\sinh^{-1}\left(\frac{1}{2}\right)}^{\frac{\pi}{2}+i\cdot\sinh^{-1}\left(\frac{1}{2}\right)} \frac{dx}{\sqrt{2\left[\frac{1}{2}+\cos(x)\right]}} = 7.2104248983 + 0.7781143655i \qquad (4.27)$$

a complex period is obtained. So far, we consider such complex period as physically unachievable.

By choosing the initial position x_0 at the origin, Fig.(4.22) shows a single trajectory, which is not a closed orbit and after a while, the particle is no longer confined within the same region and attracted by adjacent pair of turning points. Since this classical behavior resembles quantum tunneling, we call it as "**classical tunneling**", which is caused by allowing the particle to possess complex or purely imaginary energy and the ability to travel in the complex plane instead of real axis. The energy for this trajectory is well-behaved since, numerically, $\mathrm{Re}(E)$ stays at 0 and $\mathrm{Im}(E)$ at $\frac{1}{2}i$ all the time with any wiggle. This implies that during the given time the trajectory might have not crossed any branch cut, so that the trajectory on Fig.(4.22) is still on a single Riemann sheet, on which the trajectory never intersects itself.

Figure 4.23: *A classical trajectory for complex pendulum with* $E_0 = 0.5 + 0.1i$ *and* $x_0 = 0$

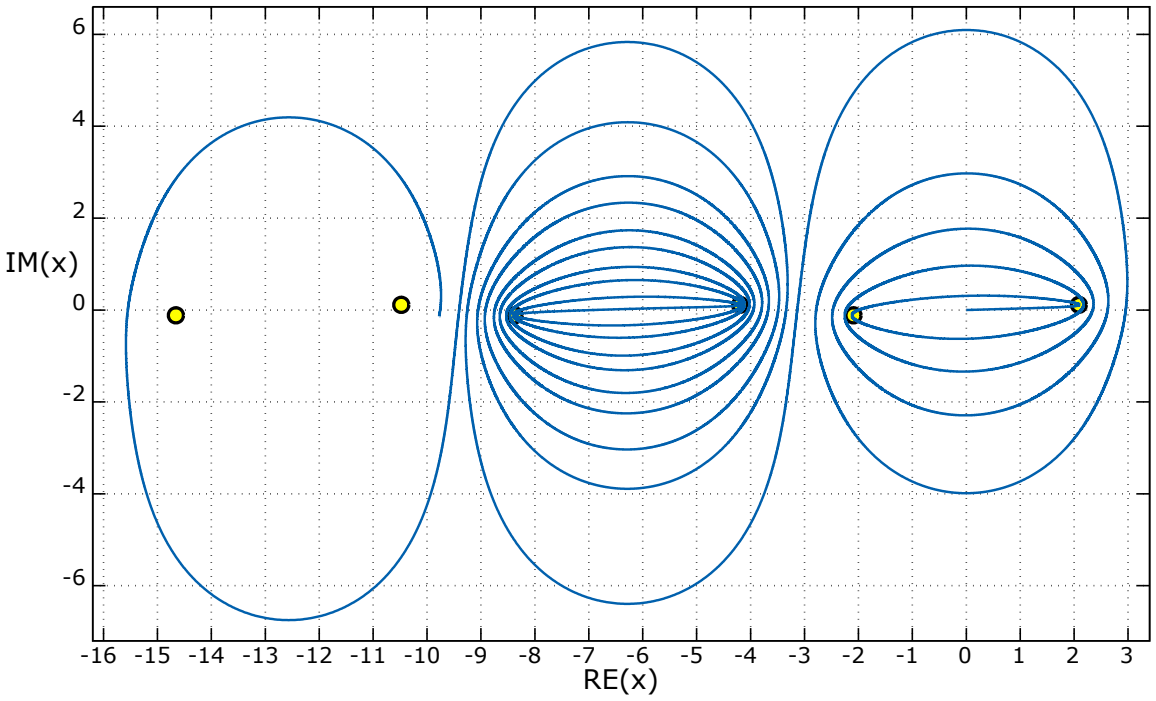

However, it's more instructive to add a little imaginary energy into a real-energy-system and observe its behavior. Let's set $E_0 = 0.5 + 0.1i$ so that the energy of the particle is dominated by real energy which is five times of its imaginary part. By (4.20) the turning points for $E_0 = 0.5 + 0.1i$ are

$$x_* = \arccos(-0.5 - 0.1i) = \frac{\pi}{2} + n\pi + (-1)^n \sin^{-1}(0.5 + 0.1i) \qquad n \in \mathbb{Z} \qquad (4.28)$$

where $\sin^{-1}(0.5+0.1i) = 0.5198083869 + 0.1149653221i$. As Fig.(4.23) shows, all turning points are no longer on the real axis, instead, they tilt a little bit so that each pair of turning points is asymmetric with respect to any vertical line. Such asymmetry causes the particle with initial position at the origin to leave[5] the real axis and form non-closed orbit. Eventually, the particle - again - is able to do the "classical tunneling". We find that the larger amount of imaginary energy it possesses, the shorter time the particle needs to finish tunneling and the more unstable the orbit is.

Figure 4.24: *Well-behaved energy E versus time t with $E_0 = 0.5 + 0.1i$ and $x_0 = 0$*

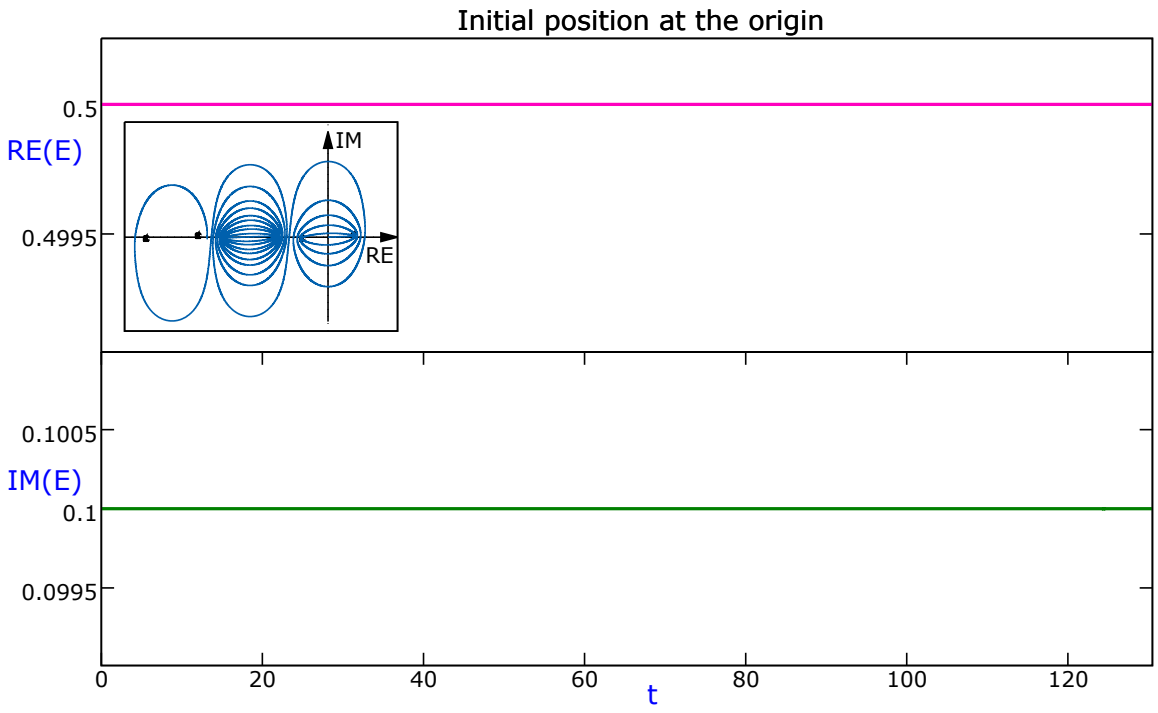

4.3.2 A deterministic model to explain why large object can not tunnel

In our real life, why can't a large object tunnel? Well, based on our study of the complex pendulum, we make the following conjecture:

A large object consists of many small particles. All of these small particles have different and complex energies, which enable them to tunnel. The real part of all these energies is non-negative, however the imaginary part of all these energies can be positive, zero or negative. The energy of the large object is the sum of all those particles' energies, so that the real part of the energy of the large object is much larger in magnitude than its imaginary part because the positive imaginary parts of particles' energies are statistically canceled by the negative imaginary parts. Most likely, after cancellation the large object only has a tiny amount of imaginary energy, so tiny that the large object may be unable to finish tunneling during the life time of universe.

[5] If there was no such asymmetry, the particle with initial position at the origin would still be confined on the real axis and oscillate between a pair of turning points forever.

Chapter 5

Conclusion

The energy spectra for the eigenfunction $\psi(x)$ from the PT-symmetric Hamiltonian $\mathcal{H} = p^2 - (ix)^N$ were studied in detail by numerically solving the corresponding Schrodinger equation within the complex plane of x with boundary condition $\psi(x) \to 0$ and $\psi'(x) \to 0$ as $|x| \to \infty$. The WKB method and phase integral method are used to further understand the relation among the broken and unbroken PT-symmetry and non-integer N. In the end, we briefly explore the classical aspect of the Hamiltonian by solving the corresponding Hamilton's equations. We believe that our study provides an interesting, comprehensive and clear introduction about PT-symmetry and differential equation in complex plane to physics graduate students and professors.

References

[1] H. Alaeian and J. A. Dionne. Parity-time-symmetric plasmonic metamaterials. *Physical Review A*, 89(3):033829, 2014. 1.4

[2] J. Alexandre, N. Houston, and N. E. Mavromatos. Dynamical supergravity breaking via the super-Higgs effect revisited. *Physical Review D*, 88(12):125017, 2013. 1.1

[3] J. Alexandre, N. Houston, and N. E. Mavromatos. Inflation via gravitino condensation in dynamically broken supergravity. *International Journal of Modern Physics D*, 24(04):1541004, 2015. 1.1

[4] A. G. Anderson and C. M. Bender. Complex trajectories in a classical periodic potential. *J.Phys.*, A45:455101, Nov 2012.

[5] T. Aoki, T. Koike, and Y. Takei. Vanishing of Stokes curves. pages 1–22, 2002. 3.4.7.5

[6] P. Baldwin. Asymptotic estimates of the eigenvalues of a sixth-order boundary-value problem obtained by using global phase-integral methods. *Philosophical Transactions of the Royal Society of London A: Mathematical, Physical and Engineering Sciences*, 322(1566):281–305, 1987. 3.4.5, 3.4.7.2

[7] C. M. Bender. Introduction to *PT*-symmetric quantum theory. *Contemp.Phys.*, 46:277–292, 2005. 1.2

[8] C. M. Bender. Making sense of non-Hermitian Hamiltonians. *Rept. Prog. Phys.*, 70:947, 2007. 1, 1.1, 1.1, 1.2, 1.2, 1.2, 2.3.2.2, 4.1, 2, 4, 4.2.2

[9] C. M. Bender, M. Berry, P. N. Meisinger, V. M. Savage, and M. Simsek. Complex WKB Analysis of Energy-Level Degeneracies of Non-Hermitian Hamiltonians. *Journal of Physics A: Mathematical and General*, 34:L31L36, 2001. 3.4, 3.4.5, 3.4.7, 3.4.7.2

[10] C. M. Bender and S. Boettcher. Real spectra in non-hermitian hamiltonians having *PT* symmetry. *Phys. Rev. Lett.*, 80:5243–5246, Jun 1998. 1.4, 2.1, 3.2, 3.2

[11] C. M. Bender, S. Boettcher, P. N. Meisinger, and Q. Wang. Two-point Green's function in *PT*-symmetric theories. *Physics Letters A*, 302(5):286–290, 2002. 1.2

[12] C. M. Bender, S. Boettcher, and V. M. Savage. Conjecture on the interlacing of zeros in complex Sturm–Liouville problems. *Journal of Mathematical Physics*, 41(9):6381–6387, 2000. 1.2, 1.2

[13] C. M. Bender, S. F. Brandt, J. H. Chen, and Q. H. Wang. Ghost busting: *PT*-symmetric interpretation of the Lee model. *Phys. Rev. D*, 71:025014, Jan 2005. 1.1

[14] C. M. Bender, D. C. Brody, and D. W. Hook. Quantum effects in classical systems having complex energy. *Journal of Physics A: Mathematical and Theoretical*, 41(35):352003, 2008.

[15] C. M. Bender, D. C. Brody, and H. F. Jones. Complex extension of quantum mechanics. *Phys. Rev. Lett.*, 89:270401, Dec 2002. 1.2

[16] C. M. Bender, D. C. Brody, H. F. Jones, and B. K. Meister. Faster than Hermitian quantum mechanics. *Physical Review Letters*, 98(4):040403, 2007. 1.1

[17] C. M. Bender, J. H. Chen, D. W. Darg, and K. A. Milton. Classical trajectories for complex hamiltonians. *Journal of Physics A: Mathematical and General*, 39(16):4219, 2006. 4.1

[18] C. M. Bender and D. W. Darg. Spontaneous breaking of classical *PT*-symmetry. *arXiv preprint hep-th/0703072*, 2007.

[19] C. M. Bender, J. Feinberg, D. W. Hook, and David J. Weir. Chaotic systems in complex phase space. *Pramana*, 73:453–470, 2009.

[20] C. M. Bender, A. Fring, and J. Komijani. Nonlinear eigenvalue problems. *Journal of Physics A: Mathematical and Theoretical*, 47(23):235204, 2014. 1.1

[21] C. M. Bender, M. Gianfreda, and S. P. Klevansky. Systems of coupled *PT*-symmetric oscillators. *Physical Review A*, 90(2):022114, 2014. 1.4

[22] C. M. Bender, D. D. Holm, and D. W. Hook. Complex trajectories of a simple pendulum. *Journal of Physics A: Mathematical and Theoretical*, 40(3):F81, 2006. 4.1, 4.3.1

[23] C. M. Bender and D. W. Hook. Quantum tunneling as a classical anomaly. *J.Phys.*, A44:372001, 2011.

[24] C. M. Bender, D. W. Hook, and S. P. Klevansky. Negative-energy *PT*-symmetric hamiltonians. *J.Phys.*, A45:444003, 2012.

[25] C. M. Bender, D. W. Hook, N. E. Mavromatos, and S. Sarkar. Infinite class of *PT*-symmetric theories from one timelike liouville lagrangian. *Physical review letters*, 113(23):231605, 2014. 1.1

[26] C. M. Bender, D. W. Hook, N. E. Mavromatos, and S. Sarkar. *PT*-symmetric interpretation of unstable effective potentials. *arXiv preprint arXiv:1506.01970*, 2015. 1.1, 1.1

[27] C. M. Bender and J. Komijani. Painlevé transcendents and *PT*-symmetric Hamiltonians. *Journal of Physics A: Mathematical and Theoretical*, 48(47):475202, 2015. 1.1

[28] C. M. Bender and P. D. Mannheim. Giving up the ghost. *Journal of Physics A: Mathematical and Theoretical*, 41(30):304018, 2008.

[29] C. M. Bender and S. A. Orszag. *Advanced Mathematical Methods for Scientists and Engineers I: Asymptotic Methods and Perturbation Theory*. Springer, 1999.

[30] C. M. Bender and A. Turbiner. Analytic continuation of eigenvalue problems. *Physics Letters A*, 173(6):442–446, 1993. (document), 3.1, 3.3, 3.1, 3.2

[31] H. L. Berk, W. M. Nevins, and K. V. Roberts. New Stokes' line in WKB theory. *Journal of Mathematical Physics*, 23(6):988–1002, 1982. 3.4.7.6, 3.4.7.6

[32] S. Bittner, B. Dietz, U. Günther, H. L. Harney, M. Miski-Oglu, A. Richter, and F. Schäfer. *PT*-symmetry and spontaneous symmetry breaking in a microwave billiard. *Physical review letters*, 108(2):024101, 2012. 1.4

[33] I. L. Buchbinder and S. D. Odintsov. Effective action in multidimensional (super) gravities and spontaneous compactification (quantum aspects of Kaluza-Klein theories). *Fortschritte der Physik/Progress of Physics*, 37(4):225–259, 1989. 1.1

[34] John C Butcher. Implicit Runge-Kutta processes. *Mathematics of Computation*, 18(85):50–64, 1964. 2.3.1

[35] N. M. Chtchelkatchev, A. A. Golubov, T. I. Baturina, and V. M. Vinokur. Stimulation of the fluctuation superconductivity by *PT*-symmetry. *Physical review letters*, 109(15):150405, 2012. 1.4

[36] P. Dorey, C. Dunning, and R. Tateo. Spectral equivalences, Bethe ansatz equations, and reality properties in *PT*-symmetric quantum mechanics. *Journal of Physics A: Mathematical and General*, 34(28):5679, 2001. 2

[37] R. Fleury, D. Sounas, and A. Alù. An invisible acoustic sensor based on parity-time symmetry. *Nature communications*, 6, 2015. 1.4

[38] U. Günther and B. F. Samsonov. Naimark dilated *PT*-symmetric brachistochrone. *Physical review letters*, 101(23):230404, 2008. 1.1

[39] A Guo, G. J. Salamo, D. Duchesne, R. Morandotti, M. Volatier-Ravat, V. Aimez, G. A. Siviloglou, and D. N. Christodoulides. Observation of *PT*-symmetry breaking in complex optical potentials. *Physical Review Letters*, 103(9):093902, 2009. 1.4

[40] J. Heading. Phase integral methods I. *The Quarterly Journal of Mechanics and Applied Mathematics*, 15(2):215–244, 1962. 3.4.5

[41] N. Honda, T. Kawai, and Y. Takei. *Virtual Turning Points*. Springer, 2015. (document), 3.4.1, 3.4.7.5, 3.4.7.6, 3.4.7.6, 3.4.7.6, 3.13, 3.4.7.6, 3.14, 3.15, 3.4.7.6

[42] A. Iserles. *A First Course in the Numerical Analysis of Differential Equations*. Cambridge University Press, New York, NY, USA, 2nd edition, 2008.

[43] G. Källén and W. Pauli. *Dan Mat Fys Medd*, 30:No–7, 1955. 1.1

[44] S. Klaiman, U. Günther, and N. Moiseyev. Visualization of branch points in *PT*-symmetric waveguides. *Physical review letters*, 101(8):080402, 2008. 1.4

[45] T. D. Lee. Some special examples in renormalizable field theory. *Physical Review*, 95(5):1329, 1954. 1.1

[46] Z. Lin, H. Ramezani, T. Eichelkraut, T. Kottos, H. Cao, and D. N. Christodoulides. Unidirectional invisibility induced by *PT*-symmetric periodic structures. *Physical Review Letters*, 106(21):213901, 2011. 1.4

[47] B. Peng, S. K. Ozdemir, F. C. Lei, F. Monifi, M. Gianfreda, G. L. Long, S. H. Fan, F. Nori, C. M. Bender, and L. Yang. Nonreciprocal light transmission in parity-time-symmetric whispering-gallery microcavities. *arXiv preprint arXiv:1308.4564*, 2013. 1.4

[48] B. Peng, ŞK. Özdemir, S. Rotter, H. Yilmaz, M. Liertzer, F. Monifi, C. M. Bender, F. Nori, and L. Yang. Loss-induced suppression and revival of lasing. *Science*, 346(6207):328–332, 2014. 1.4

[49] H. Ramezani, D. N. Christodoulides, V. Kovanis, I. Vitebskiy, and T. Kottos. *PT*-Symmetric Talbot Effects. *Physical review letters*, 109(3):033902, 2012. 1.4

[50] H. Ramezani, J. Schindler, F. M. Ellis, U. Günther, and T. Kottos. Bypassing the bandwidth theorem with *PT*-symmetry. *Physical Review A*, 85(6):062122, 2012. 1.4, 1.4

[51] A. Regensburger, C. Bersch, M. A. Miri, G. Onishchukov, D. N. Christodoulides, and U. Peschel. Parity-time synthetic photonic lattices. *Nature*, 488(7410):167–171, 2012. 1.4

[52] J. Rubinstein, P. Sternberg, and Q. Ma. Bifurcation diagram and pattern formation of phase slip centers in superconducting wires driven with electric currents. *Physical review letters*, 99(16):167003, 2007. 1.4

[53] C. E. Rüter, K. G. Makris, R. El-Ganainy, D. N. Christodoulides, M. Segev, and D. Kip. Observation of parity-time symmetry in optics. *Nature Physics*, 6(3):192–195, 2010. 1.4

[54] J. Schindler, A. Li, M. C. Zheng, F. M. Ellis, and T. Kottos. Experimental study of active LRC circuits with *PT*-symmetries. *Physical Review A*, 84(4):040101, 2011. (document), 1, 1.4, 1.1, 1.2, 1.3, 1.4

[55] J. Schindler, Z. Lin, J. M. Lee, H. Ramezani, F. M. Ellis, and T. Kottos. *PT*-symmetric electronics. *Journal of Physics A: Mathematical and Theoretical*, 45(44):444029, 2012.

[56] S. Schmidt and S. P. Klevansky. Generation of families of spectra in *PT*-symmetric quantum mechanics and scalar bosonic field theory. *Philosophical Transactions of the Royal Society of London A: Mathematical, Physical and Engineering Sciences*, 371(1989):20120049, 2013. 2.3.3, 2.3.3, 3.2, 3.2

[57] M. Sher. Electroweak Higgs potential and vacuum stability. *Physics Reports*, 179(5):273–418, 1989. 1.1

[58] M. Sorrell. Complex WKB analysis of a *PT*-symmetric eigenvalue problem. *Journal of Physics A Mathematical General*, 40:10319–10335, August 2007. 3.4.2, 3.4.7.2

[59] A. Szameit, M. C. Rechtsman, O. Bahat-Treidel, and M. Segev. *PT*-symmetry in honeycomb photonic lattices. *Physical Review A*, 84(2):021806, 2011. 1.4

[60] N. Turok. On quantum tunneling in real time. *eprint arXiv:1312.1772*, Dec 2013.

[61] R. White. *Asymptotic Analysis of Differential Equations*. Imperial College Press, revised edition, 2012. 3.4.1, 3.4.1, 3.4.2, 2

[62] K. Zhao, M. Schaden, and Z. Wu. Enhanced magnetic resonance signal of spin-polarized Rb atoms near surfaces of coated cells. *Physical Review A*, 81(4):042903, 2010. 1.4

[63] C. Zheng, L. Hao, and G. L. Long. Observation of a fast evolution in a parity-time-symmetric system. *Philosophical Transactions of the Royal Society of London A: Mathematical, Physical and Engineering Sciences*, 371(1989):20120053, 2013. 1.1, 1.4

[64] X. F. Zhu, H. Ramezani, C. Z. Shi, J. Zhu, and X. Zhang. *PT*-symmetric acoustics. *Physical Review X*, 4(3):031042, 2014. 1.4

Appendix

Fortran Code for Gauss-Legendre Integrator

Algorithm 1 The 8th order implicit Gauss-Legendre integrator (GLI)

```
subroutine gl8(y, dt)
        integer, parameter :: s = 4 ! order of integrator is 2*s
        integer, parameter :: n = 4 ! number of dynamical variables
        real y(n), g(n,s), dt; integer i, k
! Butcher tableau for 10th order Gauss–Legendre method
        real, parameter :: a(s,s) = reshape((/ &
                0.86963711284363464343265987305499851 8Q–1,
–0.26604180084998793313385130476953109 3Q–1, &
                0.12627462689404724515056880574618093 6Q–1,
–0.35551496857956831569109818495695886 0Q–2, &
                0.18811811749986807165068554508717116 0Q0,
  0.16303628871563653565673401269450014 8Q0,  &
               –0.27880428602470895224151106418997410 7Q–1,
 0.67355005945381555153986690857037588 9Q–2, &
                0.16719192197418877317113330552529594 5Q0,
  0.35395300603374396653761913180799770 7Q0,  &
                0.16303628871563653565673401269450014 8Q0,
 –0.14190694931141142964153570476171456 4Q–1, &
                0.17748257225452261184344295646056929 2Q0,
  0.31344511474186834679841114481438220 3Q0,  &
                0.35267675751627186462685315586595340 6Q0,
  0.86963711284363464343265987305499851 8Q–1 /),(/s,s/))
        real, parameter ::   b(s) = (/ &
                0.17392742256872692868653197461099970 4Q0,
  0.32607257743127307131346802538900029 6Q0,  &
                0.32607257743127307131346802538900029 6Q0,
  0.17392742256872692868653197461099970 4Q0  /)
! iterate trial steps
        g = 0.0;
        do k = 1,16
                g = matmul(g,a)
                do i = 1,s
                        call evalf(y + g(:,i)*dt, g(:,i))
                end do
        end do
! update the solution
        y = y + matmul(g,b)*dt
end subroutine gl8
```